Galaxies in the Distant Universe: Colours, Redshifts and Star Formation

Mandakranta Banerji

Thesis submitted for the Degree of Doctor of Philosophy
of University College London

Department of Physics & Astronomy

UNIVERSITY COLLEGE LONDON

August 2009

I, Mandakranta Banerji, confirm that the work presented in this thesis is my own. Where information has been derived from other sources, I confirm that this has been indicated in the thesis.

In particular I note these contributions from third-parties:

- The work presented in Chapter 2 has been published in Abdalla *et al.* (2008*b*) as well as Lahav *et al.* (2009). I am a co-author of both these publications and the majority of the work presented in Chapter 2 is derived from, although not wholly restricted to, my contributions to these publications. Figure 2.1 was provided by Eduardo Cypriano and Figure 2.7 was provided by Filipe Abdalla

- The work presented in Chapter 3 has been published in Banerji *et al.* (2008). The code used to calculate galaxy power spectra in this chapter has been written by Filipe Abdalla. Mock catalogues for the simulations were obtained from Huan Lin and Peter Capak.

- The work presented in Chapter 4 was undertaken by myself as part of the DUNE photometric redshift working group. Mock catalogues for the simulations were obtained from Peter Capak.

- The code for calculating stellar masses in Chapter 6 was provided by Ignacio Ferreras.

- The work presented in Chapter 7 has been published in Banerji *et al.* (2009*a*) and Banerji *et al.* (2009*b*). The UCL_PDR code used in Chapter 7 was written by Tom Bell and Serena Viti.

To Mum & Dad

who always believed in me

"Looking at these stars suddenly dwarfed my own troubles and all the gravities of terrestrial life. I thought of their unfathomable distance, and the slow inevitable drift of their movements out of the unknown past into the unknown future"

— H. G. Wells (The Time Machine)

"What are these mysteries? Was there only one world after all, which spent its time dreaming of others?"

— Phillip Pullman (The Subtle Knife)

ABSTRACT

This thesis explores the properties of distant galaxies in the Universe, in particular their redshifts, morphologies, evolutionary history and star formation processes within them.

The first part is concerned with photometric redshift estimation. I present different photo-z methods and compare them using a sample of Luminous Red Galaxies (LRGs). Photo-z design studies are then carried out for the upcoming Dark Energy Survey as well as the planned space-based Euclid mission. I show the importance of adding near infra-red data to optical data in obtaining accurate redshift estimates for both these projects and how this may prove crucial for some of the cosmological analysis intended with them.

In Chapter 5, I present automated morphological classifications for ~ 1 million objects from the Sloan Digital Sky Survey and compare them to visual classifications of the same objects obtained as part of the Galaxy Zoo project. I find that a neural network is able to reproduce the human classifications to an accuracy of better than 90%.

In Chapter 6 I study the evolution of the luminosity and mass functions of LRGs using spectroscopic data. I find that these objects are mainly composed of old stars that were formed very early in the history of the Universe and also that the most massive objects were already well assembled at redshifts of ~ 0.8 in direct contradiction with predictions of most current models of galaxy formation.

Chapter 7 presents an alternative means of determining the approximate nature of the stellar initial mass function of extragalactic systems by considering timescales for low-mass star formation in different environments. I find that a galaxy's metallicity is a key parameter in determining the shape of its IMF and make some predictions about trends in molecular emission in different extragalactic systems with different IMFs.

ACKNOWLEDGEMENTS

First and foremost, I would like to thank my supervisor Ofer Lahav for all his help, support and wisdom that he has imparted to me over the course of the last three years. I feel very lucky to have been his student and I look forward to many more years of collaboration and learning even more from him in the future. Thank you also to the numerous other people I have discussed this work with, without whose input this thesis would not have been completed. In particular, I am indebted to Serena Viti, David Williams, Filipe Abdalla and Ignacio Ferreras for their help with many different aspects of this work. Thank you also to Paul Hewett for always replying to my somewhat frantic emails, especially through my battles with synthetic photometry, and for giving me a great job!

To the many friends I have made at UCL and my flatmates over the course of the three years, you know who you are! Thank you for all the good times! I will remember especially the many delightful conversations that I always walked into in G18, all the trips to the Housman Room and the numerous coffee and cookie breaks. I want to also thank my lovely office mates, particularly those in my year that have been there since the beginning and till the end. Caz: Without those chocolates, jelly beans and biscuits, I would not have survived the last few months! Shaun: Cheers for the many memorable musical interludes in the office, for all the whingeing about code, bugs and job-hunting and for the many football games we watched at the Rocket! And Bethan: Thanks for dragging me to the gym (sometimes against my will, I'll admit), for all the moral support at those first few astronomy conferences (sharing a double bed with anyone else at that first ever summer school would have been traumatic!) and finally for being such a wonderful flatmate. I'll be on the lookout for the first conference I can find in Baltimore!

Thank you also to the Cambridge crew: Kaj, Emma, Eric, Greg, Steve etc. who have made living in London a lot of fun these last three years!

CONTENTS

LIST OF FIGURES

LIST OF TABLES

INTRODUCTION

In this introductory chapter, I provide some of the theoretical framework necessary to understand the work presented in this thesis. I start with an overview of the current standard model of cosmology set within the framework of Einstein's theory of relativity. I then move on to a discussion of galaxies in our Universe and the tools used to infer their properties and evolution. Bearing in mind the close link between galaxy evolution and star formation, I introduce some of the key physical processes involved in the collapse of a molecular cloud and formation of a star. The last part of this chapter is dedicated to a description of current and future data sets that are becoming available to astronomers over the entire range of the electromagnetic spectrum and that will allow us to make significant strides in the fields of cosmology and galaxy evolution.

1.1 Cosmology

Cosmology refers to the study of the Universe in its entirety - how it came to be, what it is made of and where it is headed. While such a study has a long history in the pages of both religion and philosophy, the study of observational or physical cosmology is a much more recent phenomenon. It was not until the early 1920s that Edwin Hubble discovered that there existed galaxies outside our own Milky Way. By observing special kinds of stars known as Cepheid variables whose intrinsic luminosity follows a well-known trend (such objects are called *standard candles*) he was able to infer their distances from their measured luminosities and concluded that they lay outside the confines of our own Milky Way (Hubble 1925). It is probably fair to say that observational cosmology began around the same time when the work of Vesto Melvin Slipher and then Hubble

led to the discovery that distant galaxies in our Universe are receding away from us with a recession velocity, v, that is proportional to their distance, d (Hubble & Humason 1931).

$$v = H_0 d, \tag{1.1}$$

The proportionality constant is known as Hubble's constant and is the Hubble parameter at the present day, t_0. This Hubble's law isn't exact. It doesn't hold for example for nearby galaxies which typically posess random motions known as peculiar velocities. However, for the majority of the galaxies studied in this thesis, Hubble's law can be taken to be fairly universal and the latest datasets suggest a Hubble constant of $H_0 = 70.1 \pm 1.3$ km s^{-1} Mpc^{-1} (Dunkley *et al.* 2009) where $1\text{pc} \simeq 3 \times 10^{16}$m. Due to the uncertainties in the Hubble constant, cosmologists often work in terms of h, where $H_0 = 100h$km s^{-1} Mpc^{-1}. The fact that all distant galaxies follow Hubble's law, tells us that we live in an expanding Universe. Due to this expansion, an object emitting light at a wavelength of λ_e would have this light observed with a different wavelength of λ_o. The change in wavelength defines the redshift, z

$$z = \frac{\lambda_o}{\lambda_e} - 1. \tag{1.2}$$

For an expanding Universe, $\lambda_o > \lambda_e$ i.e. a shift towards longer and redder wavelengths - hence the term *red*shift. The redshift of a galaxy is typically calculated by looking at the shift in standard spectral lines in a galaxy's spectrum - see § 1.2. However, this method of calculating redshifts involves obtaining a high-resolution spectrum of each galaxy using a spectrograph which can be a time-consuming process. This makes it unfeasible for many future galaxy surveys that aim to study hundreds of millions and even billions of galaxies in our Universe. We really have come a long way from the days of Hubble! In Chapters 2, 3 and 4, a new method of calculating redshifts from the colours of galaxies will be discussed and applied to future galaxy surveys.

The expansion rate of the Universe is measured in standard cosmology using a quantity called the scale factor, $a(t)$. Cosmologists most often work in terms of comoving coordinates which are carried along with the expansion and the relationship between the real distance between two points, x and the comoving distance, χ is:

$$x = a(t)\chi. \tag{1.3}$$

If the Universe is expanding today this must mean that early in its history, all points in the Universe were much closer together. In 1949, Fred Hoyle, in a popular radio broadcast used the term Big Bang to describe the origin of the Universe from some hot dense initial condition although he continued to be a proponent of the steady-state theory where the Universe does not change its look over time. The Universe is now thought to have originated from the Big Bang some 14 billion years ago and the Big Bang model has become the standard model to describe the origin and evolution of our Universe. This model has as its framework, Einstein's general theory of relativity, a geometric theory of gravitation which introduced the revolutionary idea of a four dimensional spacetime manifold with three spatial and one temporal coordinate. Within this theory, any non-trivial mass distribution will induce a non-trivial curvature on the manifold much in the same way a ball placed on a rubber sheet curves the sheet around it.

The expansion of the Universe whose discovery gave birth to the field of observational cosmology, is a logical outcome of Einstein's theory of relativity. The cosmological principle states that the Universe is both homogenous (i.e. uniform in both composition and density) and isotropic (i.e. has no preferred direction) on large scales ($> 100\ \mathrm{h}^{-1}\mathrm{Mpc}$). The latter is verified by observations of the cosmic microwave background, a uniform radiation bathing the sky in all directions with a temperature of about 3K that was discovered accidentally by Penzias & Wilson (1965) and predicted to be a relic of the Big Bang (Dicke *et al.* 1965). Homogeneity is implied by the assumptions of isotropy and the Copernican principle which states that we do not occupy a privileged position as observers of the Universe. Solving Einstein's equations after assuming the cosmological principle gives rise to the Friedmann equations:

$$\frac{\dot{a}^2}{a} = H^2 = \frac{8\pi G\rho}{3} - \frac{k}{a^2}, \tag{1.4}$$

$$\ddot{a} = \frac{-4\pi G(\rho + 3p)a}{3}, \tag{1.5}$$

where ρ is the mean energy density of the Universe which is composed of components from matter, ρ_m as well as any other unknown energy often referred to by cosmologists as dark energy, ρ_Λ. p is the associated pressure, k is the curvature of the Universe, $a = a(t)$ is the scale factor and G is the gravitational constant. The curvature, k relates to the geometry of the Universe such that $k = 0$ corresponds to a flat Universe where parallel light remains parallel, $k < 0$ corresponds to an open Universe where parallel light rays will eventually diverge and $k > 0$ corresponds to a closed Universe where parallel light rays eventually converge.

The Big Bang theory gave rise to a number of problems which were eventually solved by a theory proposed by Guth & Tye (1980); Guth (1981) known as inflation. In inflationary theories, the Universe is subject to a phase of accelerated expansion very early in its history and this helps explain among other things the growth of inhomogenous structures such as stars and galaxies from the early homogenous Universe.

1.1.1 The Standard Cosmological Model

The standard model of cosmology was born from observational evidence that the Universe was correctly described by the equations of general relativity. Inflation predicts that the Universe should be flat with $k = 0$ and this is confirmed by observations of the cosmic microwave background (Bennett *et al.* 2003; Dunkley *et al.* 2009) after assuming a prior on h. For convenience, we define the matter energy density, $\Omega_m = 8\pi G\rho_m/3H^2$, the dark or vaccum energy density, $\Omega_\Lambda = 8\pi G\rho_\Lambda/3H^2$ and the curvature, $\Omega_k = -k/(aH)^2$. Therefore, Eq 1.4 simplifies to

$$\Omega_m + \Omega_\Lambda + \Omega_k = 1. \tag{1.6}$$

Assuming a flat Universe with $\Omega_k = 0$ means $\Omega_m + \Omega_\Lambda = 1$. For many years it was believed that $\Omega_\Lambda = 0$ and that the Universe's energy density was composed entirely of matter. It was not until the early 1990s that several authors (Efstathiou *et al.* 1990; Carroll *et al.* 1992; White *et al.* 1993; Ostriker & Steinhardt 1995) found evidence for a non-zero Ω_Λ from measurements of the large-scale structure of the Universe, the age of the Universe and the baryonic content of galaxy clusters. See Calder & Lahav (2008) for a review of the history of dark energy. A non-zero Ω_Λ was confirmed later by the studies of Riess et al. (1998); Schmidt *et al.* (1998); Perlmutter *et al.* (1999) and since then observational evidence from many independent experiments has been mounting in favour of $\Omega_m = 0.3$ and $\Omega_\Lambda = 0.7$. The matter part of this equation can also be split into further components. Baryons such as the protons and neutrons that make up atoms, molecules and us, only account for 4% of the Universe's energy density ($\Omega_b = 0.04$). The rest of the matter ($\Omega_c = 0.26$) is invisible or dark - it interacts only gravitationally but not electromagnetically and was first discovered by Zwicky in 1933 by studying the velocities of galaxies in the Coma Cluster (Zwicky 1933). Zwicky called this dark matter the *missing mass*. The dark matter is thought to be *cold* which means that the particles that it is composed of travel at slow speeds which are much smaller than the speed of light. This assumption is necessary to explain the observed structures of our Universe. Galaxies in our Universe clump together to form clusters and superclusters of

galaxies that exist in huge filaments punctuated by massive voids. As the galaxies formed these structures through gravitational interaction between both the dark and baryonic matter that makes them up, the scale of the structures they form depends crucially on the velocity of the dark matter particles.

The aim of many modern cosmology experiments is to pin down the cosmological parameters such as Ω_m, Ω_Λ and h to the utmost precision. Different cosmological probes are now used to constrain the values of these parameters. These include the clustering pattern of galaxies in our Universe e.g. (Eisenstein et al. 2005; Cole *et al.* 2005) which will be described in more detail in §1.1.4 as well as Chapter 3 of this thesis. Other probes include weak gravitational lensing (Wittman *et al.* 2000; Bacon *et al.* 2000; Van Waerbeke *et al.* 2000; Hoekstra *et al.* 2006; Semboloni *et al.* 2006) which involves measuring the bending of light from distant galaxies by the intervening dark matter (see Chapter 4), counting the number of galaxy clusters as well as measuring the light from supernovae in distant galaxies which are known to act as standard candles (Riess et al. 1998; Perlmutter *et al.* 1999; Schmidt *et al.* 1998). The latter has proven to be the major observational evidence for a non-zero Ω_Λ as these observations show that distant galaxies are not only receding away from us but that their expansion is now accelerating. This can only be explained if the Universe has in addition to its baryonic and dark matter, some additional and mysterious form of dark energy. By designing experiments that aim to probe both the nature of dark energy and dark matter, cosmologists hope to better understand these elusive entities and perhaps even challenge the current standard cosmological model. Throughout this thesis however, I work within the framework of the standard cosmological model with $\Omega_b = 0.04$, $\Omega_c = 0.26$, $\Omega_\Lambda = 0.7$ and $h = 0.7$.

1.1.2 The Age of the Universe

Distant galaxies in our Universe are observed as they were very early in the history of the Universe due to the finite amount of time that it takes for the light from them to reach us. In observational cosmology therefore, it is important to be able to link the distance or redshift of a galaxy to the epoch at which it is observed to be. The lookback time is defined as the difference in time between an event which happened at redshift, z and today. It is given by:

$$\Delta t = \frac{1}{H_0} \int_0^z \frac{(1+z)^{-1}dz}{(1+z)^2(1+\Omega_m^0 z - z(2+z)\Omega_\Lambda^0)},$$ (1.7)

assuming a Universe composed of matter and some form of dark energy. The age of the Universe

is simply the integral evaluated to ∞.

1.1.3 Distance Measures in Cosmology

In an expanding and possibly curved space-time, the distance between two objects is not uniquely defined as is the case in standard Euclidean geometry. As the Universe is expanding, one can work either in terms of the comoving distance which remains fixed as the Universe expands or the physical distance which grows as the Universe expands. The study of observational cosmology considers how distant objects with given properties such as luminosity and size would appear to us given the geometry and composition of the Universe. In this section, some standard distance measures are described that will be used throughout this thesis.

The redshift has already been described as involving the ratio of the wavelength of light emitted by a distant object to the wavelength at which the light is observed - Eq 1.2. The redshift in turn is related to the scale factor $a(t)$ by:

$$1 + z = \frac{a(t_o)}{a(t_e)}. \tag{1.8}$$

The comoving distance, χ is the simplest measure of distance and is the distance between two points measured along a path defined at the present cosmological time. For objects moving with the Hubble expansion, the comoving distance remains constant with time.

$$\chi = \int_{t_e}^{t} \frac{c\,dt'}{a(t')} = \int_{a}^{1} \frac{da'}{a'^2 H(a')} = \frac{c}{H_0} \int_{0}^{z} \frac{dz'}{h(z')}, \tag{1.9}$$

where a is the scale factor, t_e is the time at which the light from the object is emitted and t is the present day. The integral is often more usefully expressed as an integral over the scale factor or redshift.

The luminosity distance, D_l is a way of expressing the amount of light received from a distant object. If we assume that the flux of an object decreases with distance according to an inverse square law, D_l is the distance that the object would consequently appear to have. This is not in fact the actual distance both because the Universe need not be flat and due to the fact that it is expanding. The luminosity distance is related to the comoving distance as follows

$$D_l = (1 + z)\chi. \tag{1.10}$$

The angular diameter distance, D_A is a measure of how distant objects of a known physical size appear to be once again under the assumptions of Euclidean geometry. For a flat Universe, it is related to the comoving distance and the luminosity distance by

$$D_A^{flat} = \frac{\chi}{(1+z)} = \frac{D_L}{(1+z)^2}.$$
(1.11)

If the Universe is curved, the equation for D_A becomes

$$D_A = \frac{a}{H_0\sqrt{|\Omega_k|}} \begin{cases} \sinh(\sqrt{\Omega_k}H_0\chi) & \Omega_k > 0 \\ \sin(\sqrt{-\Omega_k}H_0\chi) & \Omega_k < 0 \end{cases}$$

For objects at low redshift that are relatively nearby, the separations are approximately Euclidean and so these three distance measures roughly coincide.

1.1.4 Galaxy Clustering as a Cosmological Probe

One of the most remarkable features of our Universe is the degree to which galaxies are clustered given the initial homogeneities in the early Universe that they grew out of. In order to understand this clustering pattern, one has to understand the process of structure formation in our Universe. After inflation has taken place, the Universe is thought to consist of a soup of hot thermal particles and the energy density is entirely dominated by radiation. As the Universe cools and expands, the particles begin to slow down and ordinary matter starts to dominate. Eventually atoms form as free electrons bind to nuclei. The photons that were previously scattering off the free electrons through Thomson scattering are no longer bound to the matter and escape making the Universe transparent. The time at which this occurs is known as the epoch of recombination. These photons are today seen as the cosmic microwave background. As the matter starts to dominate, tiny inhomogeinities left by inflation are amplified by gravitational collapse. Matter falls towards denser regions making the rarefied regions even more rarefied. The density inhomogeneities go from being described by simple linear differential equations to highly non-linear equations and it is in the non-linear regime that structures such as galaxies and galaxy clusters begin to grow. As stars form and light up the galaxy, electromagnetic processes become important and drive the evolution of the galaxies and clusters (§ 1.2).

In this section however, we are concerned with how the large-scale structure of galaxies in our Universe can be used to constrain the cosmological parameters that define our Universe. The

clustering pattern of galaxies is often measured in terms of two variables that condense the vast amounts of information present in large galaxy samples to easily quantifiable properties. The two-point correlation function, $\xi(r)$ measures the excess probability above random of two galaxies having a given separation, r and the power spectrum, $P(k)$ decomposes the clustering pattern into waves with wavenumber, $k = 2\pi/\lambda$ and gives the typical amplitude at a particular wavenumber. Mathematically, transforming from the distance space to a wavelength space is equivalent to taking a Fourier transform of the correlation function to give the power spectrum.

The initial power spectrum of density fluctuations in the early Universe is given by

$$P(k) = Ak^n T^2(k),\tag{1.12}$$

where $T(k)$ is known as the transfer function and encompasses important physics from the very early Universe. This function depends crucially on the matter density of the Universe as well as the Hubble parameter. In Chapter 3, I will be using the analytical expression for the transfer function derived by Eisenstein & Hu (1998). The parameters, A and n define the form of the initial density perturbations of the Universe and can be constrained using cosmological data sets. In 1977 Harrison & Zeldovich proposed a value of $n = 1$ which is also consistent with inflationary theories. There are many codes such as CMBFAST (Seljak & Zaldarriaga 1996) that exist for computing the theoretical matter power spectrum given a set of cosmological parameters. What one measures from a galaxy survey however, is the galaxy power spectrum which has the same shape as the matter power spectrum but may be *biased* with respect to the matter power spectrum. This is because the galaxy power spectrum gives the statistical distribution of luminous matter in our Universe which may or may not be the same as the distribution of dark matter. If we assume that the galaxies linearly trace the underlying matter distribution and that the bias is independent of scale, the galaxy power spectrum in the linear regime is given by:

$$P_g(k,z) = D^2(z)b^2(z)P(k),\tag{1.13}$$

where $D(z)$ is the linear growth factor normalised to the present day and $b(z)$ is the bias. The growth factor describes the growth of the initial density fluctuations over time as these evolve to form the galaxies, clusters and superclusters we see today and therefore it modifies the amplitude of the observed galaxy power spectrum. The presence of dark energy changes the growth factor at late times. The bias tells us how the galaxy clustering is different from the dark matter clustering.

Although this bias can be redshift dependent, in Chapter 3 where I compute the galaxy power spectrum, I assume a constant bias.

1.2 Galaxies

Galaxies in our Universe not only act as beacons of light that can be used to probe the dark Universe but they are themselves very interesting and complicated systems to study. While the distribution of mass in our Universe is governed by the laws of gravity and is thought to be relatively well understood owing mainly to progress in the field of N-body simulations (Aarseth 2003; Springel *et al.* 2005), the distribution of light depends on more complicated and non-linear processes such as gas cooling, star formation, supernova feedback and dust obscuration which are much harder to model and often require a semi-analytic approach (Somerville 1997; Bower *et al.* 2006). However, as the light from distant galaxies has taken a finite amount of time to reach us, distant galaxies are seen as they were several millions or billions of years ago. By observing these galaxies in a careful and well-defined manner and comparing them to models, we can therefore hope to understand how they form and evolve into structures like our own Milky Way.

1.2.1 Morphological Classification

Edwin Hubble was the first man to classify galaxies according to their morphology and devised the now well known *tuning fork* diagram shown in Figure 1.1 (Hubble 1926). He originally thought that the elliptical galaxies to the left of the tuning fork were younger systems that evolved into the spirals on the right. Even though we now know that this is not the case and in fact that the opposite is true in some sense, the nomenclature of describing elliptical galaxies as *early types* and spiral galaxies as *late types* has stuck. There are many sub-divisions within ellipticals and spirals. However in most of this thesis, I will make reference to only early and late type systems. In Chapter 5, I attempt to classify galaxies morphologically by means of automated machine-learning algorithms.

The morphological classifications are also correlated in some sense with more fundamental properties of the galaxies themselves. For example, most present day elliptical galaxies are thought to be composed of old stars such as red giants and are not thought to have experienced any recent episodes of star formation. These red giants give elliptical galaxies their characteristic red colours and a spectrum that is dominated by the 4000 Åbreak. Most of these early type systems also contain little gas or dust. Such systems are thought to have formed through the merging of
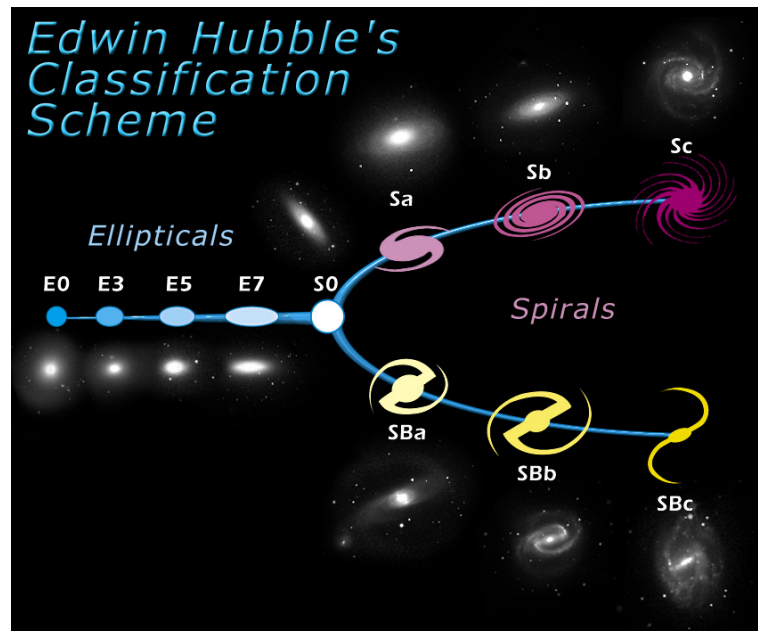
Figure 1.1: Hubble's tuning fork diagram for morphological classification of galaxies. Image provided courtesy: skyserver.sdss.org

two or more similarly-sized component galaxies. Spiral galaxies on the other hand like our own Milky Way, are actively star forming and tend to have bluer colours. These galaxies contain numerous clouds of gas and dust and their spectrum is dominated by the presence of emission lines originating from the significant gas component. While elliptical galaxies are found to be more common in dense clusters, spirals tend to vastly outnumber them in the field. This is known as the morphology-density relation where the morphology of a galaxy is correlated with the density of the environment in which it lives (Dressler 1980). Much of this thesis deals with elliptical galaxy populations and I therefore describe these objects now in a little more detail.

Elliptical Galaxies: As elliptical galaxies are some of the oldest objects in our Universe, they are often considered testbeds for theories of galaxy formation and evolution. There are currently two highly debated views as to how these objects formed and evolved. In the ΛCDM cosmology already described, elliptical galaxies are thought to be built up through successive mergers of smaller components (Toomre & Toomre 1972). This hierarchical picture of massive galaxy formation is supported by the detailed simulations of White & Rees (1978); Croton *et al.* (2006); De Lucia *et al.* (2006). Although observations of massive elliptical galaxies suggest that the stars in these objects are very old and were formed in a burst very early in the history of the Universe,

this can be reconciled with the simulations by requiring that the stars are formed early in relatively small units before merging at later times to form the massive ellipticals we see today. The formation of more younger stars during the merging process can be *switched off* in the simulations by invoking feedback processes that suppress the condensation of gas in massive halos for example the presence of active galactic nuclei (AGN). However, some recent observations suggest not only that these massive ellipticals contain old stars, but also that they were already well assembled at high redshifts with the most massive objects being the first ones to be assembled (Cimatti *et al.* 2006). This is in direct contradiction to the hierarchical picture of galaxy formation and requires a different more classical formation theory known as the *monolithic collapse* scenario where the galaxies are formed and assembled at very high redshifts and have been passively evolving since then (Larson 1975). In Chapter 6, I study a sample of massive ellipticals in order to distinguish between these two theories of galaxy formation.

1.2.2 Galaxy Evolution

Galaxy evolution is a complicated and as yet poorly understood process and so far it has mainly been approached from two points of view. Studying the dynamical evolution of galaxies involves understanding its formation, collapse and the distribution of mass and light within the galaxy. On the other hand, spectral evolution deals with the study of the galaxy's stellar populations and how they evolve over time and hence analysing the evolution of the galaxy's combined spectrum, luminosity and colour. In this thesis, I will primarily be concerning myself with the latter and so I describe spectral evolution models of galaxies in more detail. However, note that in Chapter 5, I look at the morphologies of distant galaxies in our Universe which are predominantly shaped by their dynamical rather than star formation history.

1.2.2.1 Evolutionary Synthesis Modelling

The spectral evolution of galaxies is most often studied using evolutionary synthesis modelling. Originally developed by Tinsley (1972*a,b*), this method involves modelling the galaxy's spectrum at different epochs after assuming an analytical expression for the initial mass function - the mass distribution of the galaxy's stellar population - as well as the star formation rate of the galaxy. Together, the initial mass function and the star formation history tell us the relative numbers of stars of different masses in the galaxy at a given epoch. The other important ingredients in an evolutionary synthesis model are the stellar evolutionary tracks e.g. (Alongi *et al.* 1993; Bressan *et al.* 1993; Girardi *et al.* 1996) of one or more metallicities (Schaller *et al.* 1992; Charbonnel *et al.*

1996), stellar spectral libraries e.g. (Lejeune *et al.* 1997, 1998; Prugniel & Soubiran 2001) and some sort of chemical enrichment law. The stars evolve according to these prescriptions and at any given epoch, the galaxy's spectrum can then be built up by adding the spectra of all the stars. In such models, the galaxy is taken to be a closed system and it is assumed that the gas returned by dying stars is transformed back into new stars. I will now describe three of the fundamental inputs into these spectral evolution models in more detail, which will be relevant in discussions throughout the rest of this thesis.

The Star Formation Rate: There are two main prescriptions that are commonly used to model the star formation rate of a galaxy in evolutionary synthesis models. The first is where all the stars are formed in a single burst of star formation occuring at the age of the galaxy. This prescription is usually used to model very old elliptical galaxies. If however there is some residual star formation still occurring, an exponentially declining star formation rate is used such that SFR(t)$\propto$exp(-t/τ). The star formation timescales, τ required to reproduce the observed broadband colours of different galaxy types shown in Figure 1.1 are given in Figure 1.2 along with the galaxy spectra subsequently produced using the PEGASE (Fioc & Rocca-Volmerange 1997) evolutionary synthesis code. These star formation timescales for each galaxy type have been taken from the HyperZ photometric redshift package user manual[1]. An irregular galaxy has constant star formation.

The Initial Mass Function: The initial mass function in evolutionary synthesis models is often stated in terms of a series of power-laws where $N(M)dM$, the number of stars with masses in the range M to $M+dM$ is proportional to $M^{-\alpha}$. The work of Edwin Salpeter favoured an IMF with $\alpha = 2.35$ now known as the Salpeter function (Salpeter 1955). Later authors extended this work by discovering variations in α for different mass ranges - e.g. Kennicutt (1983); Kroupa *et al.* (1993); Baldry & Glazebrook (2003); Chabrier (2003). The IMF cannot be directly observed but rather is inferred from looking at the luminosity function of stars - the number of stars per unit brightness - and converting this to a mass function after assuming a mass-to-light ratio based on stellar evolution models. In Chapter 7, an alternative way of determining the approximate nature of the IMF by looking at the efficiency of low-mass star formation in different environments, will be introduced.

Dust Extinction: The term extinction in astronomy is used to describe the absorption and scattering of electromagnetic radiation emitted by astronomical objects, by intervening dust and gas between the emitting object and the observer. It is usually expressed in terms of visual magnitudes. The extinction mainly arises due to the interstellar medium and the interstellar extinction

---

[1]http://webast.ast.obs-mip.fr/hyperz/manual.html
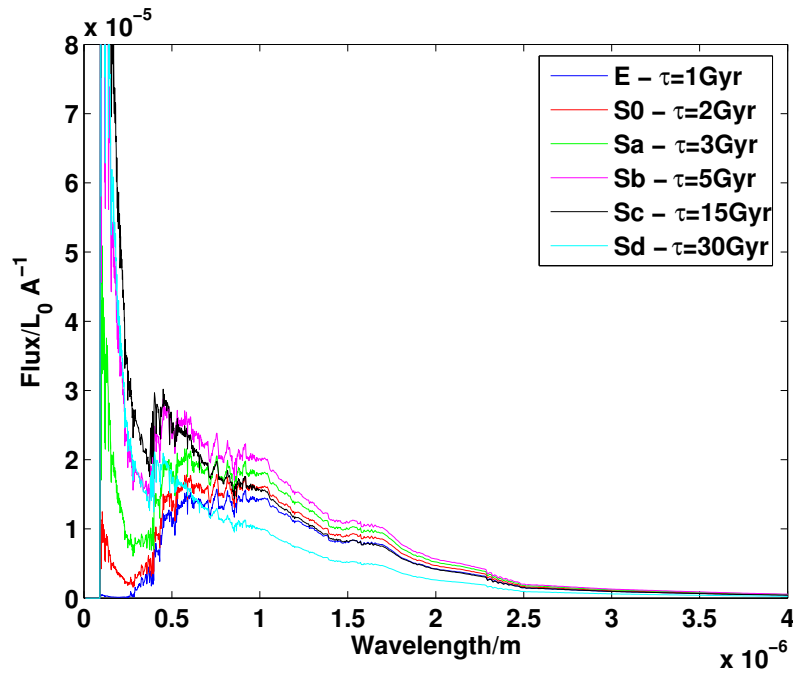
Figure 1.2: Spectra for galaxies of different morphological types with different star formation histories as output by the PEGASE (Fioc & Rocca-Volmerange 1997) evolutionary synthesis model.

varies with wavelength such that the extinction is stronger and therefore light is more attenuated at shorter wavelengths. Superimposed on this trend are various absorption features arising from for example dust grains in the interstellar medium. The extinction in our own Milky Way is fairly well characterised and dust maps have been constructed for the distribution of dust in our ISM (Schlegel *et al.* 1998). This extinction is usually represented by the single parameter, $R(V) = A_v/(A_B - A_v)$ $\simeq 3.1$. The extinction is also related to the column density of hydrogen atoms, $n(H)$ by $n(H)/A_v$ $\simeq 1.8 \times 10^{21}$ atoms cm^{-2} mag^{-1}. However, as will be seen in Chapter 7, the properties and composition of the ISM can be very different in external galaxies outside our Milky Way and significant star formation in such systems can lead to heavy obscuration by dust. Therefore, one may also have to account for dust extinction produced in the host galaxies from which the light is being emitted. As the dust preferentially attenuates light at shorter wavelengths, the light appears redder and therefore the term *reddening* is often used to signify dust extinction in external galaxies. The way in which the light is attenuated may also depend on the geometry and the angle at which we are viewing the galaxy. Some common extinction laws used to model the reddening of light from external galaxies are those of Allen (1976); Seaton (1979); Fitzpatrick (1986); Prevot *et al.* (1984); Calzetti et al. (2000). In almost all of this thesis, I will be using the Calzetti et al. (2000) law where

necessary.

Spectral evolution models have been widely developed in the literature and are commonly available as public packages - e.g. GALAXEV (Bruzual & Charlot 2003), PEGASE (Fioc & Rocca-Volmerange 1997), Starburst (Leitherer *et al.* 1999), GALEV (Kotulla *et al.* 2009) and the models of Maraston (1998, 2005) to name a few. Once a library of theoretical spectra has been built up using these models, these can be matched to observations in order to infer the spectral type, age, metallicity and other fundamental properties of the observed galaxy. These models can also be used in conjunction with broadband photometric observations where the galaxy is imaged in a set of broadband filters instead of obtaining a high resolution spectrum using a spectrograph. In the remainder of this section, I provide some technical details on calculating theoretical or *synthetic* magnitudes and colours from spectral evolution models in order to compare to photometric observations.

Synthetic Photometry: In order to obtain the theoretical fluxes in each of the broadband filters, i, from the model spectra, the filter transmission function, $S_i(\nu)$ is convolved with the spectrum, $F(\nu)$. The apparent magnitude of the galaxy seen through band i is then calculated after normalising the flux through the filter. The normalisation that is chosen depends on the particular photometric system that is being used. In the Vega system, the fluxes are normalised to the flux of the standard star Vega. In this thesis, I mainly work in the AB magnitude system which is defined such that a spectrum with constant flux per unit frequency has zero colour. In most spectral evolution models however, the flux density is given per unit wavelength. The magnitude in the AB system is then related to the flux per unit wavelength of the spectrum, F_λ by:

$$m_{AB} = -2.5 \log_{10} \left(\frac{\int \frac{\lambda}{hc} F_\lambda S_{i,\lambda} d\lambda}{\int \frac{\lambda}{hc} F^0_{AB,\lambda} S_{i,\lambda} d\lambda} \right), \tag{1.14}$$

(Girardi *et al.* 2002). The factors of $\frac{\lambda}{hc}$ come because in modern surveys, CCDs are used instead of bolometers that count the number of photons instead of measuring the total energy. The normalisation, $F^0_{AB,\lambda} = F^0_{AB,\nu} c/\lambda^2$ where $F^0_{AB,\nu}$=3.631×10^{-20} erg s^{-1} cm^{-2} Hz^{-1} is chosen such that a spectrum with constant flux per unit frequency has zero colour. For a CCD detector therefore Eq

1.14 simplifies to:

$$m_{AB} = -2.5 \log_{10} \left(\frac{\int \frac{\lambda}{hc} F_\lambda S_{i,\lambda} d\lambda}{\int \frac{1}{h\lambda} S_{i,\lambda} d\lambda} \right) - 48.6 \qquad (1.15)$$

The magnitudes obtained using this prescription from theoretical spectra of galaxies generated using evolutionary synthesis models, can be compared to observed magnitudes in order to infer a host of different galaxy properties including the age, metallicity, star formation history and stellar masses (see Chapter 6) and even a crude estimate of the redshift (see Chapter 2).

1.3 Star Formation

Galaxies are essentially huge conglomerations of $\sim 10^{10}$ to 10^{12} stars. As well as stars, galaxies may contain vast amounts of gas and dust from which the stars have been or are presently being formed. In the last section, it has already been demonstrated how the distribution of light in a galaxy and its observed broadband properties such as luminosity and colour depend fundamentally on the masses and ages of the stars that make it up. This forms the basis of evolutionary synthesis modelling of galaxies described in the previous section. Clearly an understanding of galaxy evolution requires a detailed understanding of the processes involved in star formation. While current telescopes allow us to look deep into molecular clouds - the birthplaces of stars - within our own galaxy (see Figure 1.3) and even some other nearby galaxies, such systems are difficult to resolve in galaxies in the distant Universe. However, an understanding of the processes involved in star formation allow us to make some reasonable guesses as to how these processes could be different in distant galaxies with properties that are quite different from our own Milky Way. I briefly describe some of the key processes involved in star formation here. For a more detailed description of star formation processes and the timescales involved, see Chapter 7.

The main driver for the collapse of a molecular cloud and formation of a star is clearly gravity. When a molecular cloud reaches a certain critical density, it collapses under its own weight leading to the dissipation of gravitational potential energy. Although the collapse may be hindered somewhat by thermal and turbulence pressures within the molecular cloud, in general the time taken for this collapse to occur can be roughly underestimated by considering the free-fall time which just depends on the density of the collapsing gas, ρ. This corresponds to a scenario with
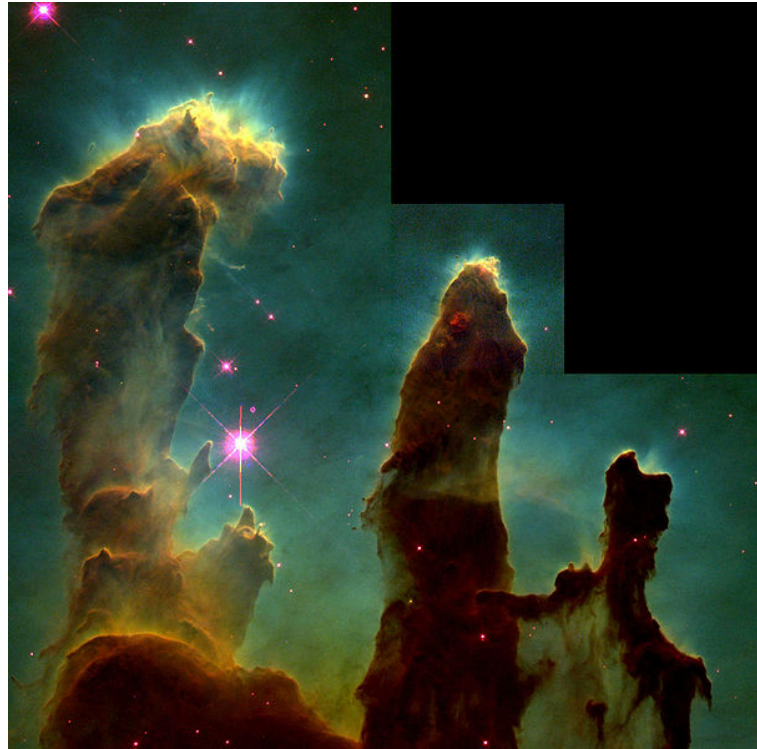
Figure 1.3: The *Pillars of Creation*: star-forming regions within the Eagle Nebula in our own Milky Way imaged using the Hubble Space Telescope. Image provided courtesy hubblesite.org

zero pressure.

$$t_{ff} = \sqrt{\frac{3\pi}{32G\rho}}.$$
(1.16)

There are two main factors that oppose the collapse of a molecular cloud under its own weight. Firstly, in order for the gas cloud to continue to collapse, it must lose energy through radiative cooling. This cooling process usually occurs through line emission in various atomic and molecular transitions or thermal emission from dust grains. The atomic and molecular transitions have characteristic spectral signatures that can be observed as tracers of star formation. If the gas cloud is unable to cool however, the high temperatures and densities will serve to stop the collapse and formation of the star.

Secondly, magnetic fields threading the cores of dense molecular clouds play an important role in supporting these clouds and many of the fragments within them (Mouschovias & Ciolek 1999). Magnetic field support was first invoked into star formation processes in order to solve two main problems. In a fully formed star, thermonuclear reactions in the core of the star balance the inward

pull of gravity but this is not the case in molecular clouds. If there were no other forces supporting molecular clouds, they would have collapsed into stars a long time ago. A process called ambipolar diffusion is responsible for the magnetic pressure that balances gravity within molecular clouds. In a star-forming region, ions and electrons are tied to the magnetic field and therefore resist collapse. Neutral particles are also indirectly tied to the magnetic field through collisions with the ions. However, if the fractional ionisation in a molecular cloud is low, the neutral particles are relatively unhindered and can therefore collapse due to gravitational instabilities.

The ability of magnetic fields to provide support against gravitational instability is determined by the ratio of the mass contained within an enclosed region of gas to the magnetic flux passing through the surface. The critical value of this ratio below which a cloud will be supported against gravitational collapse is given by

$$\left(\frac{M}{\Phi} \right)_{crit} = \frac{0.79}{\sqrt{\pi \mu_0 G}}, \tag{1.17}$$

where M is the mass enclosed, Φ is the magntic flux, μ_0 is the permeability of free space and G is the gravitational constant (Mouschovias & Spitzer 1976; Mestel 1999; Mac Low & Klessen 2004). Less than this critical value, the cores are *subcritical* and stable against collapse and above this the cores are *supercritical* and collapse on the free-fall timescale. Magnetic field support and therefore ambipolar diffusion is only important in critical and subcritical cores.

A second problem in the absence of magnetic fields arises due to angular momentum. As molecular clouds coalesce to form stars, the material rotates faster and faster creating extra angular momentum. This angular momentum must be transferred in some way otherwise the star would fly apart. Results of detailed simulations of star formation show that by flinging a small amount of matter outwards along magnetic field lines, the magnetic waves can remove a huge amount of angular momentum thus making star formation possible (Price & Bate 2007).

Magnetic fields have now been measured in different interstellar molecular clouds of different densities (Crutcher *et al.* 1987; Crutcher 1999) thus supporting the idea that they play a crucial role in star formation processes. However, a recent and slightly more controversial view is that the magnetic fields in star-forming regions are weak and it is turbulence pressure that inhibits the collapse of a molecular cloud (Elmegreen 2000; Mac Low & Klessen 2004). See McKee & Ostriker (2007) for a comprehensive review of the theory of star formation and the role of both magnetic fields and turbulence.

The balance of gravity, cooling as well as magnetic pressure determines the efficiency of the

formation of stars of different masses and therefore the form of the stellar initial mass function. Hydrodynamical simulations of star formation have already been relatively successful in reproducing the form of the observed IMF (Bate *et al.* 2003) although these simulations do not include the effects of magnetic or radiative pressure. In Chapter 7, I take a predominantly analytical approach incorporating all the relevant physical mechanisms involved in star formation, including magnetic and radiative pressure, in order to make predictions for the form of the IMF in different environments.

1.4 The Golden Age of Data

This is indeed an opportune time for the study of cosmology and galaxy evolution! Less than a hundred years ago, Edwin Hubble signalled the birth of observational cosmology by discovering that there are other galaxies outside our own Milky Way. Today we have datasets of millions of galaxies and in the next decade we will be pushing the boundaries of our observable Universe even further by observing hundreds of millions and even billions of galaxies back to a time when the Universe was only a fraction of its present age. This golden age of data will allow us to test with unprecedented accuracy both the standard model of cosmology as well as theories of galaxy formation and evolution. In this section I highlight some of the different data sets becoming available across the full range of the electromagnetic spectrum that will enable us to make new strides in observational cosmology. This thesis focusses on fully exploiting many of these new data sets.

1.4.1 Optical and Near Infra-red Wide-Field Imaging Surveys

The discovery of a non-zero Ω_Λ in the late nineties heralded the birth of a new generation of experiments designed to pin down the exact nature of this mysterious dark energy. Most cosmological probes require statistically significant samples of galaxies in order to map out the distribution of dark matter and dark energy in the Universe. Therefore there has been a great push to design galaxy surveys that can image hundreds of millions and even billions of galaxies across our observable Universe. The current largest data set is that from the Sloan Digital Sky Survey which has just been completed and has obtained photometric data in five different bands for ~ 360 million celestial objects (Abazajian et al. 2009). About 1 million of the galaxies also have high resolution spectra available. This data set has already been used to constrain cosmological models through measurements of the galaxy power spectrum (Percival *et al.* 2007) as well as for countless studies

of galaxy formation and evolution.

In the next generation, a number of large wide-field imaging surveys are being designed that will push the limits of these current data sets. In addition, spectroscopic surveys will also provide complementary means of constraining cosmological models as well as providing useful calibration sets for the photometric surveys. A summary of upcoming imaging and spectroscopic surveys is provided in Table 1.1.

The Dark Energy Survey (DES) due to start in 2011 (Annis *et al.* 2005) is an optical ground-based imaging survey covering around two fifths of the southern hemisphere. This survey will obtain photometric data in five optical bandpasses for around 300 million galaxies out to a redshift of 2. The survey will be complemented with data in the near infra-red bands from the Vista Hemisphere Survey (VHS) due to start in late 2009 (Arnaboldi et al. 2007). In Chapter 3, I look at the power of this combined data set in constraining cosmological models through measurements of galaxy clustering. Other larger and deeper ground-based optical photometric surveys such as the Large Synoptic Survey Telescope (LSST) are also planned over the next decade (Ivezic *et al.* 2008). LSST will image the entire southern sky and obtain photometric data of unprecedented depth ($\sim$ hundred million times fainter than can be seen by the unaided eye) for almost a billion galaxies in the Universe. Figure 1.4 gives a taste for what the night sky will look like with LSST. The survey however will cover an area 50,000 times greater than is shown in this image and in six optical bands.

Other experiments are planned that involve putting large mirrors into space to conduct all-sky galaxy surveys. The lack of an atmosphere in space means the image quality is far superior than is obtained from the ground allowing us to measure tiny distortions in the galaxy images induced as a result of the intervening dark matter between us and the observed galaxy. A space-based experiment called Euclid that has been designed to study exactly such distortions will be discussed in more detail in Chapter 4.

All these wide optical and near infra-red imaging surveys both from the ground and space, when combined with data from experiments that measure the cosmic microwave background and its temperature fluctuations, will enable us to test the standard model of cosmology to the utmost precision and perhaps even lead to the dawn of alternative theories of gravity to Einstein's GR.

1.4.2 Deep Spectroscopic Surveys

Although wide-field imaging surveys are extremely powerful in terms of obtaining statistically significant numbers of galaxies to test cosmological models, spectroscopy still remains the most

Survey	Area (deg^2)	Depth (Mag or Redshift)	Filters/Resolution	Schedule
KIDS (+Viking)	1500	$r < 24.4$	$ugri\,ZYH$	2008-2013
DES (+VHS)	5000	$r < 24$	$grizYJHK$	2011-2016
Pan-STARRS1 (PS1)	15000	$r < 24$	$grizy$	2008-2012
Pan-STARRS4 (PS4)	30000	$r < 25.6$	$grizy$	2012-2017
SkyMapper	15000	$g < 22.9$	$uvgriz$	2008-2011
HyperSuprime	2000	$r < 25$	$BVRiz$	2011-2016
PAU	8000	$i < 23$	50 narrow bands	2010-2015
LSST	30000	$g < 26$	$ugriz$	2014-2018
SNAP	4000	$R < 28.3$	9 visible & IR	2015-2021
Euclid - Photometric	20000	$RIZ < 24.5$	$RIZ + YJH$	2017-2020
WiggleZ	1000	$r < 22.5$ (+UV)	$\sim$400	2006-2009
BOSS (SDSSIII)	10000	$r < 20$ (LRG)	2000	2009-2014
HetDex	200	$1.8 < z < 3.8$	850	2009
WFMOS (z=1)	2000	$R < 22.7$	5000	2011-2016
WFMOS (z=3)	300	$R < 24.5$		2011-2016
SNAP	4000	$0.3 < z < 1.7$	$\sim$200	2015-2021
ADEPT	2000	$z > 0.8$		2015
SKA	20000	$z < 1.5$		2020
Euclid - Spectroscopic	20000	$z < 2.1$	400	2017-2020

Table 1.1: Summary of upcoming imaging and spectroscopic surveys
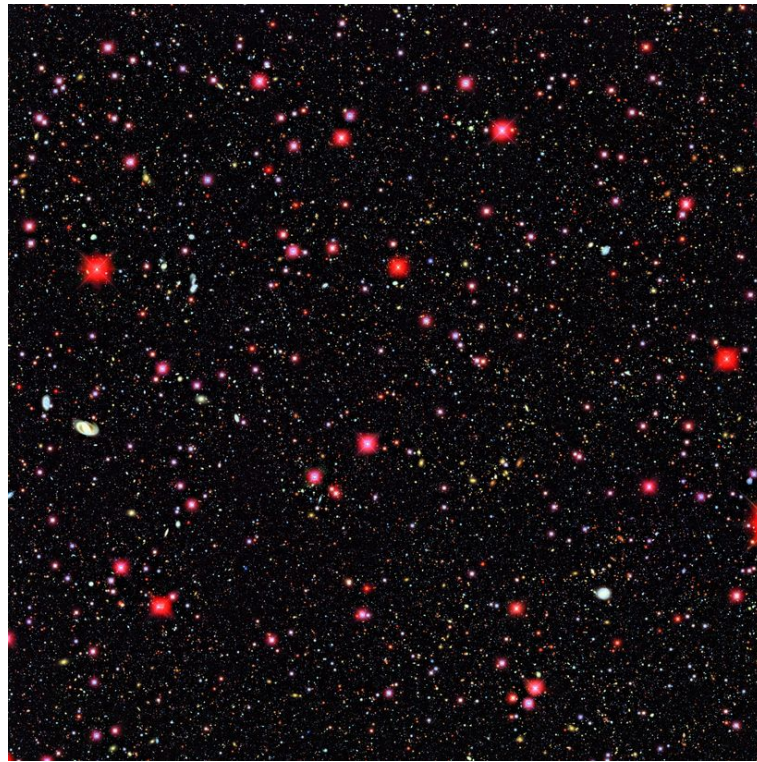
Figure 1.4: Taste of what the night sky will look like with the next generation Large Synoptic Survey Telescope (LSST). Image provided courtesy the LSST website: www.lsst.org

efficient means of understanding a galaxy's evolutionary history mainly owing to the richness of information encoded in a galaxy's spectrum. A galaxy spectrum can be thought of as containing the unique fingerprints of a galaxy's stellar population. Spectroscopic data sets although much smaller than photometric data sets due to the time involved in obtaining spectra, often go down to much fainter flux limits e.g. (Le Fèvre et al. 2005, 2004; Davis et al. 2003) than the wide-field surveys previously mentioned. This depth allows us to collect galaxy spectra over several epochs and by matching them to theoretical models such as those described in § 1.2.2.1, we are able to build up a picture of the evolutionary history of galaxies in our Universe.

Modern surveys are able to use multi-object spectrographs where the light from several hundred galaxies can be collected simultaneously and fed to a spectrograph using fiber optic cables. In Chapter 6, I will be using a spectroscopic data set of a particular class of galaxies known as Luminous Red Galaxies to understand their spectral evolution. These galaxies are some of the brightest and most massive objects known in our Universe and can therefore be observed out to a much higher redshift than most other data sets. Being early type systems, they are also very old and thereby allow us to place stringent constraints on theories of galaxy formation.

Spectroscopic data sets are also useful for photometric surveys. In Chapters 2, 3 and 4, I will be discussing redshift estimation techniques for photometric surveys and will show that the more accurate redshifts obtained from galaxy spectra are in fact required to calibrate the photometric redshift estimates.

1.4.3 Radio and Sub-mm Surveys

Much of the power of current astronomical data sets lies in the fact that they encompass the full-range of the electromagnetic spectrum. While optical data allows us to look at the stars in a galaxy, moving to the infra-red and radio and sub-mm surveys allows detection of dust and molecular gas - the fuel for star formation. As already mentioned, the process of star formation is accompanied by radiative cooling through various atomic and molecular line transitions. The main molecule present in molecular clouds is hydrogen but this does not emit under the conditions typically present in molecular clouds and therefore cannot be detected. The next most abundant molecule, CO has a weak dipole moment which means that its rotational levels are easily excited by collisions with hydrogen molecules. The lower rotational levels are easily observed at radio and sub-mm wavelengths with ground-based telescopes and can be used to trace regions with a high density of molecular hydrogen that are likely to be star forming. The molecule CO has now been detected in systems out to a redshift of $\sim$6.4 (Bertoldi *et al.* 2003) which corresponds to a lookback time of $\sim$12.6 Gyr! This has provided us with compelling evidence that star formation was already taking place very early in the Universe's history. Recently other molecules such as HCN (Gao & Solomon 2004), HCO^{+} (García-Burillo *et al.* 2006) and CS (Bayet *et al.* 2008*a*) have also emerged as tracers of very high-density regions of star formation in distant galaxies. While these molecules are readily observed in nearby galaxies, current instruments are unable to detect them easily in the distant Universe and they are only seen in the most luminous systems at high redshift.

New radio and sub-mm facilities such as the Atacama Large Millimeter Array (ALMA) (Carilli *et al.* 2008), currently under construction, and the Square Kilometer Array (SKA) which is in its design phase, will allow us to detect molecules in star forming galaxies like our own Milky Way out to very high redshifts. This will present us with an opportunity to detect the first signals from some of the very first galaxies to be formed in our Universe. In Chapter 7, I make some predictions for these upcoming radio and sub-mm surveys in terms of the molecules that could be observed with them and how they can be used to infer the physical conditions of their host galaxies.

1.5 Thesis Layout

In this thesis I study galaxies in the distant Universe focusing in particular on their redshifts, colours, morphologies and star formation processes within them.

- In **Chapter 2** I start by describing the photometric redshift estimation technique for obtaining redshifts of galaxies from their broadband colours and discuss the different methods currently used for this problem.

- **Chapter 3** applies one photometric redshift algorithm based on artificial neural networks to simulations for the upcoming Dark Energy and Vista Hemisphere Surveys. In particular, I consider the requirements on this photometric redshift estimate for measurements of the clustering pattern of galaxies in our Universe.

- **Chapter 4** describes photometric redshift design studies undertaken for the space-based Euclid mission concept.

- In **Chapter 5** I move on to applying the artificial neural network algorithm to a different problem - the morphological classification of almost 1 million objects from the Sloan Digital Sky Survey. I compare results obtained using the machine learning algorithm to those obtained by the human eye as part of the web-based Galaxy Zoo project[2] and consider whether the human classifications can be used to train machine learning codes for future surveys.

- In **Chapter 6** I study the evolution of the luminosities, colours and stellar masses of Luminous Red Galaxies from the 2dF and SDSS LRG and QSO (2SLAQ) spectroscopic survey and show that these observations present a significant challenge for current models of galaxy formation.

- Finally in **Chapter 7** I focus on studying star formation processes in distant galaxies. A chemical model is used to calculate various timescales associated with star formation, the balance of which tells us the ratio of low to high-mass stars in galaxies with different physical conditions and therefore the form of the initial mass function. The final part of this chapter looks at some molecular tracers of different kinds of initial mass functions and makes predictions for observations that could be made with the next generation of radio and sub-mm surveys.

---

[2]www.galaxyzoo.org

I conclude this thesis with a summary of the key results and some discussion about future work which will be interesting to conduct in order to follow-up some of the results presented here.

PHOTOMETRIC REDSHIFT ESTIMATION METHODS

The work described in this chapter is an extended version of the publications: **Abdalla, Banerji, Lahav & Rashkov 2009, MNRAS, Submitted, arXiv:0812.3831** *as well as* **Chapter 13 of Bayesian Methods in Cosmology (Cambridge University Press) by Lahav, Abdalla & Banerji.**

2.1 Introduction

Estimating the distance to an astronomical object is a fundamental problem in Astronomy. Distances to galaxies are usually estimated from their redshifts as defined in Eq 1.2. Ideally the redshift is derived from a high resolution spectrum. The alternative is the photometric redshift technique. Using the colours of a galaxy in a selection of medium- or broad-band filters we can gain a crude approximation of the galaxy's spectral energy distribution or SED, from which its redshift and spectral type may be found. Figure 2.1 illustrates how the colours of a galaxy change with redshift and how the major spectral features can be picked up in each band.

The technique is very efficient compared with spectroscopic redshifts, since the signal-to-noise in broad-band filters is much greater than the signal-to-noise in a dispersed spectrum. Furthermore, a whole field of galaxies may be imaged at once while spectroscopy is limited to individual galaxies or those that can be positioned on slits or fibres. However, photometric redshifts are only approximate at best and are sometimes subject to large errors. For many applications though, large sample sizes are more important than precise redshifts and photometric redshifts may be used to good effect.
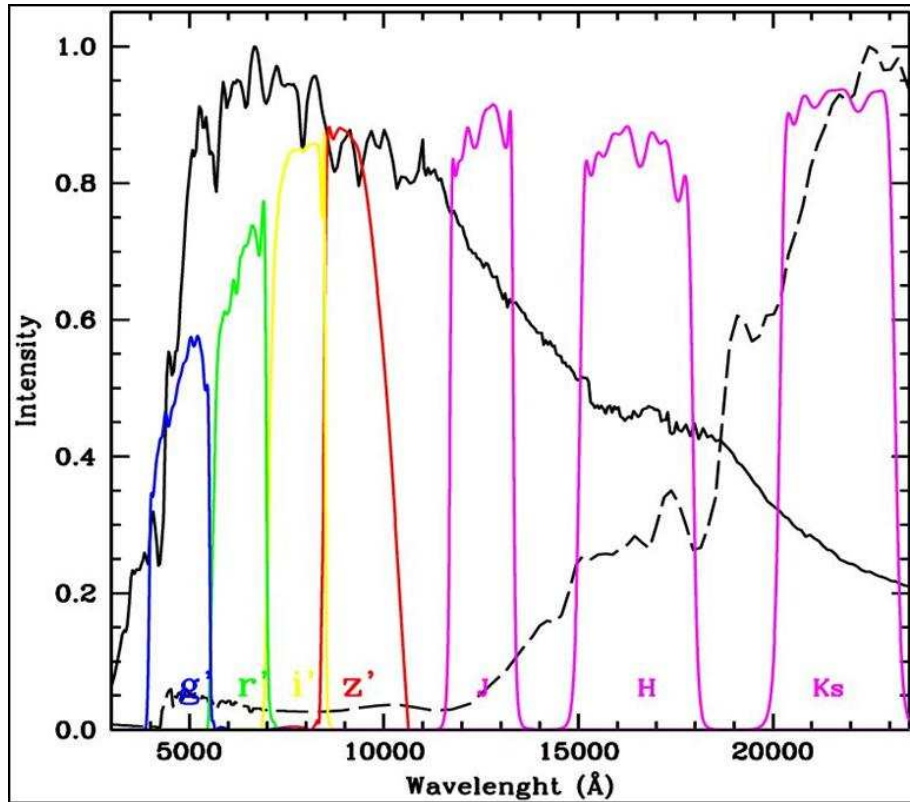
Figure 2.1: The SED of an elliptical galaxy at redshift $z = 0$ (solid line) and the same galaxy at $z = 3$ (dashed line) as seen through a set of broad-band optical ($griz$) and near infra-red (JHK_s) filters. The $4000\mathring{A}$ break moves from the g-band at $z = 0$ to the NIR bands as the galaxy is redshifted to $z = 3$.

Photometric redshifts date back to Baum (1962). For reviews see Weymann *et al.* (1999); Koo (1999). The methods have been used extensively in recent years on the ultra-deep and well-calibrated Hubble Deep Field observations (e.g. Connolly *et al.* (1998)).

The photo-z approach has re-gained popularity with the planning of wide field deep imaging surveys such as those summarised in Table 1.1. The accuracy with which photometric redshifts can be calculated for these surveys is crucial for the determination of cosmological parameters such as the Dark Energy equation of state. This point will be addressed in detail in Chapters 3 and 4.

For a statistician, photo-z estimation is an inverse problem: going from the colour space to the redshift, type and other galaxy properties. There are two common approaches to the problem: (1) Template methods (e.g. Hyper-Z) and (2) Training methods (e.g. ANNz) as described below. Note that training methods can also be used on synthetic data, so they are not necessarily 'empirical' as

they are sometimes referred to as.

There are also different deliverables required from the photo-z estimation technique, e.g., a catalogue where a photo-z and associated error is given per galaxy, or, as required for certain applications, just the redshift distribution $N(z)$. A final comment is that different techniques have been developed for the photo-z for field galaxies and clusters of galaxies. The focus of this chapter and much of the rest of the thesis is predominantly on field galaxies.

In the remainder of this chapter, the different methods for photometric redshift estimation are described. Details of specific publicly available photometric redshift packages are also given and some of these are used in a comparison study. Photometric redshifts are calculated using these codes for a sample of luminous red galaxies for which spectroscopic redshifts are already available thereby allowing an assessment of the relative performance of each of the different public codes. Luminous red galaxies have been chosen for this comparison as the presence of a strong 4000 Åbreak in these galaxies means the photometric redshift estimates for these objects are likely to be reasonably accurate. The codes are also used in the construction of a new photometric redshift catalogue of more than 1.5 million luminous red galaxies using photometric data from the Sloan Digital Sky Survey, Data Release 6. Finally, some work undertaken as part of the Photometric Redshift Accuracy Testing (PHAT) program[1] is presented before drawing some general conclusions about photometric redshift methods and their relative performance.

2.2 Methods

As already stated, there are two main methods for photometric redshift estimation although extensions and modifications to these have also been developed. In this section, the principles behind the two methods will be outlined.

2.2.1 Template Fitting Methods

These methods involve compiling a library of template spectra which can be either theoretical SEDs from population synthesis models (e.g. `GISSEL` – Bruzual & Charlot (1993) - BC hereafter) or empirical SEDs (e.g. Coleman *et al.* (1980) - CWW hereafter). The expected flux through each survey filter is calculated for each template SED on a grid of redshifts, with corrections for the interstellar medium (ISM), intergalactic medium (IGM) and galactic reddening where necessary. A redshift and spectral type are estimated for each observed galaxy by minimizing χ^2 with respect

---

[1]http://www.astro.caltech.edu/twiki-phat/bin/view/

to redshift, z, and spectral type, SED, where

$$\chi^2(z, \text{SED}) = \sum_i \left(\frac{f_i - \alpha(z, \text{SED}) t_i(z, \text{SED})}{\sigma_i} \right)^2, \tag{2.1}$$

f_i is the observed flux in filter i, σ_i is the error in f_i, $t_i(z, \text{SED})$ is the flux in filter i for the template SED at redshift z and $\alpha(z, \text{SED})$,the scaling factor normalizing the template to the observed flux, is determined by minimizing Equation 2.1 with respect to α, giving

$$\alpha(z, \text{SED}) = \left(\sum_i \frac{f_i t_i(z, \text{SED})}{\sigma_i^2} \right) / \left(\sum_i \frac{t_i(z, \text{SED})^2}{\sigma_i^2} \right). \tag{2.2}$$

The template-fitting photometric redshift technique makes use of the available and reasonably detailed knowledge of galaxy SEDs and in principle it may be used reliably even for populations of galaxies for which there are few or no spectroscopically confirmed redshifts. However, crucial to its success, is the compilation of a library of accurate and representative template SEDs. Empirical templates are typically derived from nearby bright galaxies, which may not be truly representative of high redshift galaxies. Conversely, while theoretical SEDs can cover a large range of star formation histories, metallicities, dust extinction models and other input parameters, not all combinations of these parameters at any particular redshift are realistic, and the ad hoc inclusion of superfluous templates increases the potential for errors when using observations with noisy photometry.

2.2.2 Bayesian Methods

An extension of the above maximum likelihood approach is to incorporate priors, through the Bayesian framework. Benitez (2000) formulated the problem as follows. The probability of a galaxy with colour C and magnitude m having a redshift z is

$$p(z|C, m) = \frac{p(z|m)p(C|z)}{p(C)} \propto p(z|m)p(C|z), \tag{2.3}$$

where the term $p(C|z)$ is the conventional redshift likelihood employed in simple template-fitting methods, and $p(C)$ is just a normalization. The new important ingredient is $p(z|m)$, which brings in the prior knowledge of the magnitude redshift distribution. With the aid of the extra information (prior), this approach is effective in avoiding catastrophic errors of placing a galaxy at an unrealistic redshift given its magnitude and colours.

Although a magnitude or luminosity prior is used in the most common implementations of this method, recently, a new idea has been proposed - to use the galaxy surface brightness as a prior (e.g. Kurtz *et al.* (2007); Stabenau *et al.* (2008)). As the surface brightness dimming is

proportional to $(1 + z)^{-4}$ in any conventional cosmology, it can serve as a natural prior. Indeed, using this prior eliminates a large fraction of outliers.

2.2.3 Training Set Methods

When a sufficiently large and representative sample of galaxies with spectroscopic redshifts is available, one can use these to derive a functional relation between the colours and redshifts of the galaxies. This forms the basis of the training set method. The functional relation could be a simple polynomial fit (Connolly et al. 1995) or a more complicated mapping as is the case for training set methods such as artificial neural networks (e.g. Collister & Lahav (2004)) and support vector machines (e.g. Wadadekar (2005)). Once the redshift is known as a function of the magnitude, this relation can be applied to a data set where only the magnitude is known in order to determine the redshift.

When a representative and well calibrated training set is available, this method generally provides more accurate photometric redshifts than the traditional template fitting codes. Furthermore, the method is flexible in that other galaxy properties such as size (e.g. Firth *et al.* (2003)), concentration indices (e.g. Oyaizu *et al.* (2008*b*)) and radial light profiles (e.g. Wray & Gunn (2008)) can also be used to derive a functional relationship for the redshift.

2.3 Publicly Available Photometric Redshift Codes

In recent years, many photometric redshift packages have been developed and made publicly available to the community via web-based interfaces. Table 2.1 provides a list of those that are currently available online.

Code	Authors	Method	Web link
HyperZ	Bozonella et al.	Likelihood	http://webast.ast.obs-mip.fr/hyperz/
BPZ	Benitez	Bayesian priors	http://acs.pha.jhu.edu/~txitxo/bpzdoc.html
ANNz	Collister & Lahav	Neural Networks	http://zuserver2.star.ucl.ac.uk/~lahav/annz.html
ImpZ	Babbedge et al.	Template	http://astro.ic.ac.uk/~tsb1/ImpZlite/ImpZlite.html
ZEBRA	Feldmann et al.	Bayesian, Hybrid	www.exp-astro.phys.ethz.ch/ZEBRA
Kcorrect	Blanton	Model templates	http://cosmo.nyu.edu/blanton/kcorrect/
Le Phare	Arnouts & Ilbert	Template	www.oamp.fr/people/arnouts/LE_PHARE.html
EAZY	Brammer et al.	Template	www.astro.yale.edu/eazy/
LRT Libraries	Assef et al.	Template	www.astronomy.ohio-state.edu/~rjassef/lrt/

Table 2.1: Publicly available software packages for photo-z estimation

In addition, the literature gives numerous examples of photometric redshift codes that have been used on large data sets but are as yet not publicly available e.g. Wadadekar (2005); Kurtz *et al.* (2007); Carliles *et al.* (2008); Way *et al.* (2009) etc. Given the plethora of codes now available to the user, it is important to understand and quantify similarities and differences between them. This section provides a description of some of the public codes available. In the next section, results from comparing all the codes on a sample of Luminous Red Galaxies from the 2SLAQ survey, is presented. In order to perform the comparison, all codes were run in various different configurations and the configuration found to produce the best photometric redshifts was subsequently used to obtain the final result for that code. In this section therefore, the optimal configuration in which each of these codes was run, is also described. It has to be stressed that these configurations only apply for the particular sample on which the code is being run, in this case the Luminous Red Galaxies.

2.3.1 HyperZ

HyperZ (Bolzonella *et al.* 2000) was the first publicly available photo-z code and has consequently been widely used in the literature for photometric redshift estimation. It is a simple template fitting code that can be used in conjunction with two sets of basis SEDs, namely the observed CWW templates or the synthetically generated BC templates. HyperZ takes as its inputs the photometric catalogue of galaxies with magnitudes and errors on magnitudes through the different filters specified in the filter set, as well as a list of spectral templates to be used in the χ^2 minimisation. Various different reddening laws can also be implemented in order to account for the effect of interstellar dust on the shape of the SED. The damping of the Lyα forest increasing with redshift is modelled according to Madau (1995).

The code was run on the sample of Luminous Red Galaxies in conjunction with a variety of different basis template sets including the four CWW templates and interpolations between them as well as the 8 synthetic BC templates. The BC templates produced considerably better photo-z's with a smaller scatter than the CWW and interpolated CWW template sets. In order to demonstrate the effects of using two different template sets to calculate photometric redshifts with the same code, results obtained using both the four CWW templates roughly corresponding to types E,Sbc,Scd and Im and the eight BC templates roughly corresponding to types Single Burst, E, S0, Sa, Sb, Sc, Sd and Im, are presented.

Photo-z outputs with no correction for galactic reddening and with a Calzetti reddening law (Calzetti *et al.* 1994) applied to the templates, were both considered. In all cases it was found that

including a reddening correction slightly worsened the photometric redshift estimate. The final HyperZ outputs therefore make no correction for the galactic reddening due to dust in external galaxies. Magnitudes in all five SDSS optical bands have been used even though the photometric uncertainties in the u-band are large and therefore would contribute to a larger scatter in the photo-z estimate. Removing the noisier u-band photometry actually worsens the photo-z estimate due to the corresponding loss in colour information.

Other simple template-based methods are also available for photo-z estimation such as ImpZ (private communication: M. Rowan-Robinson), k-correct (Blanton & Roweis 2007), EAZY (Brammer *et al.* 2008) and the LRT Libraries (Assef *et al.* 2008). These are not presented in this comparison study.

2.3.2   BPZ

BPZ (Benítez 2000) was the first Bayesian code developed for photometric redshift estimation and allows the implementation of a luminosity prior. In its publicly available form however, only a luminosity function prior from HDF-N or a flat prior can be incorporated. BPZ can function in a Bayesian and Maximum Likelihood (ML hereafter) module and therefore produces two outputs for the photometric redshift. The ML method simply picks the highest maximum over all the likelihoods as its redshift estimate whereas the Bayesian method averages over all the likelihoods after weighting them by their prior probabilities.

BPZ also takes as its input a photometric catalogue with magnitudes in different filters and their corresponding errors. The BPZ templates include the four CWW templates as well as the spectra of two star-bursting galaxies from Kinney et al. (1996). In this study nine interpolations between each of the four CWW templates were added to the BPZ template list to produce a more complete list of basis SEDs. This gives a set of 38 basis templates for BPZ to use. It was found that ~17 of these templates concentrated towards the early types are sufficient to produce the best photometric redshift estimate for our sample of LRGs. Adding more templates does not improve the photo-z scatter. Two further points of interpolation between each of the templates in colour space were also used as specified by the INTERP parameter in BPZ. A flat prior was used throughout the calculation resulting in very similar results from the Bayesian and ML runs.

The BPZ output includes two photo-z estimates from the Bayesian and ML runs as well as a quantity called *odds* that is the amount of probability contained between $-0.12(1 + z)$ and $0.12(1 + z)$ around the Bayesian photo-z estimate. In order to select galaxies which only have

a single compact peak in their probability distribution, one needs to consider those galaxies with $odds > 0.95$ at the very least and $odds > 0.99$ for a robust estimate (private communication: N.Benitez). In the first case, 4811 of the 5482 galaxies are selected and in the second case there are 3689 of the 5482 galaxies. The Bayesian output from BPZ with galaxies with $odds > 0.99$ selected, gives the best photo-z estimate and it is this result that is used as the BPZ output in the comparison plots.

2.3.3   Le PHARE - PHotometric Analysis for Redshift Estimations

Le PHARE is very similar to HyperZ in that a set of template SEDs together with a filter set are used to determine a set of model magnitudes used in the photometric redshift calculation. These are then compared to the observed magnitudes using a χ^2 minimisation in order to compute the redshift of an object. The Le PHARE package includes various template sets used to construct the library of model magnitudes. These include the CWW and Kinney et al. (1996) star-burst templates, an extended CWW template set with 72 interpolations between the standard CWW templates, 42 synthetic GISSEL templates as well as the observed templates of Poggianti *et al.* (2001). All of these template sets were used to derive photometric redshifts for the sample of LRGs. The best photometric redshifts were obtained using the 8 Poggianti templates corresponding to galaxy types Ell, S0, Sa, Sb, Sc, Sd, SB2 and SB1. The 42 GISSEL templates give slightly worse photo-z's than the Poggianti templates but the scatter on the photometric redshift when using the extended sample of 72 interpolated CWW templates is ∼30% worse than that obtained using the 8 Poggianti templates. Therefore it can be seen that in a template-based method, one does not necessarily gain in redshift accuracy by adding more model SEDs to the library as this probably introduces additional degeneracies.

Le PHARE also includes various prescriptions to correct for galactic reddening but the photometric redshift estimate is always worsened when correcting for the reddening using any of these prescriptions. The final Le PHARE output is therefore obtained using the 8 Poggianti templates and neglecting the effects of galactic reddening. 5-band $ugriz$ photometry in the SDSS filters is used as this gives significantly more accurate photometric redshifts compared to if the u-band photometry with the largest photometric errors was removed.

2.3.4 SDSS template fitting code.

This code is a hybrid template fitting and training code that was developed and has been applied to data from the Sloan Digital Sky Survey (SDSS) (Padmanabhan *et al.* 2005). A linear combination of templates is used and the photometric redshift is found via χ^2 minimisation. The greatest disadvantage of the traditional χ^2 fitting techniques is the potential mismatch between the templates used for the fitting and the properties of the sample of galaxies for which one wants to estimate the redshifts. In a hybrid method, the templates are calibrated using a training set with known spectroscopic redshifts and similar properties to the galaxies whose redshifts need to be estimated, in order to better represent the studied galaxy sample. The SDSS code used here applies a hybrid method to the LRG sample using a modified elliptical galaxy template, adjusted to represent an LRG spectrum after three iterations of correction (Padmanabhan *et al.* 2005). Given that early type galaxies evolve passively, only one template is necessary for this galaxy sample.

2.3.5 ZEBRA - Zurich Extragalactic Bayesian Redshift Analyzer

The Zurich Extragalactic Bayesian Redshift Analyzer (Feldmann *et al.* 2006) is a more sophisticated Bayesian template-fitting photometric redshift code compared to its predecessor, BPZ. The basic principles of estimating redshifts using templates and Bayesian priors remains as described in §2.3.2 but among the novel techniques employed within the ZEBRA package are the photometry check mode that checks and corrects the photometry in certain filters, a template optimisation mode to improve the standard set of templates in specified redshift bins using a training set of galaxies with spectroscopic redshifts and the ability to calculate a prior self-consistently from the photometric catalogue when ZEBRA is run in its Bayesian mode.

The photometry check mode of ZEBRA is not employed in this analysis as applying a correction to the catalogues using this mode in fact produces less accurate photometric redshifts.

ZEBRA's template set consists of the standard E, Sbc, Scd and Im galaxies (Coleman *et al.* 1980) as well as the SEDs of the two star-bursting galaxies SB2 and SB3 (Kinney et al. 1996). These are further interpolated in logarithmic space by ZEBRA during the photo-z estimation. Including the E, Sbc and Scd templates produces better results than including all six templates. Furthermore, ZEBRA's template optimization mode is used to construct improved templates from these three basis templates in two redshift bins - $0 < z < 0.5$ and $0.5 < z < 1.0$. A regularisation parameter of $\rho = 0.05$ and a pliantness parameter of $\sigma = 2$ are used. Feldmann *et al.* (2006) gives details of these parameters and how to optimise them so as to produce the most realistic templates

and the values adopted here are taken directly from this paper. The effects of IGM absorption are not included in the templates as this produces better photometric redshifts. The optimisation procedure produces 39 basis templates and these are used along with the three original templates in the photometric redshift calculation.

The Bayesian mode of ZEBRA produces considerably better photometric redshifts than the Maximum Likelihood mode and only the outputs from the Bayesian mode are presented in the comparison plots and used when calculating figures of merit. The Bayesian mode is run using four iterations to calculate the prior self-consistently from the photometric catalogue. Further iterations slightly worsen the photo-z estimate. A smoothing kernel is also used to smooth the prior after every iteration.

2.3.6 ANNz

When a representative training set is available training methods become a viable option to use instead of template-fitting methods. Artificial Neural Networks (Collister & Lahav 2004) have been shown to produce competitive results compared to other training set methods (Firth *et al.* 2003) and have been used for photo-z estimation on current data sets (Collister *et al.* 2007) as well as forecasts of photometric redshifts for future surveys (Abdalla *et al.* 2008*a*; Banerji *et al.* 2008). The neural network is made up of several layers, each consisting of a number of nodes. The first layer receives the galaxy magnitudes in different filters as inputs and the last layer outputs the estimated photometric redshift. All nodes in the hidden layers in between are interconnected and connections between nodes i and j have an associated weight, w_{ij}. Each node i is assigned a value u_i and an activation function $g_i(u_i)$

$$g_i(u_i) = \frac{1}{1 + exp(-u_i)}. \tag{2.4}$$

The value of a subsequent node j is then calculated as the summation of the weighted values of the activation functions of all nodes i pointing to it:

$$u_j = \sum_i w_{ij} g_i(u_i). \tag{2.5}$$

ANNz, like all other empirical methods, requires a training set that is used to minimise the

cost function, E (Eq. 2.6) with respect to the free parameters w_{ij}.

$$E = \sum_k (z_{phot}(w_{ij}, m_k) - z_{train,k})^2 \qquad (2.6)$$

To avoid an over-fitting, every network is tested on a validation set of galaxies, whose spectroscopic redshifts are also known. The network with the lowest value of E as calculated on the validation set is selected and the photometric sample is run through it for redshift estimation (Collister & Lahav 2004).

The neural network setup is illustrated in Figure 2.2. During the initial setup, one has to specify the architecture of the neural network - the number of hidden layers and nodes in each hidden layer. This is chosen to be N:2N:2N:1 throughout this work unless otherwise mentioned, where N is the number of filters used for photometry. Note that changing both the number of hidden layers as well as the number of nodes in each hidden layer makes very little difference to the photometric redshift estimate as the chosen architecture is probably complex enough to be able to reproduce the relationship between the redshift and the galaxy magnitudes.

The neural network code also produces an estimate of the error associated with each photometric redshift estimate in addition to the photo-z estimate. This error depends on the noise on the neural network inputs and not on the difference between the spectroscopic and photometric redshifts. The variance that this noise on the input would introduce into the output of the network is given by a simple chain rule expression as follows:

$$\delta_z{}^2 = \sum_i \left(\frac{\partial z}{\partial m_i}\right)^2 , \delta_{m_i}^2 \qquad (2.7)$$

where the sum i is a sum over all the network inputs and δ_{m_i} is the photometric error on the magnitude in band i. The derivative $\frac{\partial z}{\partial m_i}$ is obtained using the formalism described in Bishop (1995). This algorithm is fully implemented within ANNz (Collister & Lahav 2004).

2.4 Errors on photo-z

Each different method described above has a way of obtaining error estimates which reflects the degree of confidence with which one can rely on the photometric redshift obtained.

In template methods the χ^2 can be computed for each potential redshift value. This produces a probability distribution function and the errors are obtained from the points where the probability

Input layer $\longrightarrow$ Hidden layer $\longrightarrow$ Output layer
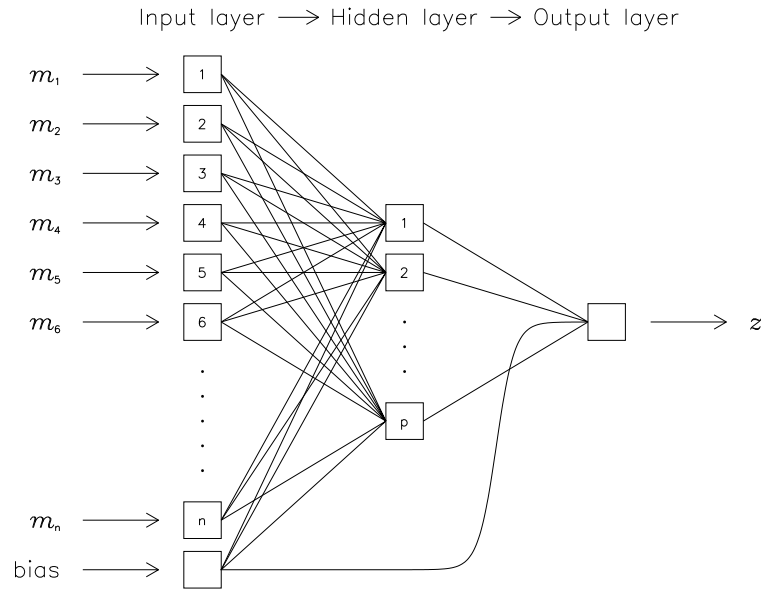
Figure 2.2: Schematic diagram of neural network as implemented by ANNz from Collister & Lahav (2004). The input layer consists of nodes that take magnitudes in the different filters used for photometry. A single hidden layer consisting of p nodes is shown here although more hidden layers could be used. The output layer has a single node that gives the photometric redshift. Once again further nodes for more outputs such as spectral type could be added to this layer. Each connecting line between nodes carries a weight, w_{ij}. The bias node allows for an additive constant when optimising weights.

falls 1σ away from the best fit value. As other techniques use different methods for photometric redshift estimation they have to obtain error estimates in a different way. For example, in a neural network method, the error estimate is obtained through a chain rule which relates errors in the original magnitudes to errors on the final redshift (Collister & Lahav 2004). The estimated magnitude errors can then be used to obtain a redshift error estimate. Recently a more general method based on nearest neighbours has been devised and can be applied to any sample with a training set independently of the photo-z estimator used. This method, described in Oyaizu *et al.* (2008*a*), uses the differences between the spectroscopic redshift and the photometric redshift of the galaxies in a training set as a function of the magnitudes. An error estimate is obtained by a nearest neighbour interpolation of this training data in magnitude space and produces very good results.

The error, or more generally the probability distribution function attached to each redshift, is a a very important quantity. For example, galaxies with large errors in the photo-z can be removed

(*clipped*) from the sample before using them for any kind of cosmological analysis. Depending on the science question being addressed, there will be a trade-off between the amount of clipping applied to remove undesired outliers, and the number of galaxies required to keep the shot-noise levels low. For an illustration of the clipping procedure as applied to weak lensing studies and galaxy power spectrum measurements, see Abdalla *et al.* (2008*a*) and Chapter 3 of this thesis, respectively.

2.5 Comparison of Codes on the 2SLAQ LRG Sample

The beginning of this chapter has already illustrated the many different methods currently used for photometric redshift estimation and the many public codes that are available for these purposes. In this section, the publicly available codes already described are run in their optimal configuration on a sample of Luminous Red Galaxies from the 2dF and SDSS LRG and QSO (2SLAQ) survey (Cannon *et al.* 2006). This is a spectroscopic survey with redshifts measured for ~ 13000 LRGs for which photometric redshift estimates are expected to be reasonably good given the presence of a strong 4000 Åbreak in these objects. The 2SLAQ LRGs are selected using colour cuts that are described in detail in Cannon *et al.* (2006) and Chapter 6 of this thesis. For the purposes of this chapter however, the important point is that these early type galaxies are expected to produce reasonably accurate photometric redshift estimates that can then be used for cosmology (Blake *et al.* 2007, 2008; Cabré & Gaztañaga 2009).

The 2SLAQ LRGs have been subdivided into a training and a testing sample. The training sample is used in those codes that need a training set of galaxies with spectroscopic redshifts. The testing sample of 5482 LRGs chosen at random from the entire data set, is consistently used as the evaluation set in all codes. All magnitudes have been corrected for dust extinction in the Milky Way using the maps of Schlegel *et al.* (1998).

It should be emphasised that this comparison study is a *high-level* comparison. In other words, we are comparing end products (the photometric redshift estimate) without decomposing the problem into smaller parts in order to determine where discrepancies in the codes are arising. The codes plus galaxy libraries supplied with them are essentially treated as a *black box* in such an analysis. This, however, is still a valid comparison as we compare what is available to the photo-z user online. A fuller analysis is no doubt needed in order to have the highest level of confidence in photometric redshift estimates. This work is being carried out as part of the PHAT collaboration[2]

---

[2]http://www.astro.caltech.edu/twiki-phat/bin/view/

and some of the preliminary work undertaken as part of this collaboration is presented at the end of the chapter.

For the purposes of our *high-level* analysis, each of the photo-z codes detailed in § 2.3 have been run several times using different parameters in order to optimise them to produce the best photo-z estimate. The final output files from each code used in this analysis are ones that gave the best photo-z estimate. Hence this is not only a code comparison it is a code plus library comparison which is the final publicly available product to the non-expert on-line. It should also be noted that this is not a comparison which is meant to contrast equal values. For instance it is already well accepted that training codes work much better within the redshift and spectral energy distribution range present in the training set but template methods are superior if there are objects in the survey outside this range. Also, codes such as BPZ provide an automatic selection of the objects with the best photo-z's via for example the odds parameter. The purpose here is to compare the full packages, including SEDs and features available from different codes. Furthermore, the chosen sample of Luminous Red Galaxies has a very narrow range of SEDs and this comparison therefore does not highlight the strength of photometric redshift codes with a broad range of library templates that would be more suitable for other samples.

Figure 2.3 shows density plots of the spectroscopic redshift versus photometric redshift for each of the six different codes. The HyperZ outputs have been presented using two different template sets. The redshift resolution for all codes has been chosen so as to ensure that the main uncertainty is related to the photo-z uncertainty and not to numerical effects.

In order to evaluate the precision with which each of these different codes calculates the photometric redshift, several different figures of merit are defined and evaluated. Many of these will also be used throughout the next two chapters of this thesis.

For example, one can consider the 1σ scatter between the true (spectroscopic) redshift and the photometric redshift in each spectroscopic redshift bin. This is defined as follows:

$$\sigma_z = \left\langle \left(z_{phot} - z_{spec} \right)^2 \right\rangle^{\frac{1}{2}}. \tag{2.8}$$

This quantity is plotted in the left-hand panel of Figure 2.4. As expected, the empirical photo-z estimator, ANNz seems to work best at intermediate redshifts ($0.5 \leq z_{spec} \leq 0.7$) where there are a large number of representative training set galaxies. At high redshifts ($z_{spec} > 0.7$), HyperZ BC provides the best estimates of the photometric redshift. At low redshifts ($z < 0.5$), the SDSS code and Le PHARE template fitting codes perform the best. None of these codes use the more
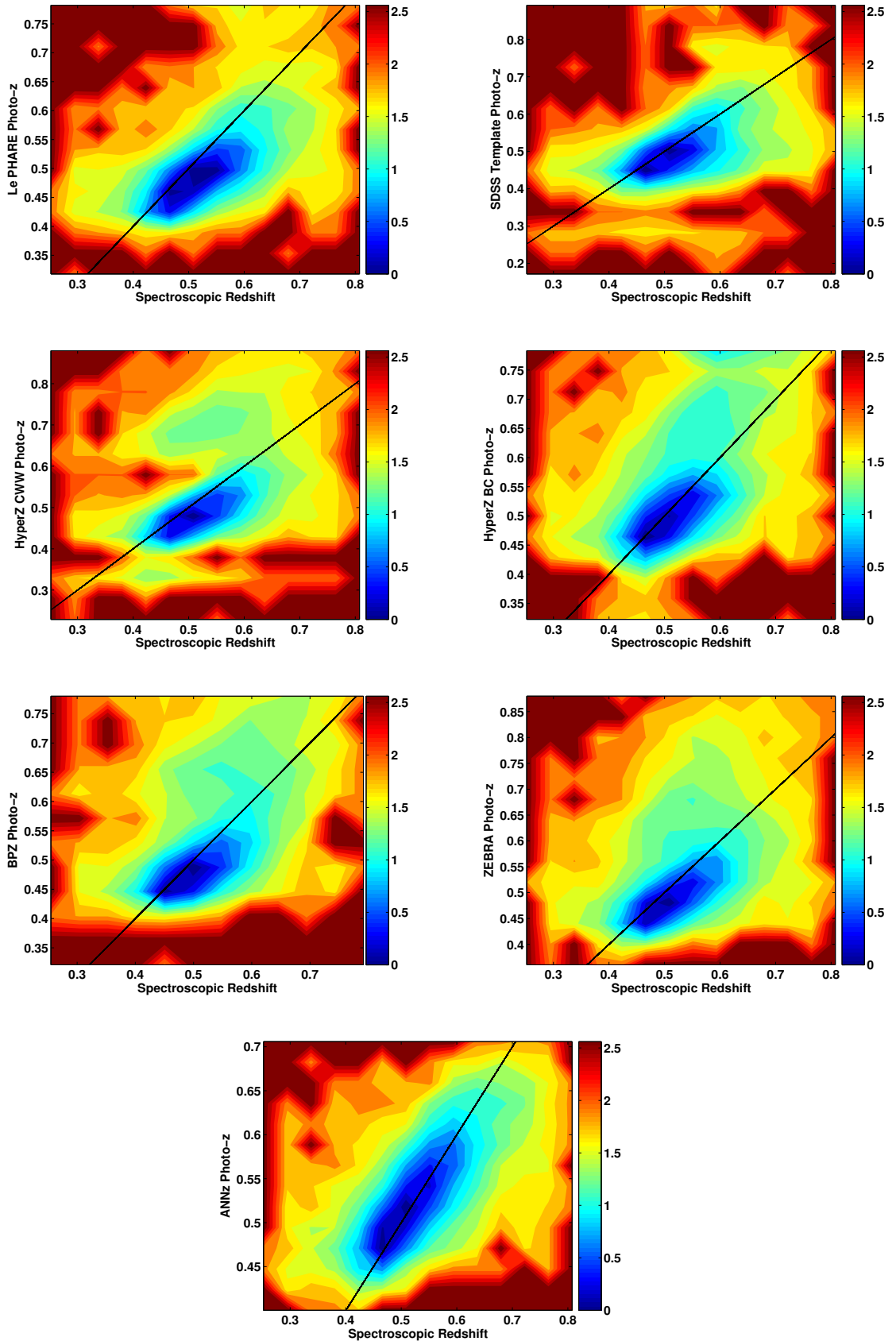
Figure 2.3: Density plots of spectroscopic versus photometric redshift for each of the public photo-z codes described in § 2.3. The plots are colour-coded and the scale is exponential. A colour difference of one is equivalent to the density being decreased by a factor of e. The solid black lines show where the spectroscopic redshift is equal to the photometric redshift.
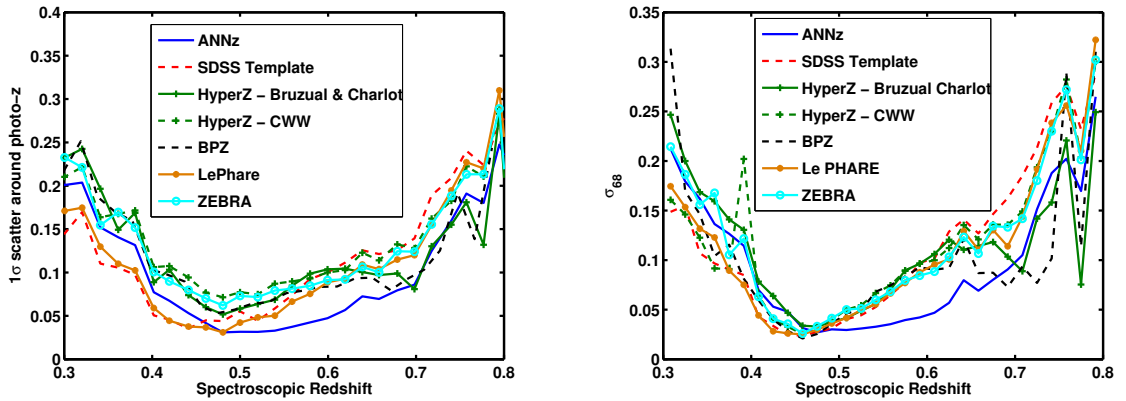
Figure 2.4: 1σ scatter on the photometric redshift around the true spectroscopic redshift defined as per Eq.2.8 for each of the public photo-z codes described in § 2.3 in the left-hand panel and σ_{68} as a function of the spectroscopic redshift for each of the public photo-z codes described in § 2.3 in the right-hand panel.

standard CWW templates suggesting that these templates are not a good match to the LRGs that are being analysed in this study.

As can be seen in Figure 2.3 however, there are many outliers present in our sample. Another useful quantity to consider is therefore σ_{68} which is the interval in which 68% of the galaxies have the smallest difference between their spectroscopic and photometric redshifts. This will give some indication of the scatter in the photometric redshift estimate once the outliers have been removed and is plotted in the right-hand panel of Figure 2.4. A similar trend is seen as was observed with the 1σ scatter.

The bias on the photometric redshift estimate in each spectroscopic redshift bin is defined as:

$$b_z = \langle z_{phot} - z_{spec} \rangle. \tag{2.9}$$

This quantity is plotted for each of the different codes, in the right-hand panel of Figure 2.5. All codes are seen to give a bias that is a strong function of the spectroscopic redshift. Low redshifts are systematically overestimated and high redshifts are systematically underestimated. Both Padmanabhan *et al.* (2005) and Ilbert *et al.* (2006) show that the bias can be systematically corrected for by adapting the template set and correcting for photometric offsets. In order to get a feel for the error on the photometric redshift once this bias has been corrected for, the 1σ scatter around the mean photometric redshift estimate in each spectroscopic redshift bin is plotted in the

left-hand panel of Figure 2.5. This is defined as follows:

$$\sigma_{z2} = \left\langle (z_{phot} - \bar{z}_{phot})^2 \right\rangle^{\frac{1}{2}}. \tag{2.10}$$

As can be seen, the scatter is now reduced for most of the codes as one is not accounting for any systematic shift that can be corrected for. The bias is largest at high redshifts for the SDSS and Le PHARE template fitting codes and these codes have the biggest improvement in the scatter at high redshifts when one takes the moment around the mean rather than the true redshift.

A more useful quantity in terms of future surveys is to plot the bias and scatter as a function of the photometric redshift as in Figure 2.6. The 1σ scatter around the mean spectroscopic redshift estimate in each photo-z bin is defined as follows:

$$\sigma_{z3} = \left\langle (z_{spec} - \bar{z}_{spec})^2 \right\rangle^{\frac{1}{2}}. \tag{2.11}$$

One can also compare the right-hand panels of Figure 2.5 and Figure 2.6 to each other. It can be seen that the bias follows the same trend as a function of spectroscopic redshift for all the different photo-z codes and is fairly similar for all these codes. However, the bias as a function of the photometric redshift is very different for the different photo-z codes and more indicative of how much the photo-z estimate has to be corrected for systematic errors. This bias is almost flat for the training method which has enough training set galaxies to effectively minimise the bias through the training process. The integral under the curve is also small for ZEBRA as shown in Table 2.3 as the template optimisation technique here was able to remove the average bias for the entire redshift range. However, a remaining bias was found at high and low redshifts with the values of the ZEBRA configuration parameters used in this analysis[3].

As an alternative statistic, Table.2.2 presents the fraction statistics for the methods described in § 2.3. The fractions f_i are defined as the fraction of galaxies in certain regions of the photo-z/spec-z plane. If one divides this plane in rectangular regions by binning galaxies both in photo-z and spec-z, the fraction f_0 is the fraction of galaxies which is on the diagonal of the matrix defined by the rectangles. The fraction f_1 is the fraction of galaxies in bins adjacent to the diagonals and so on for f_2, f_3 etc. The area could have been subdivided along the diagonals and this would have

---

[3]It is possible that a better choice of template optimisation parameters could be found resulting in a removal of the bias at low and high redshifts. However, as the philosophy of this work is to perform a code comparison from the point of view of the photo-z user rather than the photo-z developer, and it is not obvious what this better choice of parameters would be, the results are presented as they are.
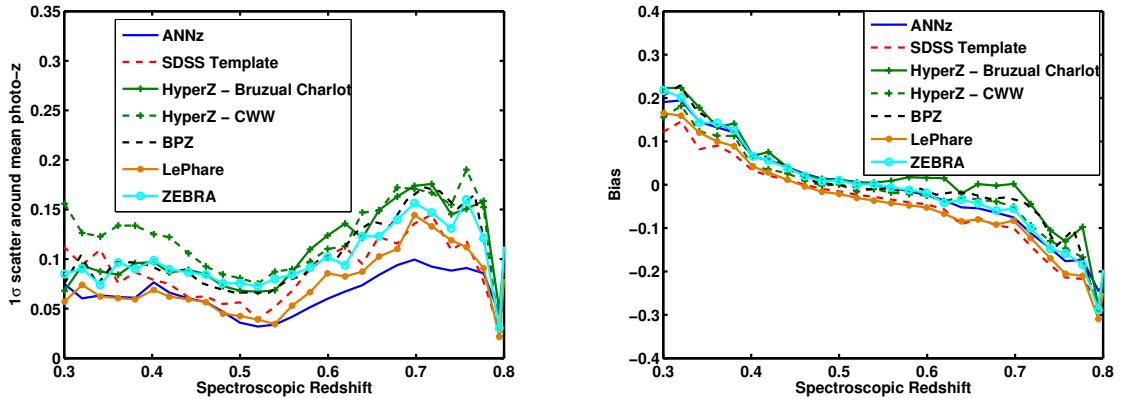
Figure 2.5: 1σ scatter around the mean photometric redshift plotted as a function of spectroscopic redshift according to Eq.2.10 (left panel) and bias as a function of spectroscopic redshift (right panel).
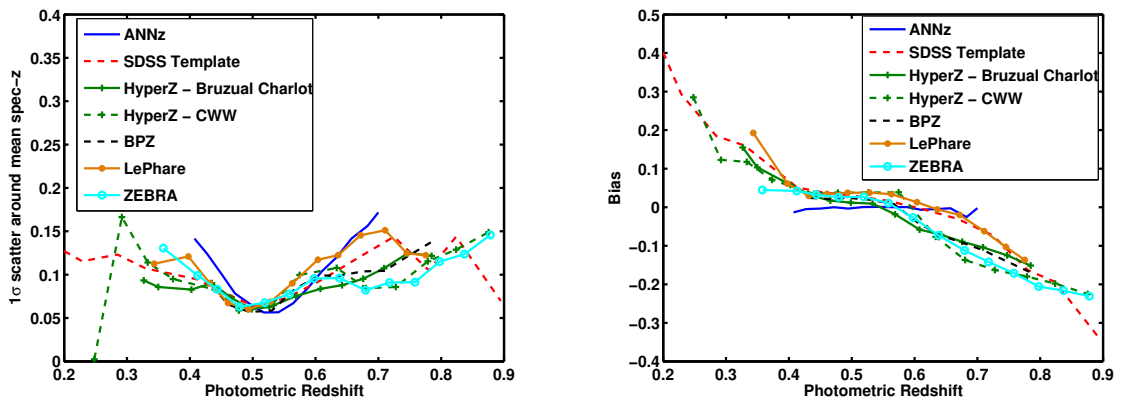
Figure 2.6: 1σ scatter around mean spectroscopic redshift as a function of photometric redshift according to Eq.2.11 in the left panel and bias as a function of photometric redshift in the right panel.

$Method$	$f0$	$f1$	$f2$	$f3$	$f4$
$ANNz$	37%	28%	31%	4%	0.02%
$SDSS$	27%	31%	37%	4.5%	0.8%
$HyperZCWW$	24%	32%	35%	7%	1.5%
$HyperZBC$	26%	32%	32%	7%	1.5%
$LePHARE$	26%	34%	34%	4%	0.5%
$ZEBRA$	26%	34%	34%	5%	0.8%
BPZ	24%	32%	36%	6%	1%

Table 2.2: Fraction statistics for the different public photo-z codes presented and compared in this chapter.

been a suitable statistic as well. However there are reasons for which the statistic that is quoted in Table 2.2 is interesting. For instance if one is interested in cosmological probes where the galaxies are separated in photo-z bins then a subdivision along the photo-z axis is more natural. Given that these galaxies have relatively good photometric redshifts, one can see that the fraction of outliers is small for all estimators. However there is still a difference between different implementations of publicly available codes.

The integrated bias and scatter for all the codes and libraries used is presented in Table 2.3. It can be seen that the training code performs best which is to be expected with a complete training set and that the bias here is very small. However this statistic does not show the redshift dependence of the scatter or bias which may be of interest depending on the application.

2.6 MegaZ LRG DR6: Photometric Redshift Catalogue for LRGs in SDSS DR6

Given the differences in photometric redshift estimates that are present between different publicly available codes, it seems sensible to construct photometric redshift catalogues with estimates from more than one code. Having tested six publicly available codes on a sample of LRGs with spectroscopic redshifts from the 2SLAQ survey, all six codes are now used in the construction of a photometric catalogue of over 1.5 million LRGs from SDSS DR6 with redshift estimates and errors on these. The 2SLAQ galaxies are used as a training set for the photometric sample. The

$Method$	σ_z	$bias$
$ANNz$	0.0575	0.0014
$SDSS$	0.0808	-0.0264
$HyperZCWW$	0.0973	-0.0076
$HyperZBC$	0.0862	0.0160
$LePHARE$	0.0718	-0.0302
$ZEBRA$	0.0898	0.0013
BPZ	0.0933	0.0112

Table 2.3: Average 1σ scatter (Eq. 2.8) and bias (Eq. 2.9) for the entire sample for different methods. Note that the definition of the 1σ scatter here is different from that in Collister *et al.* (2007) Eq. 10

increase in area surveyed when going from the spectroscopic sample to the photometric sample, is clearly illustrated in Figure 2.7 which maps the 2SLAQ and SDSS DR6 LRGs in the sky.

The catalogue, MegaZLRG DR6, is an extension to the MegaZ LRG catalogue of Collister *et al.* (2007). The photometric sample has been extended from SDSS DR4 to SDSS DR6 imaging thereby allowing the addition of ∼300,000 LRGs to the original sample. Furthermore redshift estimates from six publicly available codes are provided along with errors on these. Trained empirical values are also provided to perform star/galaxy separation based on a set of 15 photometric parameters as in Collister *et al.* (2007). The extended MegaZ-LRG catalogue contains 1543596 objects over more than 8000 square degrees of the sky. As in previous studies, LRGs are expected to be about 95% of the sample and M type stars are expected to be 5% of the sample. All the parameters included in the revised catalogue are described in Table 2.4. The data is publicly available from the following website[4].

Table 2.4: Parameters included in the updated MegaZ-LRG DR6 photometric redshift catalogue.

SDSS Parameter	Description
objID	SDSS objID
	Continued on next page

Table 2.4 – continued from previous page

SDSS Parameter	Description
ra	J2000 right ascension
dec	J2000 declination
dered_u	
dered_g	
dered_r	Dereddened model magnitudes
dered_i	
dered_z	
err_u	
err_g	
err_r	Magnitude errors
err_i	
err_z	
deVMag_i	Dereddened de Vaucouleurs magnitude
z_annz	ANNz photometric redshift
z_annz_err	ANNz photometric redshift error
delta_sg	ANNz galaxy probability
delta_err_sg	ANNz galaxy probability error
z_sdss	SDSS photometric redshift
z_sdss_err	SDSS photometric redshift error
z_hzcww	Hyper-z CWW photometric redshift
z_hzcww_chi	Hyper-z CWW chi squared
z_hzcww_errl	Hyper-z CWW photometric redshift 68% lower confidence limit
z_hzcww_errh	Hyper-z CWW photometric redshift 68% higher confidence limit
z_hzbc	Hyper-z BC photometric redshift
z_hzbc_chi	Hyper-z BC chi squared
z_hzbc_errl	Hyper-z BC photometric redshift 68% lower confidence limit
z_hzbc_errh	Hyper-z BC photometric redshift 68% higher confidence limit
z_bpz_bayes	BPz bayesian photometric redshift
z_bpz_errl	BPz photometric redshift 90% lower confidence limit

Table 2.4 – continued from previous page

SDSS Parameter	Description
z_bpz_errh	BPz photometric redshift 90% higher confidence limit
z_bpz_odds	BPz bayesian odds parameter
z_bpz_ml	BPz maximum likelihood photometric redshift
z_bpz_chi	BPz chi squared
z_zebra	ZEBRA photometric redshift
z_zebra_errl	ZEBRA photometric redshift 68% lower confidence limit
z_zebra_errh	ZEBRA photometric redshift 68% higher confidence limit
z_lp	Le PHARE photometric redshift
z_lp_prob	Le PHARE percentage PDF between $dz = z_{best} \pm 0.1(1 + z_{best})$

A comparison of the different photometric redshift estimates from each code is now presented for the MegaZLRG DR6 catalogue. Figure 2.8 shows histograms of the difference between photo-z for each pair of codes that have been used in the analysis.

For instance, comparing ANNz to other codes there seem to be some outliers at a redshift difference of 0.1 compared to Hyperz CWW, BPZ and Hyperz BC. Similarly other pairs of codes produce outliers which indicates that this is not only a difference between template codes and training codes. Note that for instance comparing ZEBRA with codes such as HyperZ CWW or SDSS code there is a good agreement on the scatter but there is a small bias between the codes which may suggest that the templates used might not have been optimal in some codes.

Although all the photometric redshift estimates are of relatively good quality, there are still considerable differences between the codes. There is therefore a need to deconstruct the effects of the algorithm and the template libraries in order for one to understand these differences and have even more reliable photo-z's in the future.

2.7 The Photometric Redshift Accuracy Testing Program

The Photometric Redshift Accuracy Testing Program is a large community-based project to test and improve the accuracy of photometric redshifts. The objective is to test the different codes currently used for photometric redshift estimation, different template sets, the influence of noise on the photometry on redshift estimates, different approaches to galaxy photometry as well as
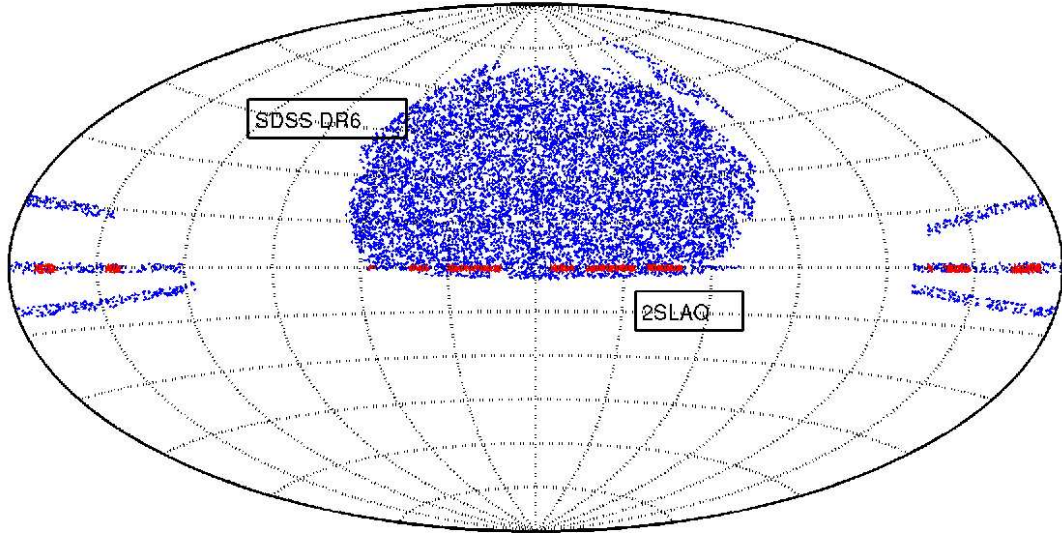
Figure 2.7: Map of the MegaZ-LRG sample (blue) covering the SDSS DR6 area as well as the 2SLAQ sample (red). For clarity only a random subsample of galaxies have been plotted.

different filter sets. So far, there have been two testing steps within PHAT. These are described and some preliminary results presented in this section.

2.7.1 Phase0

The first step, Phase0, was to run different photometric redshift codes on a very simple basic simulation generated using the LePhare code by Stephane Arnouts. This was used to investigate the lowest level of accuracy between codes. The simulations were created based on six templates from Coleman *et al.* (1980) and Kinney et al. (1996). The filter set comprised of optical $ugriz$ filters from the CFHTLS survey, near infra-red $YJHK$ filters modelled as idealised filter curves as well as the Spitzer IRAC 3.6μ and 4.5μ bands. The magnitudes were corrected for IGM absorption according to Madau (1995) and the objects distributed in the mock catalogue according to an SED dependent luminosity function. Finally the sample was flux limited at $r < 24$ and noise was added.

Fifteen different photometric redshift estimates were obtained in Phase0 from different members of the community. The photometric redshifts from the neural network code, ANNz are plotted in Figure 2.9 along with those obtained using LePhare from which the simulations were generated. A complete training set has been assumed for the neural network. Note that differences between the model and photometric redshifts in this case indicate that the codes are inconsistent with Le-
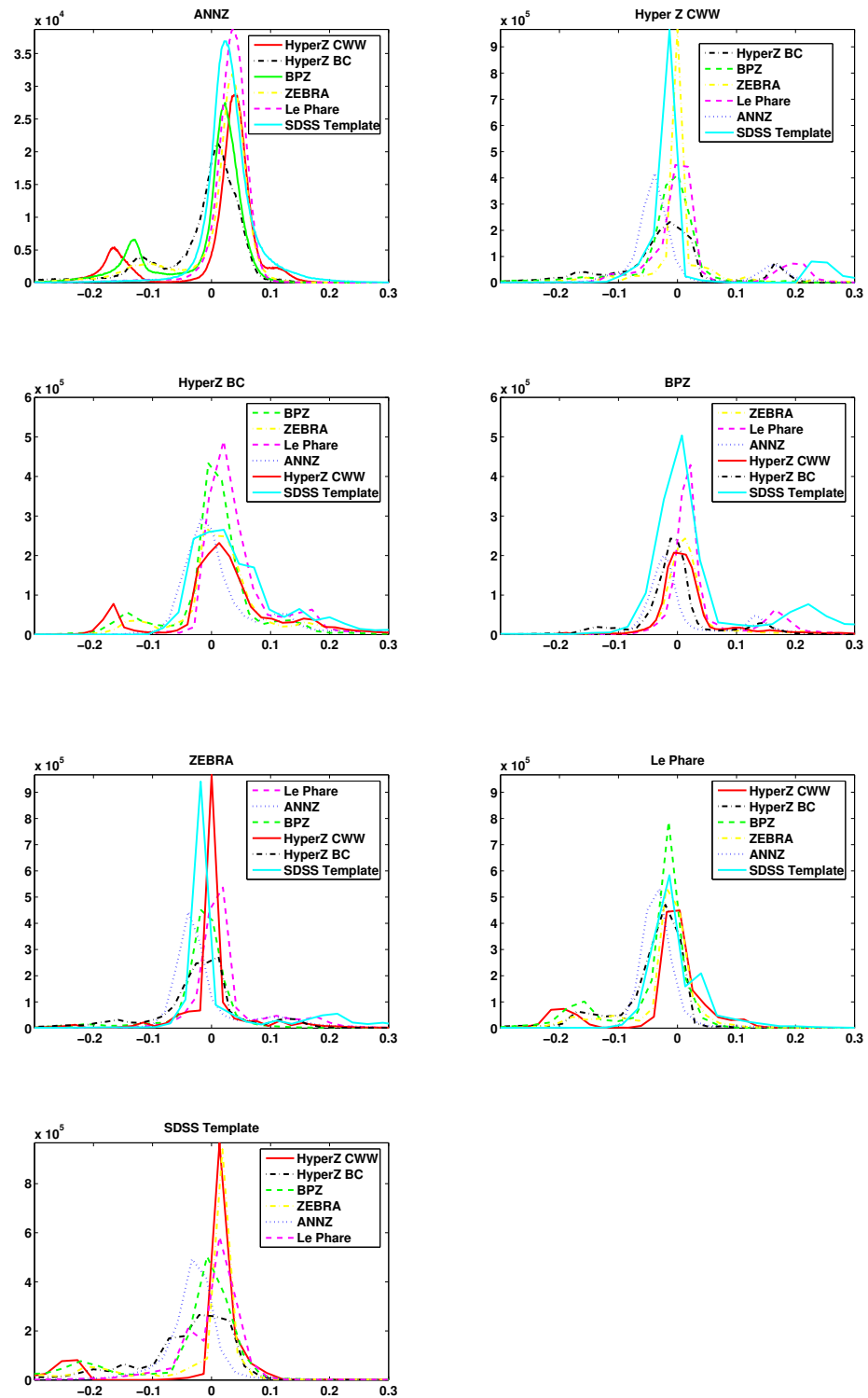
Figure 2.8: Histogram of the difference between the photometric redshift estimation between all pairs of codes used in this analysis.
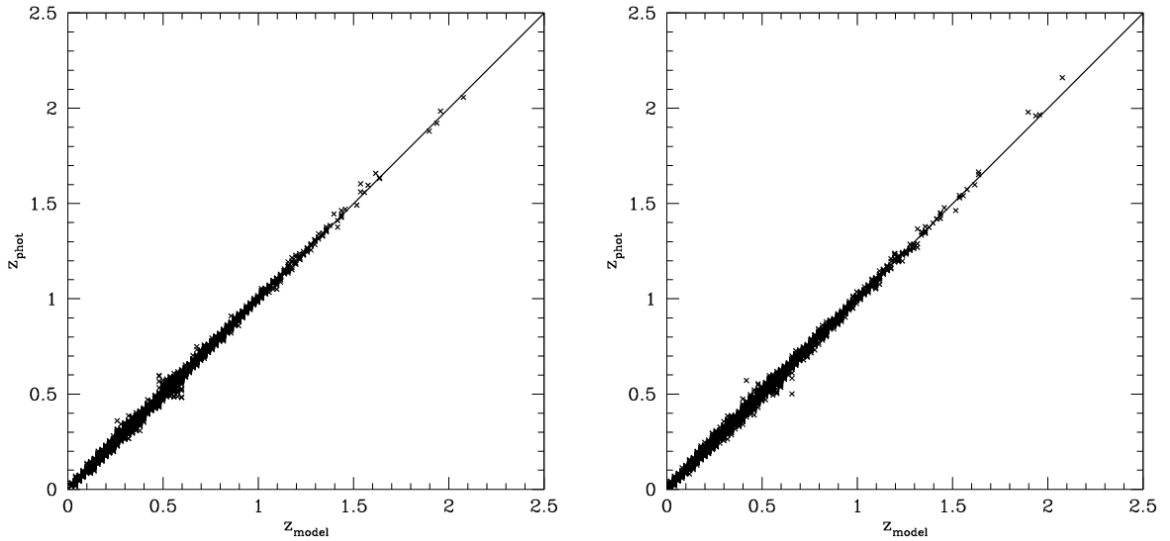
Figure 2.9: Results of PHAT Phase0 testing from LePhare (right) which has been used to create the basic simulations and ANNz (left). Deviations from the $y = x$ line on the left occur due to the addition of noise to the photometry.

Phare but not necessarily incorrect. Figure 2.9 indicates however that the results from ANNz and LePhare are consistent for this initial, basic simulation assuming a complete and representative training set is available for ANNz.

2.7.2 GOODS-N Catalogue

In the second stage of PHAT, photometric redshift estimates were produced for real observational data obtained in the GOODS-N field. The catalogue contains photometry in 18 bands for 1984 objects originating from many different observing programs and spanning a wide redshift range. One quarter of the objects have spectroscopic redshifts available for training purposes which is probably not sufficient for most training methods and therefore will highlight the impact of incomplete training sets on the photometric redshift estimate in these codes. The photometry available is in bands: U (Kitt Peak National Observatory), BVRIZ (Subaru), JH (WFCAM), H/K, K, F435W, F606W, F775W, F850LP (ACS), IRAC 3.6μ, IRAC 4.5μ, IRAC 5μ and IRAC 8μ (Spitzer).

So far, photometric redshifts have been obtained from this data set from nine members of the community. The results of running ANNz on this data set with and without the four Spitzer IRAC bands, are illustrated in Figure 2.10. As can be seen, the results are now considerably worse than was the case for the basic simulations highlighting the importance of a complete training set for
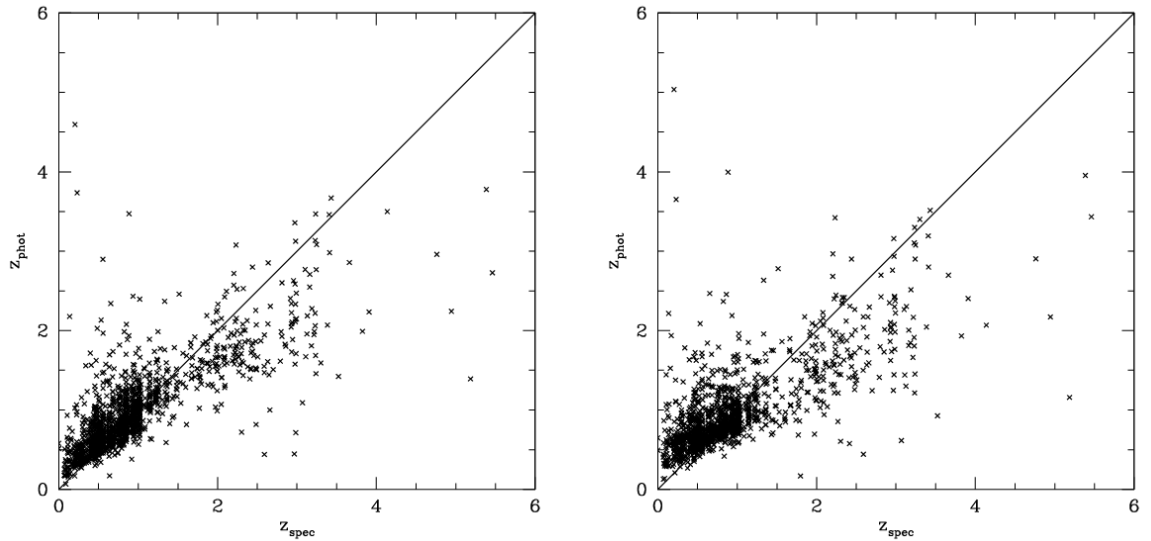
Figure 2.10: Results of running ANNz on the GOODS-N catalogue with (left) and without(right) far-infra red data from Spitzer IRAC.

ANNz. No particular improvement in the photometric redshift estimates is seen on addition of the mid-infrared data from Spitzer.

The photometric redshift estimates obtained from different codes are considerably discrepant from each other for this observational data set. Future testing steps within PHAT will investigate the cause of these discrepancies in more detail.

2.8 Conclusions

In this chapter, the different methods for photometric redshift estimation have been introduced and several publicly available codes for photo-z estimation described in detail. Six publicly available codes have been compared on a sample of luminous red galaxies from the 2SLAQ survey with available spectroscopic redshifts. This *black box* comparison of the code and template library ensemble has illustrated the need for a more thorough comparison where the effects of these two components can be distentangled. Several figures of merit have been used to assess the photometric redshift performance of each code for the sample of LRGs leading to the following specific conclusions:

- As expected the availability of a complete training set for this sample means the training method, ANNz performs best in intermediate redshift bins where there are plenty of spec-

troscopic redshifts available.

- Le Phare performs very well, particularly in the lower redshift bins suggesting that the Poggianti templates may be a better fit to the LRGs at these redshifts compared to the other templates used in this comparison.

- HyperZ run with the BC templates produces considerably better results than using the same code with the CWW templates once again highlighting the importance of template choice in photometric redshift estimation.

- The SDSS template code gives very good results compared to other codes at the highest photo-z bins despite having only one evolving template for the LRGs. Given the narrow range in SEDs of our sample of Luminous Red Galaxies, the strengths of template-based codes with extensive template libraries are not adequately highlighted by this comparison.

- ZEBRA shows a small average bias indicating the importance of the template optimisation technique in removing biases.

- There is a discrepancy between the scatters found for all the codes and the values range from 0.057 to 0.097. Both are considered good results for photo-z estimates as one would expect from LRGs.

- The six public codes have been used to construct a new photometric redshift catalogue of ~1.5 million LRGs from SDSS DR6 (MegaZLRG-DR6). This catalogue contains the photometric redshift as well as error estimates from all the codes and will no doubt prove valuable for studies of both cosmology and galaxy formation and evolution.

Given that all the differences illustrated between the codes will also depend on galaxy type and training set size, it is imperative that a more thorough comparison is carried out where the effects of codes and templates are deconstructed, in order to understand what factors affect the photo-z accuracy. Preliminary results have been shown from the Photometric Redshift Accuracy Testing Program (PHAT) which is currently in the process of carrying out such a comparison. In the next two chapters of this thesis, photometric redshifts are forecast for future galaxy surveys and the implications of photometric redshift errors on cosmological parameter constraints are investigated in some detail.

PHOTOMETRIC REDSHIFTS FOR THE DARK ENERGY SURVEY AND VISTA AND IMPLICATIONS FOR COSMOLOGY

*The work described in this chapter is an extended version of the paper **Banerji, Abdalla, Lahav & Lin, 2008, MNRAS, 386, 1219***

3.1 Description of Surveys

The Dark Energy Survey is a proposed ground-based photometric survey that will image 5000deg^2 of the South Galactic Cap in the optical $griz$ bands as well as the Y-band. The survey will be carried out using the Blanco 4-m telescope at the Cerro Tololo Inter-American Observatory (CTIO) in Chile. The main objectives of the survey are to extract information on the nature and density of dark energy and dark matter using galaxy clusters, galaxy power spectrum measurements, weak lensing studies and a supernova survey. This will be achieved by measuring redshifts of some 300 million galaxies in the redshift range $0 < z < 2$, tens of thousands of clusters in the redshift range $0 < z < 1.1$ and about 2000 Type 1a supernovae in the redshift range $0.3 < z < 0.75$ (The Dark Energy Survey Collaboration 2005). Observations will be carried out over 525 nights spread over five years between 2011 and 2016 and when completed, DES will provide a legacy archive of data extending around two magnitudes deeper than the Sloan Digital Sky Survey which is currently the largest existing CCD survey of the Universe by volume. The DES volume is estimated to be

$23.74h^{-3}Gpc^3$ in the range $0 < z < 2$, about ten times that of the SDSS LRG sample (Blake *et al.* 2007). This is assuming a 10σ AB magnitude limit of $r \lesssim 24$.

The DES survey area overlaps with that of several other important current and future surveys, for example, the southern equatorial strip of the Sloan Digital Sky Survey and the South Pole Telescope SZE cluster survey. The entire DES region will also be imaged in the near infra-red bands on two public surveys being conducted on the Visible and Infra-Red Survey Telescope for Astronomy (VISTA) at ESO's Cerro Paranal Observatory in Chile.

Most of the time on the VISTA telescope has been dedicated to large-scale public surveys. Two of these surveys that are relevant to cosmology are the Vista Hemisphere Survey (VHS) and the Vista Kilo-Degree Infra-red Galaxy Survey (VIKING) - (Arnaboldi et al. 2007).

The VISTA Hemisphere Survey is a proposed panoramic infra-red survey that will image the entire southern sky ($\sim$20000deg^2) in the near infra-red $YJHK_s$ bands when combined with other public surveys. About 40% of the total VHS time has been dedicated to VHS-DES, a 4500deg^2 survey being carried out in the DES region over 125 nights in order to complement the DES optical data with near infra-red data. The initial proposal is for the survey to image in the JHK_s bands with 120s exposure times in each band reaching 10σ magnitude limits of $J = 20.4, H = 20.0$ and $K_s = 19.4$. A second pass may then be obtained with 240s exposures in each of the three NIR filters in order to reach the full-depth required by DES. The VHS-DES survey assumes that Y-band photometry will come from the Dark Energy Survey.

The remaining 500deg^2 of the DES area not covered by VHS-DES, will be imaged by VIKING which is a near infra-red survey designed to provide an important complement to the optical KIDS project being carried out on the VST. The details for all these surveys are summarised in Table 3.1.

3.2 Simulating Mock Data

In this work, two sets of mock galaxy samples have been used as simulations of data from DES and VHS. In this section the way in which these data samples are generated is described. Both catalogues are generated using Monte Carlo methods after assuming relevant redshift, magnitude and type distributions.

Survey	Bands	10σ magnitude lims	Area
DES	g	24.6	5000deg^2
	r	24.1	
	i	24.3	
	z	23.9	
	Y	21.6	
VHS-DES	J	20.4	4500deg^2
	H	20.0	
	K_s	19.4	
VIKING	Z	22.4	1500deg^2
	Y	21.6	
	J	21.4	
	H	20.8	
	K_s	20.5	
KIDS	u'	24.1	1500deg^2
	g'	24.6	
	r'	24.4	
	i'	23.4	

Table 3.1: Areas and 10σ magnitude limits for the surveys discussed in this chapter. The magnitudes are in the AB system.

3.2.1 DES5yr Sample

The first mock catalogue is that of Oyaizu *et al.* (2006) and Lin *et al.* (2004*a*) - DES5yr hereafter. It adopts the galaxy magnitude-redshift distribution derived from the luminosity functions of Lin *et al.* (1999) and Poli et al. (2003) and a type distribution derived using data from the GOODS/HDF-N field (Capak et al. 2004; Wirth et al. 2004; Cowie *et al.* 2004) and the CWW template SEDs (Coleman *et al.* 1980). A flux-limited sample is constructed with $0 < z < 2$ and $20 < i < 24$. The photometric errors on each object are computed according to the DES 10σ $griz$ magnitude limits. Note, no attempt is made here to fit a reddening value to each galaxy.
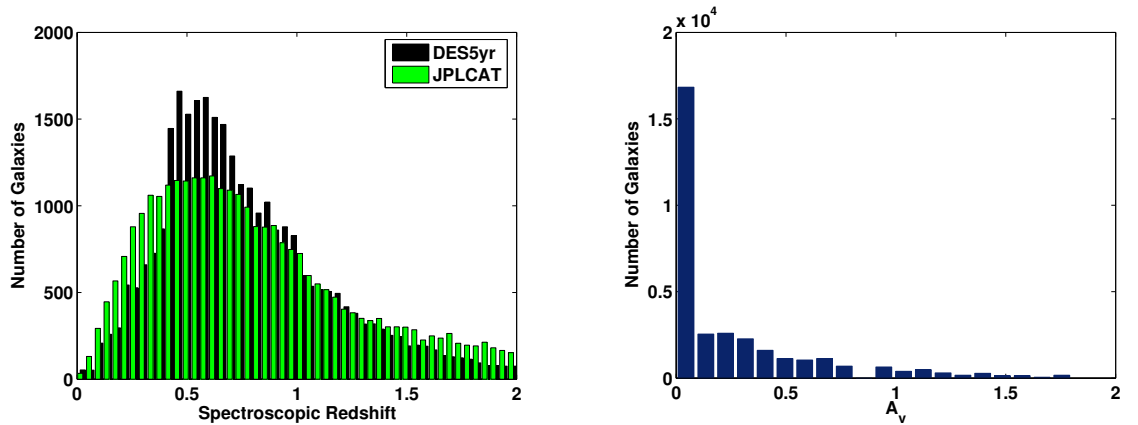
Figure 3.1: The distributions characterising our simulated catalogues for the DES and DES+VHS samples. The left-hand panel shows the redshift distribution for ~ 30000 galaxies in the DES5yr and JPLCAT simulations. All galaxies have $20 < i < 24$ and $0 < z < 2$. The right-hand panel shows the distribution of galaxies as a function of the extinction parameter, A_v for the JPLCAT sample.

3.2.2 JPL Mock Catalogue

The second catalogue is described in Abdalla *et al.* (2008*a*) - JPLCAT hereafter. Templates constructed from broadband photometry using a method similar to Budavári et. al (1999) were fit to real objects from the GOODS-N spectroscopic sample (Cowie *et al.* 2004; Wirth et al. 2004) in order to generate this catalogue. The templates were de-reddened and at the time of fitting, the best fit SED and reddening value were found simultaneously. A Calzetti reddening law (Calzetti 1997) was used. Further details of the method used to create photometric data for the catalogue with the correct redshift distribution and luminosity evolution, can be found in §2 of Abdalla *et al.* (2008*a*). For the purposes of this chapter, however, the important difference between this and the DES5yr sample is the fact that the galaxies are reddened and corrected for dust extinction. The JPLCAT sample also uses two more templates from Kinney et al. (1996) to fit the galaxies in addition to the CWW templates used for the DES5yr sample. For the work described in the rest of this chapter, the JPLCAT sample when used has been cut so as to have the same magnitude and redshift limits as the DES5yr sample. The redshift distribution for both samples cut to include the same number of galaxies, as well as the distribution of galaxies in the JPLCAT sample for different values of the extinction parameter, A_v, are shown in Figure 3.1.

Note that the JPLCAT sample is more complex and hence the results from it are likely to be more pessimistic than those for the DES5yr sample. However, both catalogues are generated by fitting models to real data and it is not obvious which of these models captures the true colour variance best. Hence both can be taken as realistic possibilities for modelling the DES and VHS data samples. [1]

3.3 Photometric Redshift Analysis

The artificial neural network method for photometric redshift estimation, ANNz (Collister & Lahav 2004) is used to calculate photometric redshifts in all the work that is described in this chapter. The code has already been introduced in § 2.3.6 in the previous chapter and is used as described there.

3.3.1 Choice of Filters

In this section the impact of different filter combinations and survey depths on the photometric redshift estimate is considered. This is done by running the neural network code described in §2.3.6 on the DES5yr sample described in §3.2. ANNz was run on the mock data for five different filter configurations. These are summarised in Table 3.2. Photometric redshifts were computed for each of these cases and from the available true redshifts, the scatter on the photo-z estimate, σ_z, (Eq 2.8) was also determined.

Figure 3.2 and Figure 3.3 show the results of this study. It can be seen that inclusion of the NIR filters leads to an improvement in σ_z by $\sim$30% for $z > 1$. σ_z is 0.2 for $z > 1$ for the DES only sample and 0.15 for the DES+VHS sample in the same redshift range. Increasing the exposure time in the NIR also leads to improved scatter on the photometric redshift. The scatter is high at low redshifts due to lack of u-band imaging. These results are consistent with those of Abdalla *et al.* (2008*a*), The Dark Energy Survey Collaboration (2005) and Oyaizu *et al.* (2006).

As can be seen in Figure 3.2 however, there are many outliers present in the sample. Therefore, the quantity σ_{68} defined in § 2.5 is also considered. For DES $grizY$ photometry, σ_z is 0.13 across the entire redshift range of $0 < z < 2$ whereas σ_{68} is 0.08. When one adds the VHS JHK_s photometry to this, σ_z improves to 0.11 across the entire redshift range and σ_{68} improves to 0.07.

---

[1]Since this study was completed, more sophisticated simulations of the Dark Energy Survey data have become available through a series of Dark Energy Survey *Data Challenges*. However, these are not used in this analysis.
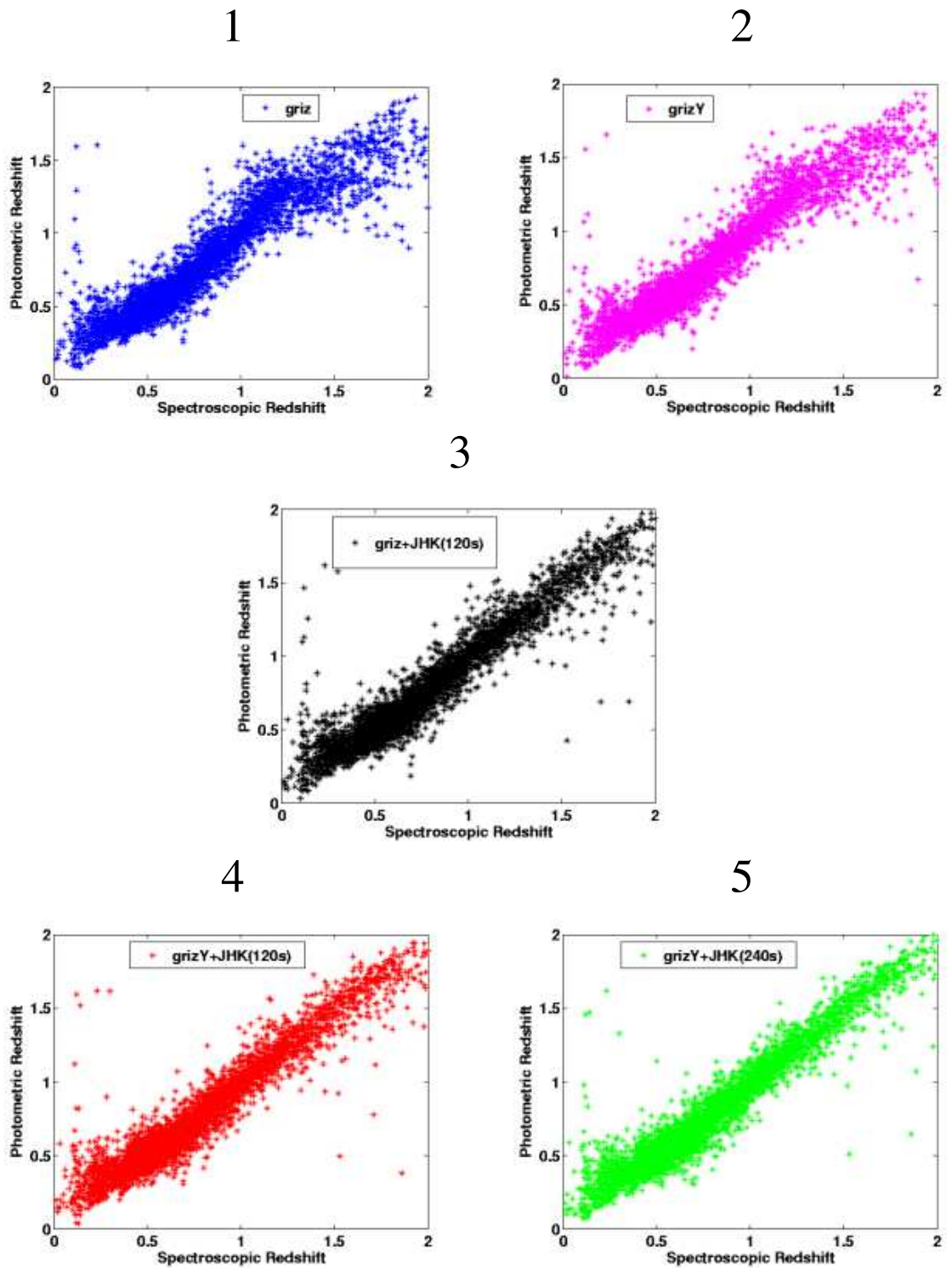
Figure 3.2: Scatter plots of photometric redshifts as a function of the true redshifts for each of the different survey configurations detailed in Table 3.2. These plots are generated for a sample of 5000 randomly selected galaxies.

No.	Filters	Exposure Time	10σ magnitude limits
1	DES g	400s	24.6
	DES r	400s	24.1
	DES i	1200s	24.3
	DES z	1600s	23.9
2	DES $griz$	As in 1	As in 1
	DES Y	400s	21.6
3	DES $griz$	As in 1	As in 1
	VHS J	120s	20.4
	VHS H	120s	20.0
	VHS K_s	120s	19.0
4	DES $griz$	As in 1	As in 1
	DES Y	As in 2	As in 2
	VHS JHK_s	As in 3	As in 3
5	DES $griz$	As in 1	As in 1
	DES Y	As in 2	As in 2
	VHS J	240s	21.2
	VHS H	240s	20.8
	VHS K_s	240s	20.2

Table 3.2: Summary of filter configurations of DES and VHS considered in §3.3.1.

3.3.2 Impact of Galactic Reddening

In this section, the impact of reddening on the photometric redshift estimate is considered. The DES5yr and JPLCAT samples differ in their inclusion of reddening in the galaxy samples and this has already been described in § 3.2. In order to assess how this difference affects the photo-z estimate, the neural network code is run on the JPLCAT sample with 5-band DES optical photometry as well as 8-band DES+VHS photometry with an exposure time of 120s in the NIR. The results are shown in Figure 3.4 where the 1σ scatter defined in Eq. 2.8 is plotted as a function of the spectroscopic redshift for both the DES5yr and JPLCAT samples for each of the two filter configurations. Note that before comparing the two catalogues, the JPLCAT sample has been cut to have the same magnitude and redshift limits as the DES5yr sample i.e. $0 < z < 2$ and $20 < i < 24$.
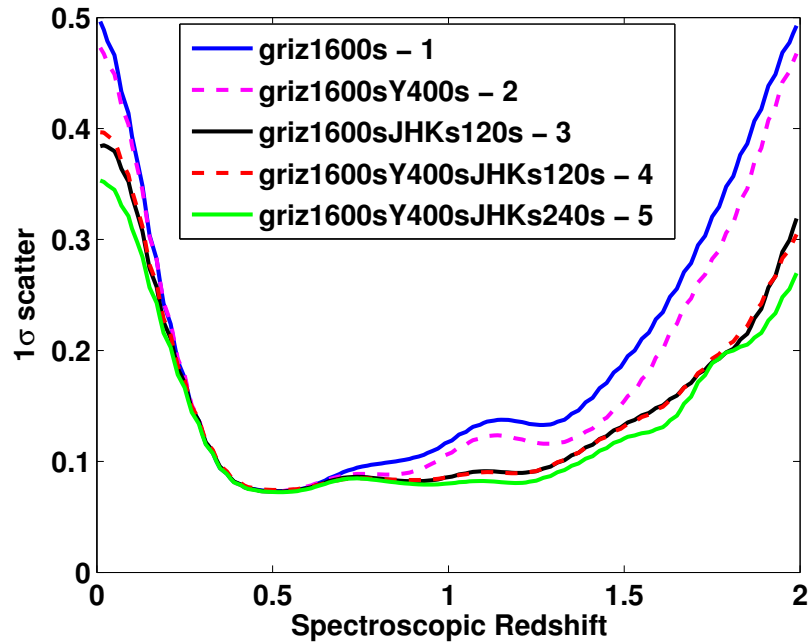
Figure 3.3: The 1σ scatter on the photometric redshift as a function of the spectroscopic redshift for each of the survey configurations detailed in Table 3.2. Curves are labelled 1 to 5 corresponding to the numbers in Table 3.2.

Although the same improvement is noted with inclusion of the NIR filters as discussed in §3.3.1, the effects of reddening worsen the photo-z scatter overall by $\sim 30\%$ in some regions. This can be explained by the fact that there exists a degeneracy between redshift and galaxy reddening which means that faint reddened galaxies at low redshift can often appear to have the same colours as brighter galaxies at high redshift with no reddening (Abdalla *et al.* 2008*a*). However Figure 12 of Abdalla *et al.* (2008*a*) shows that this degeneracy is broken in the redshift range $1.1 < z < 1.5$ and the reddened DES only catalogues have a similar scatter to their unreddened counterparts in this redshift range. These authors have also shown that galaxies with small values of A_v have relatively good photo-z estimates whereas those with high A_v are scattered towards higher photometric redshifts. Figure 3.1 shows that most of the galaxies in the JPLCAT sample have relatively small values of A_v and therefore while one needs to be aware that any amount of dust extinction is likely to affect the photo-z estimate, this effect should only be small for the DES sample.

In order to account for this effect of the dust extinction on the photometric redshift estimate, some authors attempt to include the dust extinction, A_v as a free parameter in their codes (e.g.
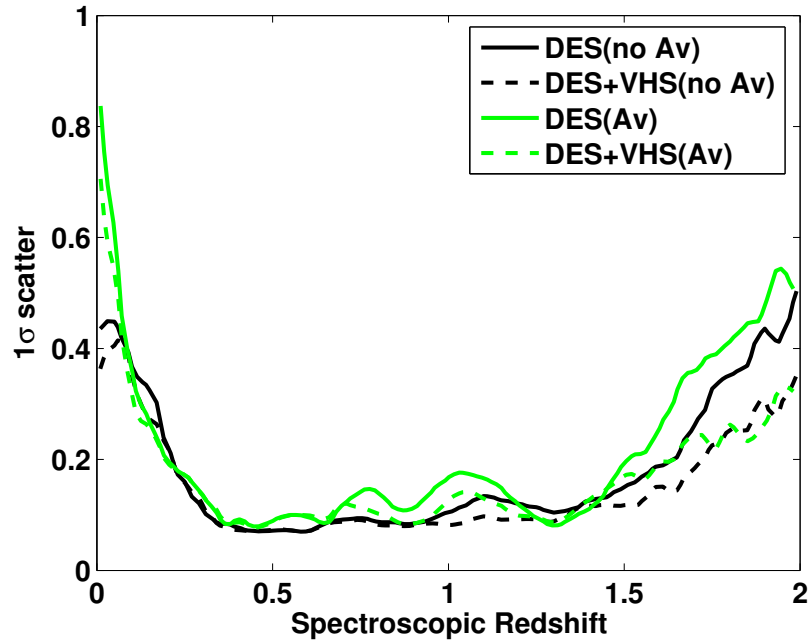
Figure 3.4: The 1σ scatter on the photometric redshift for DES with and without VHS NIR data for two different mock catalogues. The black lines are produced by DES5yr catalogues that do not include the effects of reddening. The green lines are produced by the JPLCAT mocks which include the effect of reddening. The solid lines show the scatter without VHS NIR data while the dashed lines include VHS NIR data.

Rowan-Robinson (2003); Bolzonella *et al.* (2000)) and simultaneoulsy solve for this and the photometric redshift. The neural network code has been modified to produce estimates for the A_v and SED type of the galaxy using the JPLCAT sample with 8-band DES+VHS photometry. A 8:16:16:2 architecture is used for the neural network and this marginalises over the galaxy redshift which isn't constrained.

The results are shown in Figure 3.5 where density plots of the true A_v against the predicted A_v and the true type against the predicted type are shown.

The rms scatter around the mean of the A_v estimate is found to be 0.27 and the bias to be 0.0031. The predicted A_v is found to be biased towards lower values of A_v for galaxies with a high degree of reddening and towards higher values of A_v for galaxies with a low value of reddening. The scatter on the type is found to be 7.7 and the bias to be -0.0048. The JPLCAT sample has been generated using six SED templates - E, Sbc, Scd, Im (Coleman *et al.* 1980) and SB2, SB3 (Kinney et al. 1996) corresponding to types 0, 10, 20, 30, 40 and 50. As the error on the type is smaller than the difference between these templates, ANNz can effectively be used to
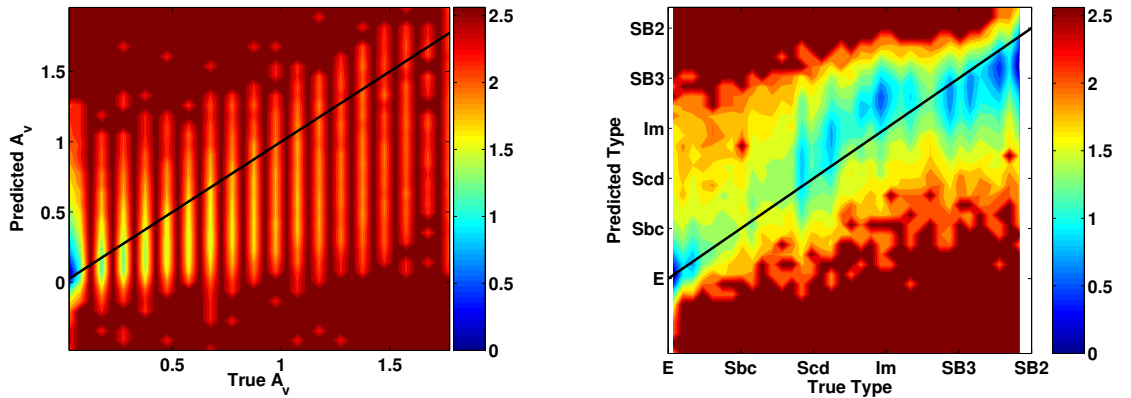
Figure 3.5: Density plot of the ANNz output when the neural network code is used to simultaneously predict the A_v and type of an object. The left-hand plot shows the predicted dust extinction, A_v as a function of the true A_v. The right-hand plot shows the predicted SED type of each galaxy as a function of the true type. The plots are colour-coded and the scale is exponential; a colour difference of one is equivalent to the density being decreased by a factor of e. The solid black lines show where the true A_v and true type are equal to the predicted A_v and predicted type.

classify these galaxies into $50/7.7 =$ about six or seven spectral types within the context of DES.

Note that in this work, no attempt has been made to optimise the neural network for the calculation of the A_v and type as the objective is to demonstrate that it is possible to use the neural network code to produce estimates for these quantities as well as the redshift and that this may be useful for samples where there is a high degree of reddening.

Through the rest of this work, the DES5yr sample which does not include the effects of reddening has been used for all the analysis.

3.3.3 Clipped Catalogues

In the previous sections it was seen that catastrophic errors in the photometric redshift estimate can arise depending on the exact filter configuration and the galaxy formation science encoded within mock catalogues. Given that there are likely to be a host of different reasons why the photometric redshift estimate may be prone to large errors, a lot of which are not fully understood, it seems sensible to devise some way of *clipping* a sample. This is done by removing galaxies with large photo-z errors before using the photo-z estimate for cosmological analysis. In most situations where photometric redshift analysis is particularly powerful, the spectroscopic redshift of the galaxies is not known and therefore there is no way of using this information to assess
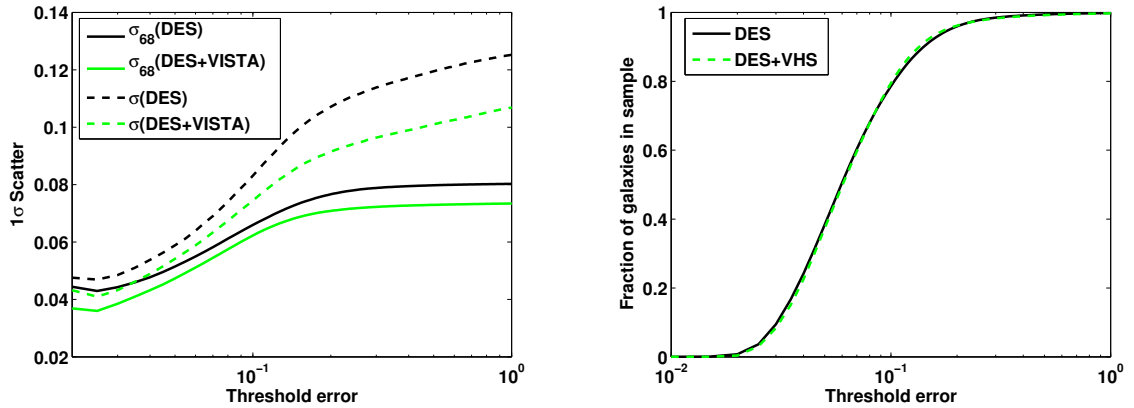
Figure 3.6: The left hand plot shows the scatter, σ_z, and σ_{68} as a function of the clipping threshold, which is the threshold on the neural network error defined in Eq 2.7. The right-hand plot shows the fraction of galaxies remaining in the sample as a function of the clipping threshold when galaxies with neural network errors above the clipping threshold are removed from the sample.

whether the photo-z estimate is accurate. However, the photo-z prediction will depend strongly on the errors in the photometry and this information could potentially be used to *clip* the sample as in Abdalla *et al.* (2008a). In order to do this, the neural network error estimate on the photometric redshift for each galaxy is used, as given by Eq. 2.7. All galaxies that have an estimated neural net error greater than a chosen threshold are removed from the sample, therefore resulting in a *clipped* catalogue of galaxies. The quantity, σ_{68} introduced in § 2.5 is used to quantify the scatter in the photometric redshift estimate once the outliers have been removed. In this section, the variation of the scatter with different clipping thresholds for the neural network error is considered.

Figure 3.6 illustrates the results of this study. In this figure the fraction of galaxies that remain in the sample once the clipping thresholds are applied, is also plotted. In each case, the results of using a 5-band DES optical $grizY$ catalogue as well as an 8-band DES+VHS optical and NIR catalogue are illustrated.

As expected, applying smaller threshold errors at which to cut the sample results in galaxies with poor photometry being removed from the sample and consequently a fall in the 1σ scatter on the photometric redshift for the entire sample. σ_{68} also decreases as one reduces the threshold error although this decrease is less steep than the decrease in σ_z. Both the scatter and σ_{68} are larger for the DES sample compared to the DES+VHS sample. It can be seen that applying a fairly conservative cut of 0.1 to the neural network error estimate for these mock samples results in a reduction in σ_z by a factor of ~ 1.5 for both the DES and DES+VHS samples. In both

cases about 80% of the original sample is retained after this cut. Smaller threshold errors can also be applied in order to reduce the scatter on the photometric redshift estimate even further. However, this results in more and more galaxies being lost from the original sample and at some point the number of galaxies remaining will prove insufficient for statistical analysis. This point is addressed in more detail in §3.4.1.

3.3.4 Impact of Training Sets

3.3.4.1 Effect on the Photo-z Scatter

All the photometric redshift analysis carried out in the previous sections assume that the training set used to train the neural network is totally representative of the testing set. However in reality, this may not always be the case. In this section, the impact of using different training sets with different imposed colour and magnitude cuts on the photometric redshift estimate, is considered.

The Dark Energy Survey region overlaps with that of several other current and future photometric and spectroscopic surveys thereby providing it with a fairly complete sample of training set galaxies. Some of these are detailed in Table 3.3. Here, two of the deeper surveys, namely DEEP2 and VVDS-Deep are considered and the training sets are modelled on the redshift distributions of these surveys before performing the usual photometric redshift analysis. Note that as DES overlaps the VVDS-Deep and DEEP2 fields, it is assumed that objects in these spectroscopic surveys will be imaged in all the DES bands and spectroscopic redshifts will be obtained with the highest level of confidence for all these objects. This is an idealised situation and unlikely to be the case for a real survey. As the DES5yr sample is magnitude limited as described in §3.2, the SDSS and 2dFGRS training sets are not considered as these objects are brighter than the mocks considered here.

DEEP2 is an ongoing spectroscopic survey being carried out by the DEIMOS spectrograph on the Keck II telescope. On completion, it will have obtained spectroscopic redshifts for ~ 54000 objects over an area of $3.5\mathrm{deg}^2$. The survey has been designed to sample the redshift range of $0.75 < z < 1.5$ and the spectrograph is capable of obtaining moderately high resolution spectra between $6300\mathring{A}$ and $9100\mathring{A}$. Targets are pre-selected using BRI imaging on the CFH12k camera on the Canada-France-Hawaii Telescope with a magnitude limit of $R_{AB} < 24.1$ and the colour cuts detailed in Table 3.3 imposed in order to sample the redshift range of interest.

In this study, 4681 objects with spectra from DEEP2 DR1 (Davis et al. 2003) are used to construct the normalised redshift distribution for the DEEP2 survey. This is plotted in Figure 3.7.

REDSHIFT SURVEY	SELECTION CRITERIA	NO.OF REDSHIFTS
SDSS Stripe 82	$r < 20$	70000
2dFGRS	$b_J < 19.45$	90000
VVDS Shallow	$I_{AB} < 22.5$	~ 26000
VVDS Deep	$I_{AB} < 24$	~ 60000
DEEP2	$(B - R) < 0.4$	~ 54000
	$(R - I) > 1.25$	
	$(B - R) < 2.35(R - I) - 0.54$	

Table 3.3: Summary of some of the spectroscopic surveys that will provide useful training sets for DES along with their imposed colour and magnitude cuts and the number of redshifts they are expected to obtain on completion.

As can be seen, there are very few objects with redshifts less than ~ 0.7 and greater than ~ 1.4. This is because the wavelength range for the spectrograph has been chosen such that the strong [OII] doublet which has a rest-frame wavelength of $3727\mathring{A}$ lies outside these wavelengths for all other redshifts. Note that data from the Groth Survey Strip region has not been included in this study. This survey field has no imposed colour cuts and therefore may be useful for sampling the low-redshift range of DES.

The VVDS spectroscopic surveys are being carried out using the VIMOS spectrograph on the Very Large Telescope (VLT). There is a shallow survey out to $I_{AB} = 22.5$ planned in 5 fields and a deeper survey out to $I_{AB} = 24$ in a single field. Targets are pre-selected using magnitudes from the imaging survey being carried out in the $UBVRI$ bands using the CFH12k camera on the CFHT. The latest catalogue contains 8981 objects upto $I_{AB} = 24$ in the redshift range $0 < z < 5.228$ (Le Fèvre et al. 2005, 2004) and has been used to construct the normalised VVDS-Deep redshift distribution plotted in Figure 3.7. Note that for both the DEEP2 and VVDS-Deep samples, stars and other objects with very low redshifts as well as high-redshift objects with $z > 2$ have been removed before plotting the redshift distributions so as to match the redshift range of the DES5yr sample.

Having obtained the redshift distributions for both DEEP2 and VVDS-Deep, accurate training sets are constructed, that simulate these surveys and that are to be used in the training of the neural network. This is done as follows. The DES5yr sample of 1 million objects is first separated
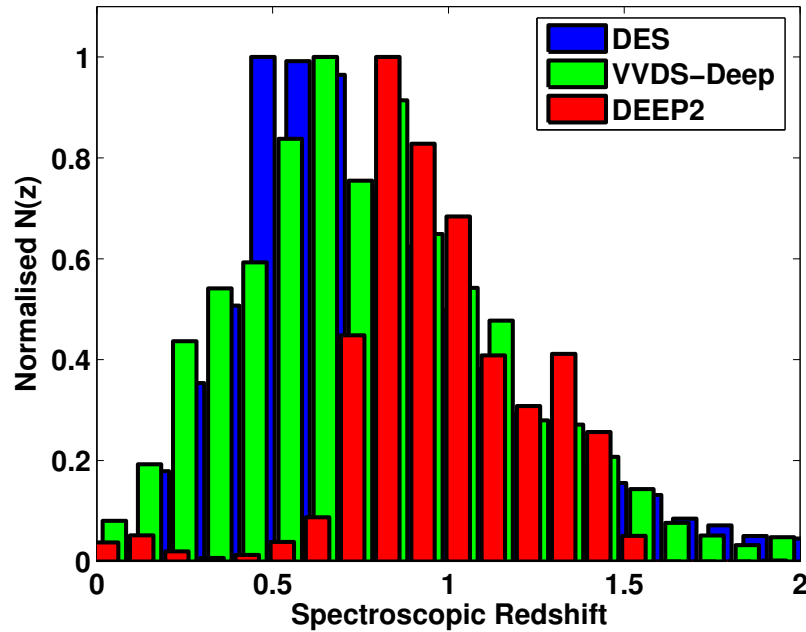
Figure 3.7: The normalised redshift distributions for DES, VVDS-Deep and DEEP2 surveys between $0 < z < 2$.

into two equal sized training and testing sets. The training set is then divided into 20 redshift bins and from the DEEP2 and VVDS-Deep redshift distributions, N_i, the number of galaxies from these surveys that would be present in each redshift bin, i once the survey is complete, is calculated. This assumes that on completion each survey will have obtained spectra for the number of objects given in Table 3.3. N_i galaxies are then randomly chosen from the DES5yr training set to be put into redshift bin i and in this way a new training set of galaxies that has the same redshift distribution as the real spectroscopic surveys, is constructed. The new training sets are then split further in order to create validation sets for ANNz to run on. This is done for a DES catalogue with optical $grizY$ photometry as well as a DES+VHS catalogue with 8-band optical and NIR JHK_s photometry. The simulated DEEP2 sample has many more galaxies at intermediate redshifts whereas the simulated VVDS-Deep survey samples the low and high redshift regimes better than DEEP2.

The neural network code is then run on the two DES catalogues using three different training sets each time - a training set with a DES redshift distribution, one with a DEEP2 redshift distribution and one with a VVDS-Deep redshift distribution. The results are shown in Figure 3.8 where the scatter on the photometric redshift is plotted as a function of the spectroscopic redshift for all
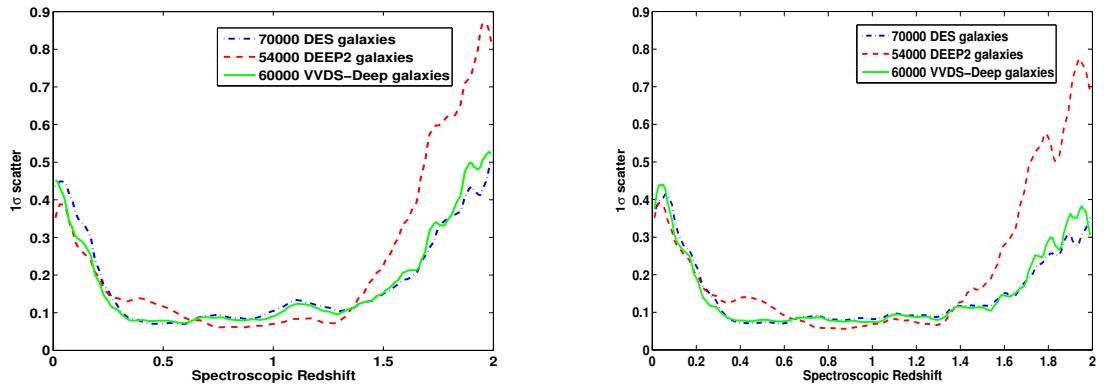
Figure 3.8: The scatter on the photometric redshift as a function of the spectroscopic redshift when the DES, DEEP2 and VVDS-Deep redshift distributions are used to construct the training set used by the neural network. The left-hand plot shows the scatter for a catalogue with optical $grizY$ photometry and the right-hand panel shows the scatter for a catalogue with 8-band optical and NIR JHK_s photometry.

these cases.

At low redshifts, the scatter is large for all three training sets due to lack of u-band data. At intermediate redshifts of $0.75 < z < 1.4$, the DEEP2 sample does better than the other training sets by $\sim 40\%$ as all its galaxies are concentrated in this region. As one moves to even higher redshifts, the DEEP2 sample gives very poor results due to a lack of training set galaxies in this redshift range whereas the DES and VVDS-Deep samples perform better. For $1.4 < z < 2$, the DEEP2 scatter is worse by a factor of ~ 2 compared to the VVDS-Deep and DES training sets. As expected, the scatter is smaller overall when NIR photometry is included for all three training set scenarios. The improvement is particularly noteworthy in the high redshift regime. Here, the scatter is reduced more for the VVDS-Deep and DES training sets with the addition of the NIR and not as much for the DEEP2 training set.

Assuming that both DEEP2 and VVDS-Deep obtain good quality spectroscopic redshifts across their entire redshift range, using a combination of these surveys to calibrate the DES photometric redshifts, is already as good as having a training set that is complete in redshift space. However, it should be noted that very few VVDS objects at $z > 1$ are likely to have high confidence redshifts. Also, this study has neglected other sources of incompleteness - e.g. the spectroscopic surveys may not obtain data for the full range of galaxy types covered by DES. However, it is promising that different methods have recently been developed to deal with this problem of

incomplete spectroscopic training sets e.g. (Newman 2008; Lima *et al.* 2008).

3.3.4.2 Effect on the Photo-z Bias

The bias on the photometric redshift estimate, b_z, in a given redshift bin between z_1 and z_2 is given by Eq 2.9. This bias can arise from various sources. The performance of the neural network will introduce some difference between the photometric and spectroscopic redshifts. Furthermore, having an incomplete training set or a cosmic variance limited sample also leads to biases in the photometric redshift estimate. If this bias does not depend on the testing set however, it can be quantified exactly using the training set and consequently subtracted from the photometric redshift estimate no matter how large it is. This method of removing the bias has already been shown to be effective in different photo-z codes described in Chapter 2. Once this bias has been removed, the residuals give some indication of the dependance of the photo-z error on the testing set. This error on the bias cannot be corrected for and it is this quantity that is evaluated in this section. In particular the effects of size and incompleteness of both the training and testing sets is considered. All the analysis carried out here is for the DES+VHS dataset and the incomplete training sets are modelled by imposing the DEEP2 colour cuts detailed in Table 3.3 on galaxies from the DES5yr catalogue.

The standard deviation on the bias in each bin can be defined as follows assuming Poisson statistics:

$$rms(b_z) = \frac{\sigma_z}{\sqrt{N_s}}, \tag{3.1}$$

where σ_z is the 1σ scatter on the photometric redshift given by Eq. 2.8 and N_s is the number of spectroscopic training set galaxies. This is a reasonable approximation to the error arising from the neural network and the analytical expression for the error on the bias agrees with the error from the neural network to within 15%. Given a suitably large number of training set galaxies with spectroscopic redshifts, this error on the bias can be effectively ignored as it does not depend on the testing set. In order to better understand some of the other sources of error on the bias that do depend on the testing set, the samples detailed in Table 3.4 are studied.

The first exercise is to quantify the differences in photometric redshift bias that arise when using different numbers of galaxies in the training set. Note that the differences in the bias calculated here are used as empirical estimators of the systematic shift one would get when dealing with data. SET3 and SET4 are used as training sets to calculate photometric redshifts for SETe.

	Number of Galaxies	Colour Cuts
SET1	50000	None
SET2	50000	Same as DEEP2
SET3	70000	None
SET4	200000	None
SETa	250000	None
SETb	250000	None
SETc	102643	Same as DEEP2
SETd	102589	Same as DEEP2
SETe	500000	None

Table 3.4: Summary of training (1-4) and testing (a-e) sets used to quantify differences in estimates of the photometric redshift bias.

All three samples are complete and have no imposed colour cuts. In Figure 3.9 the biases obtained for each of the two cases and the difference between these is plotted. This shows that changing the size of the training set by a factor of ~ 3 leads to a difference in the biases of the order of 10^{-3}.

Next, the effects of incomplete training sets on the photometric redshift bias is considered. SET1 and SET2 are used as training sets to calculate the photometric redshifts for samples SETa, SETb, SETc and SETd. SET1 is a complete training set while SET2 has been cut to reflect the colour cuts of the DEEP2 survey. SETa and SETb are both complete testing sets with different galaxies in them from the DES5yr mock catalogue, while SETc is generated by imposing the DEEP2 colour cuts on SETb and SETd by imposing the DEEP2 colour cuts on SETa. The biases on the photo-z estimate obtained for each of the different configurations of training and testing sets, are shown in Figure 3.10. Note that throughout this analysis, bins of width 0.04 in redshift space have been used.

From Figure 3.10 the following general conclusions can be drawn. Changing the galaxies that are present in the testing set when training with a complete and fully representative training set, leads to a change in the bias of the order 10^{-3}. Using an incomplete training set on these samples also leads to the same difference in the bias between them (Figure 3.10 - right panel, broken line). When using an incomplete training set such as that provided by the DEEP2 survey (SET2) on a testing set of galaxies with no imposed colour cuts (SETa and SETb), the bias in the photometric
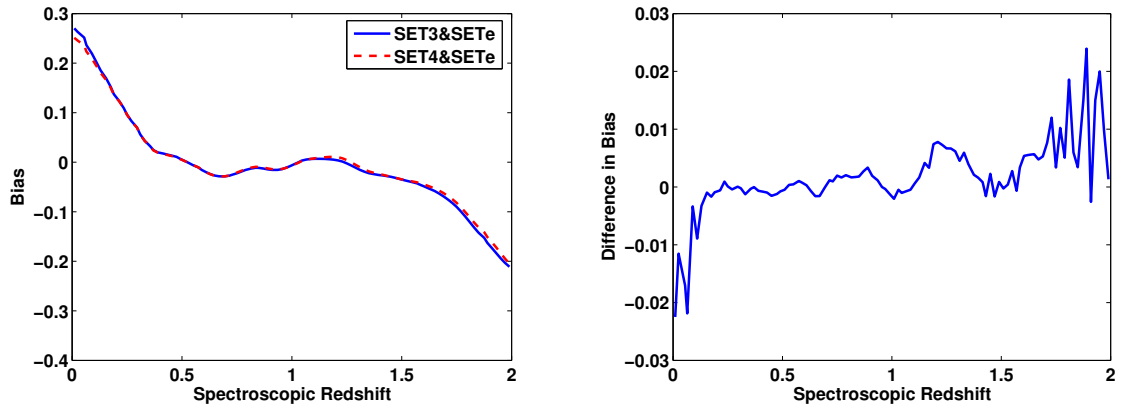
Figure 3.9: The bias on the photometric redshift estimate when using a training set of 70000 galaxies (SET3) and when using a training set of 200000 different galaxies (SET4) on the same testing set. The right hand panel plots the difference between the two biases.
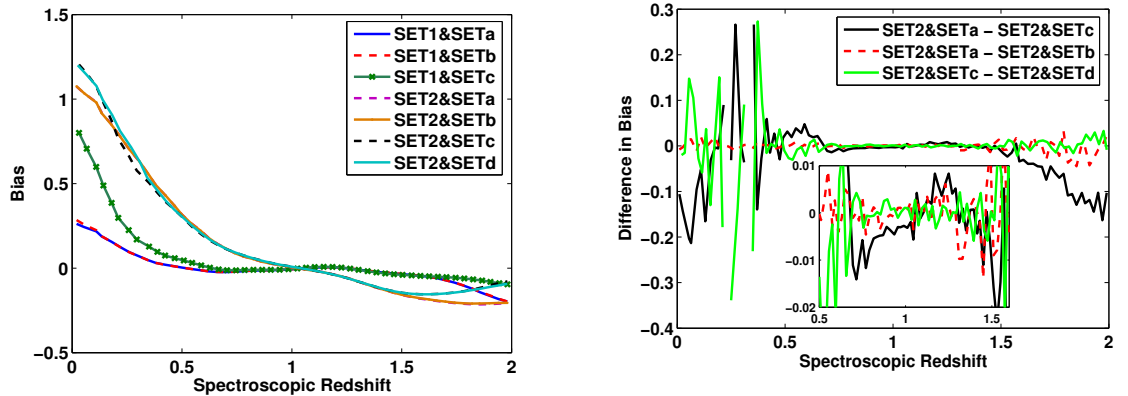
Figure 3.10: The left-hand panel shows the biases on the photometric redshift estimate when using each of the different configurations of training and testing sets detailed in Table 3.4. The right-hand panel plots the difference in the bias when using two different sets of DES5yr galaxies with an incomplete training set (broken line), two different sets of DEEP2 galaxies with an incomplete training set (green solid line) and the difference in the bias when using a complete testing set and a testing set with the same colour cuts as the incomplete training set (black solid line). These plots are generated using bins of width 0.04 in redshift space.

redshift is worsened as expected. However, if the same colour cuts as DEEP2 are imposed on the testing set (SETc), the bias is improved by $\sim$20% for $z < 0.7$ and by $\sim$40% for $z > 1.4$ - i.e. in the redshift ranges where the training set is incomplete. The difference in the bias when using a testing set with no colour cuts and one with imposed colour cuts to match those of the incomplete training set, is of the order of 5×10^{-3} and always smaller than 10^{-2} in the redshift range of the incomplete training set - inset, left-hand panel of Figure 3.10.

In §3.4.2, the propagation of these errors on the photometric redshift bias onto estimates of the dark energy equation of state parameter, w, will be considered.

3.4 Implications for Cosmology

3.4.1 Optimal Estimation of the Galaxy Power Spectrum

In this section, the impact of photometric redshift estimation on dark energy science is considered, the emphasis being on the measurement of dark energy using galaxy power spectra and baryon acoustic oscillations.

The galaxy angular power spectrum is a measure of the clustering in the galaxy population within time bins extending from the present to a time when the Universe was only a fraction of its present age. Large-scale surveys like DES provide ideal data sets for studying the clustering properties of galaxies and therefore the clustering properties of their underlying dark matter distribution and hence are useful probes for mapping how the dark matter distribution evolves with time. Furthermore, many characteristic features appear in the power spectrum which provide *standard rulers* that can be used to determine the angular diameter distance, D_A, as a function of redshift. Baryon acoustic oscillations are one such feature of interest which appear as *wiggles* on the power spectrum. These wiggles result from oscillations in the photon-baryon fluid at the epoch of recombination when the radiation decouples from the matter. The position of the peaks and troughs of these wiggles in Fourier space can be used to determine a set of cosmological parameters (e.g. Blake & Glazebrook (2003) and Seo & Eisenstein (2003)).

The accuracy with which one can measure this typical acoustic scale is proportional to the average fractional error in the power spectrum, $\delta P/P$. The fractional error on the power spectrum arises from two sources. Firstly, the number of independent spatial modes that can be measured in a given volume, V, is finite and this will lead to errors in the power spectrum that are proportional to $1/\sqrt{V}$. This is known as cosmic variance. Secondly, there is a contribution from shot noise due to imperfect sampling of the fluctuations as one only has a finite number of tracers of these

fluctuations within a given volume. If one assumes a density field that follows Gaussian statistics, Feldman *et al.* (1994) show that the error on the power spectrum measurement, P is weighted in the following way:

$$\frac{\delta P}{P} \propto \frac{1}{\sqrt{V}} \left(1 + \frac{1}{nP} \right), \tag{3.2}$$

where n is the mean number density in a given volume as seen by an observer and can be written in terms of the galaxy redshift distribution as follows:

$$\frac{dN}{dz} = f_{sky} \frac{dV}{dz} n(z), \tag{3.3}$$

where f_{sky} is the fraction of the sky covered by the survey and dV/dz is the comoving volume element.

The first term in Eq. 3.2 denotes the effect of cosmic variance while the second term is the contribution from shot noise. In order to minimise the error on the power spectrum, one has to design a survey with maximum volume provided there are enough sources within this volume for the shot noise contribution to be minimal. If $nP > 3$ the power spectrum is well estimated and there is no significant advantage to be gained with more galaxies (Seo & Eisenstein 2003). In this work, it is assumed that to obtain a reasonable estimate of the power spectrum one needs to satisfy the condition, $nP \gtrsim 1$. Taking into account the galaxy bias, b that scales the galaxy power spectrum to the matter power spectrum, and including the scaling of the matter power spectrum with redshift as a linear growth factor, $D(z)$ the following expression for nP_{gal} is obtained:

$$n(z)P_{gal}(k_*) = n(z)b^2(z)D^2(z)P(k_*). \tag{3.4}$$

The formalism for the transfer function set out in Eisenstein & Hu (1998) has been used to calculate the power spectrum at $k_* = 0.1hMpc^{-1}$ as this is well within the linear regime of the power spectrum. At larger values of k, non-linearities due to clustering and other structure formation start to dominate and make it harder to detect the BAO signal.

A survey with $0 < z < 2$ and $f_{sky} = 0.119$ is considered. The bias is assumed to be 1.2 [2]. In Figure 3.11, nP_{gal} is plotted as a function of the redshift. This is done for the entire catalogue

---

[2]While it is true that these results are dependent on the bias, it is difficult at this point to make an educated guess of what b will be for DES galaxies. A reasonable scale independent bias has therefore been used in these calculations.
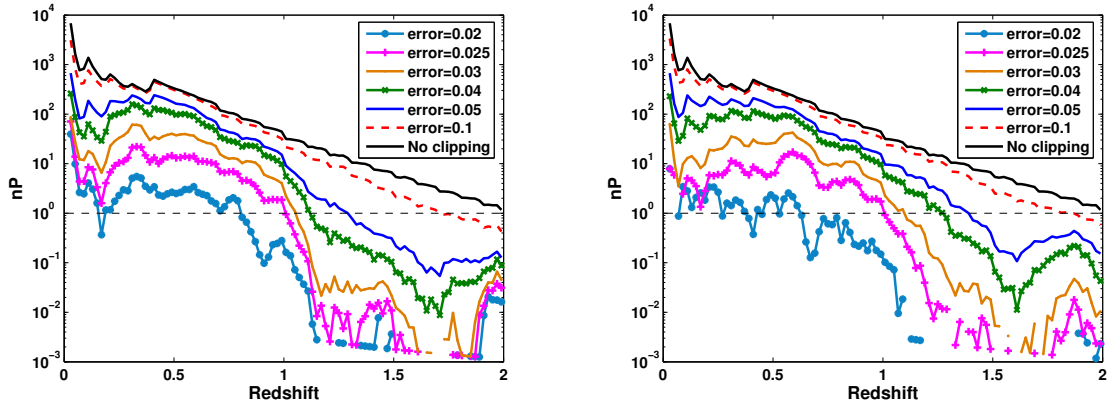
Figure 3.11: nP as a function of the redshift for different levels of clipping. The left-hand plot is generated using DES $grizY$ photometry only whereas the right-hand plot is produced from a catalogue with 8-band DES+VHS photometry.

and for clipped catalogues with different clipping thresholds. The same analysis is performed for optical only DES data as well as optical and NIR data from DES+VHS. The results are summarised in Table 3.5 and Figure 3.11.

From these results it can be seen that applying a threshold error at which to cut the photometric redshift catalogue proves effective in removing outliers from the sample before performing any kind of cosmological analysis on it. For the DES catalogue of redshifts obtained using $grizY$ photometry, all galaxies with a threshold error of more than ~ 0.03 can be removed in order to obtain an accurate measurement of the galaxy power spectrum out to a redshift of 1. This results in only 10% of the original sample remaining but this sample has a scatter on its photometric redshift that is a factor of ~ 2.7 times better than that of the original sample and is therefore more effective in constraining the cosmology. For the DES + VHS catalogue, a threshold error of 0.025 can be applied to effectively constrain the galaxy power spectrum to redshift 1. In this case, only 3% of the original sample remains, but the overall scatter on the photometric redshift has been reduced by a factor of ~ 2.75. This is equivalent to performing an LRG selection on the survey as these galaxies have more accurate large-scale structure signals and more accurate photometric redshifts due to the prominence of their 4000Å break (Blake *et al.* 2007; Padmanabhan *et al.* 2005).

In order to provide a reasonable measurement of the galaxy power spectrum for the entire DES redshift range of $0 < z < 2$, a threshold error cut of > 0.1 can be applied to the DES only sample and most of the galaxies used in the analysis. When NIR photometry from VHS is added to this sample, a less conservative clipping cut of 0.05 can be applied and only 37% of the galaxies used

DES $grizY$ **photometry**

Threshold Error	Redshift Range for $nP \gtrsim 1$	σ	σ_{68}	Fraction of Galaxies Remaining
None	$0 < z < 2$	0.128	0.08	1
0.100	$0 < z < 1.7$	0.084	0.065	0.79
0.050	$0 < z < 1.3$	0.058	0.052	0.38
0.040	$0 < z < 1.1$	0.055	0.047	0.24
0.030	$0 < z < 1.05$	0.048	0.044	0.095
0.025	$0 < z < 0.95$	0.047	0.043	0.035
0.020	$0 < z < 0.8$	0.047	0.045	0.007

DES $grizY$ **+ VHS** JHK_s **photometry**

Threshold Error	Redshift Range for $nP \gtrsim 1$	σ	σ_{68}	Fraction of Galaxies Remaining
None	$0 < z < 2$	0.11	0.074	1
0.100	$0 < z < 1.9$	0.074	0.062	0.80
0.050	$0 < z < 1.4$	0.054	0.048	0.37
0.040	$0 < z < 1.3$	0.049	0.043	0.22
0.030	$0 < z < 1.1$	0.043	0.039	0.09
0.025	$0 < z < 1.0$	0.041	0.037	0.03
0.020	$0 < z < 0.65$	0.041	0.037	0.005

Table 3.5: Summary of the redshift ranges over which optimal measurements of the galaxy power spectrum can be obtained for different clipping threshold errors along with the corresponding values of σ, σ_{68} and the fraction of galaxies remaining in the sample for each of these cases. The top table is for DES $grizY$ photometry and the bottom table for DES+VHS JHK_s photometry.

to reduce the scatter on the photometric redshift by a factor of ~ 2. Note that σ_{68} is also reduced in these cases although not to the same extent as the reduction in σ. A reduction in σ_{68} corresponds to a reduction in the intrinsic scatter of the sample minus the outliers.

By clipping catalogues in this way before performing any kind of cosmological analysis on them, the errors in the measurement of the galaxy power spectrum have been effectively reduced without compromising on the precision with which this measurement has been made. Adding NIR data from VHS to the DES photometry has also allowed the catalogues to be clipped more effectively and therefore enabled more precise measurements of the galaxy power spectrum out to higher redshifts. However, in all these calculations, there is no explicit dependance of $\delta P/P$ on the photo-z scatter.

The formalism of Blake et al. (2006) and Blake & Bridle (2005) is now followed whereby the photometric redshift errors are explicitly accounted for in the galaxy power spectrum analysis. These authors have shown that the fractional error on the galaxy power spectrum is related to the photometric redshift error as follows:

$$\frac{\delta P}{P} \propto \sqrt{\sigma_r}, \tag{3.5}$$

where σ_r is the rms error in comoving coordinates in units of $h^{-1}\mathrm{Mpc}$. This can be related to the redshift error already introduced in Eq. 2.8 as follows:

$$\sigma_r = \sigma_z \frac{c}{H(z)} = \frac{\sigma_z c}{H_0 \sqrt{(\Omega_m(1+z)^3 + \Omega_k(1+z)^2 + \Omega_\Lambda)}}. \tag{3.6}$$

The fractional error in the power spectrum is now given by:

$$\frac{\delta P}{P} \propto \sqrt{\frac{\sigma_r}{V}} \left(1 + \frac{1}{nP}\right). \tag{3.7}$$

The usable volume is now modified by an additional factor of $\sqrt{\sigma_r}$ which represents the fact that the number of usable spatial modes is diminished due to the photometric redshift error which smears out the signal in the radial direction. Fourier modes on small scales with $k \gtrsim 1/\sigma_r$ are damped out by the photometric redshift error and the number of usable spatial modes therefore needs to be reduced by a factor of σ_r.

The fractional error on the power spectrum can be calculated for different values of the clipping threshold. This is done for an optical DES sample as well as an optical and NIR DES+VHS sample

in redshift bins of width 0.02. A DES comoving survey volume, V of $23.7h^{-3}Gpc^3$ is assumed between $0 < z < 2$. This choice of redshift is motivated by Figure 3.11 where it can be seen that there are enough galaxies in the survey out to a redshift of 2 for shot-noise errors not to be significant, provided that the sample is not clipped. As the fractional error in the power spectrum is being calculated in redshift bins, the effective volume in a redshift bin is defined as follows:

$$\delta V_{eff} = \left[\frac{n(z)P}{(n(z)P + 1)} \right]^2 \delta V. \tag{3.8}$$

The fractional error on the power spectrum in a redshift bin can then be re-written as:

$$\frac{\delta P}{P} \propto \sqrt{\frac{\sigma_r}{\delta V_{eff}}}. \tag{3.9}$$

As can be seen, decreasing the threshold error at which to clip the sample reduces the scatter on the photometric redshift and therefore σ_r leading to smaller fractional errors on the power spectrum. However this also reduces nP and therefore δV_{eff}, thereby increasing the shot-noise contribution to the error in the power spectrum due to a lack of sufficient galaxies in the sample. Clearly, there is an optimum threshold error that needs to be determined.

The results of determining this optimum threshold error are shown in Figure 3.12 and Table 3.6 where the fractional error in the power spectrum, $(\delta P/P)_{clip}$, is plotted for different levels of clipping divided by the fractional error in the power spectrum obtained using the entire sample, $(\delta P/P)_0$. This is only done for clipping thresholds greater than or equal to 0.03 as below this, shot noise is dominant across the entire redshift range. If the plotted quantity is less than one for a given clipping threshold, the fractional error after clipping is smaller than the fractional error before clipping and cutting the sample using this threshold improves the constraints on the galaxy power spectrum.

From these results it can clearly be seen that there exists a trade-off between the shot-noise contribution to the error on the power spectrum and the contribution from cosmic variance. At high values of the threshold error, most of the galaxies in the sample are used for analysis and shot-noise is not a problem. However, the scatter on the photometric redshift is large leading to larger errors in the power spectrum measurement. At very low values of the threshold error, the photo-z scatter is reduced but there are too few galaxies in the sample and shot noise begins to dominate. There is an optimum value of the threshold error at which the fractional errors in the power spectrum are at a minimum. This value is different for different redshift ranges as well as for the two different catalogues.
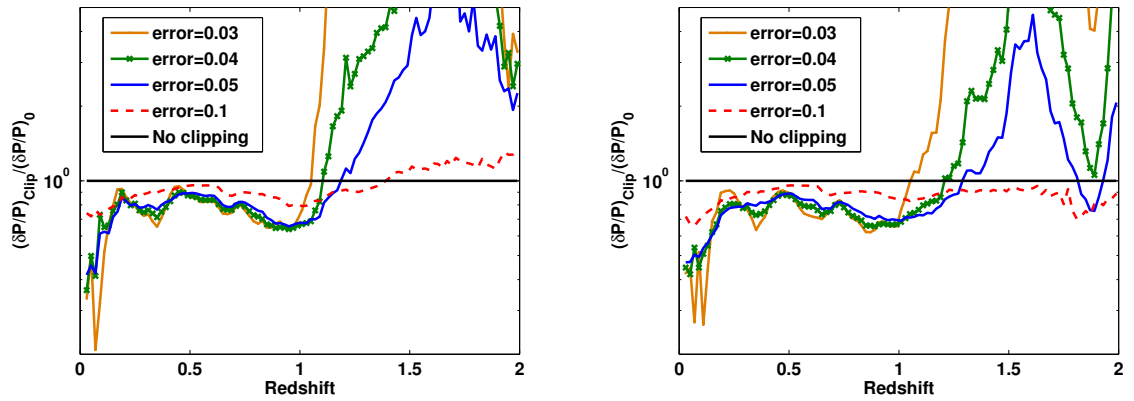
Figure 3.12: Ratio of fractional error on the galaxy power spectrum pre and post clipping, as a function of the redshift. The left-hand plot is generated using DES $grizY$ photometry only whereas the right-hand plot is produced from a catalogue with 8-band DES+VHS photometry.

DES $grizY$ photometry

Redshift Range	Optimum Clipping Threshold	Fraction of galaxies used	Improvement in $\delta P/P$
$0 < z < 0.1$	0.025	4%	75%
$0.1 < z < 0.9$	0.03	10%	20-30%
$0.9 < z < 1.0$	0.04	24%	35%
$1.0 < z < 1.2$	0.05	38%	10-15%
$1.2 < z < 1.4$	0.1	79%	4%
$1.4 < z < 2$	None	100%	None

DES $grizY$ + VHS JHK_s photometry

Redshift Range	Optimum Clipping Threshold	Fraction of galaxies used	Improvement in $\delta P/P$
$0 < z < 1$	0.03	8%	30%
$1 < z < 1.3$	0.05	37%	10-15%
$1.3 < z < 2$	0.1	80%	15-20%

Table 3.6: Summary of the optimum threshold error to be applied in different redshift ranges in order to minimise the fractional error on the power spectrum. The top table is for DES $grizY$ photometry and the bottom table for DES+VHS JHK_s photometry.

When the VHS NIR data is added to the DES optical catalogue, one can apply a smaller clipping threshold out to the same redshift range compared to the DES only case in order to minimise the error in the power spectrum. This means more outliers are removed from the DES+VHS catalogue and thereby the photometric redshift errors are reduced without compromising on the precision with which one can do cosmology. Also, it can be seen that using the DES only catalogue, it is not possible to clip in the highest redshift bin of $1.4 < z < 2$ as this increases the shot noise errors in the power spectrum. However, when one adds the VHS NIR photometry, $\sim 20\%$ of the galaxies can be removed in this bin to produce a power spectrum that is 15-20% more accurate than that obtained using all the galaxies.

This analysis shows that in the absence of large spectroscopic surveys like the proposed WF-MOS survey (Bassett *et al.* 2005), photometric surveys could prove competitive in constraining dark energy through galaxy power spectrum measurements if the outliers were effectively removed.

It is worth noting though that when applying this clipping procedure to a real survey, one would choose the optimal clipping threshold based on the training sets available and not from simulations as is the case here.

3.4.2 Effect of Photometric Redshift Bias on Dark Energy Equation of State

In this section the effect of the photometric redshift bias on the dark energy equation of state parameter, w is considered. In §3.3.4.2 it was already seen that systematic errors in the photometric redshift bias can arise when different numbers of galaxies are used in the training and testing sets and also when one or both of these samples is in some way incomplete. The errors in the bias given by the right hand panels of Figure 3.9 and Figure 3.10 can be translated into an error on the the value of w calculated using baryon acoustic oscillations as a probe. The position of the BAO peaks can be used to find the angular diameter distance, D_A which in turn gives information about the expansion history of the Universe and hence w. If there is a systematic uncertainty on the photometric redshift bias, Δ_b, this can be related to the uncertainty in w using the angular diameter distance, in the following way:

$$\Delta w = \frac{\partial D_A}{\partial z} \frac{\partial w}{\partial D_A} \Delta_b. \tag{3.10}$$

By assuming that Δ_b is given by the difference curves plotted in the right hand panels of Figure 3.9 and Figure 3.10, an estimate of Δw for each of the cases investigated in §3.3.4.2 can be
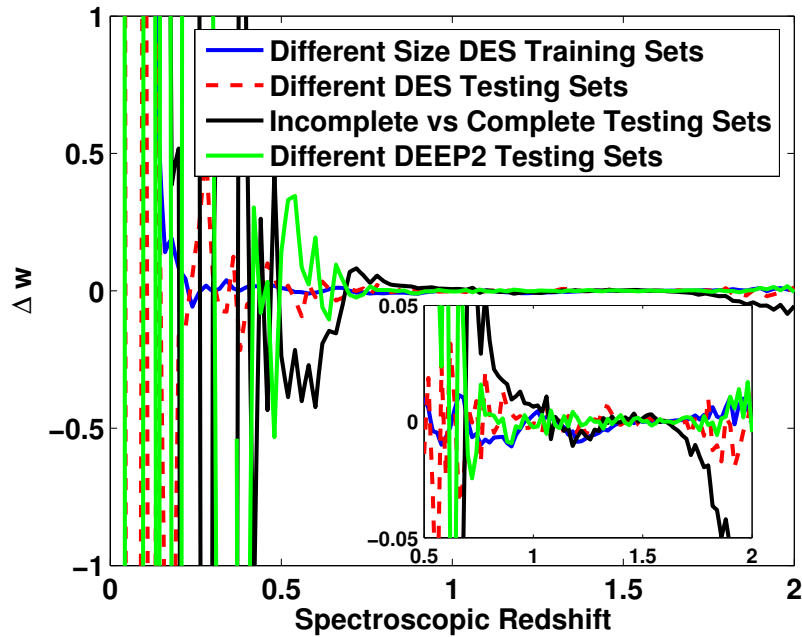
Figure 3.13: The error in w as a function of redshift due to the photometric redshift bias arising from different sources.

found. This is shown in Figure 3.13. Note that throughout this calculation all other cosmological parameters are fixed and a standard cosmology with Ω_m=0.3, Ω_Λ=0.7 and h=0.7 is used.

For interest, the product of the two derivatives in Eq. 3.10 is also plotted for four different cosmologies in Figure 3.14 as this is what links the error in the photometric redshift to the error on w. This assumes a flat universe with varying amounts of matter and dark energy as specified by the four different values of Ω_m.

It can be seen that using different size training sets or different testing sets leads to an error in w at a given redshift [3] that is of the order of 0.01 for $z > 0.5$. The error in w is of the order of 0.08 for $0.5 < z < 1$ and $z > 1.5$ when an incomplete testing set is used with an incomplete training set as opposed to a complete testing set with an incomplete training set. The error is smaller - around 0.01 in the redshift range $1 < z < 1.5$. The error in all cases is very large at $z < 0.5$. As using different training and testing sets is equivalent to using galaxies from different patches of the sky and therefore having a cosmic variance limited sample, it is concluded that systematics on the photo-z bias due to cosmic variance do not hinder the calibration of w to a percent level. However,

---

[3]This does not correspond to the error one would get from fitting a constant w but rather the error of measuring w at that given redshift.
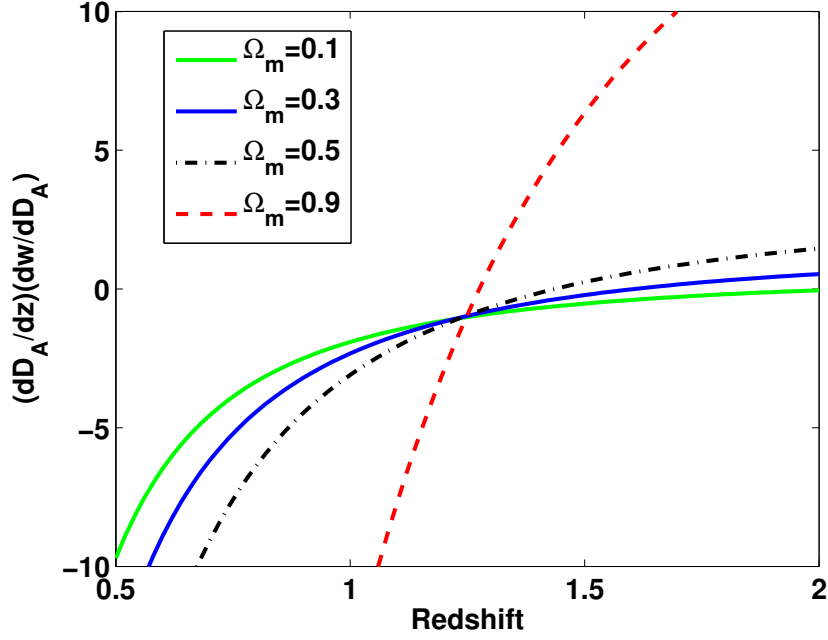
Figure 3.14: $\frac{\partial D_A}{\partial z}\frac{\partial w}{\partial D_A}$ for four different cosmologies with $\Omega_m = 0.1$, $\Omega_m = 0.3$, $\Omega_m = 0.5$ and $\Omega_m = 0.9$. All models assume a flat universe so $\Omega_\Lambda = 1 - \Omega_m$.

the black solid line of Figure 3.13 shows that using a training set that is incomplete in redshift space, to calibrate photometric redshifts for DES would lead to large uncertainties in w unless the sample being tested was cut to match the training set. These results are relatively insensitive to the clipping procedure introduced in § 3.3.3 and therefore have been carried out in all cases for the unclipped catalogues of galaxies.

Although this is a rough calculation, it gives a feel for the uncertainties in calculating the dark energy equation of state that can arise due to the differences in the photometric redshift bias. In order to get the exact uncertainty on w due to uncertainties in the photometric redshift, one would have to conduct a full Fisher matrix analysis applied to baryon acoustic oscillations such as that done by Ma *et al.* (2006) for weak lensing. This involves translating the error on the bias and scatter in the photometric redshift to an error on w by marginalising over all other cosmological parameters.

From this work, it can be seen that neural networks can be used to obtain photometric redshifts by extrapolating from an incomplete training set. If this is done with a survey such as DES it will create systematic errors on w of the order of ~10%. Template-fitting methods such as the SDSS template-fitting method (§ 2.3.4) and ZEBRA (§ 2.3.5) that use optimised templates to calculate

photometric redshifts in regions where the training set is incomplete, may prove more useful for such purposes.

3.5 Conclusions

This work has demonstrated the key role of near infra-red photometry from the VISTA Hemisphere Survey, in constraining photometric redshifts for the Dark Energy Survey. The effects of galaxy reddening and training sets on the photo-z estimate has been examined and the biases in the photometric redshift estimate when using training and testing sets with different sizes and levels of completeness, quantified. The error in the dark energy equation of state parameter, w that arises from differences in these biases has also been crudely calculated.

A method of clipping galaxy catalogues by removing outliers based on the ANNz error estimate on the photometric redshift has been introduced. Applying a threshold error to the catalogues and rejecting all objects with errors bigger than this threshold error, allows us to effectively reduce the overall scatter on the photometric redshifts of our sample.

Finally, a full galaxy power spectrum analysis has been conducted using the DES and DES+VHS catalogues and it has been shown that the clipping method can improve the uncertainties on our galaxy power spectrum measurements. There is an optimum threshold error at which one should clip catalogues and this error depends on the catalogue being used and the redshift range in which we are evaluating the power spectrum. If a high value for the threshold error is used, the scatter on the photometric redshift estimate is high leading to large positional uncertainties and therefore large errors in the power spectrum due to cosmic variance. However, if we adopt a very low value for the threshold error, we remove most of the galaxies from our sample before calculating the power spectrum and the resulting uncertainties in the power spectrum are dominated by shot noise. The optimum threshold error is found to be smaller for the DES+VHS catalogues compared to the DES only catalogues in the same redshift range and hence more outliers are removed from this sample before analysis. Adding the VHS NIR data thus helps to compute the galaxy power spectrum more accurately out to higher redshifts than for the DES only case.

In summary, the main conclusions from this work are as follows:

- NIR data from VISTA VHS helps to reduce the scatter on DES photometric redshifts by $\sim$30% for $z > 1$.

- Reddening the galaxies can increase the photo-z scatter of DES by $\sim 30\%$ in some redshift

ranges due to the degeneracy between redshift and reddening that exists in these redshift ranges. However, this is unlikely to be a major issue as most of the mock DES galaxies do not suffer from heavy extinction.

- ANNz can be used to predict the extinction, A_v of DES galaxies to an accuracy of 0.27 and to classify them into six spectral types - E, Sbc, Scd, Im, SB2 and SB3.

- The VVDS-Deep and DEEP2 spectroscopic surveys, when finished will provide a training set for DES that is reasonably complete in redshift space out to a redshift of 2. However, this assumes that all redshifts are obtained with high confidence and there isn't any incompleteness in e.g. SED type.

- Using different numbers of training set galaxies can lead to a difference in the photometric redshift bias of the order of 10^{-3}.

- If an incomplete training set is used, the photometric redshift estimate can be improved by imposing the same colour cuts on the testing set as are applied to the training set. When this is done, the improvement in the photometric redshift bias is of the order of 10% compared to if we used a complete testing set with no imposed colour cuts.

- The clipping method introduced by Abdalla *et al.* (2008*a*) can be effectively applied to the DES+VHS sample and applying a threshold error of 0.1 at which to cut our sample, reduces the scatter on the photometric redshift by $\sim$50% by removing $\sim$ 20% of the galaxies.

- A clipping threshold of 0.1 is optimal for calculating the DES power spectrum out to a redshift of 1.4. Applying this clipping threshold reduces $\delta P/P$ by $\sim$20%. When the VHS NIR data is added to the DES sample, the optimal clipping threshold in the same redshift range is 0.05 and this reduces the fractional error in the power spectrum by $\sim$20-30%. In order to calculate the power spectrum out to a redshift of 2, the addition of VHS NIR data is crucial. In this redshift range, applying the optimal clipping threshold of 0.1 results in an improvement in $\delta P/P$ by $\sim$15-20%.

- Systematic errors on the photometric redshift bias arising from cosmic variance lead to uncertainties in the dark energy equation of state parameter, w, of about a percent.

- However if an incomplete training set is used to determine photometric redshifts on a testing set that hasn't been cut to match the training set, the resulting uncertainties in the photometric redshift bias can lead to errors in w of the order of $\sim$10% if all other cosmological

parameters are fixed. Note however that this result is model specific and depends to a certain extent on the choice of mock catalogues and the algorithm used to calculate photometric redshifts, in this case, the neural networks.

In conclusion it is fair to say that this work has demonstrated that in the absence of large spectroscopic surveys, the DES and VHS datasets, when combined, will prove extremely effective in constraining dark energy through large scale structure signals like baryon acoustic oscillations. By clipping photometric redshift catalogues and carefully removing a suitable number of outliers, one can achieve reasonably precise measurements of the galaxy power spectrum out to a redshift of 2.

PHOTOMETRIC REDSHIFT DESIGN STUDIES
FOR *Euclid* (*DUNE*)

The work described in this chapter is unpublished and was undertaken by **Banerji, Abdalla & Lahav** *as part of design studies within the photometric redshift working group of the Euclid Imaging Consortium (EIC).*

4.1   Introduction

The work described in this chapter has formed part of key design studies for the imaging consortium within the planned space-based *Euclid* mission. The filter design for this mission concept has been driven primarily by the required photometric redshift performance for weak lensing analysis. Therefore the task of the photometric redshift working group was to investigate the following issues:

- The near infra-red filter configuration required to be added to the single space-based optical filter on this mission in order to achieve the required accuracy in photometric redshifts

- Requirements on optical ground-based complements to the space-based mission for optimal photometric redshift performance

- The availability and requirements on spectroscopic training sets for the calibration of photometric redshifts.

Below I describe some of my investigations into these issues that have helped shape the design of the *Euclid* mission. All of the photometric redshift analysis described in this chapter has been carried out using the training set method, ANNz (Collister & Lahav 2004) already described in detail in § 2.3.6.

4.2 The *Euclid* Mission

Euclid is a European Space Agency space-based mission concept that aims to understand how the Universe originated and what it is made of by mapping the geometry of the dark Universe. This mission concept has resulted from the merging of two separate missions - the Dark UNiverse Explorer (*DUNE*) and the SPectroscopic All-sky Cosmology Explorer (*SPACE*).

SPACE proposed to perform the first all-sky spectroscopic survey of the Universe by taking spectra between 1.6μm and 1.8μm with a spectral resolution of R=400 for more than half a billion galaxies.

DUNE was designed as a mission optimised for weak gravitational lensing studies of dark matter and dark energy. It consists of an optical and near infra-red imager on a 1.2m telescope with four broadband filters that will carry out a photometric survey of the entire sky down to a depth of 24.5 in the single broad optical filter. The stability of the PSF from space will enable high-precision measurements of small distortions in the images of distant galaxies induced due to the intervening large-scale structure. These distortions can then be used to directly map the distribution of dark matter in our Universe and to study dark energy which affects the growth of structure. The large area of the survey will also provide the necessary statistics to control systematic errors.

Euclid now incorporates both the spectroscopic (*SPACE*) and imaging (*DUNE*) capabilities and will require accurate photometric redshifts in order to estimate distances to all the galaxies and achieve its various science goals. The work described in this chapter was undertaken as part of early design studies for the *DUNE* mission concept which is now included in *Euclid*. It focusses on photometric redshift optimisation for weak lensing studies in particular the requirements on the near infra-red filters as well as ground-based complements to the space-based mission. In the rest of this chapter, the mission is referred to as *DUNE* as the design studies presented here were carried out before the merging of *DUNE* and *SPACE* into the *Euclid* mission concept.

4.3 Mock Catalogues and Filters

The mock catalogues used in this chapter have been simulated as described in Abdalla *et al.* (2008*a*) and § 3.2.2. In order to simulate these catalogues, the GOODS-N spectroscopic sample (Cowie *et al.* 2004; Wirth et al. 2004) was used. This is a flux limited sample with $R < 24.5$ and redshifts $z < 4$. The broadband photometry available for this sample in multiple wavebands, was used to generate a series of galaxy templates using a method similar to Budavári et. al (1999) but assuming a prior set of templates consisting of the observed Coleman *et al.* (1980) templates and the starburst galaxies of Kinney et al. (1996). Any reddening is removed from the photometry before template construction and the new templates used to calculate a best-fit SED value and reddening for each object assuming the reddening law of Calzetti (1997) as well as a correction for the IGM absorption according to the prescription of Madau (1995).

The model assumed for the luminosity function evolution is taken to be an interpolation between the local r-band luminosity function at redshift 0 and the Steidel *et al.* (1999) luminosity function at redshift 3. This is then used to estimate the RIZ magnitude and redshift distribution from which galaxies are drawn using a Monte Carlo technique. The fluxes for each galaxy are then calculated based on the redshift, SED type, reddening and filter profiles specified after normalising to the *DUNE* RIZ filter. Gaussian noise is added to the fluxes before calculating magnitudes and errors for the noisy sample in order to produce the final catalogue.

Figure 4.1 shows the filter transmission curves assumed for some of the surveys studied in this work. Ground-based optical surveys such as DES, PanStarrs and LSST have between four and six broadband filters whereas the design assumed for the space-based *DUNE* mission consists of a single broad optical RIZ filter and between two and four near infra-red filters. In most of the simulations presented in this chapter, the three NIR filter configuration shown in the bottom right panel of Figure 4.1 has been used.

Table 4.1 provides the assumed 10σ AB magnitude limits in each of the different filters for different surveys that are described in this work.

4.4 The Near Infra-Red Filter Configuration

The aim of this section is to determine the optimum near infra-red filter configuration for *DUNE* in terms of photometric redshift performance. The mock catalogues described in the previous section have been used after assuming different filter configurations in the near infra-red for *DUNE* and LSST ground-based data. The NIR filter configurations are illustrated in the top panel of Figure
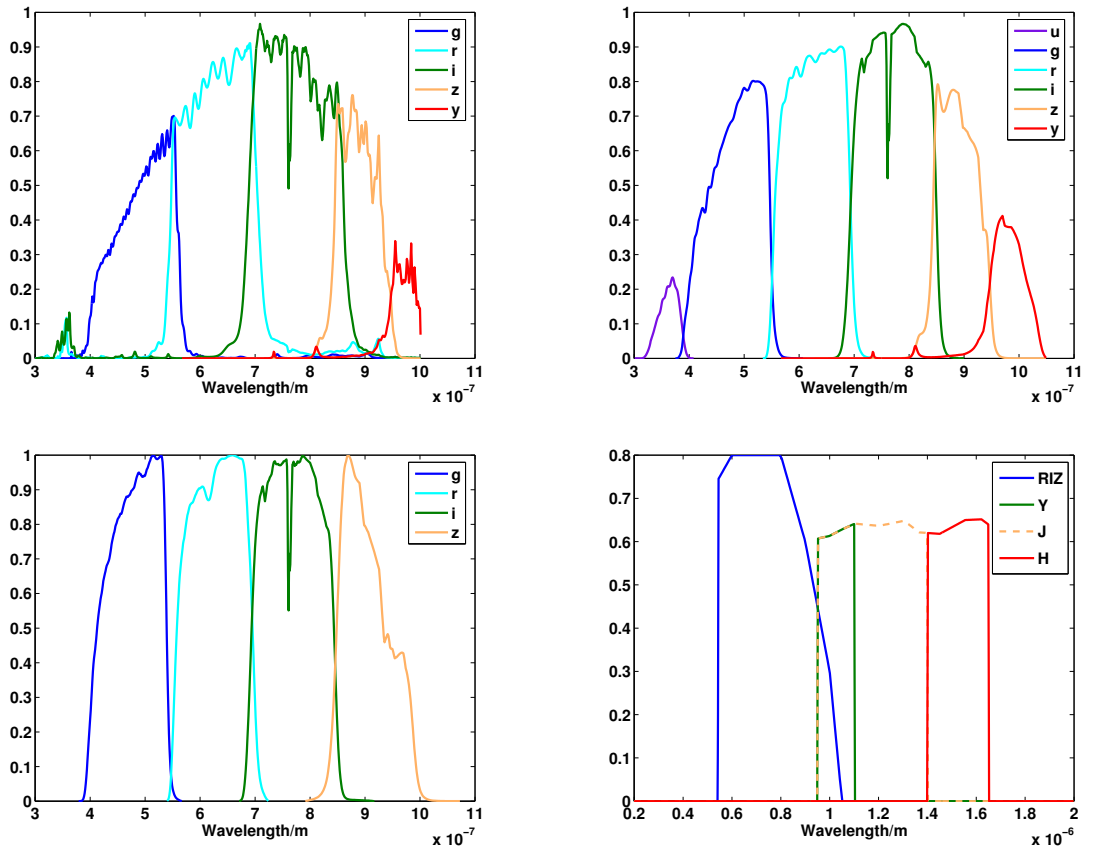
Figure 4.1: Filter transmission curves assumed for PanStarrs (top left), LSST (top right), DES (bottom left) and *DUNE* (bottom right).

4.2. Five different filter configurations are studied, details of which have been provided in Table 4.2. In all cases except N3, a total exposure time of 1500s split equally between all the NIR filters is assumed. Filter configuration N3 corresponds to the exposure time in the NIR being reduced to 75% of its original value. The magnitude limits are calculated from the exposure times using a *DUNE* exposure time calculator [1] (Fontana et al.) after assuming an efficiency of 0.7 in the filters, average background zodiacal light and an extended source.

The filter configurations as well as the bias, 1σ scatter on the photometric redshift and σ_{68} in different spectroscopic redshift bins, are plotted in Figure 4.2. From this figure it is clear that the photometric redshift estimate is not particularly sensitive to the near infra-red filter configuration chosen. Clearly there is a trade-off between colour and depth so adding more filters doesn't really improve the photo-z's as this means integrating for less time in each filter. However, reducing the

---

[1] http://lbc.oa-roma.inaf.it/cgi-bin/ETC_DUNE.pl

Band	DES	PanStarrs	LSST	CFHT	Deep Opt	*DUNE*
u	-	-	23.9	-	-	-
g	24.6	24.4	26.1	25.0	25.5/26.0	-
r	24.1	23.9	27.4	25.0	25.5/26.0	-
i	24.3	23.0	26.2	-	26.0	-
z	23.9	22.5	25.1	-	-	-
y	-	21.0	24.3	-	-	-
$RIZ/F814$	-	-	-	-	-	24.5
Y	-	-	-	-	-	23.5
J	-	-	-	-	-	24.0
H	-	-	-	-	-	23.2

Table 4.1: 10 σ AB magnitude limits for the different surveys considered in this chapter.

NO.	FILTER	CENTRAL λ (Å)	Exposure Time (s)	Magnitude Limit (10σ AB)
N1.	J	11750	750	24.2
	H	15250	750	23.5
N2.	Y	10250	500	23.5
	J'	12500	500	23.6
	H	15250	500	23.2
N3.	Y	10250	375	23.3
	J'	12500	375	23.4
	H	15250	375	23.0
N4.	Y'	10375	375	23.4
	J''	12125	375	25.7
	J'''	13875	375	25.5
	H'	15625	375	25.3
N5.	Y	10250	500	23.5
	J	11750	500	24.0
	H	15250	500	23.2

Table 4.2: Summary of near infra-red filter configurations
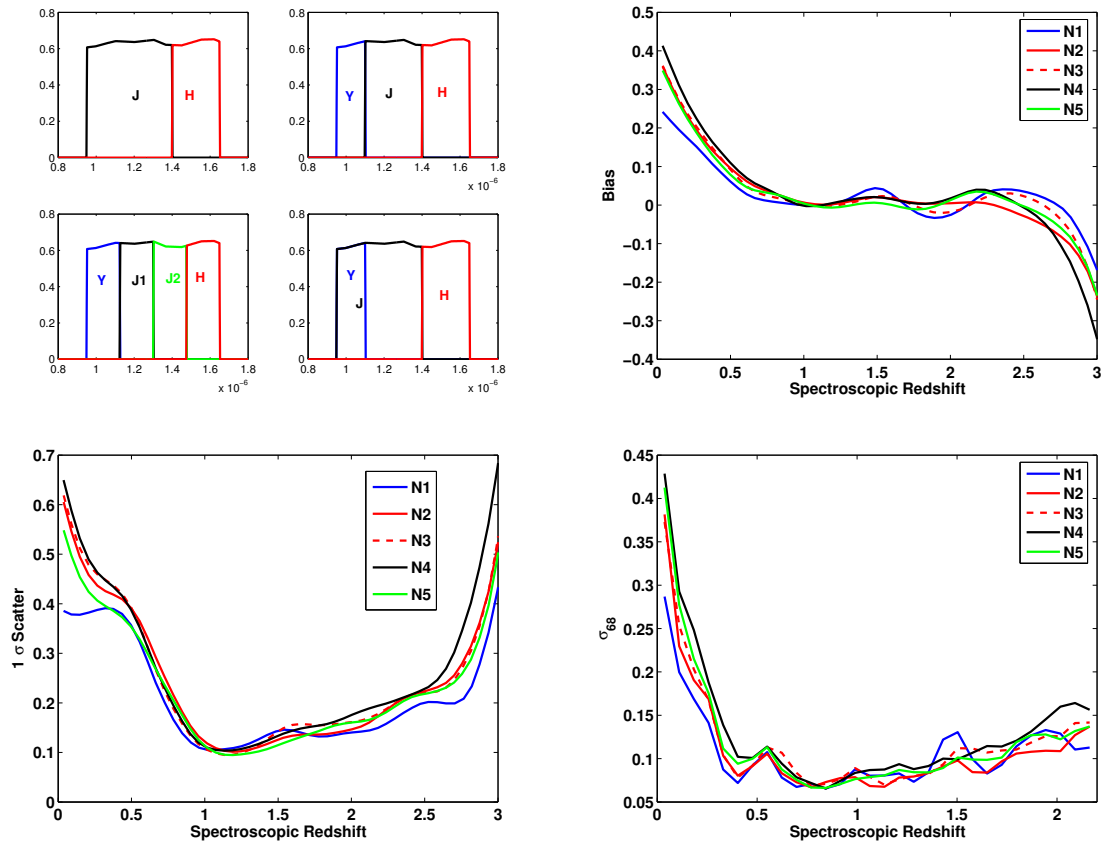
Figure 4.2: The top left panel shows four different NIR filter configurations considered for *DUNE*. In the top right, bottom left and bottom right panels the bias, 1σ scatter and σ_{68} are plotted as a function of the spectroscopic redshift for each of the different NIR filter configurations detailed in Table 4.2 with ground-based LSST data.

total exposure time in the near infra-red to 75% of its original value also does not seem to affect the photometric redshifts if one assumes that deep photometry e.g. from LSST is available from the ground. The trade-off between exposure time in the near infra-red and ground-based optical filters will be studied in more detail in § 4.5.2.

The effect of removing the *DUNE* Y-filter is illustrated in Figure 4.3. A PanStarrs1 type ground-based optical complement to *DUNE* is now assumed. The loss of the Y-filter is not here compensated with an increase in exposure time in the other two NIR filters and consequently, a degradation in the photometric redshift accuracy is seen particularly at large spectroscopic redshifts although this degradation is by no means severe. This illustrates that two near infra-red bands almost certainly capture most of the variance in the SEDs of the simulated galaxies over the *DUNE* redshift range. This hypothesis can be tested for example by using principal component

analysis.

In the remainder of this chapter, the *DUNE* near infra-red filter configuration is chosen to be N5 unless otherwise stated.

4.5 Ground-based Optical Complements

4.5.1 Optical Photometry - Depth vs Colour

In order to assess the depths necessary in ground-based optical photometry to provide accurate photometric redshifts for *DUNE*, several configurations of deep ground-based optical data are considered in this section. A CFHT like survey is simulated by assuming deep optical photometry in the g and r-bands with a 10σ AB magnitude limit of 25.0 in each. In addition, fiducial deep optical surveys with 10σ AB magnitude limits in the r-band of 25.5, in g and r of 25.5 and in g,r and i of 26.0 are also considered. The 1σ scatter, bias and σ_{68} versus spectroscopic redshift for each of these filter combinations is shown in Figure 4.3 alongside the same quantities plotted assuming a relatively shallow ground-based complement such as PanStarrs1. While the deep optical surveys are restricted to three bands or less, PS1 has five optical bands thereby giving more colour information. Note that for both DES and PS1, using only the 10σ objects down to the expected magnitude limits will almost certainly result in samples that are much too shallow to complement *DUNE*. However, the raw images from these ground-based surveys will include low signal-to-noise galaxies as well which can be used for calibration, particularly if multi-epoch data is available. All the simulations used throughout this chapter therefore include these low signal-to-noise objects.

Figure 4.3 illustrates several key points. Firstly, increasing the limiting magnitude in the two optical filters, g and r from 25.0 to 25.5 results in an improvement in the photometric redshift scatter as well as the bias. At $1 < z < 1.5$, the photo-z scatter is better with two shallow optical filters e.g. from a CFHT like survey compared to one deep optical filter. The bias is also improved at $z > 1$ with two shallow optical filters indicating that at large spectroscopic redshifts, the colour information is more important than depth in constraining the photometric redshifts. This is also illustrated by the fact that the relatively shallow PS1 optical data produces a smaller bias than is achieved with two deep optical bands. There is not much improvement in the photometric redshift performance when going from two optical filters with 10σ AB magnitude limits of 25.5 in each to three filters with 10σ magnitude limits of 26.0 for this redshift range and the photometric redshift estimates are only slightly worse if not comparable when five shallow optical bands such as those
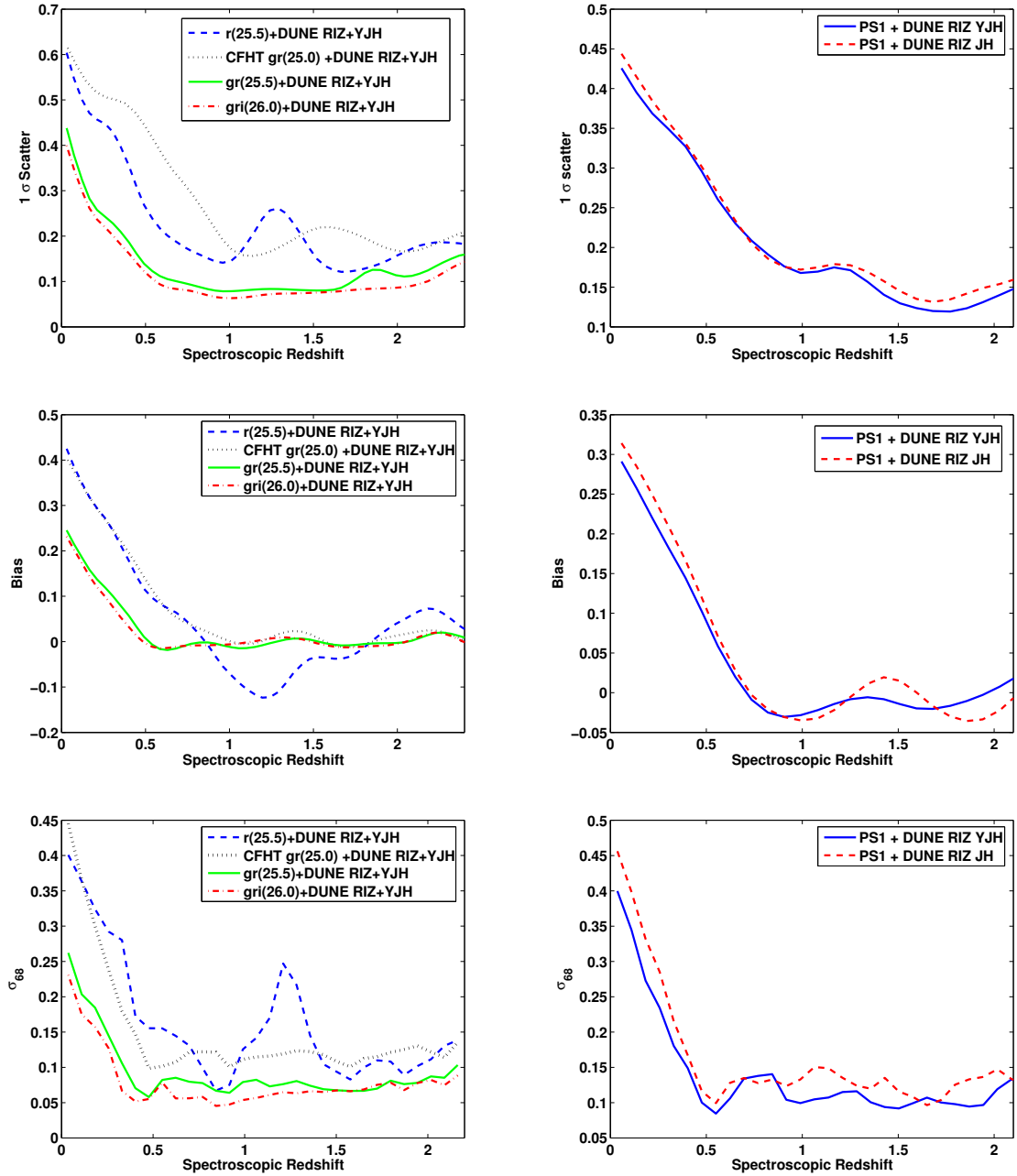
Figure 4.3: 1σ scatter, bias and σ_{68} versus spectroscopic redshift for different deep optical filter configurations (left) as well as a relatively shallow multi-band survey such as PS1 (right) when combined with *DUNE*.

Band	Exposure	$10\sigma AB$
Y	25%	22.8
J	25%	23.2
H	25%	22.5

Table 4.3: $10\sigma AB$ magnitude limits for 25% exposure in *DUNE* near infra-red filters.

from PS1 are present. This illustrates that the photometric redshift performance saturates after some reasonable amount of depth and colour has been obtained in the optical filters. Beyond this, there is no real further improvement from either increasing the exposure time in the filters or adding more filters.

The plots of σ_{68} help assess the quality of the photometric redshifts once catastrophic outliers have been removed from the sample. Unlike the 1σ scatter and the bias, this quantity is smaller when two or three deep optical bands are present rather than five shallow bands such as those in PS1.

4.5.2 Optical from the ground vs Near Infra-red from space

Abdalla *et al.* (2008*a*) have studied how data from various upcoming ground-based optical surveys can be used to complement data from *DUNE*. In this chapter, different near infra-red filter configurations as well as deep ground-based complements to *DUNE* have already been studied. This work is now extended by looking at the trade-off between depth in the ground-based optical filters and depth in the space-based NIR filters. Simulated data for DES, PanStarrs and LSST are used as the ground-based complements and the NIR exposure time reduced from 100% signified by the 10σ AB magnitude limits given in Table 4.1 to 25% and finally to 0%. The resulting change in the magnitude limit is given by Eq 4.1.

$$\log_{10}\left(\left(\frac{t_1}{t_2}\right)^{1/2}\right) = 0.4(m_1 - m_2), \tag{4.1}$$

where t_1 and t_2 are the total integration times in the filter being considered and m_1 and m_2 are the 1σ AB magnitude limits. The resulting 10σ AB magnitude limits in the *DUNE* NIR bands are summarised in Table 4.5.2. It has already been noted that reducing the NIR exposure time to 75% makes very little difference to the photometric redshifts assuming deep optical photometry from

LSST from the ground.

A plot of the 1σ scatter on the photometric redshift versus the spectroscopic redshift for all the survey cases considered is plotted in Figure 4.4. The quantity σ_{68} defined to be the interval in which 68% of the galaxies have the smallest difference between their spectroscopic and photometric redshifts is also plotted along with the bias on the photometric redshift estimate as well as the 1σ scatter as a function of the photometric redshift. It is apparent from this plot that the sensitivity of the photometric redshifts to a loss in depth in the near infra-red filters depends crucially on the quality of the complementing ground-based photometry. More specifically, one can conclude that a 25% exposure in the NIR filters is probably sufficient for photometric redshift accuracy provided there is also some deep optical photometry available from the ground.

Figure 4.4 illustrates that the photometric redshifts from *DUNE* only (100% NIR) are almost as good as those from DES+*DUNE* (0% NIR) out to z∼1.2. This highlights the key point that how much one benefits from adding NIR photometry to *DUNE* either in terms of filters or exposure time in each filter, depends crucially on what photometry is assumed from the ground. For example, for LSST+*DUNE* one might argue that there is almost nothing to be gained from increasing the exposure time in the NIR and the improvement in photo-z from adding NIR at all is nowhere near as marked as for the shallower DES+*DUNE* case.

Another interesting feature in Figure 4.4 is that one can constrain photo-z's using a single RIZ filter using the artificial neural network code, ANNz even though there is essentially no colour information present. This is because the neural network is just fitting a simple curve to the magnitude-redshift relation illustrated in Figure 4.5 and using this to derive redshifts. This curve shows the mean redshift of objects in a given magnitude bin for the *DUNE* mock sample. This kind of information could not be extracted from a template based method as in a template method, the actual amplitude of the flux is not related to the redshift as it is usually normalised by the error on the flux and is therefore dimensionless.

4.6 Calibrations for Weak Lensing

The photometric redshift accuracy is a crucial systematic that needs to be controlled for a photometric survey such as *DUNE*. The level of photo-z error that is permissible in turn depends on the specific science goals of the survey. As the *DUNE* part of *Euclid* is primarily a weak-lensing survey, the propagation of photometric redshift errors to the analysis of weak lensing tomography is briefly considered in this chapter. The requirements on the photometric redshift error are then
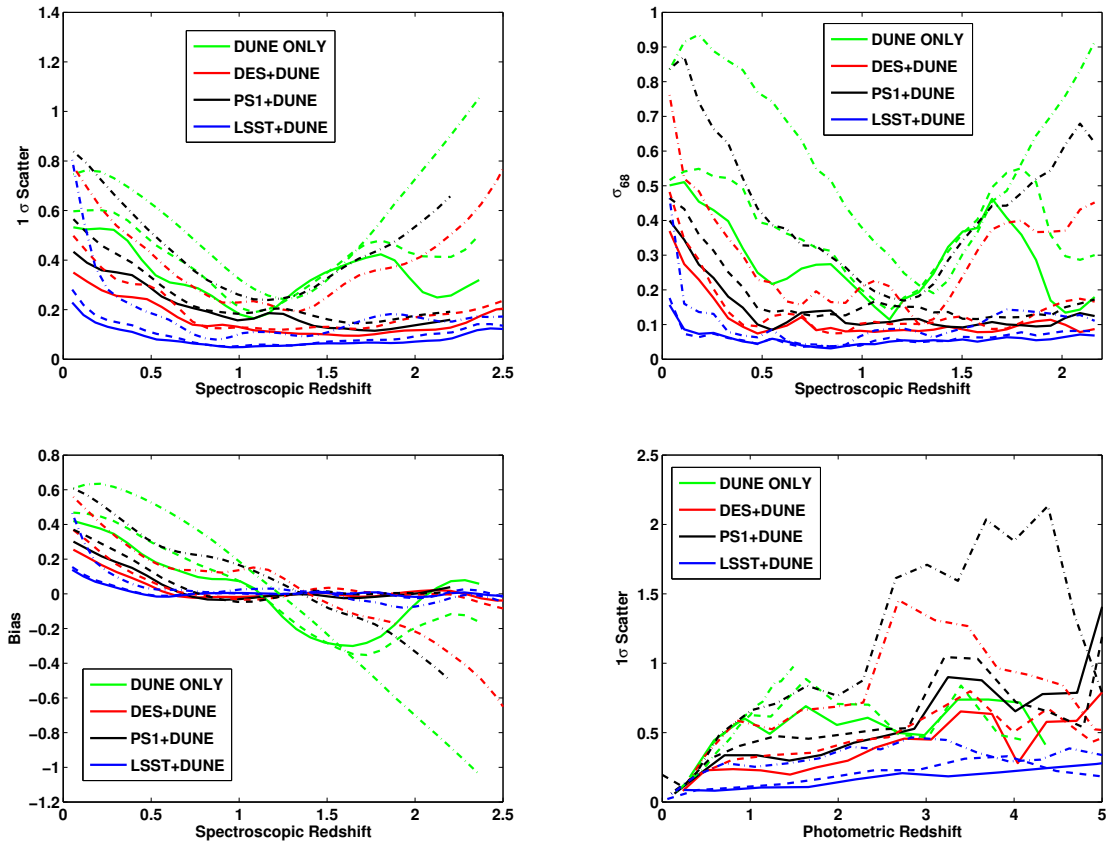
Figure 4.4: The 1σ scatter (top-left), σ_{68} (top right) and bias (bottom left) on the photometric red-shift as a function of the spectroscopic redshift and 1σ scatter as a function of photometric redshift (bottom-right) for various different ground-based optical surveys when combined with *DUNE*. The solid lines correspond to 100% exposure in the near infra-red, the dashed lines correspond to 25% exposure in the near infra-red and the dot-dashed lines correspond to 0% exposure in the near infra-red.

used to crudely determine the number of spectroscopic redshifts that will be required to calibrate the photometric redshift estimate.

In weak lensing surveys, the key observable is the lensing power spectrum. This is essentially an integral over the lensing kernel multiplied by the matter power spectrum. The lensing kernel in turn depends on the cosmological parameters as well as the redshift distribution of the survey. In a spectroscopic survey, this redshift distribution is well characterised but for a photometric survey, one needs to estimate, the photometric redshift probability distribution $p(z_p|z)$ using a finite number of galaxies with spectroscopic redshifts that form the training set. As only a finite number of galaxies are available to determine this distribution, there will be uncertainties associated with
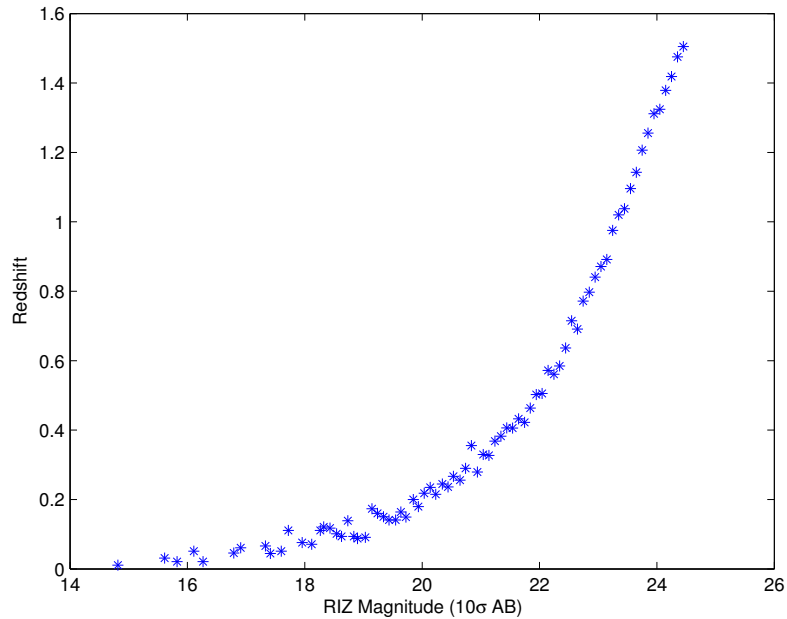
Figure 4.5: The magnitude-redshift relation for *DUNE* mock galaxies.

its estimate. These uncertainties in determining for example the mean and variance of this distribution will propagate into uncertainties in cosmological parameter estimates using weak lensing (Amara & Réfrégier 2007). This is because the parameters that determine the photo-z distribution, $p(z_p|z)$ are themselves degenerate with the dark energy parameters (Ma *et al.* 2006). These authors conclude that the limiting systematic error in degrading the cosmological parameter constraints is not the absolute size of any photo-z bias or scatter, but rather the uncertainty in knowing what that bias or scatter is. Cosmological parameter estimates could also suffer from the fraction of catastrophic outliers.

In order to quantify these systematics, the galaxy sample is divided into photometric redshift bins. Given a redshift distribution, $n(z)$ for a galaxy sample, one can define four redshifts - z_1, z_2, z_3, z_4 - where if cuts are made in the true redshift, would result in five bins each containing the same number of galaxies. These bin boundaries are defined in Table 4.4 for a *DUNE* type survey. However, when the cuts are made in photometric redshift, the galaxy distributions in each of the bins will 'leak' into other bins due to the photometric redshift error. This 'leaking' can be quantified by considering the fraction of galaxies, f_i in each bin which is simply the integral of the redshift distribution over the bin boundaries. The fraction of galaxies from this bin that have

z	0 - 0.561	0.561 - 0.741	0.741 - 0.931	0.931 - 1.181	1.181 - 3.531

Table 4.4: *DUNE* redshift bins.

	f_i	$f_{i\pm1}$	$f_{i\pm2}$	$f_{i\pm3}$	$f_{i\pm4}$
WL Req	> 78%	< 10%	< 5%	< 1%	< 1%
DES	63.3%	17.9%	3.46%	2.87%	3.98%
DES+IR	75.6%	14.3%	0.59%	0.52%	1.02%
PS4+IR	87.5%	7.63%	0.14%	0.09%	0.26%
LSST	85.9%	8.32%	0.34%	0.25%	0.51%

Table 4.5: The fraction of galaxies in each redshift bin, f_i and leakage into neighbouring bins, $f_{i\pm1}$, $f_{i\pm2}$ etc. for four of the simulated surveys as compared to the weak lensing requirements.

leaked into adjacent bins are given by $f_{i\pm1}$ and for bins beyond, $f_{i\pm2}$ etc. For the purposes of a weak lensing survey, one can place stringent requirements on these fractions based on the precision needed in the cosmological parameter estimates. These requirements are given in the top line of Table 4.5. The rest of Table 4.5 gives the fractions obtained from the photometric redshift output of the neural network code, ANNz, using several of the mock catalogues already detailed.

One can see that with the presence of near infra-red data e.g. from *DUNE* or u-band data e.g. from LSST, the weak lensing requirements on the fraction of catastrophic outliers can be met.

The two other photometric redshift statistics required for a *DUNE* type weak lensing survey, are calibration of the mean of the redshift probability distribution, $p_i(z)$ to be less than 0.001, and the calibration of variance of $p_i(z)$, to be less than 0.008.

The mean of the distribution can be defined as follows:

$$\bar{z} = \frac{1}{N_s} \sum_{j=1}^{N_s} z_{s_j}. \tag{4.2}$$

One can also define the kth moment of the distribution, μ_k, as follows:

$$\mu_k = \overline{(z - \bar{z})^k} = \frac{1}{N_s} \sum_{j=1}^{N_s} (z_{s_j} - \bar{z})^k. \tag{4.3}$$

As only a finite number of galaxies with spectroscopic redshifts, N_s are available to determine this distribution, assuming Poisson statistics, the standard deviation on the mean redshift of each bin is given by:

$$rms(\bar{z}) = \frac{\sqrt{\mu_2}}{\sqrt{N_s}}, \tag{4.4}$$

and similarly the standard deviation of the variance is given by:

$$rms(\mu_2) = \sqrt{\frac{N_s - 1}{N_s^3}[(N_s - 1)\mu_4 - (N_s - 3)\mu_2^2]}. \tag{4.5}$$

In the limit of large N_s this becomes:

$$rms(\mu_2) = \frac{\sqrt{\mu_4 - \mu_2^2}}{\sqrt{N_{spec}}}. \tag{4.6}$$

One can marginalize over both these uncertainties. The dependence on the number of spectroscopic redshifts is really an indirect expression of the scatter in $\bar{z}$ and in μ_2.

Using the ANNz output for *DUNE* with near infra-red data and various ground-based optical complements, the number of spectroscopic training set galaxies required in each redshift bin can be calculated using the weak lensing requirements. The ANNz output is used to define the probability distribution function whose variance and kurtosis can be calculated. Estimates of N_s from equations 4.4 and 4.6 are given in Table 4.6 assuming $rms(\bar{z}) < 0.001$ and $rms(\mu_2) < 0.008$. As the requirements on the spectroscopic training set is roughly the same for any optical survey with *DUNE* NIR photometry, an average value for N_s is quoted in Table 4.6 across all the surveys.

The requirements for the calibration of the mean are clearly more demanding than those for calibrating the variance and it can be seen that a total of $\sim 10^5$ spectroscopic training set galaxies are required for calibration of a weak lensing survey such as *DUNE* assuming five redshift bins. If higher order moments are investigated therefore, they should only be important if the number of galaxy spectra available is very small. These results are consistent with the more detailed analysis

z-range	μ_2	μ_4	N_s from mean	N_s from variance
0-0.561	0.013	0.0006	13000	7
0.561-0.741	0.02	0.001	20000	9
0.741-0.931	0.036	0.0035	35000	30
0.931-1.181	0.06	0.008	60000	70
1.181-3.531	0.14	0.07	140000	800

Table 4.6: The second (variance) and fourth (kurtosis) moments about the mean of the redshift distributions in each of the redshift bins and resulting requirements on the size of the spectroscopic training set, N_s. These moments are found to be roughly the same for all the mock surveys listed in Table 4.1 and the results are averages over all these surveys.

of Abdalla *et al.* (2008*a*); Ma *et al.* (2006) and Amara & Réfrégier (2007) using a Fisher matrix formalism.

These calibrations have also been carried out by other groups within the *Euclid* photo-z working group using their own photometric redshift codes and mock catalogues. Overall, the results from the different groups are very similar and lead to the same conclusions as those stated above.

4.7 Conclusions

The work described in this Chapter has helped shape the design concept for the imaging component of the *Euclid* mission which is referred throughout this chapter as *DUNE*. Specifically, the following conclusions can be drawn from this photometric redshift analysis:

- The photometric redshift estimate for a weak lensing survey such as the *DUNE* mission concept is not very sensitive to the near infra-red filter configuration as long as deep photometry for example from an LSST type survey is assumed to complement it from the ground. Reducing the exposure time in the near infra-red to 75% of its original value also does not seem to affect the photometric redshift performance when combining with data from a deep optical survey with multiple bands.

- The photometric redshift estimate is sensitive to both depth (increasing the exposure time in each filter) and colour (increasing the number of filters) in the optical bands. Two deep optical filters with 10σ AB magnitude limits of 25.5 in each produces comparable scatter

and bias on the photometric redshifts as five shallower optical bands from a survey such as PanStarrs1. However once catastrophic outliers have been removed and the quantity, σ_{68} is considered, it is seen that it is more beneficial to have depth in the ground-based data rather than colour information.

- There is a trade-off between depth in the space-based near infra-red filters and ground-based optical filters for a mission design such as *DUNE*. If there is some deep optical photometry available from the ground, e.g. from LSST or DES, even 25% exposure in the near infra-red produces good photometric redshift estimates. If the optical photometry is shallower, e.g. for a PS1 type survey, an improvement in photometric redshift performance is seen on increasing the exposure time in the near infra-red. Therefore a survey like LSST is ideal as a ground-based complement to DUNE in order to provide accurate photometric redshifts. A survey like DES would also be suitable although shallower optical surveys such as PS1 require considerable exposure in the near infra-red to meet the necessary requirements on photometric redshift performance.

- Cosmological parameter constraints from weak lensing tomography depend on the photometric redshift distribution. In order for a survey like *DUNE* to achieve its science goals with regards to these constraints, the error on the mean of the photometric redshift distribution has to be less than 0.001 and on the variance, less than 0.008. $\sim 10^5$ galaxies with spectroscopic redshifts will need to be available in order to meet these requirements.

- Cosmological parameter constraints can also be affected by the fraction of catastrophic outliers in the photometric redshift estimate. The requirements on these fractions can however be met with a *DUNE* type survey assuming there is deep optical data available from the ground, particularly in the u-band, as well as near infra-red data from space.

As a consequence of this and other work undertaken by the photometric redshift working group, the current imaging component design for *Euclid* consists of a broad optical RIZ filter as well as three near infra-red YJH bands. There are also plans for separate ground-based programs that will be undertaken as part of both the Dark Energy Survey as well as PanStarrs1, that will be able to provide multi-band optical data for the *Euclid* objects to the necessary depths required to calibrate the *Euclid* photometric redshifts.

REPRODUCING GALAXY MORPHOLOGIES VIA MACHINE LEARNING

*The work described in this chapter is an extended version of the paper **Banerji et al., 2009, arXiv:0908.2033***

5.1 Introduction

The work presented thus far in this thesis has shown that machine-learning algorithms such as artificial neural networks can be extensively applied to the problem of photometric redshift estimation with considerable success. However, artificial neural networks were first applied to astronomical data sets in order to classify objects including stars (von Hippel *et al.* 1994; Bailer-Jones *et al.* 1998) and galaxies (Storrie-Lombardi *et al.* 1992; Lahav *et al.* 1995; Naim *et al.* 1995; Folkes *et al.* 1996; Lahav *et al.* 1996). Astronomical data sets have grown considerably in size in the last decade owing largely to the advent of mosaic CCDs that can be used on large telescopes in order to image large areas of the sky down to very faint magnitudes. The Sloan Digital Sky Survey (SDSS) has led to the construction of a data set of around 230 million celestial objects. Future generations of wide-field imaging surveys such as the Dark Energy Survey, PanStarrs and LSST will reach new limits in terms of the size of astronomical data sets. Clearly, automated classification algorithms will prove invaluable for the analysis of such data sets and yet these algorithms are yet to be applied on such scales.

The Galaxy Zoo project[1] launched in 2007 has led to morphological classification of nearly

---

[1] www.galaxyzoo.org

1 million astronomical objects from the SDSS data set through visual inspection by more than 100,000 users (Lintott *et al.* 2008). This project has resulted in a remarkable data set that can be used for studies of the formation and subsequent evolution of galaxies in our Universe. This data set however also presents us with the unique opportunity to compare human classifications to those from automated machine learning algorithms, on an unprecedented scale. If the neural network is shown to be as successful as humans in separating galaxies into morphological classes, this could save considerable time and effort for future surveys while ensuring uniformity in the classifications.

In this chapter the ability of artificial neural networks in classifying astronomical objects from the SDSS into three morphological types - ellipticals, spirals and stars/unique objects - is explored.

5.2 The Galaxy Zoo Catalogue

Galaxy Zoo is a web-based project that aims to obtain morphological classifications for roughly a million objects in the Sloan Digital Sky Survey by harnessing the power of the internet and allowing members of the public to perform these classifications by eye. The first part of this project is now complete and the morphological classifications subsequently obtained have been described in detail in Lintott *et al.* (2008). These classifications have already been used in a number of interesting science papers e.g. in the identification of a sample of blue early type galaxies in the nearby Universe (Schawinski *et al.* 2009) and to study the spin statistics of spiral galaxies (Land *et al.* 2008) and the power of this data set is already proving enormous for studies of both galaxy formation and evolution. The goal is now to assess whether such morphological classifications can be reproduced for even larger data sets likely to become available with the next generation of galaxy surveys through the use of automated machine learning algorithms such as artificial neural networks.

The Galaxy Zoo catalogue that is used in this chapter is the combined weighted sample of Lintott *et al.* (2008). This contains morphological classifications for 893,212 objects into three morphological classes - ellipticals, spirals and star/other unique objects. The classification by each user on each object is weighted such that users who tend to agree with the majority are given a higher weight than those who don't. The final probability of the object is then a weighted mean of the classifications of all users who analysed it. Full details of the weighting scheme are provided in Lintott *et al.* (2008). The weighted catalogue of objects contains the SDSS object ID and three additional columns with the probability of the galaxy being an elliptical, spiral or star/other object

between 0 and 1. If the sum of the probabilities in each of these three classes is less than 1, the remaining probability is assigned to the merger class. Figure 5.1 shows examples of the different kinds of objects classified by Galaxy Zoo users.

The Galaxy Zoo catalogue was matched to the SDSS DR7 PhotoObjAll catalogue in order to obtain input parameters for the neural network code. Before input into the neural network, cuts are applied on the sample in order to remove objects that are not detected in the g, r and i bands and those that have spurious values for some of the other parameters used in this study. This leads to a sample of $\sim$800,000 objects. Further cuts are then applied to define a *gold* sample where the weighted probability for each object belonging to any one of three morphological classes, is always greater than 0.8. This gold sample contains $\sim$315,000 objects and by construction therefore has no mergers within it. The neural network is run on both the gold sample as well as the entire sample. Darg *et al.* (2009) have already discussed issues to do with merger classification within Galaxy Zoo and constructed a sample of $\sim$3000 merging pairs from the Galaxy Zoo data. In this chapter, I classify objects as ellipticals, spirals or stars, as was done by Galaxy Zoo users, using a neural network. Note that the Darg *et al.* (2009) data set may be used in future for the classification of mergers but this has not been attempted here due to the sparsity of well-classified mergers in the original Galaxy Zoo data of Lintott *et al.* (2008).

It is also the case that faint objects that are unresolved are more likely to be classified as ellipticals unless the spiral arms can be clearly seen. For this reason, a sample of objects with $r < 17$ is also considered, which is defined as the bright sample. This magnitude limit is the same as that imposed on objects that were used to determine user weights in Lintott *et al.* (2008). The bright sample contains $\sim$340,000 objects and has many fewer well classified ellipticals than the gold sample - see Table 5.3 in § 5.5.

5.3 Artificial Neural Networks

An artificial neural network code similar to the one used in Chapters 2, 3 and 4 (Ripley 1981, 1988; Bishop 1995; Lahav *et al.* 1995; Naim *et al.* 1995; Collister & Lahav 2004) is used to classify the astronomical objects. A training set is used to minimise the cost function, E (Eq. 5.1) with respect to the free parameters w_{ij}.

$$E = \sum_k (T_{NN}(w_{ij}, p_k) - T_{eye,k})^2,$$

(5.1)
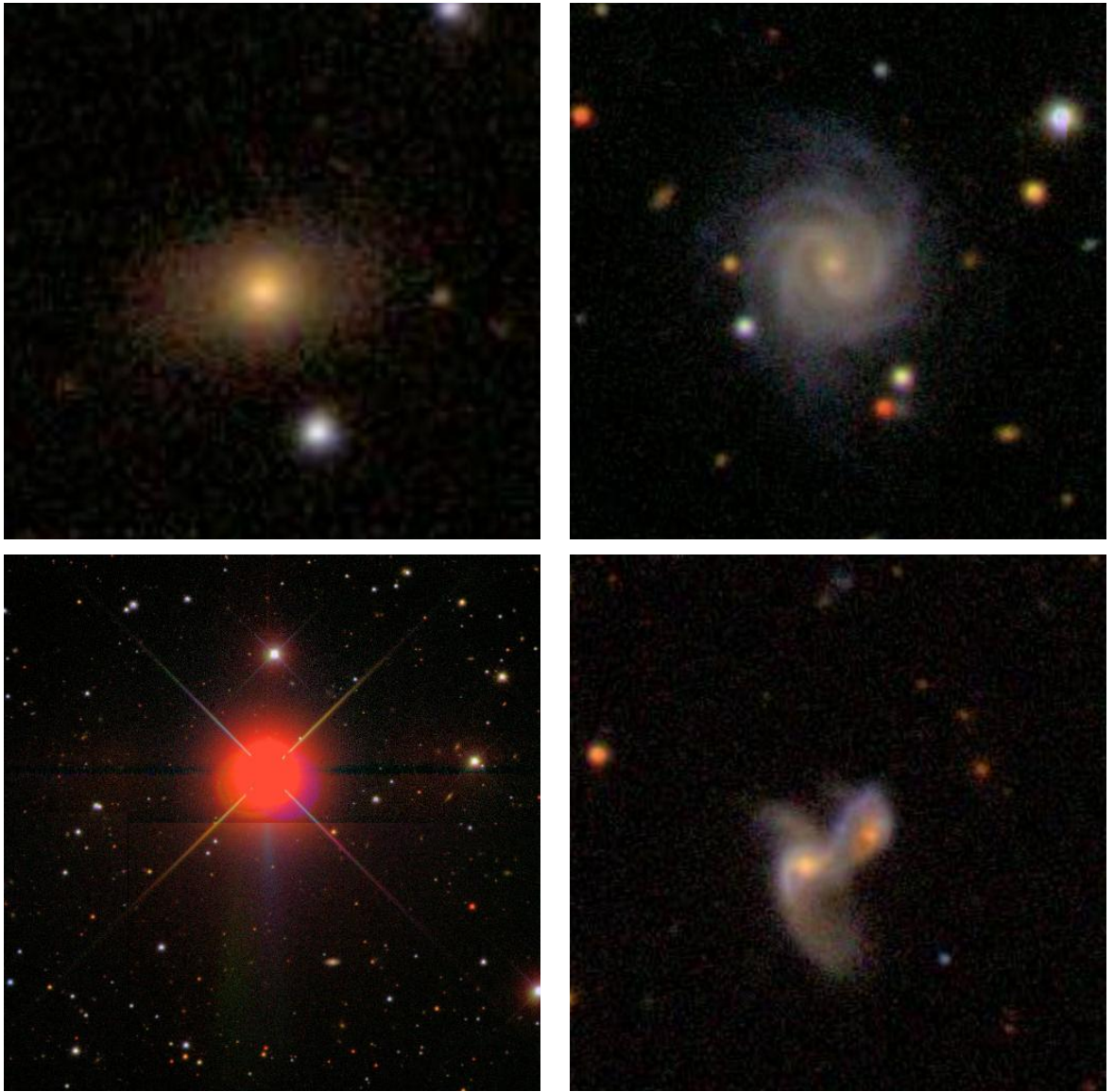
Figure 5.1: The different kinds of objects classified as part of the Galaxy Zoo project - elliptical (top left), spiral (top right), star (bottom left) and merger (bottom right)
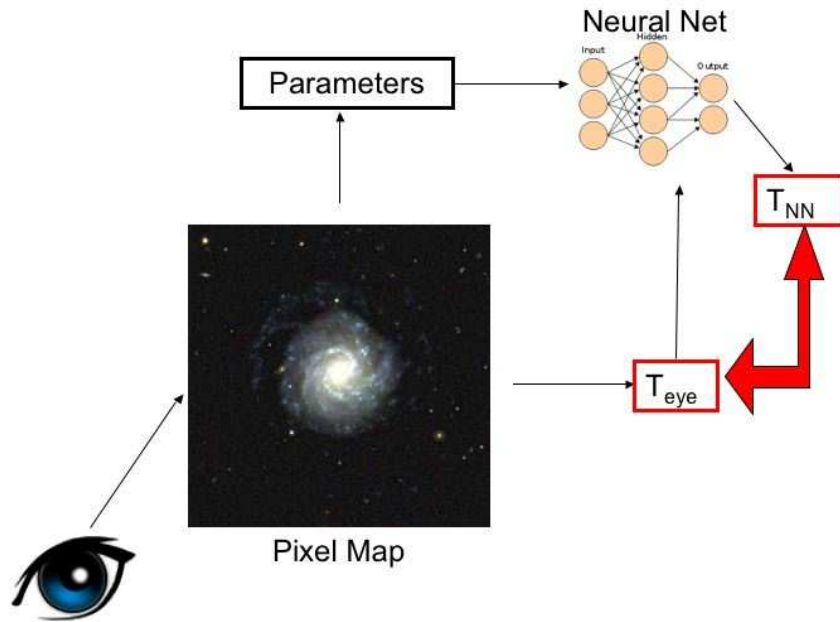
Figure 5.2: Cartoon schematic of how both the human eye as well as machine learning algorithms such as artificial neural networks perform morphological classification and determine parameters such as those listed in Table 5.1 and 5.2 from the galaxy images.

where T_{NN} is the neural network probability of the galaxy belonging to a particular morphological type, p_k are the input parameters to the network and $T_{eye,k}$ are the probabilities in the training set in this case assigned by Galaxy Zoo users.

The architecture is chosen to be N:2N:2N:3, where N is the number of input parameters. The three nodes in the output layer give the probability of the galaxy being an elliptical, spiral and star/unique object respectively. As is the case for the Galaxy Zoo weighted probabilities, if the sum of the three probabilities does not add up to 1, the remaining probability is assigned to the merger class.

5.4 Input Parameters

When using an automated machine learning algorithm, the choice of input parameters may be crucial in determining how well the network can perform morphological classifications. Ideally, one wishes to choose a set of parameters that show marked differences across the three morphological classes. In addition, it may be useful to define a set of parameters that is independent of the distance to the object. Figure 5.2 illustrates the key role that the input parameters play in the

morphological classification. The human eye sees a galaxy image and performs morphological classifications. The same image is also used to derive input parameters such as those that will be discussed in this section. The neural network uses both these parameters as well as a training set based on the human classifications to derive its own morphological classifications, T_{NN}. These are then compared to the human classifications, T_{eye} in order to assess the success of the machine-learning algorithm in reproducing what is seen by the human eye.

In this section, two sets of input parameters are considered that are based on these criteria but no additional effort is made to fine-tune and optimise these parameters to perform this morphological classification. The first set of parameters listed in Table 5.1 have been used extensively in the literature for morphological classification in the SDSS e.g. (Ball *et al.* 2004). They include the (g-r) and (r-i) colours derived from the dereddened model magnitudes although these have not been k-corrected to the rest-frame, as well as the axis ratios and log likelihoods associated with both a deVacouleurs and exponential fit to the two-dimensional galaxy image. The deVaucouleurs profile is commonly used to describe the variation in surface brightness of an elliptical galaxy as a function of radius whereas the exponential profile is used to describe the disk component of a spiral galaxy. In addition, the log likelihood of the object being a star, `lnLstar`, helps in performing star-galaxy separation. The equations representing both a deVaucouleurs and an exponential profile are given by Eq 5.2 and 5.3. The (g-r) and (r-i) colours have been chosen as the images used in the Galaxy Zoo classifications were composites of images in these three bands. The final parameter in Table 5.1 is the concentration parameter given by the ratios of radii containing 90% and 50% of the Petrosian flux in a given band.

$$I_{deV}(r) = I_0 exp\left(-7.67\left(\frac{r}{r_e}\right)^{1/4}\right),$$ (5.2)

$$I_{exp}(r) = I_0 exp\left(-1.68\left(\frac{r}{r_e}\right)\right).$$ (5.3)

The distributions of each of these parameters for the four morphological classes - ellipticals, spirals, star/other and mergers - are illustrated in Figure 5.3. These histograms are constructed using only objects with a weighted probability of greater than 0.8 in each of the four classes from Galaxy Zoo. It can immediately be seen that the different parameters allow us to distinguish between different morphological classes. While the stars and other unique objects have a very broad distribution in colour, the spirals and ellipticals have a much narrower range. The axis

Name	Description
dered_g-dered_r	(g-r) colour
dered_r-dered_i	(r-i) colour
deVAB_i	DeVaucouleurs fit axis ratio
expAB_i	Exponential fit axis ratio
lnLexp_i	Exponential disk fit log likelihood
lnLdeV_i	DeVaucouleurs fit log likelihood
lnLstar_i	Star log likelihood
petroR90_i/petroR50_i	Concentration

Table 5.1: First Set of Input Parameters based on profile fitting

ratios for ellipticals is also found to be generally larger than that for spirals, stars and mergers. Finally the average concentration parameter illustrated in the first panel of Figure 5.4 is found to be much larger for ellipticals, smaller for spirals and even smaller for the mergers and stars. This is consistent with the previous studies by Shimasaku *et al.* (2001) and Strateva et al. (2001) who find the inverse concentration index to be larger for spirals than for ellipticals.

The second set of input parameters described in Table 5.2 do not use the colours of galaxies or any parameters associated with profile fitting for morphological classification. Instead a new set of shape and texture parameters are used as well as the concentration from Table 5.1. mRrCc_i is the second moment of the object intensity in the CCD row, x and column, y, directions measured using a scheme designed to have optimal signal-to-noise ratio (Bernstein & Jarvis 2002).

$$\texttt{mRrCc} = <y^2> + <x^2>, \tag{5.4}$$

where for example,

$$<y^2> = \frac{\sum I(y,x)w(y,x)y^2}{\sum I(y,x)w(y,x)}. \tag{5.5}$$

Moments are measured using a radial gaussian weight function, $w(y,x)$ interactively adapted to the shape and size of the object. The ellipticity components, mE1_i and mE2_i defined in Eq
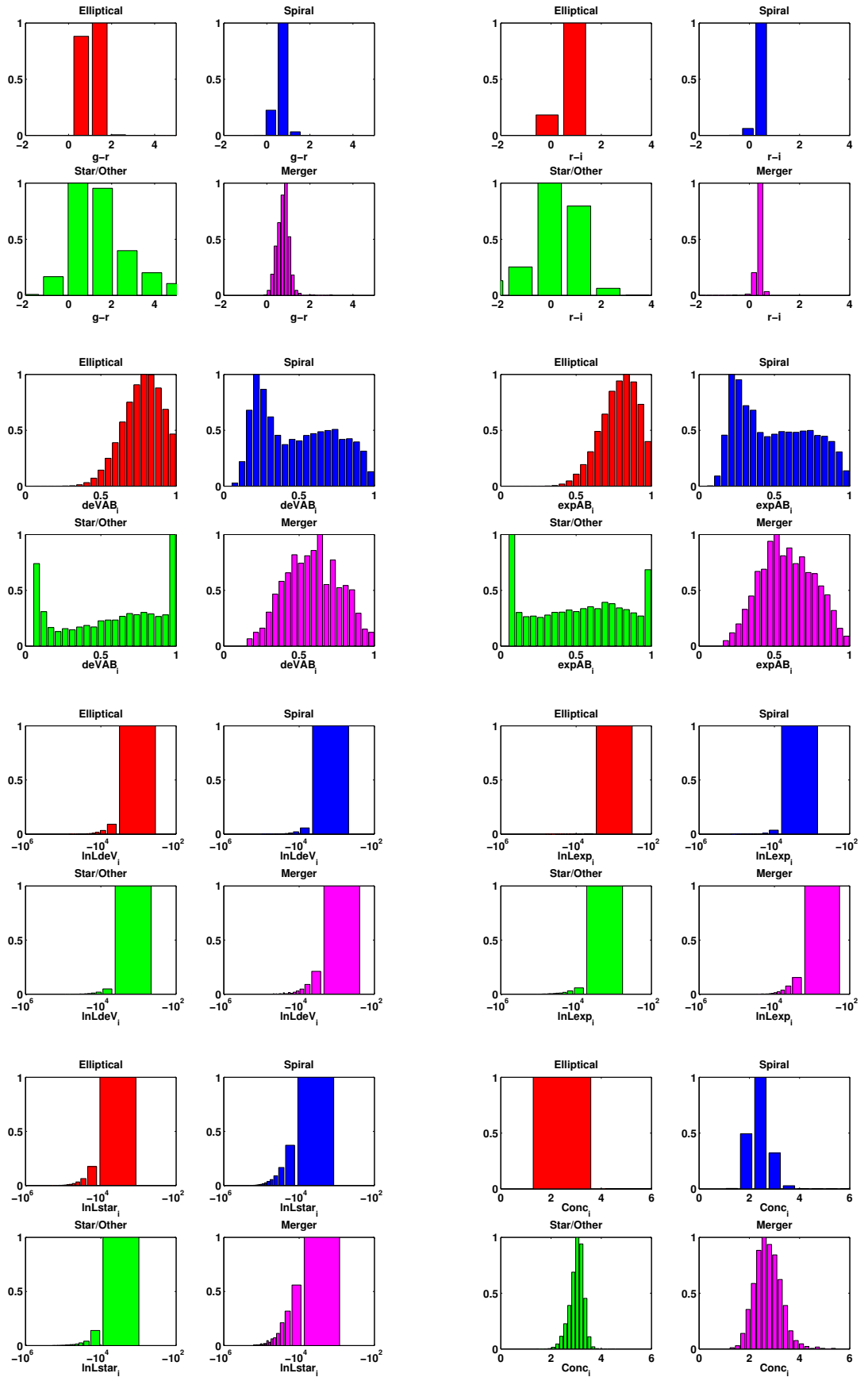
Figure 5.3: Histograms of the various input parameters in Table 5.1 for the four morphological classes.

Name	Description
petroR90_i/petroR50_i	Concentration
mRrCc_i	Adaptive (+) shape measure
mE1_i	Adaptive E1 shape measure
mE2_i	Adaptive E2 shape measure
mCr4_i	Adaptive fourth moment
texture_i	Texture parameter

Table 5.2: Second Set of Input Parameters based on adaptive moments

5.6 and Eq 5.7 and a fourth order moment (Eq 5.8) are also specified.

$$\texttt{mE1} = <y^2> - \frac{<x^2>}{\texttt{mRrCc}}, \tag{5.6}$$

$$\texttt{mE2} = 2\frac{<xy>}{\texttt{mRrCc}}, \tag{5.7}$$

$$\texttt{mCr4} = \frac{<(y^2 + x^2)^2>}{\sigma^4}, \tag{5.8}$$

where σ is the size of the gaussian weight. The final parameter in Table 5.2 is the texture or coarseness parameter described in Yamauchi *et al.* (2005). This essentially measures the ratio of the range of fluctuations in the surface brightness of the object to the full dynamic range of the surface brightness and is expected to vanish for a smooth profile but become non-zero if structures like spiral arms appear.

The distribution of each of these parameters constructed using only those objects in the Galaxy Zoo catalogue with a probability of greater than 0.8, are shown in Figure 5.4. Both the ellipticity parameters have the broadest distribution for the spirals followed by mergers and then the stars and ellipticals. The adaptive moments too are large for spirals and mergers compared to stars and ellipticals. The texture parameter is found to be much smaller for stars than for galaxies but similar for spirals and ellipticals in this sample.

The artificial neural network is run on the Galaxy Zoo catalogue in three configurations - 1) using the seven parameters specified in Table 5.1 that depend on the colours and profile fits to
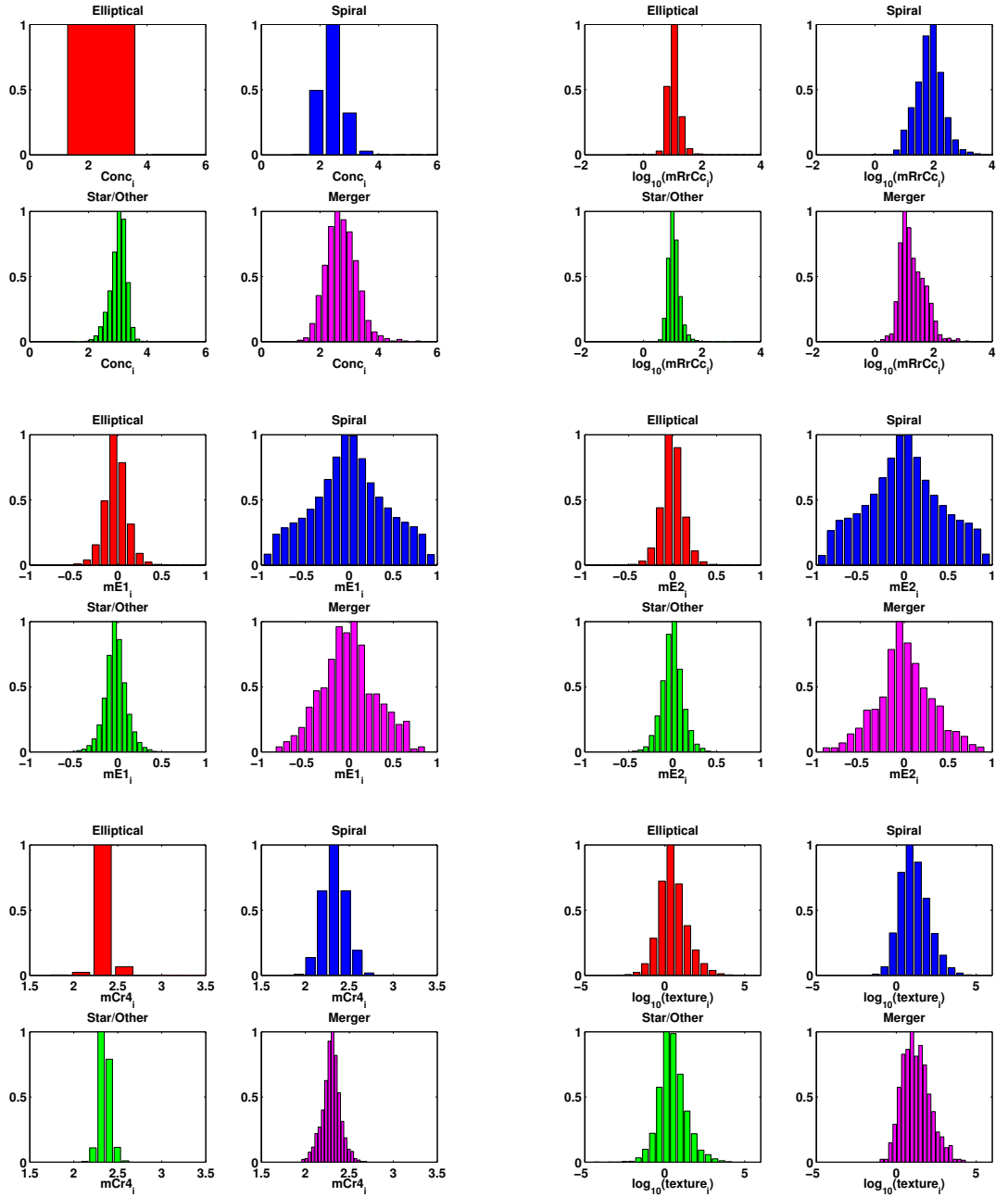
Figure 5.4: Histograms of the various input parameters in Table 5.2 for the four morphological classes.

Name	Number of Objects	Flux Limit	No. of Ellipticals	No. of Spirals	No. of Stars/Other
Entire	876,374	r<17.77	186,728	92602	7405
Gold	313,701	r<17.77	155,328	77191	6182
Bright	343,489	r< 17	71980	53489	4228

Table 5.3: Samples on which morphological classifications are performed by the neural network. The number of ellipticals, spirals and stars are calculated assuming a weighted probability of greater than 0.8 assigned by Galaxy Zoo users.

the 2D images 2) the six parameters specified in Table 5.2 that use an adaptive weighted fit to the images and 3) a combined set of 13 parameters. Note, that the concentration parameter is common between 1) and 2). The results are summarised in the next section.

5.5 Results

The neural network code is run on three samples for each set of input parameters. The first sample is the entire catalogue of $\sim$800,000 objects out of which 50,000 are used for training and 25,000 for validation. This is found to be a sufficiently large training set for these purposes and no significant improvement in the classifications is seen on increasing the size of the training set further. The second sample defined as the gold sample contains only objects with a weighted probability of greater than 0.8 assigned to them in any one of the three morphological classes by Galaxy Zoo users. This gold sample contains $\sim$315,000 objects and once again 50,000 are used for training and 25,000 for validation. Finally, a bright sample with $r < 17$ only is also considered. These various samples are summarised in Table 5.3 along with the number of ellipticals, spirals and star/other objects with a weighted probability of greater than 0.8 in each of the samples.

5.5.1 The Entire Sample

The neural network code is run on the entire sample of objects using (i) colours, concentration and profile-fitting parameters (ii) concentration and adaptive shape parameters and (iii) a combination of (i) and (ii). In Figures 5.5, 5.6 and 5.7, I plot the NN probability of the galaxy belonging to a morphological class versus the percentage of both Galaxy Zoo objects in that class that are discarded on applying this probability threshold as well as percentage of contaminants that enter the sample. This allows us to determine the optimum probability threshold for the neural network

that should be chosen for membership into each morphological class. This threshold is such that it minimises both the number of contaminants as well as the number of Galaxy Zoo objects in that class that are discarded. The optimum threshold is found to be ∼0.72 for ellipticals, ∼0.53 for spirals, ∼0.25 for stars and ∼0.05 for mergers when using the parameters in Table 5.1 and ∼0.68 for ellipticals, ∼0.50 for spirals, ∼0.10 for stars and ∼0.04 for mergers when using the parameters in Table 5.2. The low neural network probability threshold found for mergers is consistent with the fact that Galaxy Zoo users failed to classify mergers with a high probability (Lintott *et al.* 2008). Given the extremely low optimum neural network probability required for mergers and the fact that using even this optimum probability there are ∼25% contaminants and ∼25% of Galaxy Zoo mergers discarded, I do not attempt to perform merger classifications with this sample. I simply note that a larger training set of visually classified mergers will be required for such purposes.

For the Galaxy Zoo classifications, the probability threshold is considered to be 0.8 for the galaxy belonging to a particular morphological class. In Tables 5.4, 5.5 and 5.6, the results from running ANNz on the entire sample using the three different sets of input parameters are summarised. The tables give the percentage of ellipticals, spirals and stars (weighted probability>0.8) that are put into the different classes by the neural network after assuming the optimum NN probabilities already mentioned in each of the three classes. Throughout this work, the lowercase names - Elliptical, Spiral, Star/Other - correspond to the Galaxy Zoo classifications and the upper case names - ELLIPTICAL, SPIRAL, STAR/OTHER - correspond to the neural network classifications. Note that as the objective is to simultaneously minimise both the number of contaminants as well as the number of genuine objects discarded in each of the three classes, the sum of the probabilities of each object over all three classes does not necessarily add up to 100%. This is because an object with a neural net probability of greater than 0.3 for example in the STAR/OTHER class, could potentially, also have a neural net probability of greater than 0.5 in the SPIRAL class and therefore be classified as both. In the tables presented throughout this analysis, I am not summarising the results of unique classifications for every single object but rather the best results that could be obtained for each subsample assuming neural network threshold probabilities that minimise both the plotted quantities in Figure 5.5 for example. If one was to consider the best results for the entire sample as a whole, the chosen probability thresholds would probably be different.

Using the traditional colour and profile-fitting parameters, 88% of spirals, 88% of ellipticals and 95% of stars/unique objects are correctly classified by the neural network. Note however that while colours are sensitive to the star-formation history of a galaxy, the morphology essentially measures the dynamic history. Although the two are correlated, they are not necessarily the same
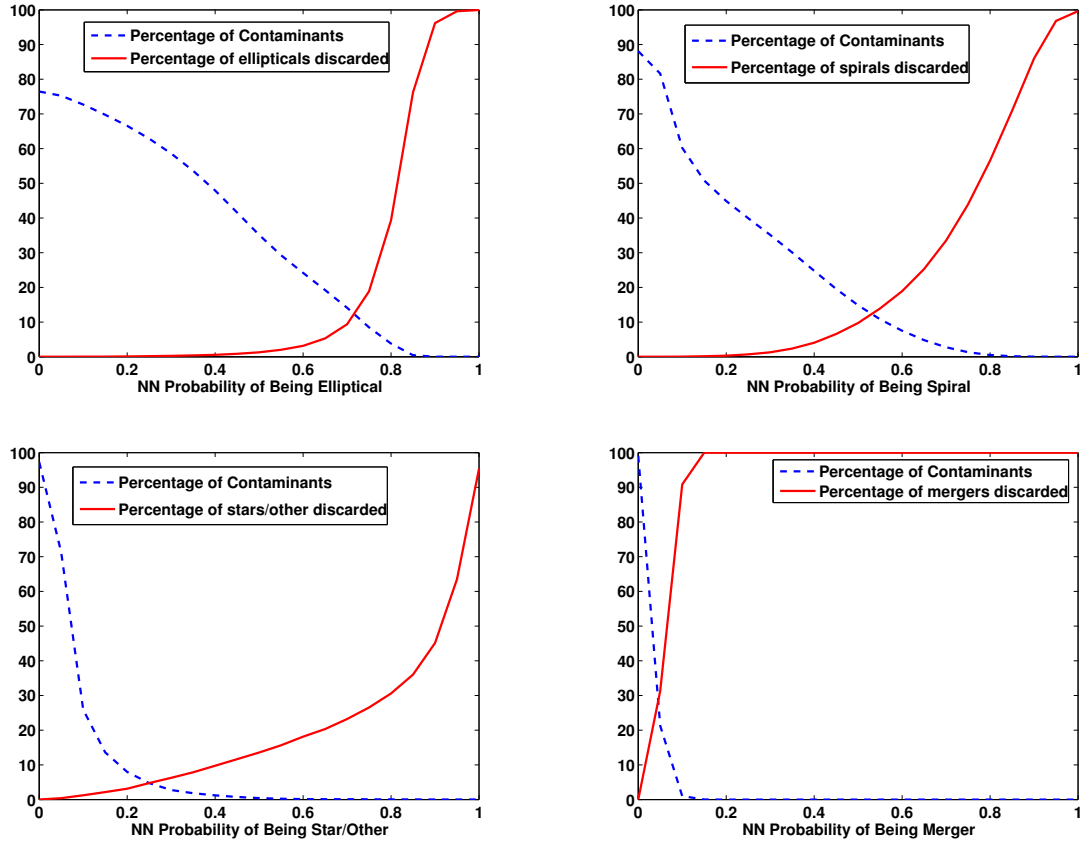
Figure 5.5: The neural network probability of a galaxy being a elliptical (top left), spiral (top right), star/other (bottom left) or merger (bottom right) versus the percentage of contaminants as well as the percentage of Galaxy Zoo objects in these classes that are discarded. These results are obtained using the 7 input parameters in Table 5.1 - colours and traditional profile-fitting.

| | | **GALAXY ZOO** | | |
		Elliptical	Spiral	Star/Other
A	ELLIPTICAL	88%	0.2%	0.3%
N	SPIRAL	0.5%	88%	1.3%
N	STAR/OTHER	0.4%	0.5%	95%

Table 5.4: Summary of results for entire sample when using input parameters specified in Table 5.1 - colours and traditional profile-fitting.
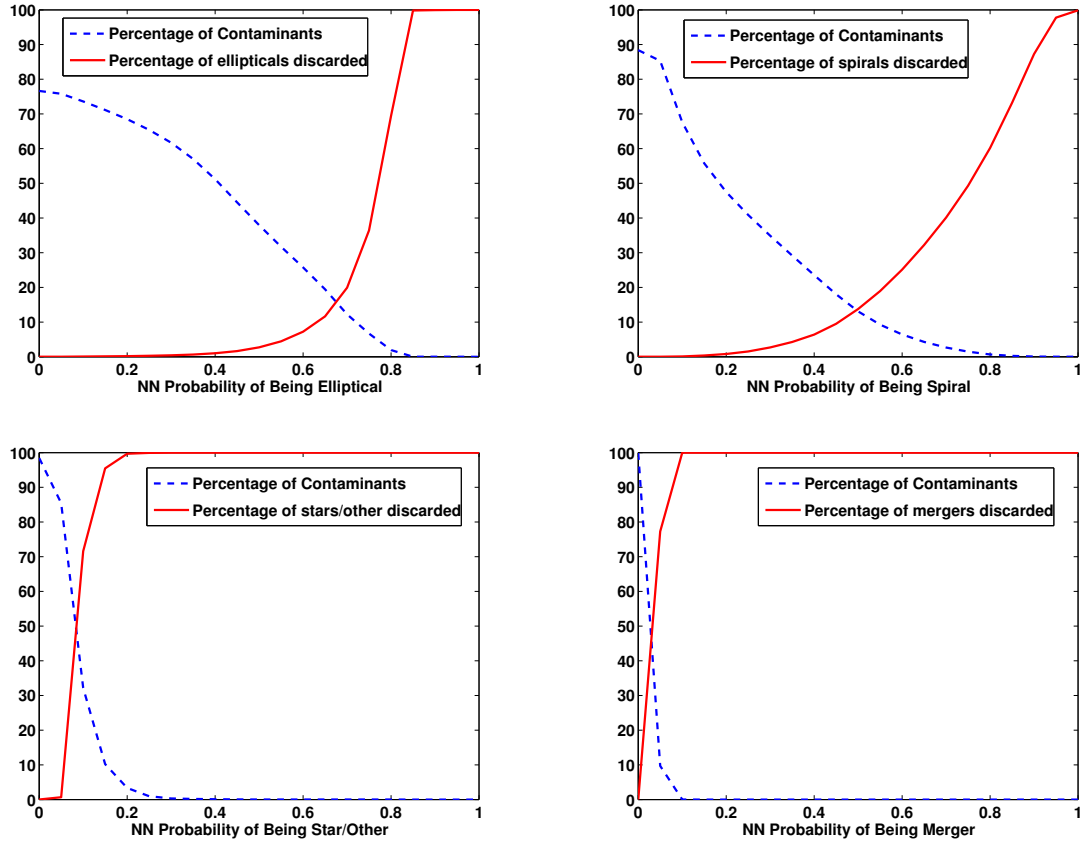
Figure 5.6: The neural network probability of a galaxy being an elliptical (top left), spiral (top right), star/other (bottom left) and merger (bottom right) versus the percentage of contaminants as well as the percentage of Galaxy Zoo objects in these classes that are discarded. These results are obtained using the 6 input parameters in Table 5.2 - adaptive moments.

		GALAXY ZOO		
		Elliptical	Spiral	Star/Other
A	ELLIPTICAL	84%	0.5%	85%
N	SPIRAL	0.9%	86%	0.7%
N	STAR/OTHER	28%	7%	28%

Table 5.5: Summary of results for entire sample when using input parameters specified in Table 5.2 - adaptive moments.
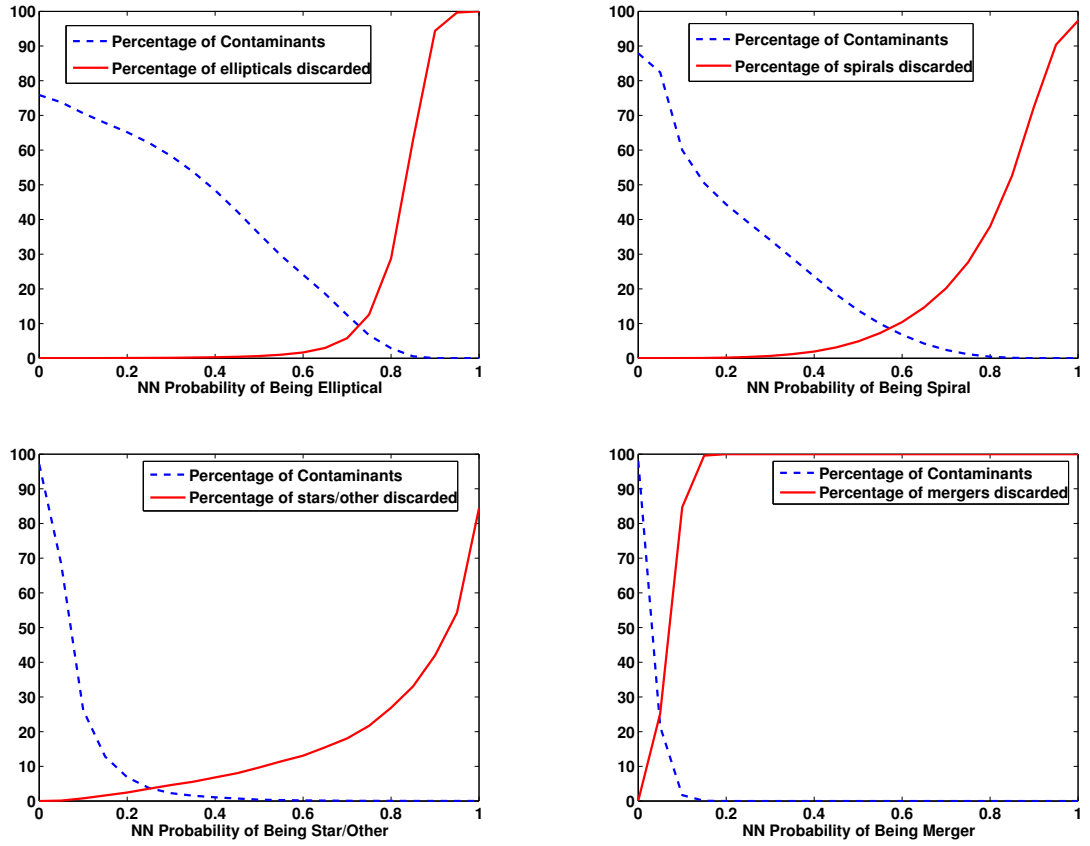
Figure 5.7: The neural network probability of a galaxy being a elliptical (top left), spiral (top right), star/other (bottom left) or merger (bottom right) versus the percentage of contaminants as well as the percentage of Galaxy Zoo objects in these classes that are discarded. These results are obtained using the combined set of 13 input parameters from Tables 5.1 and 5.2.

		GALAXY ZOO		
		Elliptical	Spiral	Star/Other
A	ELLIPTICAL	91%	0.08%	0.5%
N	SPIRAL	0.1%	93%	0.2%
N	STAR/OTHER	0.3%	0.3%	96%

Table 5.6: Summary of results for entire sample when using input parameters specified in Table 5.1 and Table 5.2

and therefore it is important to use colours in conjunction with other parameters when performing morphological classifications. Looking more closely at the Galaxy Zoo ellipticals that were misclassified by the neural net as spirals as well as the spirals that are misclassified by the neural net as ellipticals, there is some evidence that these galaxies may be red spirals or blue ellipticals. 45 Galaxy Zoo ellipticals are classified as spirals with a probability of greater than 0.8 by the neural net. Similarly, 40 Galaxy Zoo spirals are classified as ellipticals with a probability greater than 0.8. Out of these, 21 ellipticals and 9 spirals have SDSS spectra available. Using the criterion in Baldry *et al.* (2004) to isolate red and blue galaxies, 6 out of the 9 spirals are found to be red and 10 out of the 21 ellipticals are blue. In other words, the colour information used as an input to the neural network may be biasing the morphological classification. However, due to the small numbers of misclassified galaxies with SDSS spectra available, a definite statement cannot be made.

The adaptive shape parameters are very good for distinguishing between spirals and ellipticals and these parameters result in accurate classifications for 84% of ellipticals and 86% of spirals. However, this set of parameters gives very poor results for stars and only 28% are correctly classified by the neural network. This is because, these parameters are very similar for stars and ellipticals as can be seen in the histograms in Figure 5.4. As there are many more ellipticals in the training set compared to stars/unique objects, the neural network cannot differentiate between the two and assigns most of the stars to be ellipticals. Also Figure 5.6 shows that the optimum neural network probability for star classification using this set of input parameters is as low as 0.1. This means that many objects will be classified both as a star and a galaxy assuming this probability and for this reason, the sums of the columns in Table 5.5 are always greater than 100% as there are objects in common between the classes. I also investigate whether the evidence for a bias due to colour in the morphological classifications is removed once the colours are removed as input parameters to the network. With the adaptive shape parameters as inputs 208 Galaxy Zoo ellipticals are found to be misclassified as spirals with a probability greater than 0.8 by the neural network and similarly, 26 spirals are misclassified as ellipticals with the same probability. Out of these 116 ellipticals and only 8 spirals have SDSS spectra. 2 out of the 8 spirals are red but 46 of 116 ellipticals are blue once again suggesting that there may still remain a bias, especially against blue ellipticals even when the colour parameters are removed as inputs to the neural net. Hence atleast some blue ellipticals may be distinguishable from their red counterparts by structure as well as colour.

On adding the profile-fitting and colour parameters to the adaptive shape parameters, the results are now considerably improved for all three classes. 91% of ellipticals, 93% of spirals and

		GALAXY ZOO		
		Elliptical	Spiral	Star/Other
A	ELLIPTICAL	95%	0.4%	1.1%
N	SPIRAL	0.3%	92%	0.9%
N	STAR/OTHER	0.04%	0.04%	85%

Table 5.7: Summary of results for gold sample when using input parameters specified in Table 5.1 - colours and traditional profile-fitting.

96% of stars are correctly classified by the neural network. Lintott *et al.* (2008) have compared the Galaxy Zoo classifications to those by professional astronomers and find an agreement of better than 90% between these samples. However, the samples used in Lintott *et al.* (2008) are the MOSES sample of Schawinski *et al.* (2007) whose objective was to generate a very clean set of elliptical galaxies, and the detailed classifications of Fukugita *et al.* (2007) which are very sensitive to the E/Sa boundary. If the professional astronomers were set the same task as the Galaxy Zoo users - i.e. a clean division of spirals and ellipticals in SDSS - the scatter between them and the Galaxy Zoo users may well be worse than 90%. It has been shown that with a set of thirteen intelligently chosen parameters, that are easily available but still by no means optimal for performing morphological classification, the neural network results agree to better than 90% with those from Galaxy Zoo.

5.5.2 The Gold Sample

The results of running ANNz on the gold sample using the three different sets of input parameters are now described. These results are summarised in Tables 5.7, 5.8 and 5.9 where we consider the percentage of Galaxy Zoo ellipticals, spirals and stars/unique objects that have also been put into these classes by the neural network assuming a probability of greater than 0.8 for the neural network classification. Once again it can be seen that the second set of input parameters involving just the concentration and the adaptive shape parameters, performs very poorly in classifying the stars/unique objects. However, the combined set of input parameters leads to correct neural network classifications for 97% of ellipticals and 96% of spirals. The success for stars is somewhat lowered compared to using the entire sample. This is because when considering the entire sample it has been assumed that all objects with a neural network star probability of greater than 0.2 are

		GALAXY ZOO		
		Elliptical	Spiral	Star/Other
A	ELLIPTICAL	91%	0.7%	91%
N	SPIRAL	0.6%	88%	0.5%
N	STAR/OTHER	0%	0%	0%

Table 5.8: Summary of results for gold sample when using input parameters specified in Table 5.2 - adaptive moments.

		GALAXY ZOO		
		Elliptical	Spiral	Star/Other
A	ELLIPTICAL	97%	0.2%	1.2%
N	SPIRAL	0.1%	96%	0.4%
N	STAR/OTHER	0.04%	0.01%	85%

Table 5.9: Summary of results for gold sample when using input parameters specified in Table 5.1 and Table 5.2

indeed stars whereas in this section we require the probability to be greater than 0.8.

5.5.3   The Bright Sample

In this section, the neural network code is run on the bright sample $r < 17$ using the combined set of thirteen input parameters. This allows us to perform two tests. Firstly, I look at whether the bright galaxies in general have better classifications compared to the entire sample. This is done by comparing Tables 5.6 and 5.10. Secondly, the neural network is trained on the bright sample and this trained network is used to perform morphological classifications for the entire sample. This allows us to quantify the effects of magnitude incompleteness in the training set on the morphological classifications. The results are summarised in Table 5.11.

Comparing Tables 5.6 and 5.10, it can be seen that the results are very similar when performing morphological classsifications on the entire sample with $r < 17.77$ and the bright sample with $r < 17$, in both cases using a complete training set. When the training is performed using an incomplete training set with $r < 17$ and all objects with $r < 17.77$ classified, the neural network

		GALAXY ZOO		
		Elliptical	Spiral	Star/Other
A	ELLIPTICAL	93%	0.08%	0.4%
N	SPIRAL	0.2%	96%	0.5%
N	STAR/OTHER	0.2%	0.2%	98%

Table 5.10: Summary of results for bright sample when using input parameters specified in Table 5.1 and Table 5.2

		GALAXY ZOO		
		Elliptical	Spiral	Star/Other
A	ELLIPTICAL	92%	0.08%	1%
N	SPIRAL	0.2%	96%	0.5%
N	STAR/OTHER	3%	0.2%	96%

Table 5.11: Summary of results for entire sample when using input parameters specified in Table 5.1 and Table 5.2 and only bright galaxies with $r < 17$ to train the network.

still manages to perform these classifications with more than 90% agreement with Galaxy Zoo users. The magnitude incompleteness in the training set doesn't seem to affect the classifications as most of the input parameters to the neural network considered in this study have been chosen to be distance independent and so their distribution doesn't really change from a shallow to a deeper sample. This is promising for using automated machine learning algorithms to perform morphological classsification for future deep surveys using the Galaxy Zoo classifications on the shallower SDSS survey as a training set.

5.6 Conclusion

In this study, a machine-learning algorithm based on artificial neural networks has been used to perform morphological classifications for almost 1 million objects from the Sloan Digital Sky Survey that were classified by eye as part of the Galaxy Zoo project. Similar work was already done for example by Naim *et al.* (1995); Lahav *et al.* (1995, 1996) where galaxies were classified into up to 16 different morphological types with considerable success. However, the size of current

astronomical data sets means these methods can now be applied on unprecedented scales. The neural network is trained on 75000 objects and using a well defined set of input parameters that are also distance independent, the human classifications can be reproduced for the rest of the objects to better than 90% in three morphological classes - spirals, ellipticals and stars/unique objects. Specifically, the following conclusions can be drawn:

- Using colours and profile-fitting parameters as inputs to the neural network, 88% of elliptical classifications, 88% of spiral classifications and 95% of star/other classifications agree with those obtained by the human eye. However, there is some evidence to suggest that a non-negligible fraction of red spirals and blue ellipticals are misclassified by the network when using this set of parameters.

- When parameters that rely on an adaptive weighted scheme for fitting the galaxy images are used, the neural network is unable to distinguish between ellipticals and stars.

- A combination of the profile fitting and adaptive weighted fitting parameters results in better than 90% agreement between classifications by humans and those by the neural network for all three morphological classes. This is comparable to the success of Galaxy Zoo users in reproducing the classifications by professional astronomers.

- The optimum neural network probability for a galaxy belonging to a particular morphological class is such that it minimises both the percentage of contaminants as well as the percentage of genuine objects in that class that are discarded on cutting the sample using this threshold. This optimum probability depends both on the input parameters as well as the morphological class of the object. Ellipticals are generally found to have a high optimum probability (~ 0.7) whereas stars/other objects have a very low optimum probability (~ 0.2) Therefore the same object could be put into more than one class by the neural network if the classifications were performed using the optimum threshold probabilities.

- For the gold sample, the spiral and elliptical classifications by the neural network match those by the human eye to better than 95%.

- Using a bright sample to train the neural network and performing morphological classifications for a deeper and fainter sample still results in better than 90% agreement between the neural network and human classifications in all three morphological classes. This is because the input parameters have deliberately been chosen to be distance independent.

- However, other sources of incompleteness in the training sets also need to be examined before the role of the Galaxy Zoo data in training morphological classifiers for future surveys, can be fully understood.

The penultimate point in particular illustrates the power of the machine learning algorithm in fully exploiting data from future wide-field imagning surveys. Such surveys will obtain images for hundreds of millions of objects down to very deep magnitude limits. It has been shown that by using the wealth of information made available through the Galaxy Zoo project as a training set, the machine learning algorithm can quickly and accurately classify the vast numbers of objects that will make up future data sets into ellipticals, spirals and stars. However, if the Galaxy Zoo catalogue is to be used as a training set for automated machine learning classifications of mergers with the next generation of galaxy surveys, a more robust catalogue of visually classified mergers needs to be obtained. Also, it is worth emphasising that the images obtained from the next generation of wide-field surveys will need to have the necessary pixel size and resolution required to derive photometric parameters such as those used as inputs to the neural network in this chapter. This work has also examined the effect of magnitude incompleteness in the training set on automated morphological classifications. In the future, more work needs to be done on investigating other sources of incompleteness in the training set before this data can be used effectively to train machine-learning morphological classifiers for future surveys. For example, in this work some evidence has been found that a non-negligible proportion of galaxies that are misclassified by the neural network are either red spirals or blue ellipticals. By training on a sample of red ellipticals and using them for morphological classification of blue ellipticals such as those identified by Schawinski *et al.* (2009) for example, we can hope to quantify the colour bias in morphological classifications. Provided this is done, morphological classification via machine-learning looks promising in allowing for many more detailed studies of the processes involved in galaxy formation and evolution with the next generation of galaxy surveys.

THE EVOLUTION OF LUMINOUS RED GALAXIES

*The work described in this chapter is an extended version of the paper **Banerji, Ferreras, Abdalla, Hewett & Lahav, 2009***

6.1   Introduction

Luminous Red Galaxies are arguably some of the brightest galaxies in our Universe allowing us to study their evolution out to much higher redshifts than is possible with samples of more typical galaxies. LRGs are known to form a spectroscopically homogenous population that can be reliably identified photometrically by means of simple colour selections (Eisenstein *et al.* 2001; Cannon *et al.* 2006). The presence of a strong 4000 $\mathring{A}$ break in these galaxies also means that accurate photometric redshifts can be derived for large samples where spectroscopy is difficult to obtain (Chapter 2 and Padmanabhan *et al.* (2005); Collister *et al.* (2007)). Consequently, samples of luminous red galaxies have emerged as an important data set both for studies of cosmology (Blake *et al.* 2007, 2008; Cabré & Gaztañaga 2009) and galaxy formation and evolution (Wake *et al.* 2006; Cool *et al.* 2008).

The study of massive galaxies in our Universe is particularly interesting since these galaxies present a long-standing problem for models of galaxy formation. While in the standard ΛCDM cosmology, galaxies that reside in massive halos are thought to be built up through successive mergers of smaller systems (White & Rees 1978), many observations now suggest that these galaxies were already well assembled at high redshifts (Glazebrook *et al.* 2004; Cimatti *et al.*

2006; Scarlata *et al.* 2007; Ferreras *et al.* 2009*b*; Pozzetti et al. 2009). At the same time, star formation and merging activity has also been seen in such systems between $z \sim 1$ and the present day (Lin *et al.* 2004*b*; Stanford *et al.* 2004) and the studies of Bell *et al.* (2004) and Faber *et al.* (2007) have found evidence that the luminosity density of massive red galaxies has remained roughly constant since z~1 implying a build up in the number density of these objects through mergers. Most observational results now support downsizing in star formation - i.e. galaxies in the most massive halos having lower specific star formation rates than their less massive counterparts - and many galaxy formation models are able to reproduce these observations e.g. by invoking quenching mechanisms such as AGN feedback (Croton *et al.* 2006; De Lucia *et al.* 2006). However, the more recently observed trend of downsizing in the mass assembly (Cimatti *et al.* 2006) presents more of a challenge for galaxy formation models which generally predict that the most massive galaxies were assembled later than their less massive counterparts.

Many of the contradictions in observational studies of massive galaxy formation arise principally for two reasons. Firstly, the way in which early-type galaxies are selected in different surveys can be considerably different. Morphological selection compared to colour selection of such objects will almost certainly result in different samples being chosen, particularly at high redshifts. The colour selection is also usually different for different samples of massive galaxies as I will point out later in this chapter. Secondly, many of the studies of massive galaxy formation mentioned so far are deep and narrow spectroscopic samples that will suffer from biases due to the effects of cosmic variance. In addition, one has to be careful in interpreting observational results as in current galaxy formation models, star formation and mass assembly in galaxies are not necessarily concommitant. So while the stars in early-type galaxies may have formed very early in the Universe's history, they may have formed in relatively small units and only merged at lower redshifts to create the massive early-type galaxies we see today.

Studies of the evolution of luminous red galaxies such as those analysed in this chapter have already supported the evidence that massive galaxies have been passively fading and show very little recent star formation (Wake *et al.* 2006; Cool *et al.* 2008). In this analysis, the work of these authors is extended by also considering the mass assembly of these systems. The 2dF and SDSS LRG and QSO (2SLAQ) survey presents a comprehensive improvement in volume for massive galaxy samples. The survey covers an area of 186 deg^2 and reaches out to a redshift of 0.8 making it a promising data set to study the evolution of massive red galaxies. Furthermore, much of the 2SLAQ area is now covered by the UKIDSS Large Area Survey (LAS) that provides complementary data in the near infra-red bands for the optically selected LRGs. The advantage of near

infra-red data is that the mass-to-light ratios and k-corrections are largely insensitive to the galaxy or stellar type and therefore the total infra-red flux in for example the K-band provides a good estimate of the total stellar mass of the galaxies. This stellar mass estimate allows us to study not only the star formation history but also the mass assembly history of these systems. As is the case for optically selected spectroscopic samples of massive galaxies, the K-band selected surveys have so far been restricted to relatively small and deep patches of the sky (Mignoli *et al.* 2005; Conselice *et al.* 2007). Clearly a large spectroscopic survey of massive galaxies with optical and near infra-red photometry, will allow for better constraints on the evolution of these systems.

In this chapter, I utilise a spectroscopic sample of colour-selected massive red galaxies from the 2SLAQ survey between redshifts 0.4 and 0.8. Optical photometry is obtained from the Sloan Digital Sky Survey supplemented with near infra-red data from the UKIDSS Large Area Survey (LAS). I consider the evolution of these galaxies in terms of their observed colours, luminosities and comoving number densities focussing particularly on the effects of colour selection on the inferred evolution. Wake *et al.* (2006) have presented a comprehensive analysis of the luminosity function of Luminous Red Galaxies using data from both the Sloan Digital Sky Survey and the 2SLAQ Survey. These authors use a subset of data from the 2SLAQ survey in the redshift range 0.5 to 0.6 and by comparing this galaxy population to a lower redshift population at $0.17 < z < 0.24$ from SDSS, they are able to establish that the LRG LF does not evolve beyond that expected from a simple passive evolution model at these redshifts. Meanwhile, Cool *et al.* (2008) have compared the low-redshift SDSS LRG population to their own high-redshift sample at redshifts of ~ 0.9 and once again find little evidence for evolution beyond the passive fading of the stellar populations. I extend the work of these authors by considering now most of the galaxies available in the 2SLAQ data set. This enables the redshift range of 2SLAQ galaxies used to be broadened to $0.4 \leq z < 0.8$. The 2SLAQ luminosity function is presented for 8625 LRGs as compared to the 1725 used by Wake *et al.* (2006). These results are useful in filling the gap between redshift 0.4 and 0.5 and redshift 0.6 and 0.8 in the Wake *et al.* (2006) and Cool *et al.* (2008) data sets. The sample is split into four redshift bins and the evolution of the luminosity and colour of LRGs between these redshift bins is considered. In addition, I also consider the evolution of the stellar mass function of these galaxies with redshift. Furthermore, various different stellar population synthesis models that are commonly used in the literature are utilised in order to model the LRGs, including the new models of Maraston *et al.* (2009). The sensitivity of the luminosity function estimate to changes in these models is also quantified. The optical colours of LRGs have long been difficult to model using standard spectral evolution models (Eisenstein *et al.* 2001) and this

problem has only recently been solved (Maraston *et al.* 2009) thereby allowing us to utilise the most accurate spectral evolution models of LRGs to date in order to infer their evolution.

6.2 Data

The dataset used in this analysis is a sample of Luminous Red Galaxies from the 2dF and SDSS LRG and QSO (2SLAQ) survey (Cannon *et al.* 2006). This is a spectroscopic survey conducted on the 2-degree Field (2dF) spectrograph on the 3.9m Anglo-Australian Telescope. The survey recorded spectra for $\sim$10000 LRGs with a median redshift of 0.55 and $\sim$10000 faint $z < 3$ QSOs selected from SDSS imaging data. The survey covers an area of 186 deg^2 and extends to a redshift of ~ 0.8 for the LRGs. This section provides a description of the 2SLAQ data as well as optical and near infra-red photometry for these galaxies obtained using the SDSS and UKIDSS LAS respectively.

In the 2SLAQ survey, the following colour and magnitude cuts have been applied using SDSS DR4 photometry in order to isolate the main LRG population to target with spectroscopy (Cannon *et al.* 2006):

$$c_{\parallel} = 0.7(g - r) + 1.2(r - i - 0.18) \geq 1.6, \tag{6.1}$$

$$d_{\perp} = (r - i) - (g - r)/8.0 > 0.65, \tag{6.2}$$

$$17.5 \leq i_{deV} - A_i \leq 19.8, \tag{6.3}$$

where i_{deV} is the i-band deVaucouleurs magnitude and A_i is the extinction in the i-band. These cuts are for the primary sample defined as Sample 8 in Cannon *et al.* (2006) which has the highest completeness and this is the sample that is used throughout this chapter. Note that these colour cuts are usually different for different surveys. For example the colour cuts used to isolate LRGs in the SDSS LRG sample (Eisenstein *et al.* 2001) results in a distribution that is redder than that of the 2SLAQ galaxies. If these different LRG samples are to be compared therefore, further cuts must be applied to them to ensure a consistent colour selection as in Wake *et al.* (2006).

In the case of the 2SLAQ LRGs, the effect of the $d_{\perp}$ cut is to select early-type galaxies at increasingly high redshifts whereas the $c_{\parallel}$ cut eliminates late-type galaxies from the sample. Most
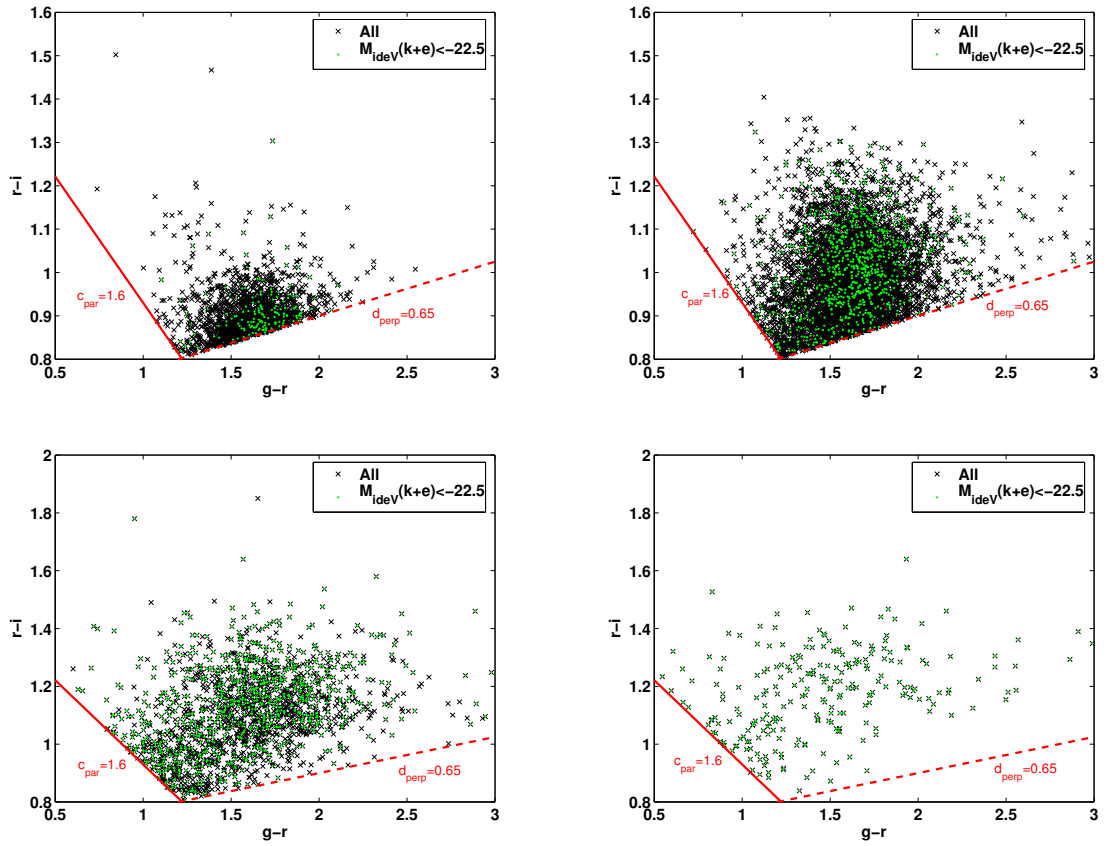
Figure 6.1: The (g-r) versus (r-i) colours of 2SLAQ galaxies in the observed frame in four redshift bins - $0.4 \leq z \leq 0.5$ (top left), $0.5 \leq z \leq 0.6$ (top right), $0.6 \leq z \leq 0.7$ (bottom left) and $0.7 \leq z \leq 0.8$ (bottom right). The dark points correspond to all galaxies in that redshift bin whereas the light points show the brightest galaxies with $M_{ideV} < -22.5$.

of the sample has redshifts of $0.2 < z < 0.8$ with $\sim 5\%$ contamination from M-type stars (Cannon *et al.* 2006). In order to capture the main redshift distribution of this primary sample, only galaxies with $0.4 \leq z < 0.8$ are used in this work. Furthermore, only galaxies with a redshift quality flag of greater than 2 have been selected. This results in a sample of 8625 LRGs and the redshift completeness for this sample is 76.1% (David Wake:private communication).

In Figure 6.1, the LRGs are plotted in the observed (g-r) versus (r-i) plane in redshift bins of width 0.1. Isolating bright galaxies only with $M_{ideV} < -22.5$ and plotting them in the same colour-colour plane shows clearly how the red sequence is truncated in the lowest redshift bin due to the redshift dependent colour selection. The effect of this truncation on the luminosity function estimate will be described in more detail in § 6.4.

In order to obtain accurate stellar masses for the LRGs, the 2SLAQ data is matched to near
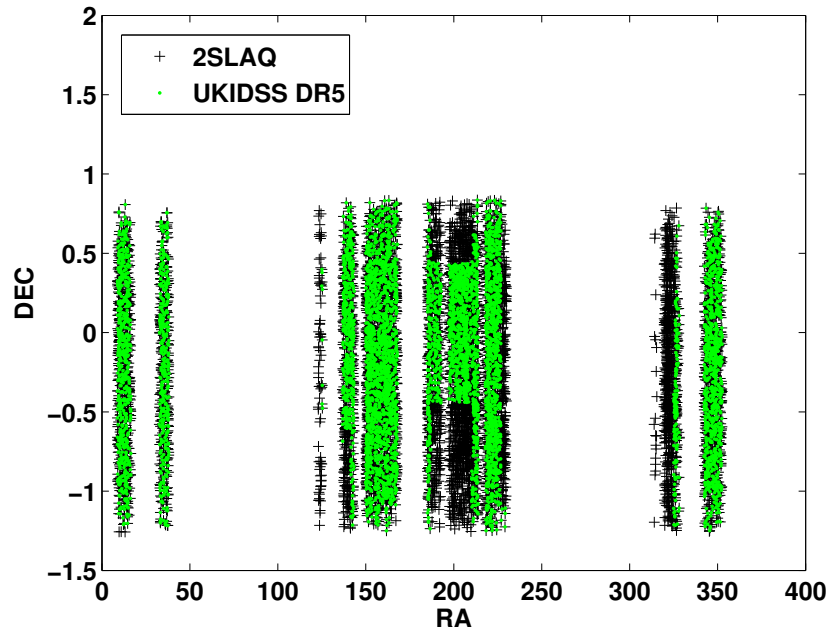
Figure 6.2: Figure showing the 2SLAQ LRGs studied in this chapter in RA and DEC and the overlap with UKIDSS DR5 K-band data.

infra-red data from the UKIDSS Large Area Survey (LAS) DR5 which has a depth of K_{Vega}=18.4. The galaxies are matched to within 1.1 arcsecs in position using the WFCAM science archive[1] and only galaxies with detections in the K-band are selected. Figure 6.2 overplots the 2SLAQ LRGs for which K-band detections have been obtained using UKIDSS DR5 on all the 8625 2SLAQ LRGs considered in this chapter. Out of our total sample of 8625 2SLAQ LRGs, K-band data is available for 6476 galaxies which represents ∼75% of the sample. The UKIDSS K-band magnitudes are in the Vega system and have been corrected to the AB system using the corrections of Hewett *et al.* (2006).

6.2.1   Photometric Errors

Wake *et al.* (2006) have conducted a detailed analysis of the effect of photometric errors on the 2SLAQ LRG sample. These photometric errors could induce a systematic bias in the sample by scattering galaxies both in and out of the sample across the colour selection boundaries. For $i < 19.3$, the effect of the photometric errors is relatively insignificant and the colour-magnitude distributions of LRGs selected using single-epoch photometry and those selected using multi-

---

[1]http://surveys.roe.ac.uk/wsa/index.html

epoch photometry are almost identical (Wake *et al.* 2006). Fainter than this however, the photometric errors may present a significant systematic bias to the inferred colour and luminosity evolution of LRGs in this survey. The effect of these photometric errors on the luminosity function estimate is considered in § 6.4.2.5. It turns out that different estimators of the luminosity function have different sensitivity to the photometric errors and this point is addressed in more detail later in the chapter.

6.3 K+e Corrections

In order to calculate the rest-frame properties of LRGs and infer their evolution, the observed properties need to be transformed into the rest-frame by means of a k-correction. In addition, one can also correct for any evolutionary changes expected in the galaxy spectra by means of an e-correction. Motivated by the work of Padmanabhan *et al.* (2005), I start by using a Pegase (Fioc & Rocca-Volmerange 1997) template to model the spectral evolution of the LRGs. In this template, the stars are formed in a single burst 11Gyr ago ($z \simeq 2.5$). A Salpeter (1955) IMF is assumed as well as solar metallicity and no galactic winds or substellar objects.

However, it has been noted by several authors that stellar population synthesis models such as Pegase and those of Bruzual & Charlot (2003) fail to reproduce the observed colours of LRGs (Eisenstein *et al.* 2001; Maraston 2005). Improvements to these models have subsequently been made that involve changes to the input stellar libraries as well as including an additional metal-poor sub component to the stellar population in order to create a composite model (Maraston *et al.* 2009). Such models predict siginificantly bluer (g-r) colours compared to simple stellar population models and are better able to reproduce the observed broadband colours of individual LRGs. For this reason, a Maraston model of age 12Gyr corresponding to a galaxy mass of 10^{12} M$_\odot$ is also considered in this work.

Finally, the models of Charlot & Bruzual 2007 (Bruzual & Charlot 2003; Bruzual 2007) - CB07 hereafter - are also considered. These models have a range of different metallicities and star formation histories and these are used to quantify the systematics associated to the different prescriptions, isochrones and stellar libraries of the population synthesis models. All the CB07 templates assume a formation redshift of $z_F = 3$ and a Chabrier (2003) IMF.

K and k+e corrections in the r-band derived from each of these models, are illustrated in Figure 6.3. In addition, k-corrections are also derived from stacked LRG spectra from the SDSS LRG survey (Eisenstein *et al.* 2001) at redshifts 0.2 and 0.5. These are very similar to each other
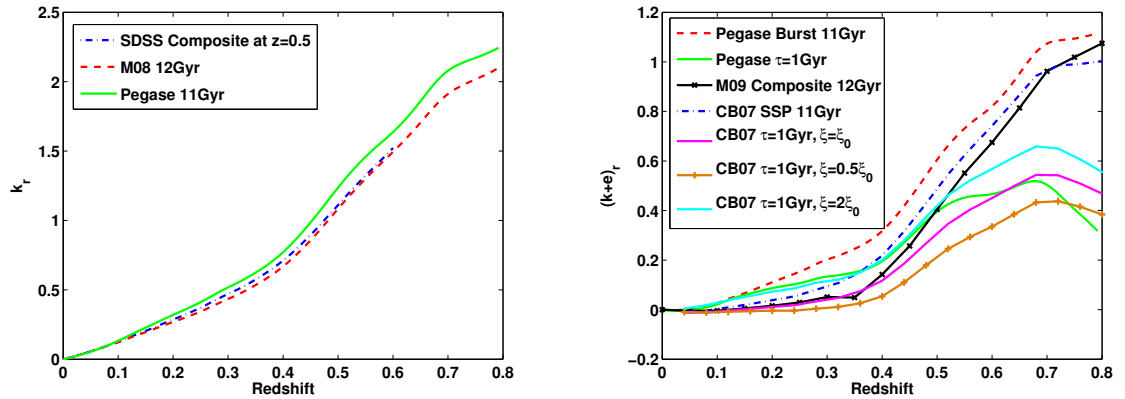
Figure 6.3: The k and k+e corrections in the r-band for LRGs derived using stacked SDSS spectra as well as various spectral evolution models with different star formation histories and metallicities, ξ.

suggesting that there is little or no colour evolution in the SDSS LRGs between redshifts of 0.2 and 0.5. As the 2SLAQ LRG spectra are not flux calibrated, a similar derivation of the k-corrections using these was not possible. Although the SDSS LRGs are selected using different colour cuts, it is still interesting to compare their k-corrections to the ones derived using the various spectral evolution models and it can be seen that the empirical k-corrections best match those derived from a Maraston model. For this reason, the composite 12Gyr model from Maraston *et al.* (2009) has been used throughout this chapter unless otherwise stated. One can also see from the right-hand panel of Figure 6.3 that the e-correction is very sensitive both to the star-formation history of the galaxy as well as the metallicity as galaxies with some residual star formation as well as those at high metallicity have more negative e-corrections.

Figure 6.4 illustrates the rest-frame (g-r) and (r-i) colours of LRGs derived using the different spectral evolution models as a function of redshift. Once again it is seen that the Maraston model is able to reproduce the colours derived from SDSS composite spectra almost exactly unlike the Pegase model. However, note that unlike in Maraston *et al.* (2009), it is found that including the evolutionary correction to the Maraston models, creates a mismatch in the colours of the model and the SDSS composite spectra. The SDSS observed colours are found to be redder than the evolving Maraston model. It has already been noted that the SDSS LRG colour distribution is redder than that of the 2SLAQ galaxies used in Maraston *et al.* (2009) for comparison to their models so this difference is perhaps to be expected. It should also be noted that the observed colours derived from the spectra are derived from the fiber magnitudes of the galaxies. As the fibers only enclose
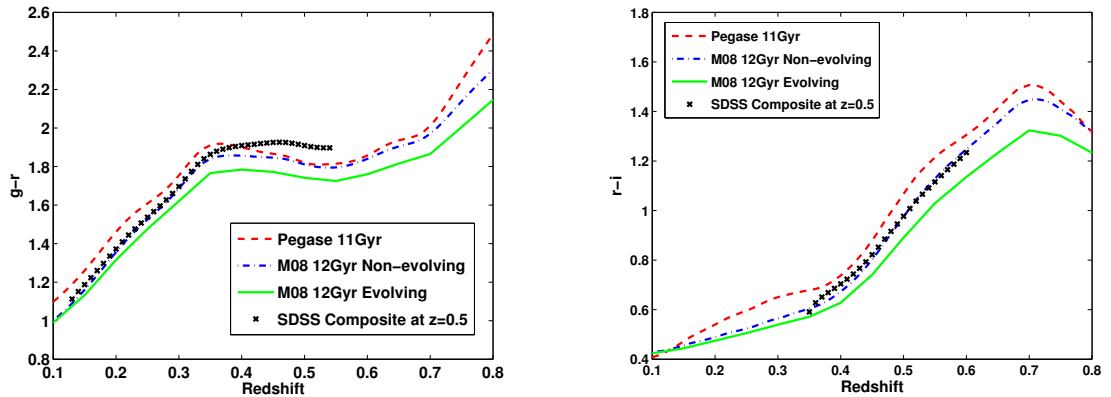
Figure 6.4: The (g-r) and (r-i) colours of LRGs as a function of redshift.

light within a 3" aperture and it is well known that early type galaxies have colour gradients (Vader *et al.* 1988; Franx & Illingworth 1990; Ferreras *et al.* 2005, 2009*a*), this could be why the colours appear redder but it is unlikely that this effect would be significant especially at redshifts of 0.5. Finally, the redshift 0.5 LRGs in the SDSS survey are the brightest and therefore expected to be the reddest galaxies in this survey (Bernardi *et al.* 2005; Gallazzi *et al.* 2006). All these factors may help explain the discrepancy in the observed and model colours derived using the evolving Maraston model.

Figure 6.5 shows the 2SLAQ LRGs in the observed (g-r) versus (r-i) colour-colour plane along with the main colour selection boundaries as well as the tracks produced in this plane by different stellar population synthesis models as well as SDSS composite spectra. It can be seen that both the Maraston as well as Pegase burst models only enter the $d_\perp$ selection at redshifts of $\sim$0.45. Star forming galaxies with $\tau > 2$Gyr are clearly excluded at all redshifts by the $c_\parallel$ selection.

6.4 The Optical Luminosity Function

The luminosity function for 2SLAQ LRGs is calculated in this section in order to infer any evolution in the observed number density of these objects. The non-parametric V_{max} estimator is used to calculate luminosity functions and a gaussian parametric form is fit to the V_{max} data points by means of a χ^2 minimisation where appropriate. The gaussian parametric form provides a better fit to the luminosity function of early-type galaxies compared to the more commonly used Schechter
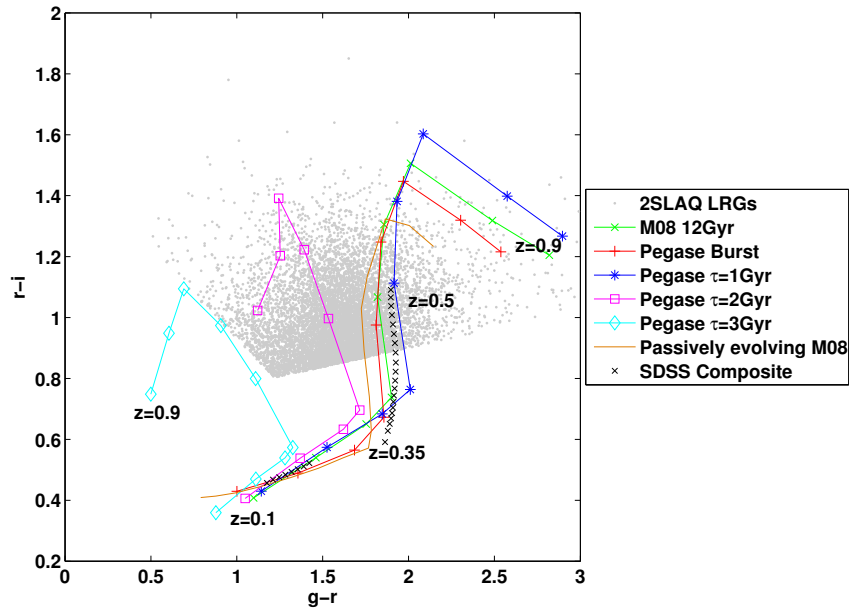
Figure 6.5: The (g-r) versus (r-i) colours of 2SLAQ galaxies in the observed frame along with tracks produced by several different stellar population synthesis models as well as composite LRG spectra from SDSS. In the case of the models, the markers are located at redshift intervals of 0.1. In the case of the SDSS composite spectrum, the markers are located at redshift intervals of 0.01.

function and has three free parameters, ϕ_*, M_* and σ_g. The parametric form is given by:

$$\Phi(M) = \frac{\phi_*}{\sigma_g \sqrt{2\pi}} \exp\left(\frac{-(M - M_*)^2}{2\sigma_g^2}\right).$$ (6.4)

The commonly used parametric estimator of Sandage *et al.* (1979) (STY hereafter) is prone to biases for this data set and therefore has not been presented in most of the figures. Details of the STY estimator and the biases induced on it are given in § 6.4.2.5.

The V_{max} estimator relies on measuring the maximum volume occupied by a galaxy given the survey selection criteria. For the 2SLAQ survey, this depends on the maximum redshift out to which the galaxy could be observed given the flux limit of $i_{dev} - A_i < 19.8$ as well as the minimum redshift at which the galaxy would be included in the survey given the $d_\perp$ and $c_\parallel$ colour selection criteria. The maximum volume for each galaxy is then given by:

$$V_{max} = \int_0^\infty S_{d_\perp}(z) S_{c_\parallel}(z) S_{i_{deV}}(z) \frac{dV}{dz} dz,$$ (6.5)

where $S_{d_\perp}(z)$, $S_{c_\parallel}(z)$ and $S_{i_{deV}}(z)$ are the selection functions for each galaxy due to the two primary colour cuts (Eq 6.1 and 6.2) and the flux limit (Eq 6.3). Once this maximum volume has been derived for every galaxy in the sample, the luminosity function which is simply the number density of galaxies per unit brightness, is given by:

$$\Phi(M)dM = c \sum_i \frac{1}{V_{max,i}}, \tag{6.6}$$

where c is the redshift completeness of the sample assumed to be 76.1% and the index, i runs over all galaxies in the absolute magnitude bin dM.

The errors on the luminosity function are assumed to be Poissonian unless otherwise stated and are given by:

$$\sigma_\Phi(M)dM = c \sqrt{\sum_i \frac{1}{V_{max,i}^2}}. \tag{6.7}$$

The best-fit parametric form is derived using a χ^2 fit to the V_{max} data points where appropriate. I marginalise over the normalisation, ϕ_* which is determined independently from the observed number density of galaxies. The marginalised χ^2 to be minimised is:

$$\chi^2_{marg} = \frac{\sum_j \sum_i \sigma_{V,i}^2 \Phi_{m,j} \Phi_{V,j} (\Phi_{m,i}\Phi_{V,j} - \Phi_{m,j}\Phi_{V,i})/\sigma_{V,j}^2}{\sum_j \Phi_{m,j}^2/\sigma_{V,j}^2}, \tag{6.8}$$

where Φ_m refers to the parametric luminosity function which is assumed to be a gaussian function and Φ_V represents the V_{max} data points with errors σ_V. Once the best fit parameters have been determined, the normalisation of the luminosity function, ϕ_* is then determined by matching the parametric estimate of the luminosity function to the observed number density of galaxies using Eq. 6.9.

$$\phi_* = \frac{N_g}{\int dz f_s \frac{dV}{dz} \int dM f(M,z) \Phi(M)}, \tag{6.9}$$

where N_g is the number of galaxies, f_s is the fraction of sky covered by the survey and $f(M,z)$ represents the colour selection function obtained by summing the product of $S_{d_\perp}(z)$ and $S_{c_\parallel}(z)$ over all galaxies in the sample. The errors on the gaussian parameters M_* and σ_g are calculated using the 1σ error ellipsoid obtained by performing the minimisation using a Markov Chain Monte Carlo (MCMC) method. The main sources of error on ϕ_* come from cosmic variance and the
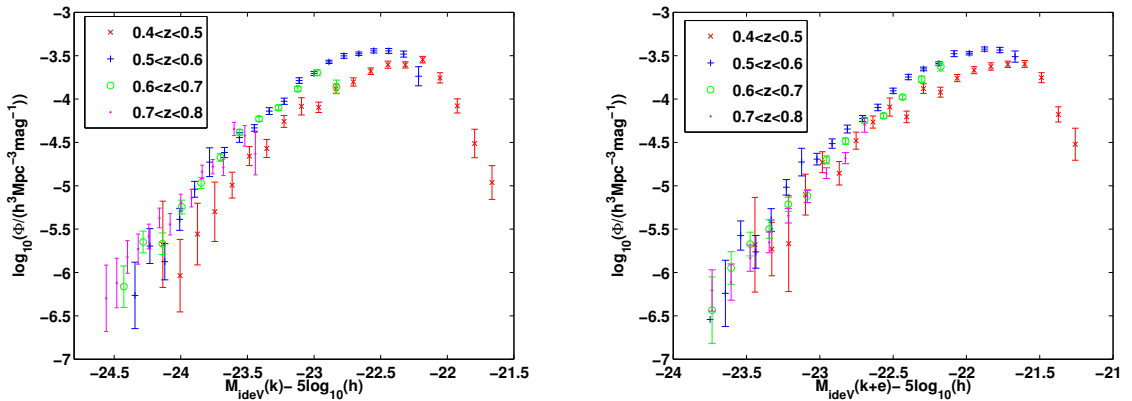
Figure 6.6: The 2SLAQ luminosity function at a rest-frame redshift 0 after k-correction (left) and k+e correction (right) assuming passive evolution.

covariance of ϕ_* with M_*. In § **??** I will show that for a large survey such as 2SLAQ, cosmic variance is unlikely to be a dominant systematic. The errors for ϕ_* quoted throughout this chapter are therefore calculated from the 1σ errors on M_*.

The dependance of the luminosity function on redshift is considered and possible sources of systematic errors to these estimates examined in this section.

6.4.1 Redshift Evolution

I examine the redshift evolution of the 2SLAQ LRG luminosity function in four redshift bins between redshift 0.4 and 0.8. The luminosity function estimates are obtained using the V_{max} estimator described above. Due to the different absolute magnitude ranges in each redshift bin, no χ^2 fits to the data points are shown as the inferred parameters would not be comparable.

In the left-hand panel of Figure 6.6 the luminosity function is plotted in four redshift bins after K correcting to redshift 0 using the 12Gyr Maraston composite model. The number density of galaxies is found to increase slightly with redshift particularly in the brightest absolute magnitude bins. In the faintest bins there is a drop in the observed number density due to the effects of downsizing in the star formation. The fainter galaxies are expected to be reside in less massive halos and therefore bluer due to their higher specific star formation rates and such objects are excluded from this sample by the colour selection criteria which only select out the reddest objects. It has also been seen in Figure 6.1 how the red sequence is truncated in the lowest redshift bin due to the redshift dependent colour selection. This is what leads to a drop in the number density in

the lowest redshift bin relative to the other bins which is not due to any evolution in the underlying galaxy population.

In the right-hand panel of Figure 6.6, the luminosity functions are plotted after correcting for passive evolution assuming the same Maraston model. The luminosity functions change little on inclusion of this evolutionary correction suggesting it is small in these redshift ranges but in general the data points for galaxies with $M_{ideV} < -22.5$ in the different redshift bins now agree better. As it is very likely that incompleteness does not affect this bright galaxy sample, these results suggest that this LRG population is evolving consistently with the assumptions of a passive evolution model.

6.4.2 Sources of Systematic Error

In this section I examine potential sources of systematic error that could bias the luminosity function estimates presented above.

6.4.2.1 Cosmic Variance

One of the main drawbacks of the V_{max} estimator is that it can suffer from biases due to cosmic variance. As massive galaxies such as the ones in this sample are thought to be strongly clustered, the evolution in their number density will be very sensitive to large-scale structure. Traditionally, this has posed a problem for many small surveys but the 2SLAQ survey should cover a significant enough volume to make this an unlikely source of problem for the LRGs being studied. In order to test this hypothesis, the LRG sample is split by declination to create two subsamples of galaxies with dec < -0.2 (4340 objects) and dec ≥ -0.2 (4285 objects) respectively. A luminosity function is then calculated for each of these subsamples as well as the total luminosity function for the 2SLAQ sample. These are plotted in Figure 6.7. No notable differences can be seen in the three luminosity function estimates confirming that cosmic variance is not a dominant systematic in this sample.

6.4.2.2 K+e Corrections: Spectral Evolution Model

In order to test whether the choice of spectral evolution model used to compute K+e corrections significantly affects the estimate of the luminosity function, luminosity functions are computed for all the 2SLAQ galaxies between redshift 0.4 and 0.8 using the 12Gyr Maraston composite model as well as a Pegase burst model, a Pegase model with an exponentially declining star formation
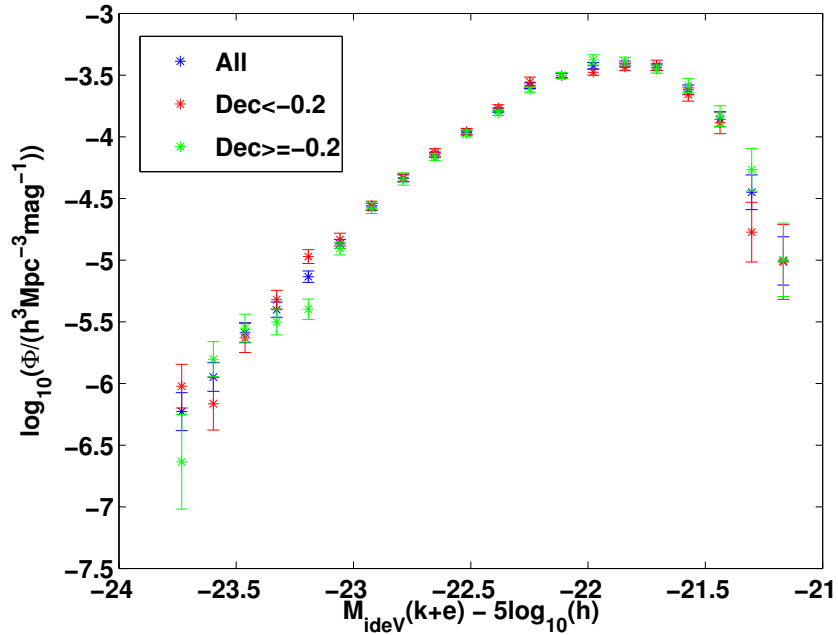
Figure 6.7: The 2SLAQ luminosity function calculated for the entire sample and in two different patches in the sky in order to assess the effects of cosmic variance.

history with $\tau = 1$Gyr and a CB07 model with an exponentially declining star formation history with $\tau = 1$Gyr. Both Pegase models have an age of 11Gyr while the CB07 model has a formation redshift of 3 corresponding to an age 11.35Gyr in the chosen cosmology. The results are illustrated in Figure 6.8 and the best-fit Gaussian parameters to these luminosity functions are summarised in Table 6.1. Both the Pegase burst and Maraston models have similar ages and star formation histories. The difference between them is the introduction of a metallicity poor sub-component to the Maraston model and the use of improved stellar librarires in order to better match the observed colours of LRGs. However, it can be seen from Figure 6.8 that there is very little difference in the luminosity function estimate obtained from using these two models.

The Pegase and CB07 models with $\tau = 1$Gyr produce very similar luminosity functions despite having different initial mass functions as the K+e corrections and therefore the luminosity function estimate is not very sensitive to the number of low mass stars. The main difference between the Salpeter IMF (assumed in the Pegase models) and the Chabrier IMF (assumed in the CB07 models) is the mass distribution for stars below $1M_{\odot}$. Changing the star formation history to have a little residual star formation shifts the luminosity function to slightly fainter absolute magnitudes and the number density in the brightest bins decreases. This is because including recent star formation
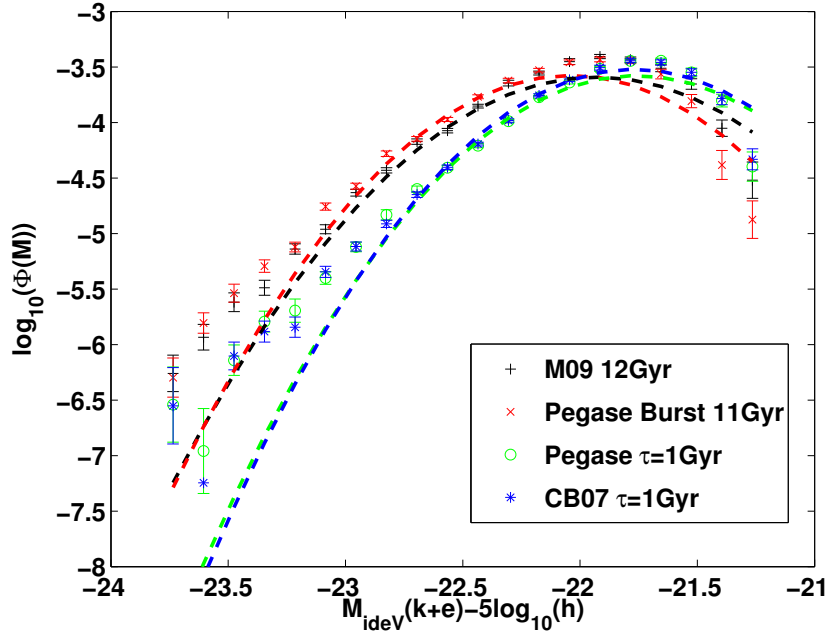
Figure 6.8: The 2SLAQ luminosity function computed using K+e corrections from different spectral evolution models along with the best χ^2 gaussian fits to these. Note that this simple Gaussian form does not adequately fit the bright-end of the luminosity function for some of the data points.

	σ_g	M_*	$\phi_*/\mathrm{h^3Mpc^{-3}mag^{-1}}$
Maraston 12Gyr	0.44 ± 0.01	-21.93 ± 0.03	$3.73 \pm^{0.24}_{0.23} \times 10^{-4}$
Pegase Burst 11Gyr	0.41 ± 0.01	-22.04 ± 0.03	$3.59 \pm^{0.22}_{0.20} \times 10^{-4}$
Pegase τ=1Gyr	0.41 ± 0.01	-21.76 ± 0.03	$3.58 \pm^{0.25}_{0.23} \times 10^{-4}$
CB07 τ=1Gyr	0.40 ± 0.01	-21.77 ± 0.03	$3.98 \pm^{0.28}_{0.25} \times 10^{-4}$

Table 6.1: Summary of best-fit gaussian parameters to the luminosity function derived using different spectral evolution models

or younger stars in the model means that the luminosity of the galaxy evolves faster and the galaxy fades quicker than in a purely passive evolution scenario.

6.4.2.3 K+e Corrections: Metallicity

The colour-magnitude relation (CMR) of early-type galaxies can be interpreted as a metallicity sequence and variations in the metallicity, ξ, dominate the slope of the CMR (Kodama & Arimoto 1997; Bower *et al.* 1992). The metallicity may therefore be an important parameter to vary in stellar population synthesis models when trying to model the spectral evolution of LRGs. In order to assess the importance of metallicity in the luminosity function estimate, luminosity functions are calculated after K+e correcting galaxies using a CB07 model at solar metallicity as well as one with variable metallicity. Both assume a formation redshift of 3 and an exponentially declining star formation history with a timescale, τ of 1Gyr. In the variable metallicity model, the metallicities are derived from the absolute magnitudes using the colour-magnitude relation of early-type galaxies in the Virgo Cluster from Bower *et al.* (1992):

$$\log_{10}\left(\frac{Z}{Z_\odot}\right) = -0.11(M_i + 21.0) - 0.18. \tag{6.10}$$

The effect of metallicity on the luminosity function estimate is illustrated in Figure 6.9. It is obvious from this figure that the metallicity is not likely to be important in the evaluation of the luminosity function for the 2SLAQ LRGs studied here. The LRGs are all found to have metallicities between 0.6 and 1.5 $Z_\odot$ with a mean metallicity of roughly solar.

6.4.2.4 K+e Corrections: Age

Figure 6.10 plots the V_{max} estimate of the luminosity function after K+e corrections to redshift 0 assuming a Pegase single burst model at three different ages ranging from 9 to 11Gyr. In the cosmological model assumed throughout this thesis, these correspond to formation redshifts for the galaxy of between ~ 1.4 and 2.6.

It is obvious from Figure 6.10 that changing the formation redshift of the galaxy to later times results in the luminosity function moving to fainter absolute magnitudes or alternatively, a decrease in the number density at a given absolute magnitude. As is the case for models with some residual star formation, the introduction of younger stars into the models means that they fade quicker thereby shifting the luminosity function estimate to fainter absolute magnitudes.
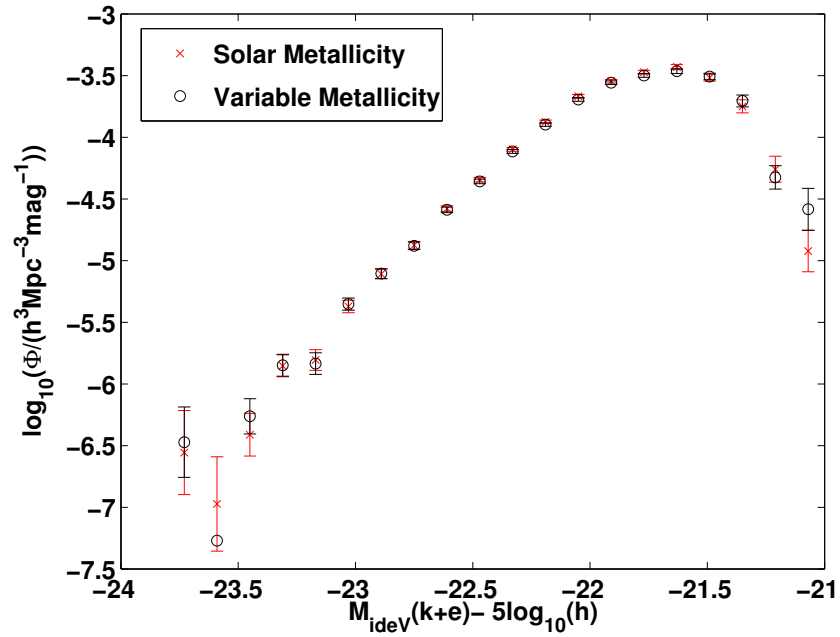
Figure 6.9: The 2SLAQ luminosity function calculated using spectral evolution models with solar and variable metallicity.
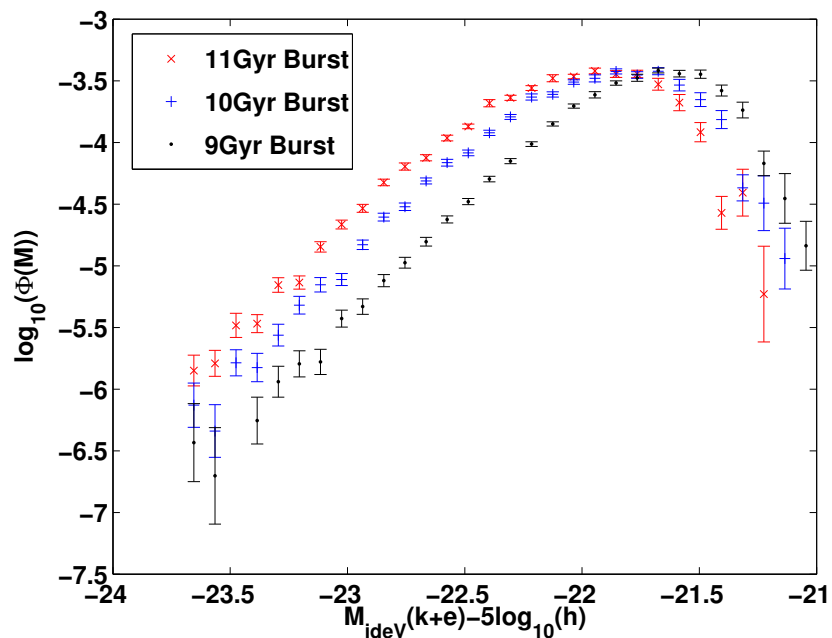
Figure 6.10: The 2SLAQ luminosity function calculated using spectral evolution models of different ages.

6.4.2.5 Photometric Errors and The STY Estimator

In order to assess the bias that photometric errors will introduce into the luminosity function estimate, the LRG sample is cut at $i < 19.3$ and the luminosity function is calculated for this reduced sample of galaxies. Note that in § 6.2.1 I have already drawn attention to the fact that previous studies (Wake *et al.* 2006) have shown that fainter than $i = 19.3$, galaxies selected through single and multi-epoch photometry start differing considerably from each other suggesting that photometric errors are significant. However, cutting the sample according to the SDSS g, r, i-band magnitude errors results in a very different sub-sample to that obtained through the i-band cut suggesting that the magnitude errors quoted are not entirely reliable in removing galaxies with large photometric errors and it is therefore essential to have multi-epoch data for these purposes.

The luminosity functions for the entire sample as well as the $i < 19.3$ sample are plotted in Figure 6.11 along with the best χ^2 gaussian fits to the data points. The $i < 19.3$ sample has 2131 galaxies as opposed to the 8625 galaxies in the entire sample. The space densities from the $i < 19.3$ sample have been renormalised by the inverse of the fraction of galaxies in the complete sample that contribute at each absolute magnitude bin. The χ^2 fit to the reduced sample with small photometric errors yields values of $\sigma = 0.61 \pm 0.05$, $M_* = -21.49 \pm 0.17$ and $\phi_* = 5.95 \times 10^{-4}$ where the normalisation for the $i < 19.3$ sample has also been corrected for the smaller space density of this sample. In this case however, a constant average correction factor is used rather than the absolute magnitude dependent corrections applied to the V_{max} data points in order to ensure that the shape of the gaussian is maintained. The χ^2 fit to the entire sample on the other hand gives $\sigma = 0.44 \pm 0.01$, $M_* = -21.93 \pm 0.03$ and $\phi_* = 3.73 \times 10^{-4}$.

As can be seen, faint galaxies are removed from the sample on applying the i-band cut, as they typically have larger photometric errors. The χ^2-fits to the two samples also yield very different values for the parameters of the gaussian and the faint-end downturn due to incompleteness is no longer present in the reduced sample with small photometric errors. This tells us that the K+e corrected luminosity function estimates are only reliable brighter than $M_{ideV} \sim -21.75$ where the space density for the entire sample matches that of the sample with small photometric errors. However, throughout this chapter the luminosity and mass functions are presented for the entire sample of galaxies although readers should note that the data points in the faintest magnitude bins may suffer highly from incompleteness and photometric errors.

It has already been seen that the faintest galaxies in the sample suffer from large photometric errors. In Figure 6.12 these faintest galaxies with $M_{ideV} > -21.75$ are plotted in the observed
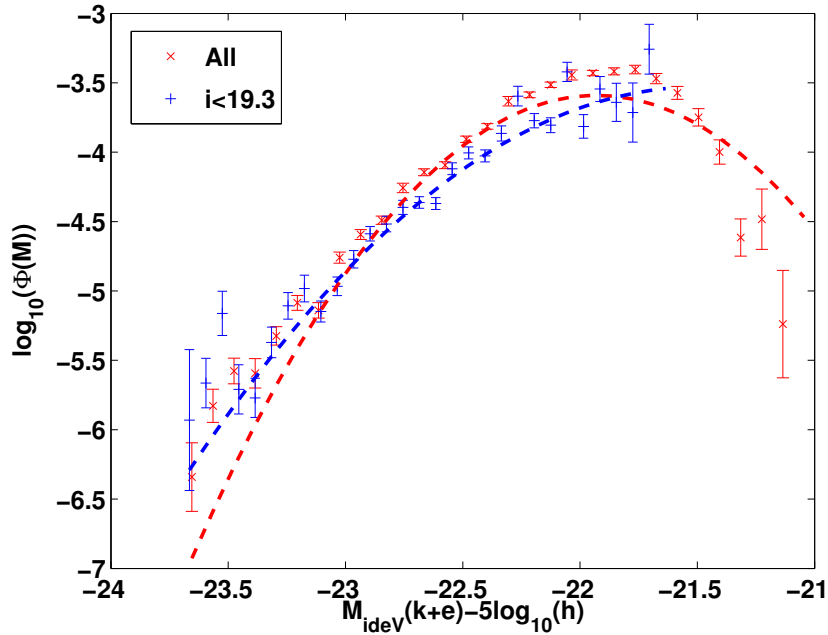
Figure 6.11: The 2SLAQ luminosity function calculated for the entire sample and galaxies with $i < 19.3$ for which photometric errors are thought to be insignificant along with the best χ^2 gaussian fits to these.

colour-colour plane. These galaxies are also the lowest redshift galaxies in the sample. It can immediately be seen that these faint galaxies occupy fairly large volumes and do not all lie as one would expect, close to the colour selection boundaries. In particular, the objects seem to be scattered away from the $c_\parallel$ selection boundary. These faint galaxies are clearly being scattered into the sample and away from the colour selection boundaries due to photometric errors. Comparing Figure 6.12 to Figure 6.5, it can also be seen that the location of these faint, low-redshift galaxies in the colour-colour plane is inconsistent with the predictions of a Maraston model which would only enter the 2SLAQ colour boundaries at a redshift of ~0.45. These faint galaxies are in fact not LRGs at all but happen to have similar colours to LRGs due to the photometric errors. Many of their spectra show evidence for the presence of strong emission lines suggesting that they are star-forming and this has already been found by Roseboom et al. (2006). However, as these galaxies are scattered to large volumes, the V_{max} estimator remains relatively insensitive to differences in the selection function that would arise if it was inferred using late rather than early-type spectral evolution models as seems appropriate for these objects. Therefore the V_{max} estimator remains reliable despite the photometric errors in the sample.
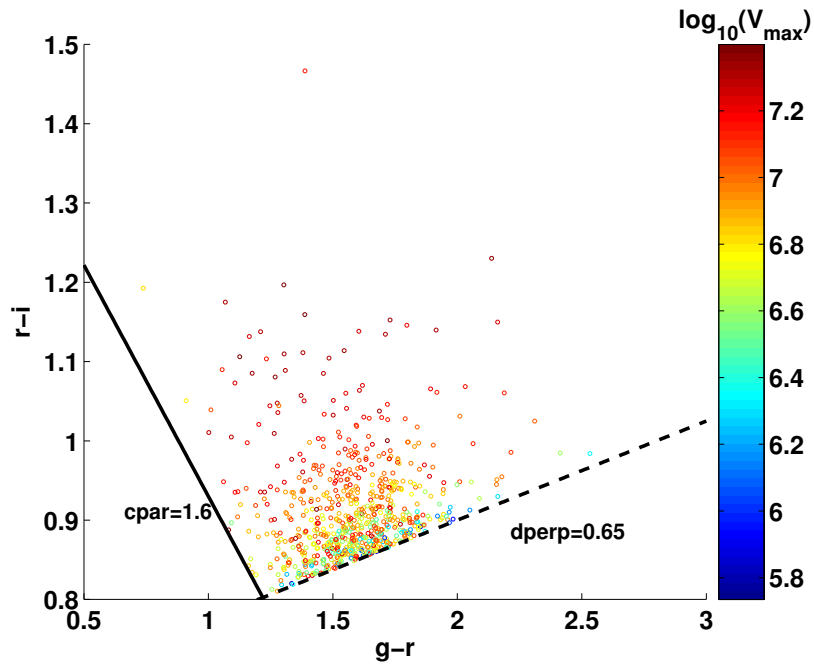
Figure 6.12: The faintest 2SLAQ LRGs with $M_{ideV} > -21.75$ in the observed colour-colour plane. The points are colour-coded according to the V_{max} of the objects calculated assuming the 12Gyr Maraston template.

The most common parametric estimator of the luminosity function is that of Sandage *et al.* (1979) (STY). A parametric form is assumed for the luminosity function e.g. a gaussian as in this chapter. The parameters, **a** are then solved for by maximising the likelihood:

$$\mathcal{L}(\mathbf{a}) = \prod_{\mathbf{i}} \mathbf{p_i}, \tag{6.11}$$

where p_i is the probability of a galaxy with absolute magnitude, M being selected in the flux limited, colour cut sample and is given by Eq 6.12

$$p_i = \frac{\Phi(M_i, \mathbf{a})\mathbf{f}(\mathbf{M_i}, \mathbf{z_i})}{\int \Phi(M, \mathbf{a})\mathbf{f}(\mathbf{M_i}, \mathbf{z_i})\mathbf{dM}}, \tag{6.12}$$

where $f(M_i, z_i)$ is the apparent magnitude incompleteness function for objects with absolute magnitude, M_i and redshift, z_i. This incompleteness occurs due to various reasons. Firstly, not all galaxies targetted in a survey will have redshifts determined succesfully. Wake *et al.* (2006) have considered this incompleteness function for 2SLAQ LRGs using carefully constructed 2SLAQ survey masks. Although they find a slight dependance of this incompleteness function on the (g-r)
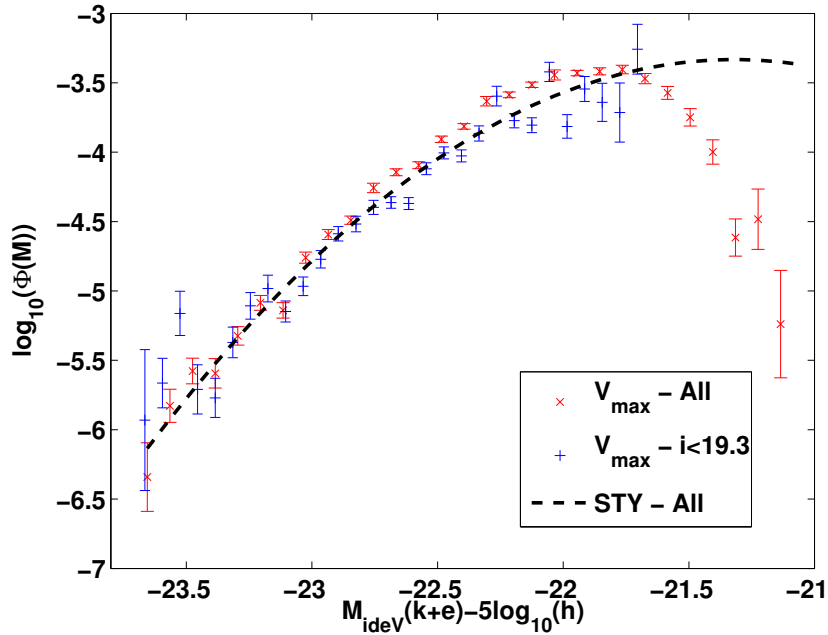
Figure 6.13: The non-parametric V_{max} data points for the LRGs in the entire sample as well as the sample with small photometric errors and $i < 19.3$ along with the STY gaussian fit for the entire sample.

colour, including this functional dependance as opposed to considering a constant incompleteness of 76.1% introduces less than a 1% change in their luminosity function estimate. I therefore assume a constant redshift incompleteness of 76.1% that is independent of both the redshift and the absolute magnitude.

In the case of a colour-selected sample such as 2SLAQ however, there may be additional sources of incompleteness as the space density of these galaxies is a function of both the flux limit and the colours. The 2SLAQ LRGs at different redshifts occupy different distributions in the colour absolute magnitude plane due to the redshift dependent colour selection. This colour selection could introduce an incompleteness function that is both a function of absolute magnitude as well as redshift and this selection function has to be explicitly included in the integral in Eq 6.12. I have checked that using the absolute magnitude averaged selection function rather than the 2d function $f(M_i, z_i)$, makes very little difference to the STY estimate of the luminosity function. In this case, the galaxy incompleteness can be taken outside the integral and the likelihood in the

STY method adjusted directly e.g. (Zucca *et al.* 1994; Willmer et al. 2006).

$$\mathcal{L}(\mathbf{a}) = \prod_{\mathbf{i}} \mathbf{p_i^{w_i}},$$ (6.13)

where the weights associated with each individual galaxy are $w_i = 1/S(m_i)$ and $S(m_i)$ represents the apparent magnitude incompleteness for galaxy i. All luminosity functions are initially calculated assuming $w_i = 1$ for the entire sample and this is shown by the dashed line in Figure 6.13. This clearly illustrates that the V_{max} and STY estimators differ considerably from each other at the faint-end. The STY fit parameters are $M_* = -21.32, \sigma = 0.65, \phi_* = 9.97 \times 10^{-4}$ for the entire sample. Figure 6.13 also illustrates that this STY fit matches well all the V_{max} data points for the sample with small photometric errors and $i < 19.3$ introduced earlier. It has already been noted that fainter than $i \sim 19.3$, photometric errors may become significant in scattering LRGs both in and out of the colour selection boundaries thereby rendering the luminosity function estimate unreliable. This analysis therefore suggests that the STY estimator is particularly sensitive to photometric errors for colour selected samples and the weights w_i start to differ significantly from 1 for galaxies with large photometric errors. In order to calculate these weights, one would have to do a Monte Carlo simulation of galaxies assuming a certain spectral evolution model, add noise to this simulation and then look at the completeness function $S(m_i)$ for each galaxy by considering which galaxies are selected on applying the 2SLAQ colour selection criteria e.g. (Fried *et al.* 2001; Wolf *et al.* 2003). This is the subject of future work. The STY estimator in its traditional form is clearly biased for a colour-selected sample with non-negligible photometric errors and for this reason, it has not been presented in most of the plots in this chapter. Note however that when we move to high redshift bins where the galaxies are generally brighter and the photometric errors smaller, the STY estimator and V_{max} estimator agree very well as it is clearly reasonable in these regimes to assume $w_i = 1$.

6.5 The Infra-Red Luminosity Function and Stellar Mass Function

So far this study has considered the evolution of the 2SLAQ LRG optical luminosity function with redshift and quantified various sources of systematic error that could arise for this estimate. This analysis shows little evidence that the LRG population evolves beyond that expected from a simple passive evolution model between a redshift of 0.4 and 0.8. However, such an analysis does not fully exploit all the available information as the evolution of elliptical galaxy populations is
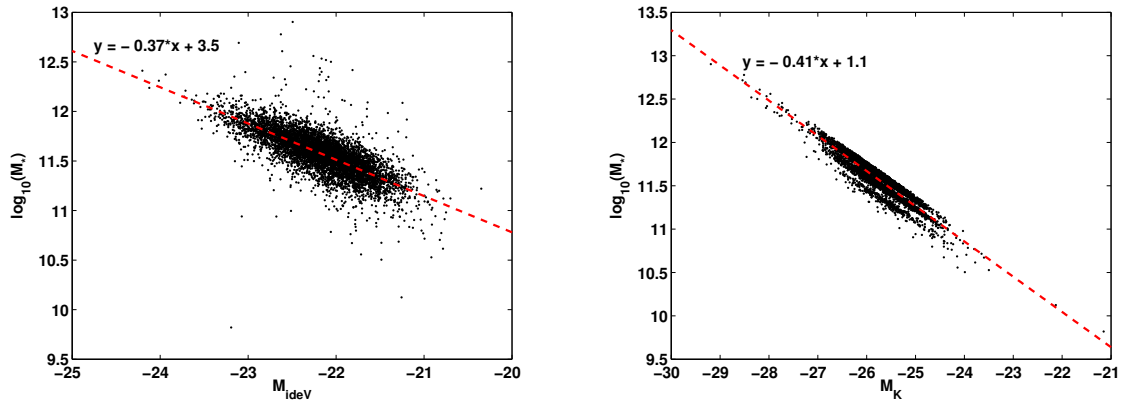
Figure 6.14: The relationship between the SDSS deVaucouleurs i-band absolute magnitude and stellar mass (left) and the UKIDSS Petrosian K-band magnitude and stellar mass (right). The gradients of the straight line fits give some indication of the stellar mass-to-light ratio.

known to be a strong function of mass (De Lucia *et al.* 2006; Cimatti *et al.* 2006; Ferreras *et al.* 2009*b*). The availability of near infra-red data for a sizeable subsample of these LRGs means we can calculate accurate stellar masses for these objects from their K-band luminosities in order to study the evolution of the stellar mass function of these galaxies.

The mass function analysis in this section is carried out for the subset of LRGs for which near infra-red photometry is available from UKIDSS DR5. This reduced sample contains 6476 galaxies. As the Maraston models do not extend to near infra-red wavelengths, the CB07 models have been used in this section to calculate the mass-to-light ratios for the LRGs. Following Ferreras *et al.* (2009*b*), the stellar masses are computed by comparing the SDSS g, r, i, z fiber magnitudes with a set of 10 τ-models with solar metallicity, formation redshifts of 3 and exponential timescales between 0 (i.e. corresponding to a Simple Stellar Population) and 10Gyr. The CB07 models are used to generate the composite populations. The best-fit model, almost always corresponding to short formation timescales, is then used to determine the mass-to-light ratio in the K-band of the UKIDSS survey assuming a Chabrier or Salpeter IMF. This best-fit along with the K-band Petrosian magnitude allows us to determine the stellar mass of the galaxy. Note that no total model magnitudes are available in the UKIDSS survey. However, the difference between the total model magnitudes in the SDSS i-band and the Petrosian magnitudes in the same band are found to be of the order of 15%. Both magnitudes can be used as reasonable estimates for the total light from the galaxy.

The relationship between both the SDSS deVaucouleurs i-band absolute magnitude as well
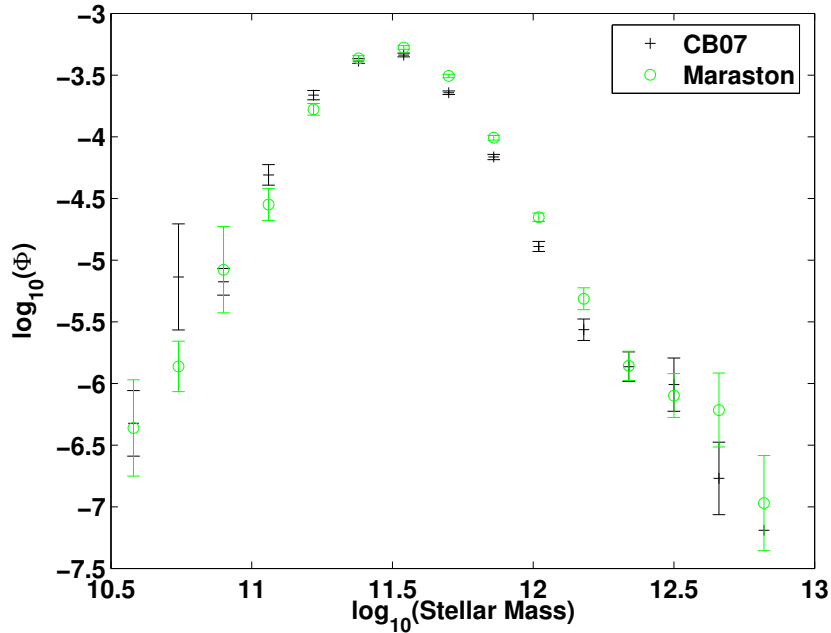
Figure 6.15: The 2SLAQ mass function calculated using the V_{max} method when V_{max} is evaluated using a single Maraston model of age 12Gyr for all the LRGs and when V_{max} is evaluated using the best-fit CB07 τ model for each LRG.

as the UKIDSS Petrosian K-band absolute magnitude and the stellar mass is illustrated in Figure 6.14. The mass functions are calculated as before using the V_{max} method described in detail in § 6.4. The difference in the mass function when V_{max} is determined using the best-fit CB07 models as opposed to a single Maraston model of age 12Gyr, is illustrated in Figure 6.15. From this figure, it can be seen that the difference is minimal when using the two different spectral evolution models. Note, however that this may not remain the case if stellar masses could be calculated directly from the Maraston models as well as determining V_{max} from it.

The mass function for the 2SLAQ LRGs in two redshift bins - $0.4 \leq z < 0.55$ and $0.55 \leq z < 0.8$ - is illustrated in the left-hand panel of Figure 6.16. These redshift limits have been chosen so as to ensure that incompleteness does not affect the high-mass end in either of these bins. On this plot, I also show the mass functions derived in two redshift bins for red sequence galaxies in the COMBO-17 survey (from Figure 9 of Borch *et al.* (2006)). For illustrative purposes, the 2SLAQ K-band luminosity function has been plotted in the two redshift bins in the right-hand panel of Figure 6.16. The K-band absolute magnitudes are also determined using the best-fit CB07 model for each LRG and after correcting to the AB system using the correction of Hewett *et al.* (2006).
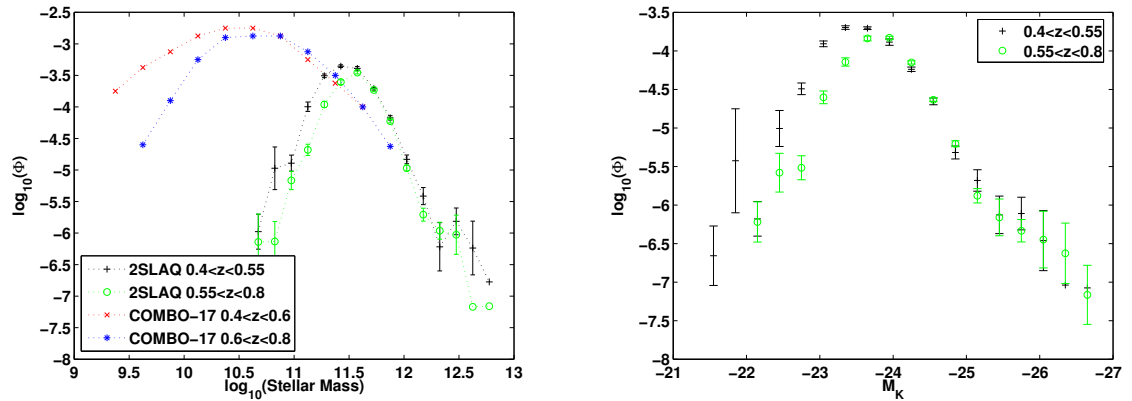
Figure 6.16: The 2SLAQ stellar mass function in two redshift bins of - $0.4 \leq z \leq 0.55$ and $0.55 \leq z \leq 0.8$ along with the COMBO-17 red sequence stellar mass functions in redshift bins $0.4 \leq z \leq 0.6$ and $0.6 \leq z \leq 0.8$ from Borch *et al.* (2006). The right-hand panel shows the 2SLAQ K-band luminosity function in the same two redshift bins.

Figure 6.16 clearly shows that the 2SLAQ data set extends to much higher stellar masses than the COMBO-17 survey occupying a very different stellar mass range to the COMBO-17 red sequence and thereby allowing us to effectively probe the high-mass end of the mass function. These most massive galaxies are the ones expected to place the most stringent constraints on current models of galaxy formation. As is the case with the COMBO-17 data, there is little evidence for any evolution in the number density at the high-mass end between a redshift of 0.4 and 0.8. This is consistent with the findings of Ferreras *et al.* (2009*b*) who find that the number density does not evolve in the highest stellar mass bins. Below $\sim 10^{11} M_\odot$ however, this sample is likely to be highly incomplete due to the redshift dependent selection criteria involved in isolating LRGs.

The discrepancy between the 2SLAQ mass function presented in this chapter and the COMBO-17 mass function of Borch *et al.* (2006) may arise due to the differing choices of IMF used in the two studies. While this study uses the Chabrier (2003) IMF, Borch *et al.* (2006) use a truncated version of the Salpeter (1955) IMF to calculate stellar masses. In order to estimate how this would affect the mass function estimate, in Figure 6.17 I plot the 2SLAQ mass function over the entire redshift range of $0.4 \leq z < 0.8$ calculated using both the Salpeter and Chabrier IMF. The Salpeter IMF pushes the mass function towards higher masses and this results in a bigger discrepancy between the COMBO-17 and 2SLAQ data points. It is well known that the simple power-law form of the Salpeter IMF overestimates the number of low-mass stars in galaxies and therefore the stellar mass (Cappellari *et al.* 2006; Ferreras *et al.* 2008) and more recent analytical forms of
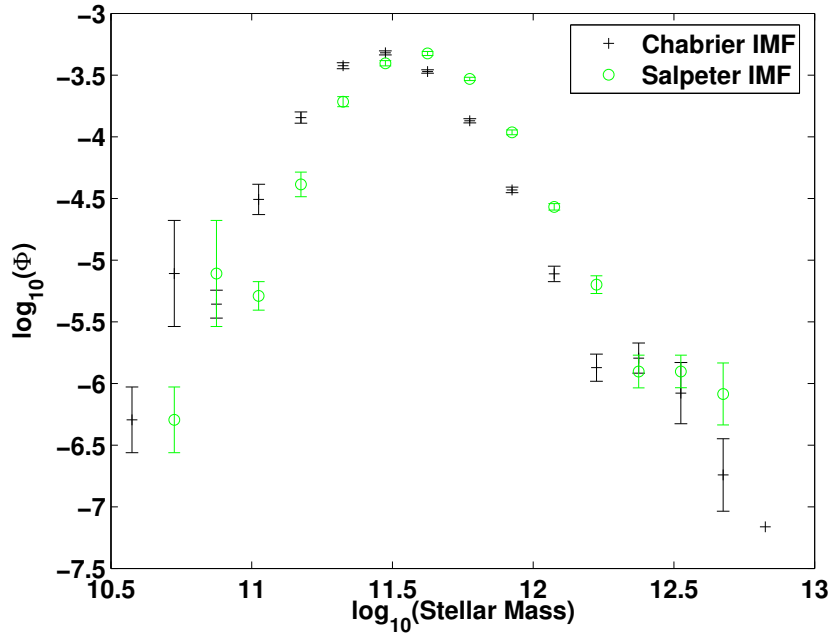
Figure 6.17: The 2SLAQ mass function calculated using the V_{max} method over the redshift range $0.4 \leq z < 0.8$ when using a Salpeter and a Chabrier IMF.

the IMF such as those of Chabrier (2003) have fewer low-mass stars and therefore predict lower stellar masses. In Chapter 7, I look at an alternative means of determining the number of low-mass stars in different extragalactic systems.

The increased number density of 2SLAQ galaxies seen at $\sim 3 \times 10^{11} M_\odot$ to $\sim 10^{12} M_\odot$ where it overlaps with COMBO-17 could be due to various reasons. Firstly, the COMBO-17 area is much smaller than that of 2SLAQ and so it is possible that there could be some incompleteness at the high-mass end of the COMBO-17 red sequence mass function due to the effects of cosmic variance. More likely however, the discrepancy probably arises due to the complicated selection of LRGs which makes it difficult to obtain a proper estimate of the volume probed. As the LRGs are selected through colour cuts in addition to the flux limit and the colour cuts remove the volume at low redshifts, the 2SLAQ galaxies will on average have a smaller V_{max} then a flux-limited sample such as COMBO-17. This will result in a larger inferred number density at any given mass.

6.6 Discussion

In this chapter I have presented luminosity and stellar mass function estimates for a sample of 8625 Luminous Red Galaxies with spectroscopic redshifts between 0.4 and 0.8 in the 2SLAQ survey. The evolution of the optical luminosity function between redshift 0.4 and 0.8 is found to be consistent with the assumptions of a passively evolving model with very little evidence for recent star formation. The number density of LRGs shows a downturn at faint magnitudes due to the effects of downsizing in the star formation whereby the less massive galaxies which are also less luminous, are bluer and therefore excluded from an LRG sample by the imposed colour selection criteria which select the reddest objects. There is also some evidence that the faint galaxies are scattered into the sample due to their non-negligible photometric errors.

The sensitivity of the optical luminosity function to changes in the spectral evolution models has also been studied. The results of this analysis are summarised in Figure 6.18 where I show the best gaussian fit parameters to the V_{max} data points for LRGs when the luminosity function is computed assuming different spectral evolution models. M_* is found to move towards brighter absolute magnitudes if a Pegase burst model is assumed instead of the Maraston model, and towards fainter magnitudes if one assumes a model with some residual star formation signified by a star formation timescale of $\tau = 1$Gyr. The width of the gaussian is also found to be slightly larger when using the Maraston models.

The K-band luminosity function is calculated for about three quarters of the LRGs for which infra-red data is available from the UKIDSS LAS DR5. The K-band luminosity function also shows little evidence for evolution in this redshift range. The K-band luminosities are used to derive mass-to-light ratios for the LRGs by fitting CB07 spectral evolution models to the multi-band optical photometry. These are then used to calculate mass functions in redshift bins. Using the best-fit CB07 model instead of the Maraston models in the estimate of the mass function, makes very little difference to the mass function. It is found that the most massive galaxies with $M > 3 \times 10^{11} M_\odot$ are already well assembled at redshifts of 0.8 and their number density does not change much in the redshift range considered in this work.

The 2SLAQ sample probes the most massive end of the mass function and can therefore be used to place stringent constraints on models of massive galaxy formation and evolution. In Figure 6.19 I plot the comoving number density of 2SLAQ galaxies as a function of redshift obtained by integrating the mass functions presented in Figuure 6.16. Note that the horizontal errorbars simply represent the size of the redshift bin in our plots. Only galaxies with $3 \times 10^{11} M_\odot < M < 10^{12} M_\odot$
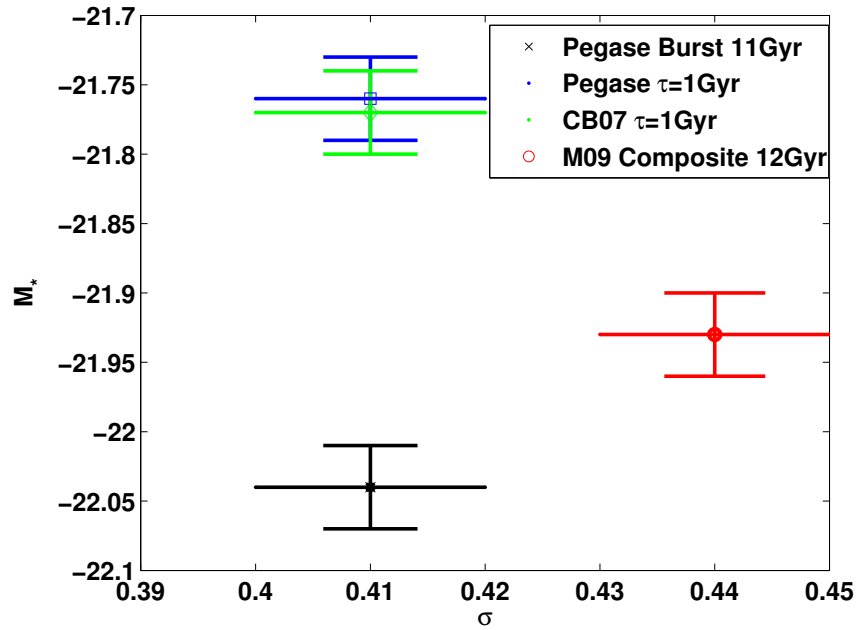
Figure 6.18: Summary of best-fit gaussian parameters assuming different spectral evolution models.

are chosen for which the redshift dependent selection criteria do not impose any incompleteness into the sample. The estimates of the comoving number density are compared with those from other surveys of massive galaxies as well as predictions from models of galaxy formation. All data points presented in this figure have been corrected to the Chabrier IMF. Table 6.2 summarises the samples plotted in Figure 6.19. The unique position of 2SLAQ among these surveys can immediately be seen. Due to the large volume this data set occupies, the vertical errorbars in Figure 6.19 are significantly reduced as compared to other massive galaxy samples.
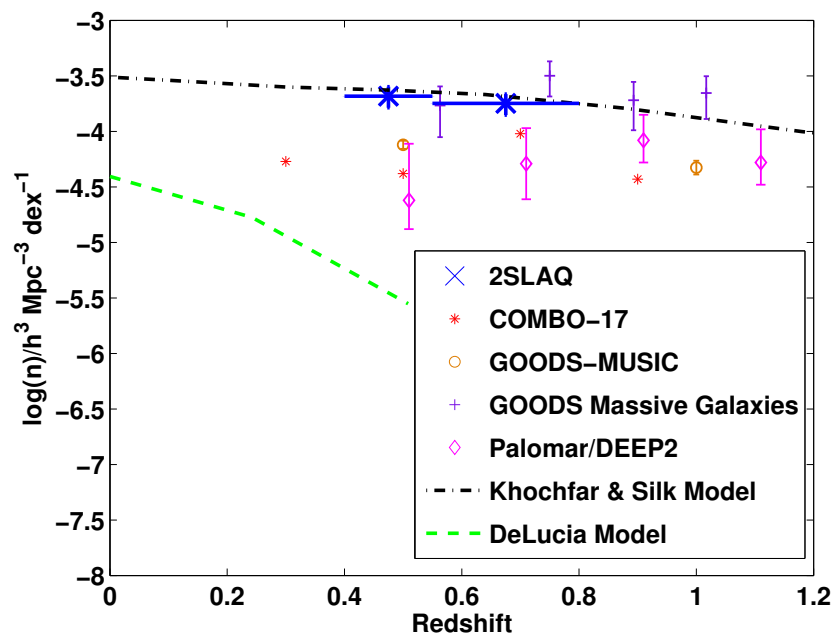
Figure 6.19: The comoving number density of massive galaxies as a function of redshift for the 2SLAQ survey - found by integrating the mass functions presented in Figure 6.17 upwards of $3 \times 10^{11} M_\odot$ along with the comoving number density from other surveys of massive galaxies as well as models of galaxy formation.

	Redshift Range	Area	Number of Galaxies	Selection
2SLAQ[1]	0.4 - 0.8	186.2 deg^2	8625	Luminous Red Galaxies
COMBO-17[2]	0.2 - 1.0	1.0 deg^2	~25,000	All Galaxies
Palomar/DEEP2[3]	0.4 - 2.0	1.36 deg^2	4571	K-band selected galaxies with M$> 10^{11} M_\odot$
GOODS-MUSIC[4]	0.0 - 4.0	143.2 arcmin^2	2931	K-band selected galaxies
GOODS Massive Galaxies[5]	0.4 - 1.2	320 arcmin^2	457	Visually classified ETGs

Table 6.2: Summary of Massive Galaxy Samples for which stellar mass functions have been calculated - [1]This Work, [2]Borch *et al.* (2006), [3]Conselice *et al.* (2007), [4]Fontana *et al.* (2006), [5]Ferreras *et al.* (2009b).

From Figure 6.19 it can be seen that this work agrees well with that of Borch *et al.* (2006); Conselice *et al.* (2007) and Ferreras *et al.* (2009*b*) and shows that the most massive galaxies were already well assembled at redshift 0.8 and there is little evidence for their number density having changed since then. Fontana *et al.* (2006) on the other hand find some evolution in the number density of massive galaxies with redshift albeit mild up to redshifts of $\sim$1.5. The differing comoving number densities for the different samples can be attributed to the fact that these samples have all been selected in very different ways as summarised in Table 6.2. However, it is encouraging that the comoving number density for this colour selected sample of LRGs agrees well with that inferred from the visually classified sample of Ferreras *et al.* (2009*b*).

These observational results seem to match well the predictions from the semi-analytical models of Khochfar & Silk (2006) which are better at reproducing observations at moderate redshifts but fail at low redshifts. These models follow the merging history of dark matter halos generated by the extended Press-Schechter formalism. The baryonic physics is modeled according to the prescriptions of Khochfar & Burkert (2005) and references therein. This model predicts that the number density of massive galaxies is almost constant upto redshifts of $\sim$1 as the number of galaxies entering a given mass bin from lower mass bins through mergers is counteracted by the number of galaxies leaving this mass bin for higher mass bins. If this were the case, one would expect the number density of galaxies in the highest mass bin to decrease as a function of redshift even if it is constant in the intermediate mass bins. The comoving number density is therefore computed in the higher mass bin of $12 < \log_{10}(M_*) < 12.5$ and in the same two redshift bins - $0.4 \leq z < 0.55$ and $0.55 \leq z < 0.8$. The number densities per unit dex in stellar mass thus obtained are $\log(n)/h^3$ Mpc^{-3} dex$^{-1} = -5.39^{+0.10}_{-0.13}$ and $\log(n)/h^3$ Mpc^{-3} dex$^{-1} = -5.56^{+0.08}_{-0.09}$ respectively. Therefore there is no evidence that the comoving number density of the most massive galaxies is decreasing with increasing redshift. The agreement between the 2SLAQ data points and the Khochfar & Silk (2006) models shown in Figure 6.19 should therefore be treated with caution as the constant number density of massive galaxies in the models, is only maintained due to a fine-tuning of objects between mass bins and these observations find no evidence that this fine-tuning actually occurs.

The results also do not match at all those generated from models based on the Millennium simulations (De Lucia *et al.* 2006) which predict a much lower merger rate at moderate redshifts as compared to the Khochfar & Silk (2006) models. In the Millennium models, AGN feedback is invoked to shut off star formation after a characteristic mass scale in order to reproduce the observed colour-bimodality and luminosity function at redshift 0. The Khochfar & Silk (2006) models presented here overpredict the number of massive late type galaxies in the local Universe.

Due to AGN feedback in the De Lucia *et al.* (2006) models, the downsizing in star formation is reproduced but the growth of massive galaxies at high redshifts of greater than 0.5 is prohibited and dry mergers become the most dominant mechanism for mass growth in such galaxies. This is clearly inconsistent with our observations which suggest not only that significant star formation in massive galaxies has ceased at a redshift of 0.8 but also that these galaxies were already well assembled at these redshifts. The difference between the De Lucia *et al.* (2006) and Khochfar & Silk (2006) models arise due to the differing star formation prescriptions rather than the fact that the former follows a numerical simulation for the evolution of the dark matter halos whereas the latter relies on an analytical approach. Therefore the star formation and quenching mechanisms invoked in the different galaxy formation models need to be revisited in light of these new constraints on the very high mass end of the stellar mass function.

Granato *et al.* (2004) on the other hand have proposed a way in which to bring about the anti-hierarchical formation of the baryonic component of galaxies in models while still working within the framework of the ΛCDM cosmology. This is essentially done by invoking feedback from supernovae as well as the nuclear activity in massive galaxies. These processes slow down star formation in the least massive halos and drive gas outflows thereby increasing the stellar to dark matter ratio in the more massive halos and ensuring that the physical processes acting on baryons are able to effectively reverse the order of formation of galaxies compared to dark matter halos. These models have already been shown to match the local K-band luminosity function of massive galaxies (Granato *et al.* 2004) as well as the luminosity function at redshifts of $\sim$1.5 (Granato *et al.* 2004; Silva *et al.* 2005). Reproducing our observational results for the most massive galaxies at intermediate redshifts would therefore be an important test for these models.

Recently Dekel *et al.* (2009) have also proposed an alternative galaxy formation model whereby bursts of star formation can occur in massive galaxies without the need for violent merging events. These authors suggest that the massive galaxies, which reside in the centers of filaments, are fed by cold gas streams that penetrate the shock heated media of massive dark matter halos thereby inducing star formation.

Given the small errorbars in these estimates of the comoving number density compared to previous studies and the fact that this sample has secure spectroscopic redshifts for all objects and a massive area that reduces errors due to cosmic variance, this new observational result presents a significant challenge for many current models of galaxy formation and requires a reinvestigation of the feedback mechanisms involved.

6.7 Conclusion

This study has examined the evolution of the optical and near infra-red luminosity function as well as the stellar mass function of 8625 LRGs from the 2SLAQ survey between redshift 0.4 and 0.8. I have demonstrated the unique position of 2SLAQ LRGs among other massive galaxy samples due to the large volume probed by the sample as well the availability of spectroscopic redshifts for all galaxies and near infra-red data for $\sim$75% of them. This has allowed us to probe the very high-mass end of the stellar mass function which places the most stringent constraints on models of galaxy formation. The spectral evolution models of Maraston *et al.* (2009) have also been used to study the evolution of these objects and these are the most accurate models of LRGs to date. However, the conclusions of this analysis change little if other models are used instead.

- The evolution of the optical luminosity function of LRGs between redshifts 0.4 and 0.8 is consistent with the assumptions of a passive evolution model where the stars were formed at high redshift with little or no evidence for recent episodes of star formation.

- A downturn is seen at the faint end of the LRG luminosity function around $M_{ideV}(k+e) \sim -21.75$. This is due to the effects of downsizing in the star formation. The faintest galaxies are expected to be reside in less massive halos and are therefore bluer than the bright objects. Such objects are excluded from the LRG sample due to the imposed colour selection of these objects which selects only the reddest galaxies.

- The LRG luminosity function is found to be unaffected by cosmic variance due to the massive volume occupied by the sample.

- The luminosity function is also relatively insensitive to the choice of spectral evolution model and the metallicity although models with some residual star formation and/or younger stars shift the luminosity function towards fainter absolute magnitudes.

- Photometric errors are found to induce a significant bias into the LRG sample causing contamination from star forming galaxies. The luminosity function estimates can therefore only be considered reliable brighter than $M_{ideV}(k+e) \sim -21.75$ where the effects of incompleteness and photometric errors is minimal.

- The stellar mass function for these LRGs above $3 \times 10^{11} M_{\odot}$ also shows little evidence for evolution between redshifts 0.4 and 0.8 suggesting that these most massive systems were

already well assembled at redshifts of 0.8. This is consistent with the emerging picture of downsizing in the mass assembly of massive galaxies.

- The stellar mass function estimate is also relatively insensitive to the choice of spectral evolution model assumed in the calculation of V_{max}. However, different choices of the stellar initial mass function will shift the mass function estimate as found in previous studies.

- The comoving number density of LRGs with $3 \times 10^{11} M_\odot < M_* < 10^{12} M_\odot$ has changed little between redshifts 0.8 and 0.4. The same is true for the most massive LRGs with $M > 10^{12} M_\odot$ which place more stringent constraints on galaxy formation models. This is consistent with other observational results for massive galaxy samples and does not agree with the predictions of most current galaxy formation models. The models of Granato *et al.* (2004) however may be promising in matching these observations although they are yet to be compared with massive galaxy samples at intermediate redshifts.

Overall, these results support the emerging picture of downsizing in both the star formation and mass assembly of galaxies and present a significant challenge for current models of galaxy formation. It has been shown that these findings are robust to changes in spectral evolution models, cosmic variance and photometric errors and it can therefore be concluded that these new observations of the most massive and most luminous galaxies in our Universe will need to be reconciled with the models if progress is to be made in the field of massive galaxy formation and evolution.

LOW-MASS STAR FORMATION AND THE STELLAR INITIAL MASS FUNCTION

The work described in this chapter is an extended version of the publications: ***Banerji, Viti, Williams & Rawlings, 2009, ApJ, 692, 283*** *and* ***Banerji, Viti & Williams, 2009, ApJ, 703, 2249***

7.1   Introduction

Recent multi-wavelength studies of galaxies have permitted estimates to be made of the evolution of the space density of the massive star formation rate (Hopkins & Beacom 2006; Lilly *et al.* 1996; Madau *et al.* 1996). While these rates are at present poorly constrained, there is currently no information on the formation at high redshift of low mass stars, a process that in the Milky Way is known to accompany the formation of massive stars. The low mass stars may be optically insiginificant, but they modify the physics of the host galaxies rather significantly. In particular, the shape of the stellar initial mass function (IMF) and its slope as specified by the ratio of low-mass to high-mass stars, are crucial for determining the star formation history and stellar mass density of a galaxy. There has been much interest in varying the stellar IMF (Elmegreen 2008; Wilkins *et al.* 2008; Davé 2008; van Dokkum 2008) and recent studies have suggested that the IMF must be top-heavy at high redshifts to explain the counts of faint submillimeter galaxies and the luminosity function of Lyman break galaxies (Baugh *et al.* 2005). However, this has by no means been proven true for all high redshift environments.

Studies of low mass star formation in the Milky Way have shown that it arises in the interplay of a number of competing processes including gravitational collapse and thermal and magnetic

support. Thermal support at the low temperatures of interstellar clouds is determined by the cooling mechanisms, while magnetic support is controlled by the ionization fraction; both are largely determined by chemistry which itself is moderated by cosmic ray and photon fluxes, and metallicity. A consideration of the timescales appropriate for the Milky Way indicates - as it should - that low mass star formation takes place under Milky Way conditions. However, the physical properties in high redshift galaxies may depart significantly from the Milky Way values. In this chapter, therefore, the variation of these relevant timescales is considered when the physical conditions of the star forming regions are modified from Milky Way values. The results are used to determine the regions of parameter space in which low mass star formation is unlikely to occur. By doing so, the form of the IMF in high redshift galaxies is crudely determined.

In addition, the star formation models used to derive timescales are also used to predict trends in molecular emission arising from extragalactic environments with different stellar IMFs. By looking at the chemistry associated with the different extragalactic systems studied, possible molecular tracers of different types of IMF can be identified, which can be used to direct observations with future projects such as ALMA. In particular, the rotational transitions of ^{12}CO as well as molecular abundances of certain key species are considered.

7.2 Timescales for Star Formation

Star formation is a complex process. While gravity is the main driver, there are many other mechanisms that compete to aid and oppose the collapse of molecular clouds. Cooling by molecular radiation leads to thermally induced collapse of a molecular cloud and if the timescale associated with this process is longer than the free-fall time, the collapse will be halted. The rate of cooling in turn is determined by the abundances of the various different molecular coolants such as CO and so we can see the role that chemistry plays. The chemistry itself is driven by cosmic ray ionisation of molecular hydrogen. In some circumstances, the surfaces of dust grains can become coated with ice due to the *freeze out* of different species onto the grains. This process is effective in removing coolant molecules from the gas phase. Energy released from H_2 formation can liberate the *frozen* species into their gaseous phase. Interstellar magnetic fields too can affect the collapse of molecular clouds. The ions are coupled to field lines and neutral atoms to the ions via collisions. The fractional ionisation therefore determines the magnetic pressure and the level of ion-neutral friction which in turn can halt collapse.

In the local universe, the timescales associated with these various competing processes are

found to be roughly of the same order of magnitude - $\sim 10^5$ yrs (Williams 1998) for a core density of $\sim 10^4 \text{cm}^{-3}$. This balance of timescales is clearly conducive to star formation. By exploring the change in these timescales for a range of initial conditions, we can effectively explore different regions of redshift space and hope to learn something about when and how the first low mass stars started to form. Note that the formation of high-mass stars occurs on much shorter timescales than those considered in this work.

7.2.1 Collapse

Low mass star formation essentially occurs by the collapse of a molecular cloud under its own weight accompanied by the dissipation of gravitational potential energy. In any situation where the star formation is not externally triggered by a violent event, for example the passage of a shock, the actual collapse time will be somewhat longer than the free-fall time due to turbulence within the cloud. In this work, the free-fall time is used as an under-estimate of the typical collapse time for a molecular cloud undergoing quiescent star formation.

The free-fall time of a collapsing core is related to the number density of hydrogen nuclei as follows:

$$t_{ff} = \sqrt{\frac{3\pi}{32G\rho}} = 0.52 \times 10^8/(n_H)^{\frac{1}{2}}\text{yrs}, \tag{7.1}$$

where $n_H = (n(H)+2n(H_2))$ is the local number density of hydrogen nuclei in cm^{-3} (Dyson & Williams 1997).

7.2.2 Cooling

In order for a cloud of gas to continue to collapse and form a star, the cloud must continue to lose energy, otherwise, the high temperatures and densities within the cloud would halt collapse before the formation of a star could occur. Energy loss occurs via different atomic and molecular transitions, while at high densities, collisions between hot gas and cooler dust grains can also be efficient in cooling the gas. The rate at which energy is lost depends on the cooling function, $\Lambda_{tot}/$ erg cm $^{-3}$ s^{-1}, which in turn depends on the abundance of various different molecular coolants. The temperatures considered in this work are too low for any cooling through the hydrogen and helium lines to be efficient and cooling through metal lines is therefore considered to be dominant.

The total cooling time is then given by:

$$t_{cool} = \frac{\frac{5}{2} n_H k T}{\xi \Lambda_{tot}} \text{yrs},$$ (7.2)

where k is the Boltzmann constant, T is the gas temperature and ξ is the metallicity in units of solar metallicity. The quantity, $\frac{5}{2} n_H k T$ represents the total energy, both thermal and internal, of the system and $\xi \Lambda_{tot}$ is the total interstellar cooling rate. Note that this analytical expression is crude in nature and does not hold at zero metallicity.

Note that the chemical models described in § 7.3, do not include the effects of removing molecular coolants from the gas phase by freeze-out. If freeze-out occurs, the cooling timescale will be underestimated in regions of parameter space where there is significant ice-formation.

7.2.3 Freeze-out

A detailed calculation of the rate per unit volume at which a species freezes out can be found in Rawlings *et al.* (1992). This quantity depends on the relative abundance of dust grains compared to hydrogen nuclei, the physical properties of the grain as well as the species whose freeze-out is being considered, and electrostatic effects to take into account the fact that ionic species will freeze-out at a different rate to neutral species. Due to the presence of more than one grain population in most systems, the grain properties need to be averaged over the grain size distribution. Rawlings *et al.* (1992) relate this size distribution to the depletion coefficient, D which depends on the abundance of very small grains and on the metallicity.

Taking these assumptions into consideration, the freeze-out timescale can be derived from the rate of freeze-out given by Rawlings *et al.* (1992):

$$t_{fo} = \frac{0.9 \times 10^6 (m_X/28)^{\frac{1}{2}}}{(T/10)^{\frac{1}{2}} (n_H/10^4) D} \text{yrs},$$ (7.3)

where m_X is the molecular mass of the species whose freeze-out is being considered and T is the gas temperature.

7.2.4 Desorption

Desorption is the process by which molecules in ices on the surface of dust grains, are returned to the ISM. The mechanism through which heat is generated for this desorption, is still debated (Roberts *et al.* 2007). In this work, only one mechanism for desorption is considered, namely

exothermic reactions occurring on the grain surface. More specifically, the liberation of energy from H_2 formation on dust grains results in a proportion of the frozen molecules on the dust grain being returned to the gas phase.

The desorption rate of CO which is the most abundant molecular species besides hydrogen, is:

$$\frac{dn(CO)}{dt}|_{des} = 3 \times 10^{-17} n(H) n_H \xi \gamma \sqrt{\frac{T}{100}}. \tag{7.4}$$

The rate depends on the metallicity which scales linearly with the dust to gas ratio, the abundance of both molecular and atomic hydrogen, the temperature, T and the number of CO molecules desorbed for every H_2 formed, γ. The coefficient 3×10^{-17} represents the canonical H_2 formation rate in the Milky Way.

From this expression, a typical timescale associated with desorption can be calculated:

$$t_{des} = \frac{1 \times 10^9}{[n_H n(H)(T/100)^{\frac{1}{2}} \gamma \xi]} \text{yrs}, \tag{7.5}$$

where n_H is the local number density of hydrogen nuclei and $n(H)$ is the column density of hydrogen atoms only. The number of CO molecules desorbed per H_2 formation, γ can be constrained by considering a pre-stellar core in the Milky Way like L1689B where significant depletion of CO molecules has been directly observed (Redman *et al.* 2002). Assuming for such an object with $n_H \sim 10^4 - 10^5 \text{cm}^{-3}$, that the timescale for freeze-out is less than half the timescale for desorption gives an upper limit on γ of ~ 0.25. A $\gamma = 0.2$ is used throughout this work and it is assumed that this number does not change in high redshift systems. This is plausible as one expects the microscopic properties of the dust in high redshift galaxies to be fairly similar to those in the Milky Way. Both the freeze-out and desorption timescales depend on these microscopic properties.

7.2.5 Ambipolar Diffusion

Magnetic fields may play an important role in supporting dense molecular clouds and many of the fragments within them. The magnetic field lines are coupled directly to the ions and indirectly to the neutral matter through frequent ion-neutral collisions. At low ionisations, the frequency of the ion-neutral collisions becomes less regular and the field lines decouple from the neutral matter thereby allowing the matter to drift in response to the gravitational potential. This process

is known as ambipolar diffusion and plays an important role in determining the rate of quiescent star formation.

The characteristic timescale associated with this process of decoupling the field from the neutral matter will depend on the relative drift velocities of the ions and neutral particles. Hartquist & Williams (1989) define the ambipolar diffusion timescale as follows:

$$t_{amb} = 4 \times 10^5 (x_i/10^{-8}) \text{yrs.} \tag{7.6}$$

This is a function only of the fractional ionisation, x_i within the cloud and is consistent with the more detailed treatment of Mouschovias (1979). However, in the earlier paper, the ambipolar diffusion timescale is shown to be a function of position within the cloud. Therefore variations in the degree of ionisation as a function of cloud depth become important. For the purposes of the rather crude calculations presented in this chapter, the positional dependence is neglected. Eq. 7.6 therefore corresponds to the Mouschovias (1979) timescale at an intermediate position towards the interior of the core. It should be noted that this timescale is only relevant for magnetically sub-critical cores.

7.2.6 Ion-Molecule Chemistry

The chemical timescale is the time taken to create molecular coolants from the initially atomic gas assuming that nearly all of the hydrogen is molecular. In other words, it is the time taken to ionise sufficient hydrogen to allow complete chemical conversion of C and O to molecular form. It is assumed from studies of star formation in the Milky Way that roughly 10^{-3} hydrogen atoms per cm^{-3} need to be ionised in order for this chemical conversion to occur. Cosmic rays are responsible for ionising the hydrogen. The relative abundances of carbon and oxygen will scale with the metallicity, ξ. The chemical timescale is

$$t_{chem} \simeq \frac{3\xi(n_C^{tot} + n_O^{tot})}{n(H_2)\zeta} = \frac{5 \times 10^6 \xi}{\zeta/1 \times 10^{-17}} \text{yrs.} \tag{7.7}$$

The chemistry is important for providing the coolant molecules and therefore must not be too long if star formation is to occur. The analytical expression for the chemical timescale represented by Eq. 7.7 depends only on the metallicity and cosmic ray ionisation rate and is rather crude. The chemical timescale is less relevant in cores than in the parent cloud which may be collapsing from a diffuse to a dark state as there isn't much change in the chemistry once cores begin to form.

7.3 Modeling

In order to model the various different timescales discussed in § 7.2 a time and depth-dependent chemical code for molecular clouds and photon-dominated regions (PDR hereafter) is used to solve simultaneously for the chemistry, thermal balance and radiative transfer within a cloud. This UCL_PDR code models the gas phase chemistry inside the cloud which is treated as a 1D semi-infinite slab of gas illuminated by a uni-directional flux of FUV photons incident on its outer surface (Bell *et al.* 2006). Differences in model geometry are unlikely to affect the chemistry significantly enough to influence these rather qualitative results (See Röllig *et al.* (2007) for a PDR benchmarking code comparison). The FUV radiation field is taken to be the standard interstellar radiation field (Draine 1978) multiplied by a factor of χ where $\chi = 1.7$ corresponds to a flux of 1.6×10^{-3} erg s^{-1} cm^{-2}, appropriate for the unshielded interstellar medium in the Milky Way. The radiation field strength declines exponentially with increasing depth within the cloud and therefore depends on the visual extinction A_v. No grain chemistry is included and hence the freeze-out and desorption of species is ignored in these models. Various different heating and cooling mechanisms are invoked within the code. Photoejection of electrons from dust grains and polycyclic aromatic hydrocarbons (PAHs) and FUV pumping and photo-dissociation of H_2 are the dominant heating mechanisms while the gas is mainly cooled through emission from collisionally excited atoms and molecules and by interactions with the cooler dust grains. The gas temperature is determined at each depth point by using an iterative procedure to balance the total heating and cooling rates. Although the chemical model is also time dependent, all outputs are considered at steady state unless otherwise stated, which is assumed to correspond to a time of 1Gyr.

The code takes as its inputs the number density of hydrogen nuclei, n_H, the metallicity, ξ, the cosmic ray ionisation rate, ζ, the strength of the incident FUV radiation field, χ, the turbulent velocity, v within the cloud and the redshift, z. As this study considers quiescent low-mass star formation only, the turbulent velocity is fixed at a value of $v = 1.5$ km s^{-1}. The redshift, z is only important in determining the contribution of the cosmic microwave background to the temperature of the various rotational lines and this effect is only significant at low densities and low visual extinctions. As most of the models described in this work looks at molecular clouds with relatively high densities and/or visual extinctions, the redshift parameter is always set to 0 and the other parameters modified in order to mimic a high-redshift system. Variations in the remaining four parameters and implications for the star formation timescales are considered in § 7.4.

The chemistry consists of a chemical network containing 83 species. These species interact in over 1300 reactions, whose rates are taken from the UMIST99 database (Le Teuff *et al.* 2000). Initially, hydrogen is assumed to be in atomic form.

Central to much of the work presented in the latter half of this chapter, are the model predictions for parameters associated with the rotational lines of CO and I therefore describe how these are obtained in more detail. The gas in PDRs mainly cools through emissions from collisionally excited atoms and molecules as well as through interactions with cooler dust grains. The code calculates the emission from the [OI], [OII] and [CII] fine structure lines as well as the CO rotational lines at each depth and time step. This is done using the escape probability formalism of de Jong *et al.* (1980) to solve the radiative transfer equations. Non local thermodynamic equilibrium (non-LTE) level populations are determined by solving the equations of statistical equilibrium using rate coefficients for CO collisions with H_2, H and He from Flower & Launay (1985), Green & Thaddeus (1976) and Green & Chapman (1978) respectively. The solutions of the radiative transfer equations give the emissivity, Λ, the intensity, I and the opacity, τ for every line at every depth and time step. Several of these outputs are used in this chapter.

Although this chapter makes references to models of extragalactic systems, it should be emphasised that we are modeling the various PDR components that make up external galaxies rather than the galaxy as a whole. Our chosen input parameters therefore mimic the average conditions in individual PDRs within a galaxy. The outputs are considered at two visual extinctions of $A_v \sim 3$ and $A_v \sim 8$. These roughly correspond to the translucent and dense PDR gas components within a galaxy. Atomic and molecular emissions from different components within the galaxy will contribute independently to the line emissions detected from the galaxy as a whole and studied in detail in § 7.5. Also, due to the fact that the PDR is modeled as a semi-infinite slab, a given visual extinction will correspond to different physical distances within the cloud under different physical conditions as the A_v depends on both the number density and the metallicity of the cloud in our models. I come back to this point later in this chapter.

7.4 Variation of Star Formation Timescales

This section describes how the various timescales associated with low mass star formation and detailed in § 7.2 change as the input parameters to the chemical model are varied. Variations in the number density of hydrogen nuclei, n_H, the metallicity, ξ, the cosmic ray ionisation rate, ζ and the strength of the incident FUV radiation field, χ are considered. When varying any of

the four parameters, the others are fixed at their *local* values namely $n_H = 10^5$ cm^{-3}, $\xi = \xi_\odot$, $\zeta = 10^{-17}$ s^{-1} and $\chi = 1.7$ appropriate for a Milky Way cloud. All outputs are considered at steady state corresponding to a time of 1Gyr and at two depths corresponding to $A_v \simeq 3$ and $A_v \simeq 8$. Outputs of the code include the cooling function, Λ_{tot}, the fractional ion abundance, x_i, the gas temperature T and the column density of hydrogen atoms $n(H)$ and these values can be substituted into equations 7.2, 7.3, 7.5 and 7.6 to calculate the cooling, freeze-out, desorption and ambipolar diffusion timescales.

For each set of initial conditions, some references are made to extragalactic objects that may exhibit these properties and hence we are able to infer if low mass star formation is likely to be encouraged or inhibited in such objects. It should be noted that these calculations are relatively crude in nature and therefore only instructive in terms of observing general trends.

7.4.1   Varying the Gas Density

The hydrogen nuclei number density is varied between 100 cm^{-3} and 10^6 cm^{-3} in this study and the effect of this variation on the low mass star formation timescales are considered. Higher density clouds are only likely to be relevant for high-mass star formation and are therefore not considered. The results are summarised in Figure 7.1.

As expected, the free-fall time decreases with increasing number density and is $\sim 10^6$ yrs at 10^4 cm^{-3} typical of a Milky Way cloud. At this density, all the different timescales converge to roughly the same order of magnitude. Thus both freeze-out and desorption proceed with desorption a slightly slower process so that molecular ices do form. Desorption maintains a population of molecular coolants in the gas phase. The free-fall time is comparable to the cooling time, thermally induced collapse occurs and stars are able to form. The ambipolar diffusion timescale is comparable to the dynamical free-fall time and star-formation can occur in magnetically sub-critical couds. These conditions are appropriate for a Milky Way type galaxy and therefore this approach indicates as expected that low mass star formation is reasonably efficient in Milky Way type systems.

However, at very high densities, the free-fall time is shorter than the cooling time and the cores will heat up during the collapse which is then arrested.

The freeze-out timescale and desorption timescale are comparable and both decrease with increasing density at the same rate suggesting that molecular ices are able to form at all densities between 100 cm^{-3} and 10^6 cm^{-3}. This also implies that the cooling time is systematically under-estimated as ice formation, which is not included in the chemical model, removes molecular

Figure 7.1: Variation of timescales relevant to star formation with number density of hydrogen at $A_v \sim 3$ (solid lines) and $A_v \sim 8$ (dotted lines). The metallicity, cosmic ray ionisation rate and incident FUV radiation intensity are fixed at $\xi = \xi_\odot$, $\zeta = 10^{-17} s^{-1}$ and $\chi = 1.7$.

coolants from the gas phase at all densities.

Looking deeper into the cloud, i.e. going from $A_v \simeq 3$ to $A_v \simeq 8$ does not seem to affect significantly the freeze-out or desorption timescales. However, the cooling time is slightly larger at higher visual extinctions as the cooling function decreases with increasing A_v. This is probably due to increased radiation trapping in the cooling lines.

The ambipolar diffusion timescale is much longer than the other timescales at very low densities. This suggests as expected that star formation cannot occur in clouds with $n_H < 10^3$ cm^{-3} that are magnetically sub-critical as the field is very slow to decouple.

7.4.2 Varying the Metallicity

The metallicity, ξ, is another important physical property that will affect low mass star formation. This parameter is particularly important for modeling high redshift systems as the primordial gas from which these objects formed is likely to be less chemically enriched than the interstellar medium in the Milky Way in some cases, and will therefore have lower metallicities. As we are interested in low metallicity objects that formed early in the history of the Universe, metallicities
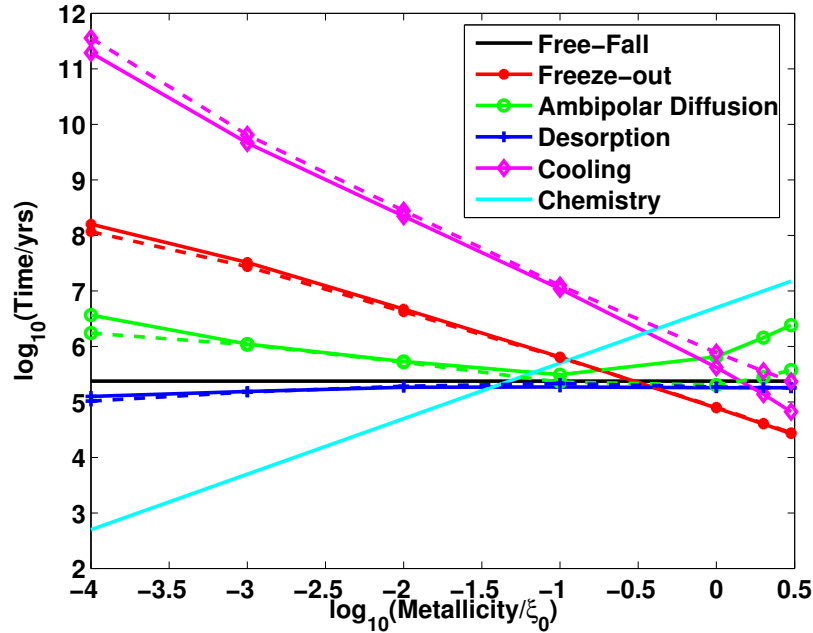
Figure 7.2: Variation of timescales relevant to star formation with metallicity at $A_v \sim 3$ (solid lines) and $A_v \sim 8$ (dotted lines). The number density of hydrogen, cosmic ray ionisation rate and incident FUV radiation intensity are fixed at $n = 10^5 cm^{-3}$, $\zeta = 10^{-17} s^{-1}$ and $\chi = 1.7$.

as low as $10^{-4}\xi_\odot$ are considered. Metallicities enhanced above solar values to upto $3\xi_\odot$ are also considered. In the chemical model, it is assumed that the elemental abundances of all metals scale linearly with metallicity. The dust to gas mass ratio is also assumed to scale linearly with metallicity. The results from this study are summarised in Figure 7.2.

As expected, the cooling time falls with increasing metallicity due to the increased abundance of molecular coolants. At metallicities below $\xi = 0.1\xi_\odot$, the cooling time is much longer than the free-fall time and collapse and star-formation are likely to be impeded by gas pressure. The freeze-out time also decreases with increasing metallicity due to the presence of more dust grains but the desorption time is independent of metallicity. At low metallicities, freeze-out is slower than desorption so ice-formation is inhibited. Temperatures however remain high due to the long cooling timescales.

The ambipolar diffusion timescale remains fairly insensitive to the metallicity. The fractional ionisation is much higher at low visual extinctions so the ambipolar diffusion timescale falls with increasing depth into the cloud. Note that the visual extinction scales linearly with metallicity so high visual extinctions in low metallicity clouds will correspond to larger physical distances within

the cloud. Hence, the calculations for $A_v \simeq 8$ are probably unfeasible for low metallicity clouds. But as the cloud is likely to be optically thick even at lower depths, the chemistry is unlikely to be very different to the $A_v \simeq 8$ case and the timescales will therefore remain roughly the same.

The chemical timescale increases linearly with metallicity as expected. Low metallicity systems therefore convert a significant fraction of available elements into molecular coolants.

7.4.3 Varying the Cosmic Ray Ionisation Rate

Although little is known about the origin of extragalactic cosmic rays, they are very important in ionising hydrogen and driving the chemistry during star formation. The level of ionisation within a dark cloud may determine whether or not the cloud is stable against gravitational collapse if magnetic fields are present.

An estimate for the cosmic ray ionisation rate in the Galaxy is $\sim 10^{-17}$ s^{-1} (Hartquist *et al.* 1978). In this study, the cosmic ray ionisation rate is varied between 10^{-18} s^{-1} and 10^{-13} s^{-1} in order to mimic both quiescent star forming systems such as those in our own galaxy as well as starburst regions and AGN which are expected to have cosmic ray fluxes of the order of 10^{-15}s^{-1} to 10^{-13}s^{-1} (Meijerink *et al.* 2006; Suchkov *et al.* 1993; Bradford *et al.* 2003). The results of varying the cosmic ray ionisation rate are summarised in Figure 7.3.

As the cosmic ray ionisation rate is increased, the cooling time falls and at $\zeta \sim 10^{-16}$ s^{-1}, it drops below the free-fall time. Cores cool more and more quickly and are therefore able to collapse to form stars. The chemical timescale is small at high values of the cosmic ray ionisation rate explaining the low cooling times as molecular coolants are quick to form in such circumstances.

The freeze-out time is greater than the desorption time and the propensity for ice-formation is reduced thereby allowing molecular coolants to remain in the gas phase to effectively cool the collapsing gas. Desorption is therefore unlikely to be a significant process. However, formally, the desorption time becomes shorter as expected with increasing cosmic ray ionisation rate as more and more hydrogen molecules are ionised thereby increasing the abundance of atomic hydrogen as well as the temperature of the gas. If ices could be formed, they would therefore be quick to evaporate off the dust grains once again replenishing the gas phase with molecular coolants and encouraging star formation.

The ambipolar diffusion timescale becomes very large as the fractional ionisation increases and the magnetic field is slow to be released from the collapsing core. Based on the results of Crutcher *et al.* (1987) and Athreya *et al.* (1998), the magnetic field strength, B of molecular clouds varies between 1μGauss and 100μGauss for densities between 1cm^{-3} and 10^5 cm^{-3}. This field
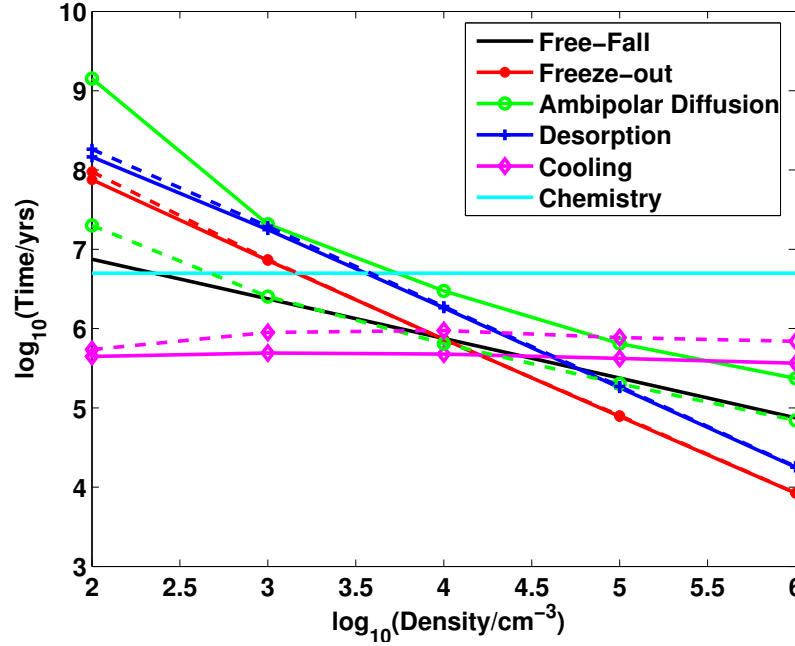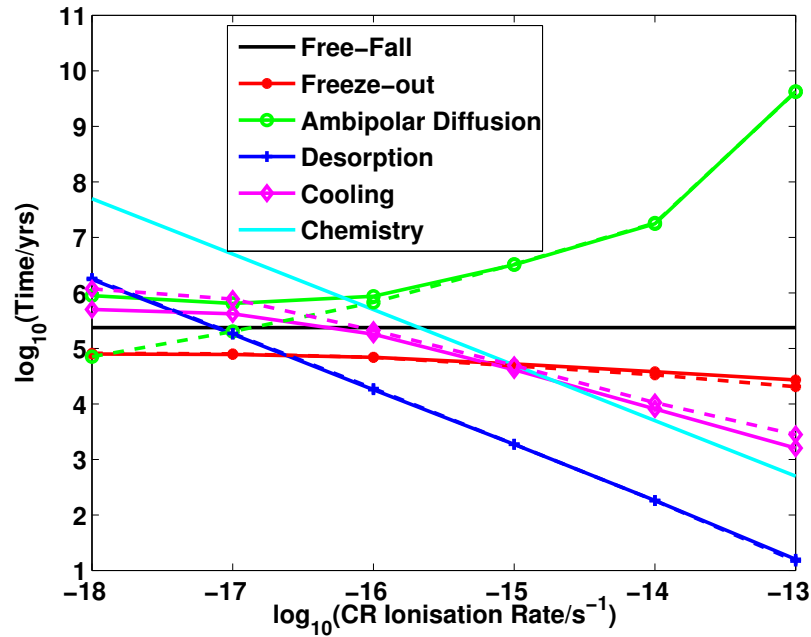
Figure 7.3: Variation of timescales relevant to star formation with the cosmic ray ionisation rate at $A_v \sim 3$ (solid lines) and $A_v \sim 8$ (dotted lines). The number density of hydrogen, metallicity and incident FUV radiation intensity are fixed at $n = 10^5 cm^{-3}$, $\xi = \xi_0$ and $\chi = 1.7$.

strength, B scales with the density as $B \propto (n_H)^\kappa$ where $\frac{1}{3} \leq \kappa \leq \frac{1}{2}$ (Mouschovias 1976) is consistent with observations. In this study, based on various observations (Crutcher *et al.* 1987; Bourke *et al.* 2001; Beck *et al.* 2005; Kim *et al.* 1990) a value of $\kappa \sim 0.4$ is considered. The ratio of the magnetic pressure to the thermal pressure, α can be calculated using Eq. 7.8:

$$\alpha = \frac{B^2}{8\pi n_H kT}. \tag{7.8}$$

For $\alpha >> 1$ the magnetic pressure dominates and for $\alpha << 1$, the thermal pressure dominates. For high cosmic ray fluxes and at a constant density of $n_H = 10^5$ cm^{-3}, α is computed to be ~ 0.4. This suggests that the magnetic pressure may in some cases be sufficient to halt the collapse but in other cases, depending on the temperature of the core and the exact value of κ, low-mass star formation can proceed unimpeded.

7.4.4 Varying the FUV Radiation Field

The FUV radiation field is a significant source of heating of neutral interstellar gas. As explained in § 7.3, the radiation field is taken to be the standard interstellar radiation field (Draine 1978)
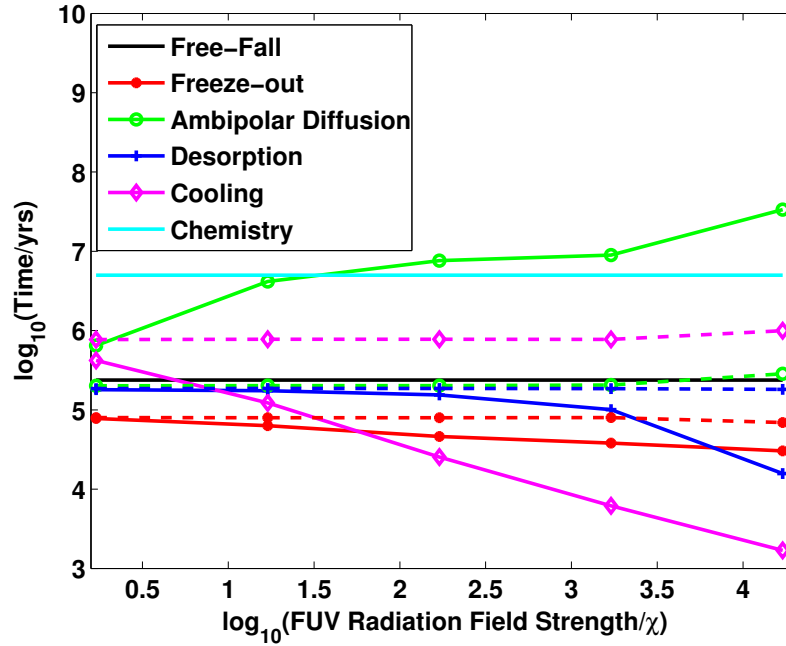
Figure 7.4: Variation of timescales relevant to star formation with the FUV radiation field strength at $A_v \sim 3$ (solid lines) and $A_v \sim 8$ (dotted lines). The number density of hydrogen, metallicity and cosmic ray ionisation rate are fixed at $n = 10^5 cm^{-3}$, $\xi = \xi_0$ and $\zeta = 1 \times 10^{-17} s^{-1}$.

multiplied by a factor of χ where $\chi = 1.7$ corresponds to a flux of 1.6×10^{-3} erg s^{-1} cm^{-2}. The FUV radiation field strength is linked to the number of massive stars in the Galaxy and given the presence of many massive stars at high redshift (Abel *et al.* 2002; Bromm *et al.* 1999) is likely to be large in these systems. In this study, χ is varied between 1.7 and 1.7×10^4 in order to study the effect of this parameter on the star formation timescales. The results are summarised in Figure 7.4.

At $A_v \simeq 10$, the FUV radiation is sufficiently attenuated to not affect the chemistry within the cloud and all the timescales therefore remain fairly constant with FUV flux strength. At lower visual extinctions, the cooling time is almost always smaller than the free-fall time and collapse and star formation are therefore encouraged. The freeze-out time is also almost always smaller than the desorption timescale except at very high FUV radiation field strengths. This suggests that the formation of icy mantles on dust grains is possible even at FUV radiation field strengths of $\chi = 1.7 \times 10^3$ at $A_v \sim 3$. The desorption time and freeze-out time are fairly comparable at all radiation field strengths so any icy mantles deposited on the dust grain are quick to evaporate. At very high FUV flux strengths, the desorption time is shorter than the freeze-out time and ice

Table 7.1: Star Formation Timescales at High-Redshift

Timescale	Model I		Model II		Model III	
Years	$A_v \sim 3$	$A_v \sim 8$	$A_v \sim 3$	$A_v \sim 8$	$A_v \sim 3$	$A_v \sim 8$
Free-Fall	5.2×10^5	5.2×10^5	1.6×10^5	1.6×10^5	1.6×10^5	1.6×10^5
Cooling	6.8×10^5	8.0×10^5	4.3×10^5	6.8×10^6	3.3×10^3	1.1×10^4
Freeze-out	1.7×10^6	1.4×10^6	5.2×10^5	1.4×10^5	4.0×10^4	3.9×10^4
Desorption	3.1×10^2	1.9×10^2	1.1×10^2	2.4×10^1	1.4×10^2	1.8×10^2
Ambipolar Diffusion	7.1×10^{10}	8.6×10^{10}	1.8×10^8	2.5×10^7	1.4×10^9	1.9×10^7
Chemistry	2.5×10^1	2.5×10^1	2.5×10^2	2.5×10^2	5.0×10^3	5.0×10^3

formation is inhibited. Both these processes mean that the ISM is always rich in molecular coolants at high FUV radiation field strengths and collapse is encouraged.

The ambipolar diffusion timescale is very large for high radiation field strengths and at low A_v. This once again suggests that magnetically super-critical cores will be stable against collapse. However, at high A_v where the radiation field cannot penetrate the cloud, the ambipolar diffusion timescale is comparable to the dynamical timescale and the magnetical criticality is less significant.

Both the FUV radiation field strengths and the cosmic ray ionisation rate are linked with the presence of massive stars in this rather simplistic analysis and therefore it is not surprising that both parameters have similar effects on the star formation timescales. The presence of massive stars resulting in an elevated FUV flux strength, therefore serves to encourage quiescent low-mass star formation in every possible way at low A_v provided the residual magnetic pressure implied by the long ambipolar diffusion timescale, does not halt collapse. The ratio of the magnetic to thermal pressure for $\chi = 1.7 \times 10^4$ is computed to be $\alpha \sim 0.5$ and so the magnetic pressure may in some cases be sufficient to halt collapse.

7.4.5   Modeling a High Redshift Object

Bayet *et al.* (2008*b*) have identified the Cloverleaf ($z \simeq 2.6$) and APM08279 ($z \simeq 3.9$) as possible examples for high redshift sources. Although the physical properties of these sources are not well

constrained, molecular detections suggest that they are actively forming stars (Lutz *et al.* 2007; Gao & Solomon 2004; Wagg *et al.* 2005). Such objects are expected to have a range of different metallicities with galaxies with significant observed dust obscuration such as HCM6A ($z = 6.56$, Chary *et al.* (2005)) likely to be more chemically enriched. The presence of many massive stars in these systems will also result in high FUV radiation field strengths and cosmic ray ionisation rates. Collapse is likely to occur at moderately high densities due to the lack of available molecular coolants compared to a Milky Way type object.

In order to model such a system, the star formation timescales are calculated for three different models - (I) $n = 10^4$ cm^{-3}, $\xi = 0.05\xi_\odot$, $\zeta = 10^{-13}$ s^{-1} and $\chi = 1.7 \times 10^4$, (II) $n = 10^5$ cm^{-3}, $\xi = 0.05\xi_\odot$, $\zeta = 10^{-14}$ s^{-1} and $\chi = 1.7 \times 10^3$ and (III) $n = 10^5$ cm^{-3}, $\xi = \xi_\odot$, $\zeta = 10^{-14}$ s^{-1} and $\chi = 1.7 \times 10^3$ - at depths corresponding to $A_v \sim 3$ and $A_v \sim 8$. As previously stated, the presence of many massive stars in high redshift systems justifies a choice of elevated FUV radiation field strengths when modeling such systems. In order to mimic starburst galaxies with high cosmic ray fluxes such as M82 (Suchkov *et al.* 1993) and NGC253 (Bradford *et al.* 2003) at high redshift, high cosmic ray ionisation rates are also adopted. Meijerink *et al.* (2006) estimate a cosmic ray ionization rate of 5×10^{-15}s^{-1} for a star formation rate of ~ 100M$_\odot$ yr^{-1} and one expects high redshift galaxies with higher star formation rates to have elevated cosmic ray fluxes. Finally, there is evidence that high redshift galaxies exist at a range of metallicities with galaxies with significant observed dust obscuration likely to be more chemically enriched and therefore both solar and sub-solar metallicities are considered in these models. The results are summarised in Table 7.1.

It can be seen that for the first model, the free-fall time is comparable to the cooling time and cores can collapse to form stars even at depths as low as $A_v \sim 3$. The formation of icy mantles is likely to be inhibited in such systems as the freeze-out time is very large compared to the desorption time.

The second model has slightly lower cosmic ray fluxes and FUV radiation field strengths but is considered to be at a higher density. In this case, the free-fall timescale is only slightly shorter than the cooling time at low A_v and cores can collapse to form stars but at $A_v \sim 8$, the cooling time is larger and the propensity for low mass star formation is reduced. Once again, the formation of icy mantles is inhibited in such a system.

The third model also has elevated FUV radiation field strengths and cosmic ray fluxes but is now considered at solar metallicity. The cooling time is now significantly lower than the free-fall time at all depths and low-mass star formation is unimpeded by thermal pressure while ice

formation still remains inhibited.

In all three cases, the ambipolar diffusion timescale is very large so the residual field may be able to halt collapse. Using the temperatures and densities of these model runs, the thermal and magnetic pressure can be calculated for each of the models in the same way as in § 7.4.3 as well as their ratio, α. In both the sub-solar metallicity models, α is computed to be ~ 0.05 so the thermal pressure dominates over the magnetic pressure. The cooling times are comparable to the dynamical free-fall time, particularly at low A_v and low-mass star formation is encouraged. The third model at solar metallicity has $\alpha \sim 0.6$ suggesting that in this case the magnetic pressure may be sufficient to halt collapse. This suggests that recent evidence for a top-heavy IMF is only supported by this study if high-redshift galaxies are considered to be at solar metallicities in which case the magnetic pressure may halt the collapse and formation of low-mass stars.

7.5 Trends in the ^{12}CO Rotational Spectrum

Carbon monoxide is one of the most commonly used tracers of molecular gas and its various rotational J transitions have been detected in many extragalactic systems both nearby (Bradford *et al.* 2003; Bayet *et al.* 2004, 2006) and in the distant Universe (Bertoldi *et al.* 2003; Nesvadba *et al.* 2009; Daddi *et al.* 2009; Knudsen *et al.* 2009). In Milky Way type conditions, the column density of molecular hydrogen along a line of sight is often related to the velocity integrated antenna temperature, T_A for the CO(1-0) transition, using the CO-to-H_2 conversion factor or X factor (Strong & Mattox 1996; Dame *et al.* 2001). The CO(1-0) line is used as it is known to be the dominant CO cooling line with the highest antenna temperature under physical conditions appropriate for a Milky Way cloud. However, this is not necessarily the case for high redshift systems with significantly different physical conditions and higher order transitions of CO may become more relevant (Sakamoto 1999; Bell *et al.* 2006, 2007). It is already known that galaxies with elevated cosmic ray fluxes have larger high-J CO line ratios (Meijerink *et al.* 2006) and that the higher order CO transitions trace denser gas than their lower order counterparts. In this section, CO rotational line transitions and ratios are examined in the context of the stellar initial mass function. We consider which of the CO transitions, if any, can be used as diagnostics for regions of both enhanced and inhibited low-mass star formation as studied in § 7.4. This study is conducted both for systems where one physical parameter is varied at a time while keeping the others fixed at their local values as well as the three high redshift systems modeled in § 7.4.5.

The UCL_PDR code outputs the integrated line intensity of the CO rotational lines with 1

$\leq \mathrm{J}_{upper} \leq 9$ in units of erg s^{-1} cm^{-2} sr^{-1} after solving the radiative transfer equations. The intensity is related to the emissivity Λ by

$$I = \frac{1}{2\pi} \int \Lambda(L)dL, \tag{7.9}$$

where L is the depth into the cloud and the factor of $1/2\pi$ takes into account the fact that the photons only emerge from the outer edge of the cloud due to the cloud being modeled as a semi-infinite slab. Integrating over larger depths will therefore obviously result in higher intensities.

In order to calculate the relative velocity integrated antenna temperature from the intensity the following equation is used:

$$\int (T_A)^{rel} dv = 10^{-6} \frac{c^3 I}{2k_B \nu^3 L_{A_v}} \mathrm{Kkms}^{-1}\mathrm{pc}^{-1}, \tag{7.10}$$

where c is the speed of light and k_B is the Boltzmann constant. As the UCL_PDR code models the PDR as a semi-infinite slab and the visual extinction, A_v in the slab is related to both the number density as well as the metallicity, a fixed A_v will correspond to different physical distances, L, for different values of the density and metallicity. In order to derive values for the relative temperatures that are comparable and independent of the size of the emitting region, the relative velocity integrated antenna temperatures are divided by the distance in parsec corresponding to the A_v at which the temperature is calculated, L_{A_v}. This distance will obviously be much larger for low density and low metallicity systems for a fixed A_v. All figures showing the variation of the CO SED with different physical conditions, therefore represent the relative velocity integrated antenna temperatures for the different ^{12}CO transitions per unit parsec except in Figure 7.10 where the relative velocity integrated temperatures is plotted as a function of A_v.

Note that the numbers calculated using Eq 7.10 are important only in terms of observing trends. In order to match the absolute values of the theoretical velocity integrated antenna temperature to those from observations, one has to consider several other factors. Firstly, all models used in this chapter assume a turbulent velocity of 1.5 km s^{-1} typical for a giant molecular cloud in the Galaxy. In reality, observed lines of CO in extragalactic sources typically have widths of several 100 km s^{-1} due to contributions from several PDR regions within the galaxy and the temperature has to be scaled accordingly. Secondly, we need to account for a surface filling factor which takes into account the size of the source as well as the telescope beam. Finally, all observational results will be affected by factors such as the atmospheric conditions and the telescope efficiency. One way of

comparing the theoretical predictions to observations however, is to consider line ratios rather than the intensities and brightness temperatures of individual lines. Assuming the emission from both lines comes from the same clouds, the various factors discussed above should cancel out when computing the ratio of either the intensity or the integrated temperature. Theoretical predictions are therefore compared to observed line ratios in § 7.5.6.

7.5.1 Density

The hydrogen atom number density of the molecular cloud is once again varied between $100\,\mathrm{cm}^{-3}$ and $10^6\,\mathrm{cm}^{-3}$ while keeping the metallicity, cosmic ray ionisation rate and FUV flux fixed at $\xi = \xi_\odot$, $\zeta{=}10^{-17}\,\mathrm{s}^{-1}$ and $\chi{=}1.7$ Draine (Draine 1978). The effect on the relative velocity integrated antenna temperature, $\int (T_A)^{rel} dv$, of the different CO rotational transitions, is illustrated in Figure 7.5. The CO(1-0) line is seen to be the brightest line at all densities and the CO SED falls off with increasing J. Higher density clouds also produce brighter antenna temperatures as expected. As the A_v is increased, the relative integrated temperatures per unit parsec drop, particularly for the higher density clouds. This is telling us that in these high density clouds, most of the emissivity in these CO rotational lines is coming from the lower A_v regions. This is also the case for the high-J transitions in the lower density clouds.

7.5.2 Metallicity

The metallicity is varied between $\xi = 10^{-4}\xi_\odot$ and $\xi = 3\xi_\odot$ while keeping the density, cosmic ray ionisation rate and FUV flux fixed at $n{=}10^5\,\mathrm{cm}^{-3}$, $\zeta{=}10^{-17}\,\mathrm{s}^{-1}$ and $\chi{=}1.7$ Draine (Draine 1978) . The dependence of $\int (T_A)^{rel} dv$ on the metallicity is illustrated in Figure 7.6. In § 7.4.2 it was found that low-mass star formation is likely to be inhibited at very low metallicities resulting in a top-heavy IMF, provided the cloud is at moderately high densities and low cosmic ray fluxes and FUV field strengths. The form of the CO SED is quite different at different metallicities. While the higher metallicity clouds produce SEDs that peak at the lower rotational numbers and drop off sharply after that, the lower metallicity clouds have flatter SEDs. For the highest rotational transitions with $J_{upper} > 7$, the sub-solar metallicity clouds actually produce emission that is brighter than that from solar metallicity clouds. As we approach sub-solar metallicities, the ratio of the high-order CO transitions to the peak CO transition tends towards unity whereas at solar metallicities it is much smaller. The physical conditions in sub-solar metallicity counterparts of Milky Way type galaxies are thought to be appropriate for the production of top-heavy IMFs.

Figure 7.5: Variation of relative velocity integrated CO antenna temperature per unit parsec with number density of hydrogen at $A_v \sim 3$ (solid lines) and $A_v \sim 8$ (dashed lines). The metallicity, cosmic ray ionisation rate and incident FUV radiation intensity are fixed at $\xi = \xi_\odot, \zeta = 10^{-17} s^{-1}$ and $\chi = 1.7$.

7.5.3 Cosmic-Ray Ionisation Rate

The cosmic ray ionisation rate is varied between $\zeta = 10^{-18}$ s^{-1} and $\zeta = 10^{-13}$ s^{-1} with the rest of the input parameters fixed at $n = 10^5$ cm^{-3}, $\xi = \xi_\odot$ and $\chi = 1.7$ Draine. The results are shown in Figure 7.7.

Apart from the highest cosmic-ray ionisation rates, the CO(1-0) line dominates the emission in almost all cases. The relative antenna temperature increases with increasing cosmic ray ionisation rate. At $\zeta = 10^{-14}$ s^{-1}, the CO(2-1) transition just starts to dominate over the CO(1-0) line but by $\zeta = 10^{-13}$ s^{-1}, the CO(5-4) line is now the brightest CO line. This line can therefore be used to trace high density systems at solar metallicity with extremely high cosmic-ray fluxes such as sources with AGN or a starburst nucleus. In § 7.4.2 it was noted that systems such as this show some evidence for having top-heavy IMFs depending on the exact core temperature and magnetic field within these galaxies. In some active galaxies with physical conditions similar to that considered here, the magnetic pressure created through ambipolar diffusion may be sufficient to halt core collapse and formation of low-mass stars.
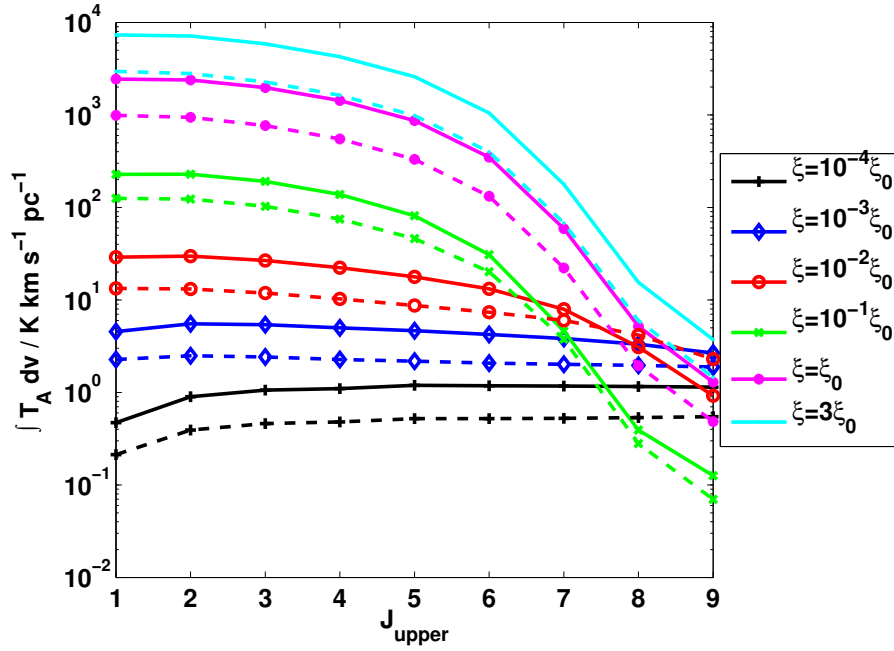
Figure 7.6: Variation of relative velocity integrated CO antenna temperatures per unit parsec with metallicity at $A_v \sim 3$ (solid lines) and $A_v \sim 8$ (dashed lines). The number density of hydrogen, cosmic ray ionisation rate and incident FUV radiation intensity are fixed at $n = 10^5 cm^{-3}$, $\zeta = 10^{-17} s^{-1}$ and $\chi = 1.7$.

7.5.4 FUV Radiation Field Strength

The FUV radiation field strength is varied between χ=1.7 Draine and χ=1.7$\times10^4$ Draine (Draine 1978) with the rest of the input parameters fixed at n=10^5 cm^{-3}, $\xi = \xi_\odot$ and ζ=10^{-17} s^{-1}. The dependence of the CO SED on the FUV radiation field strength, is illustrated in Figure 7.8.

Increasing the FUV radiation field strength results in similar behaviour as increasing the cosmic ray ionisation rate. Higher-order lines become more and more dominant and the antenna temperature increases with χ. At the maximum FUV field of $\xi = 1.7 \times 10^4$ considered here, it is the CO(8-7) line that is dominant but for a FUV radiation field that is an order of magnitude weaker, the CO(3-2) line dominates. The high-order CO transitions can therefore be used as tracers of extremely high FUV radiation fields associated with the presence of massive stars. Such systems may also have top-heavy IMFs depending on whether the magnetic pressure is sufficient to halt the collapse and formation of low-mass stars.

Note that due to the large parameter space that is modeled in this study, there will inevitably
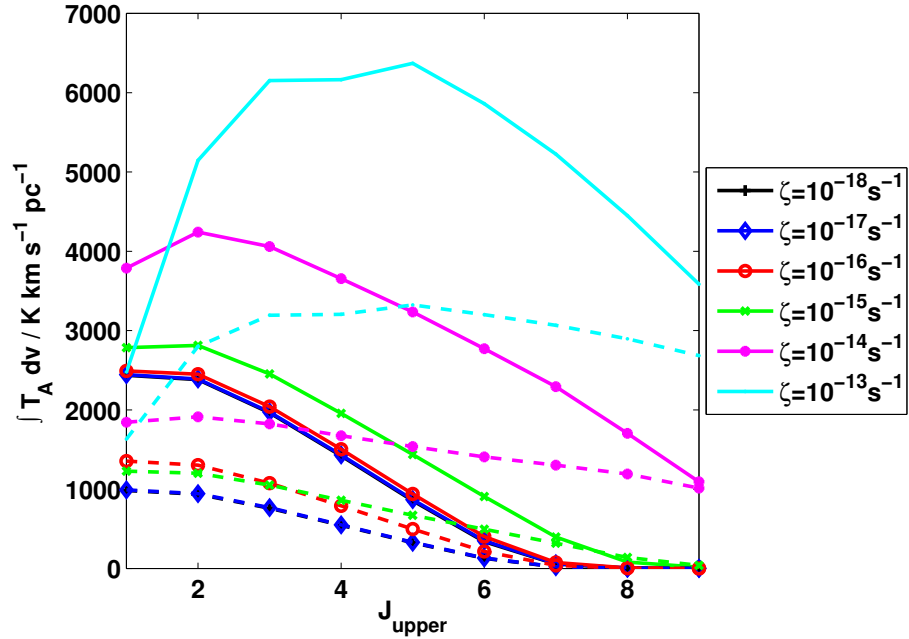
Figure 7.7: Variation of relative velocity integrated CO antenna temperature per unit parsec with the cosmic ray ionisation rate at $A_v \sim 3$ (solid lines) and $A_v \sim 8$ (dashed lines). The number density of hydrogen, metallicity and incident FUV radiation intensity are fixed at $n = 10^5 cm^{-3}$, $\xi = \xi_0$ and $\chi = 1.7$.

be degeneracies and the CO SEDs produced by models with $\chi = 1700$ and $\zeta = 10^{-14}s^{-1}$ may be observationally indistinguishable. However, as large values for both these parameters are associated with active galaxies producing massive stars in this rather simplistic analysis, it is probably fair to say that the form of the CO SED observed in these models can be taken to be roughly representative of such active systems.

7.5.5 Trends in ^{12}CO Line Emission at High-z

The relative velocity integrated CO antenna temperatures is now considered for the high redshift models described in § 7.4.5. The physical parameters associated with these models are also given in § 7.4.5 along with the IMFs associated with them. All models represent active galaxies with high cosmic ray fluxes and FUV radiation fields. Densities are also moderately high while both sub-solar and solar metallicities have been considered as the metallicity of high redshift systems still remains debated. Once again it is emphasised that these parameters are not meant to be representative of particular high redshift galaxies that have been observed in ^{12}CO but rather crudely
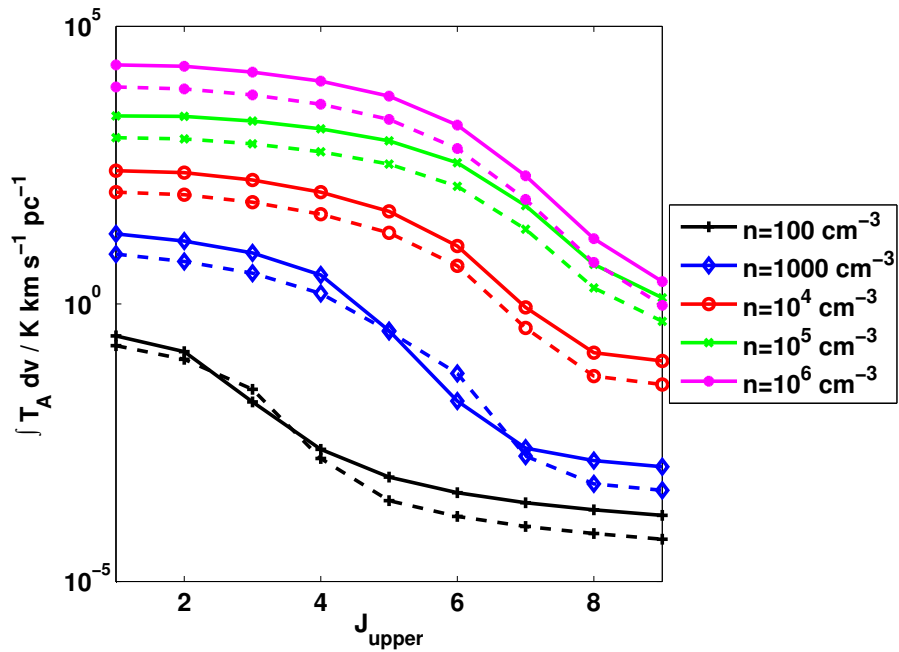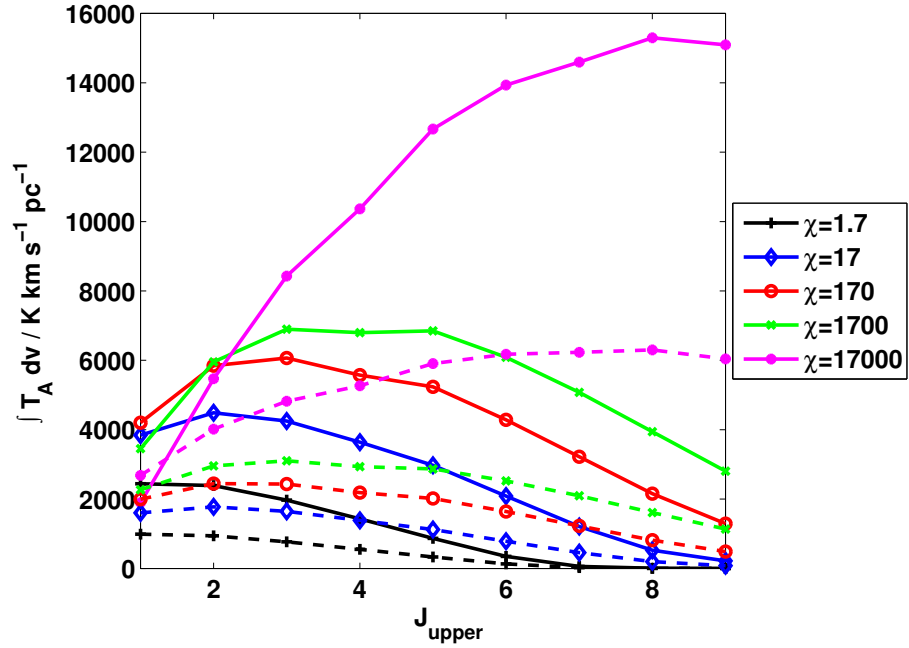
Figure 7.8: Variation of relative velocity integrated CO antenna temperature per unit parsec with the FUV radiation field strength at $A_v \sim 3$ (solid lines) and $A_v \sim 8$ (dashed lines). The number density of hydrogen, metallicity and cosmic ray ionisation rate are fixed at $n = 10^5 cm^{-3}$, $\xi = \xi_0$ and $\zeta = 1 \times 10^{-17}s^{-1}$.

represent our best guess as to the parameters that are likely to be associated with high redshift systems. In § 7.4.5 it was found that while there is no evidence for Models I or II having a high-mass biased IMF, Model III may have a high-mass biased IMF if the magnetic pressure is sufficient to halt the collapse and formation of low-mass stars. In other words, the physical conditions associated with Model III are likely to be necessary but not sufficient for a top-heavy IMF to exist. Differences in CO antenna temperatures in these three models are now considered as a possible means of distinguishing between the two IMF scenarios and the differing physical conditions in these galaxies.

Figure 7.9 plots the relative velocity integrated CO antenna temperature for the different CO rotational lines for the three high-z models. Solid lines correspond to $A_v \sim 3$ while dashed lines correspond to $A_v \sim 8$. It can immediately be seen that the CO SEDs have very different forms for the three models.

Model I has very low velocity integrated antenna temperatures compared to the other two models. This is because the extreme cosmic ray fluxes and FUV fields invoked in this model
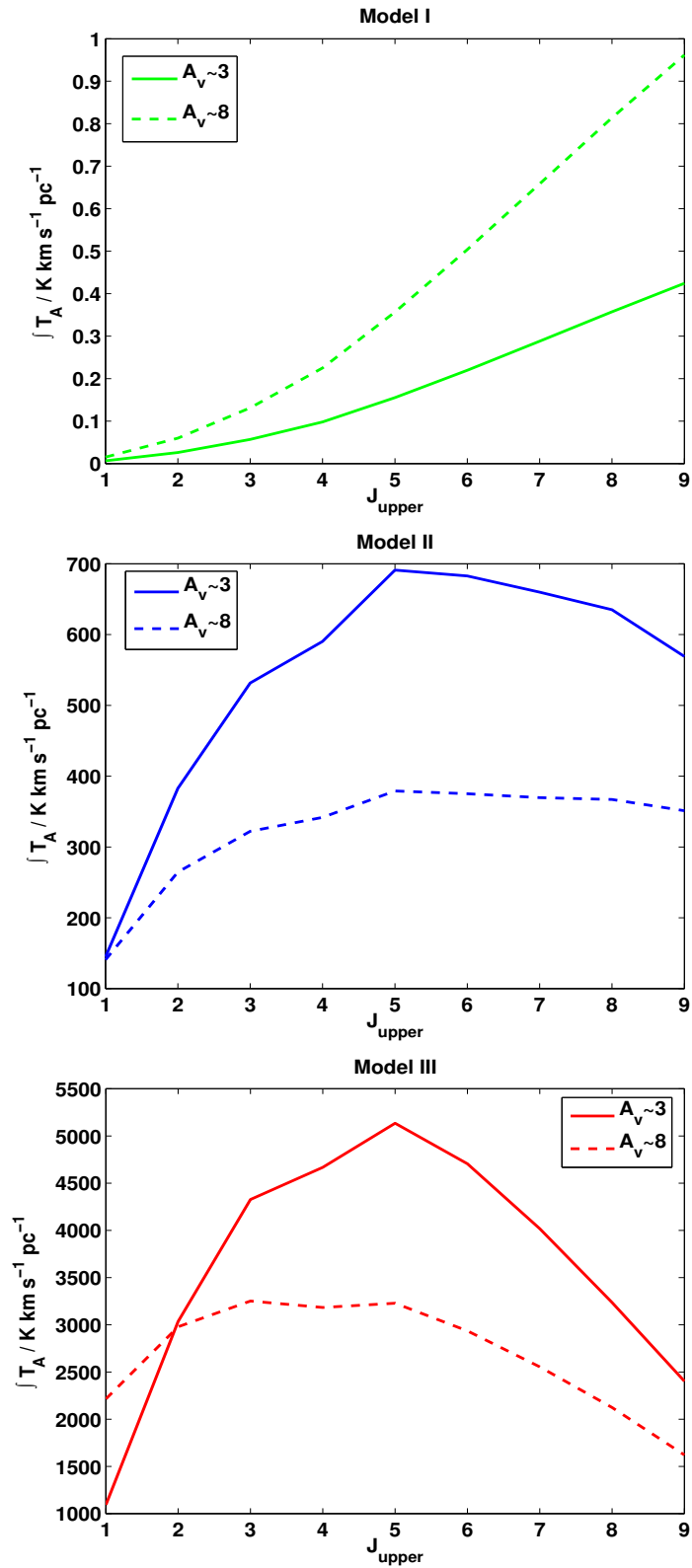
Figure 7.9: Variation of relative velocity integrated CO antenna temperatures for high redshift models (§ 7.4.5) at $A_v \sim 3$ (solid lines) and $A_v \sim 8$ (dashed lines).

destroy most of the CO, resulting in very low line intensities. The highest J transitions are found to be the brightest for this model but the temperatures associated with the lines are always very low probably indicating that such extreme conditions may be unphysical even in high redshift systems. Model II and Model III both have the same densities, cosmic ray fluxes and FUV fields, while Model II is at sub-solar metallicity, Model III has solar metallicity. The solar metallicity model is seen to produce brighter $\int (T_A)^{rel} dv$ than the sub-solar metallicity model. However, in both cases, it is the intermediate transitions that dominate the CO emission although the drop in the SED at high J is much sharper for the solar-metallicity model. At $A_v \sim 8$, the CO SED for Model II peaks at J=5 before remaining roughly constant whereas the CO SED for Model III drops significantly at high J at the same A_v. These trends may be used to distinguish between solar and sub-solar metallicity active galaxies at high redshift. Figure 7.9 clearly illustrates that the ratio of high-order CO transitions to the peak CO transition will be close to unity for physical conditions associated with an unbiased IMF at high redshift. However, this ratio is likely to be smaller (~ 0.5) for physical conditions associated with a top-heavy IMF at high redshift. Unless such low CO J-ratios are seen in active galaxies at high redshift, an unbiased IMF cannot be ruled out. Note however that the physical conditions assumed in the models in this chapter seem necessary but may not be sufficient to produce the IMFs associated with them in § 7.4.5. Also, in § 7.4.2, it was concluded that sub-solar metallicity counterparts of Milky Way type galaxies may also produce top-heavy IMFs but in this case the ratio of the high-J CO lines to the peak CO line is likely to be close to unity. Larger ratios of the CO high-J to peak transitions therefore seem to imply that the galaxy is at sub-solar metallicity and while such galaxies with normal levels of cosmic ray ionisation and FUV flux show evidence for producing top-heavy IMFs, the same galaxies at high-redshifts with elevated cosmic ray and FUV fluxes, may produce unbiased IMFs. The high-J to peak CO ratio therefore provides an useful indication of the metallicity of a galaxy and assuming it is known whether the galaxy is active, e.g., due to the presence of an AGN or starburst nucleus, the form of the IMF may be crudely inferred.

In Figure 7.10 variations in the relative velocity integrated antenna temperatures are shown for the three models as a function of depth within the cloud. In all three models, the CO rotational lines get brighter with increasing depth within the cloud. Note that due to the differing number densities and metallicities of each model, the same A_v corresponds to different physical distances for these models and figure 7.11 illustrates the relationship between A_v and size of the emitting region for the high redshift models.

The difference in the relative velocity integrated antenna temperatures of Model II (sub-solar
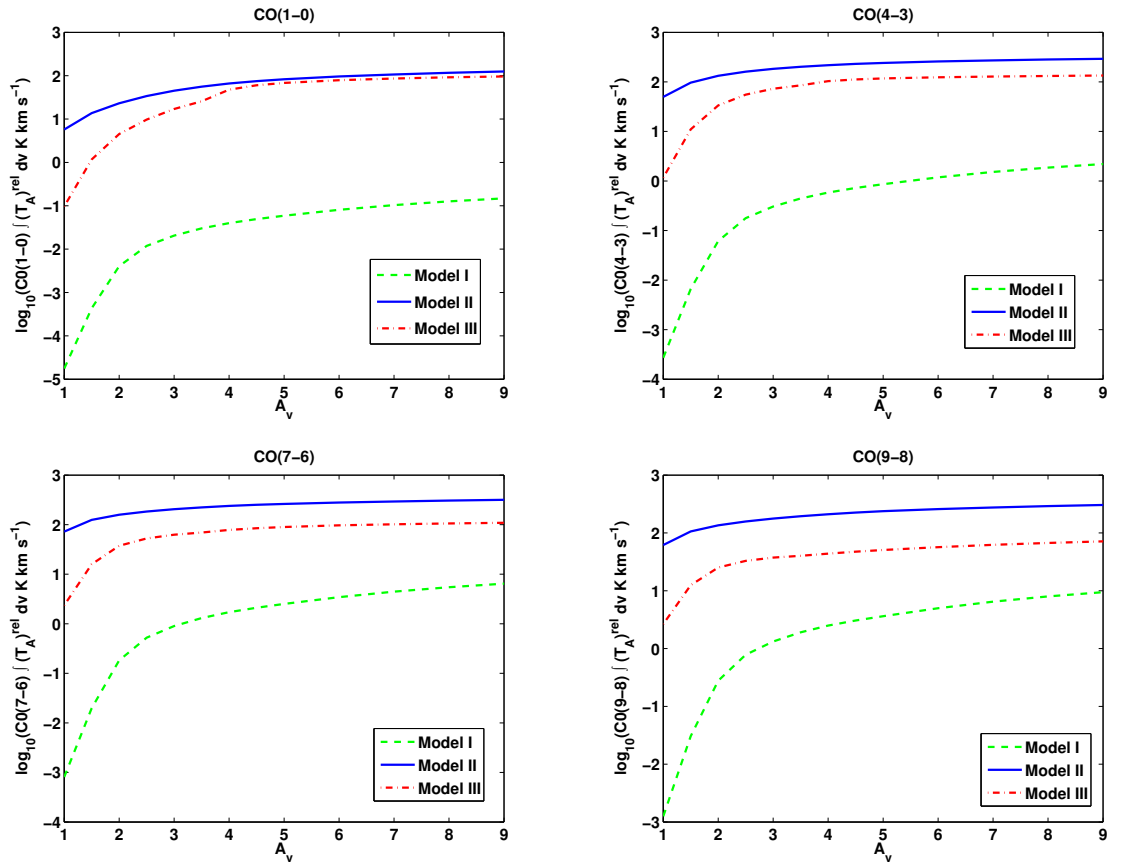
Figure 7.10: Variation of relative velocity integrated CO antenna temperatures with A_v for high redshift models described in § 7.4.5.

metallicity and unbiased IMF) and Model III (solar metallicity, top-heavy IMF) is greater for the higher order CO transitions deep within the cloud. At $A_v \gtrsim 4$, the temperatures associated with the CO(1-0) line for Model II and Model III are almost the same. However, the emitting region in Model II is several orders of magnitude larger than in Model III. The CO(7-6) or CO(9-8) transition on the other hand produces markedly different antenna temperatures at all depths for the three high-redshift models.

7.5.6 Comparison to Observations

As previously mentioned, ^{12}CO line ratios are a good way of comparing theoretical predictions directly to observations. In this section, I consider line ratios for two types of observed extragalactic sources using where available line intensities or integrated temperatures measured through the same beam size for calculating these ratios. Once again it is emphasised that none of the models
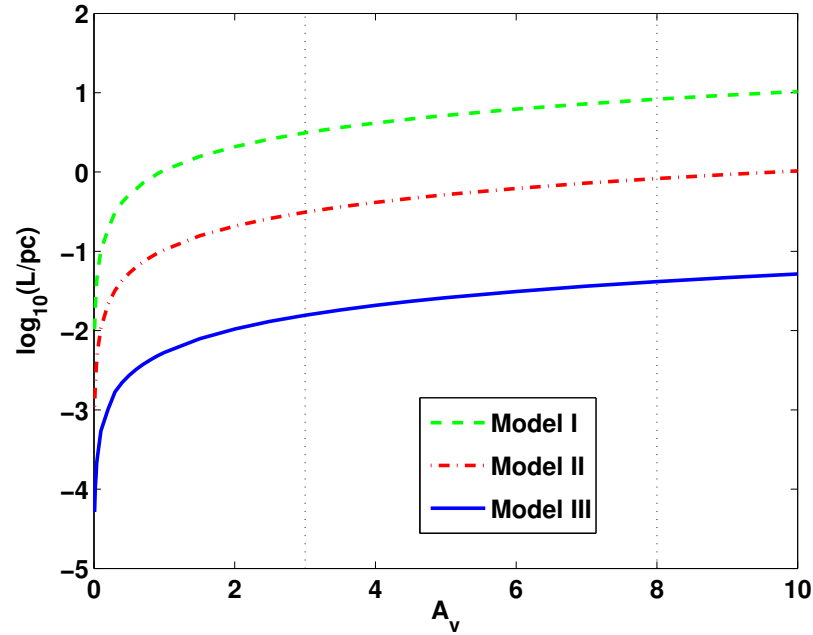
Figure 7.11: Relationship between the size of the emitting region and the visual extinction, A_v for our three high redshift models. The dotted lines correspond to the two A_vs at which we consider our outputs.

mimic the exact physical conditions in the galaxies described in this section. Rather, they may crudely represent the average conditions within a PDR in a galaxy of that type.

7.5.6.1 Nearby Starburst Galaxies - e.g. NGC253

The nearby starburst galaxy NGC253 has been extensively mapped in ^{12}CO emission by various authors (Bayet *et al.* 2004; Bradford *et al.* 2003; Güsten *et al.* 2006). Bradford *et al.* (2003) compute line intensities for various CO transitions corrected to a 15" beam. These values are used from their Table 3 (Column 6) to derive line intensity ratios for a few of the CO lines and observed line intensity ratios are found to be: $\frac{CO(2-1)}{CO(1-0)} \sim 8.0$ and $\frac{CO(7-6)}{CO(4-3)} \sim 3.3$. In § 7.4.2, NGC253 was cited as an example of a galaxy with a high cosmic-ray ionisation rate due to the presence of a starburst nucleus. The cosmic ray ionisation rate for this galaxy is thought to be ~ 800 times greater than in the Galaxy (Bradford *et al.* 2003). The theoretical line intensity ratios derived from a model with a cosmic-ray ionisation rate of $\zeta = 10^{-14}$ s^{-1} described in § 7.4.3 are $\frac{CO(2-1)}{CO(1-0)} \sim 8.3$ and $\frac{CO(7-6)}{CO(4-3)} \sim 4.1$ at $A_v \sim 8$. Taking the ratio of intensities from Table 3 of Bayet *et al.* (2004), $\frac{CO(2-1)}{CO(1-0)}$ is found to be ~ 9.3 for a beam size of 23" (Mauersberger *et al.* 1996; Harrison *et al.*

1999) in both cases and $\frac{CO(7-6)}{CO(4-3)} \sim 4.5$ for a beam size of 21.9" (Güsten *et al.* 1993) in both cases. The ratio of fluxes given in Table 1 of Güsten *et al.* (2006) gives $\frac{CO(7-6)}{CO(4-3)} \sim 2$. Given that we have not attempted to accurately model the physical conditions of this particular galaxy, the agreement between the observed and theoretical results is remarkably good. Note that these ratios are the ratios of the line intensities, I, rather than the velocity integrated temperature plotted in the figures as only the intensities in Table 3 of Bradford *et al.* (2003) are all corrected to the same beam size. The ratios of the velocity integrated temperatures agree with those in Bayet *et al.* (2004) to the same level as the intensity ratios. The predicted line intensities and ratios also agree with the theoretical work of Meijerink *et al.* (2006) (Tables 2, 3 and 4) who have looked at the effect of high cosmic-ray ionisation rates and FUV radiation fields on the ^{12}CO lines.

7.5.6.2   High Redshift Galaxies - e.g. Cloverleaf

The gravitationally lensed QSO, Cloverleaf (H1413+117) at a redshift of ~ 2.5, was cited as an example of a high-redshift source in § 7.4.5. Barvainis *et al.* (1997) report CO observations for this source and find the CO(4-3) line to be the strongest line in terms of the brightness temperature. These authors compute brightness temperature ratios of $\frac{CO(3-2)}{CO(4-3)} = 0.83 \pm 0.16$, $\frac{CO(5-4)}{CO(4-3)} = 0.73 \pm 0.16$ and $\frac{CO(7-6)}{CO(4-3)} = 0.68 \pm 0.13$ relative to the brightest line. There is therefore, a definite drop in the ratios relative to the brightest line when going from the low-J to the high-J transitions in this source. Figure 7.9 shows that for Model II at both $A_v \sim 3$ and $A_v \sim 8$ as well as Model III at $A_v \sim 3$, the CO(5-4) line is the strongest line. For Model III at $A_v \sim 8$, the CO(3-2) line is marginally brighter than the CO(4-3) line and is now the strongest line. I compute ratios relative to the brightest line for both the high redshift models II and III. For Model II which shows little evidence for having a high-mass biased IMF, the ratios go from ~ 0.7 for the low-J transitions to ~ 1 for the CO(7-6) transition relative to the brightest line. For Model III which has some of the physical conditions necessary for producing a top-heavy IMF, the ratios go from ~ 0.9 for the low-J transitions to ~ 0.7 for the CO(7-6) line relative to the brightest line. Thus, the trends predicted by Model III seem to match the observations for this source better than those predicted by Model II. Once again, it should be emphasised that no attempt has been made in the models to match the physical conditions for this source in any way whatsoever or to try and reproduce the observed SED of this galaxy. However, this theoretical work does present some evidence, albeit speculative, that the Cloverleaf source at redshift ~ 2.5 has roughly solar metallicity and potentially a top-heavy IMF. Very recently, the observational work of Bradford *et al.* (2009) has presented some evidence that the IMF is indeed top-heavy in this source and it is expected that future observational studies

will be able to further test the validity of this prediction.

7.6 Molecular Tracers of the IMF at High-z

Although the focus of the latter half of this chapter has been on the ^{12}CO SED associated with different physical conditions, the UCL_PDR code includes a network of 83 chemical species whose abundances are also output by the code. This section considers how the fractional abundances of some of these different molecular species that could potentially be observed with future surveys, change for different IMFs at high redshift. The fractional abundance is defined to be the abundance of the molecule relative to the total hydrogen abundance, $n_H = n(H) + n(H_2)$. Once again Models I, II and III in § 7.4.5 are studied. In Table 7.2 the fractional abundances of some key species are listed for all three models both at $A_v \sim 3$ and $A_v \sim 8$ typical of the translucent gas component and dense PDR gas component of galaxies respectively. In Figure 7.12 the variation of the molecular abundances of these species is also plotted as a function of depth inside the cloud for the different high-redshift models.

Table 7.2: Fractional Molecular Abundances for different IMF Models

Molecule	Model I		Model II		Model III	
	$A_v \sim 3$	$A_v \sim 8$	$A_v \sim 3$	$A_v \sim 8$	$A_v \sim 3$	$A_v \sim 8$
HCN	5.598×10^{-15}	2.813×10^{-14}	6.931×10^{-12}	2.869×10^{-9}	4.753×10^{-10}	2.253×10^{-9}
HNC	6.284×10^{-17}	3.498×10^{-17}	1.475×10^{-11}	1.770×10^{-9}	4.753×10^{-10}	2.655×10^{-9}
CS	2.905×10^{-18}	7.077×10^{-18}	2.316×10^{-13}	6.405×10^{-12}	9.496×10^{-10}	3.719×10^{-10}
CN	3.008×10^{-13}	1.153×10^{-12}	2.094×10^{-10}	4.474×10^{-9}	4.029×10^{-8}	1.758×10^{-9}
HCO^+	3.279×10^{-13}	2.685×10^{-13}	1.553×10^{-9}	1.438×10^{-8}	1.413×10^{-10}	7.832×10^{-8}
CO	8.037×10^{-9}	1.050×10^{-8}	5.063×10^{-6}	5.591×10^{-6}	3.183×10^{-5}	1.397×10^{-4}

From Table 7.2 and Figure 7.12, the following trends are observed. Assuming a limit of detectability of 10^{-12} in fractional abundance which is arbitrary but roughly satisfied in our own galaxy (Bayet *et al.* 2009), all the species apart from CO are below this limit for Model I where the extremely high cosmic ray fluxes and FUV fields serve to destroy molecules effectively even deep within the cloud. Note that these qualitative results do not change if a slightly higher or lower detectability limit is assumed.

For Model III, the fractional abundances of all molecules considered here are above the detectability limit even at low A_v where we normally do not expect complex molecules to be present. However, the high density in this model means that the systems considered here are always likely to be compact rather than diffuse and the size of the cloud is smaller than for any of the other high redshift models at a given A_v as is illustrated by Figure 7.11. The high fractional abundance of CO in this model also traces a high abundance of H_2 even at small A_v as illustrated by Figure 7.13.

While HCN and HNC are detectable in Model III at all A_v, these molecules only start becoming detectable in Model II at $A_v \sim 2$. However, the size of the emitting region in Model II is much larger than in Model III. At high A_v, the abundances of both HCN and HNC are almost the same in Models II and III corresponding to unbiased and high-mass biased IMFs respectively.

The abundance of CO and CS is found to scale linearly with the metallicity - these abundances are about two orders of magnitude greater for Model III compared to Model II at all depths and the metallicity in Model III is also about two orders of magnitude greater than in Model II. A detection of CS at a much higher level than otherwise expected in a high redshift active galaxy, may therefore signal that it is at roughly solar metallicity and has some of the physical conditions necessary for producing a top-heavy IMF. However, note that the predicted CS fractional abundance may be sensitive to the assumed initial abundance of sulphur in the models which is taken to be 2×10^{-7} here. This fractional abundance reproduces roughly the observed abundance of CS seen in TMC-1 (Ohishi & Kaifu 1998) but is still highly uncertain (Ruffle *et al.* 1999). These results for the abundance of CO and CS are consistent with the findings of Bayet *et al.* (2009) who use the same UCL_PDR code as in this work. These authors have studied the molecular tracers of various PDR dominated galaxies with different physical conditions. For a density of 10^4 cm^{-3}, a cosmic ray ionisation rate of 5×10^{-17} s^{-1} and a FUV radiation field strength of $\chi = 1.7 \times 10^3$, they find that CO and CS are linear tracers of the metallicity while CN and HCN are relatively insensitive to the metallicity. For $A_v \gtrsim 5$, the CN and HCN abundance are indeed found to be roughly the same for Models II and III. However, at lower A_v, both CN and HCN are much more abundant in Model III.
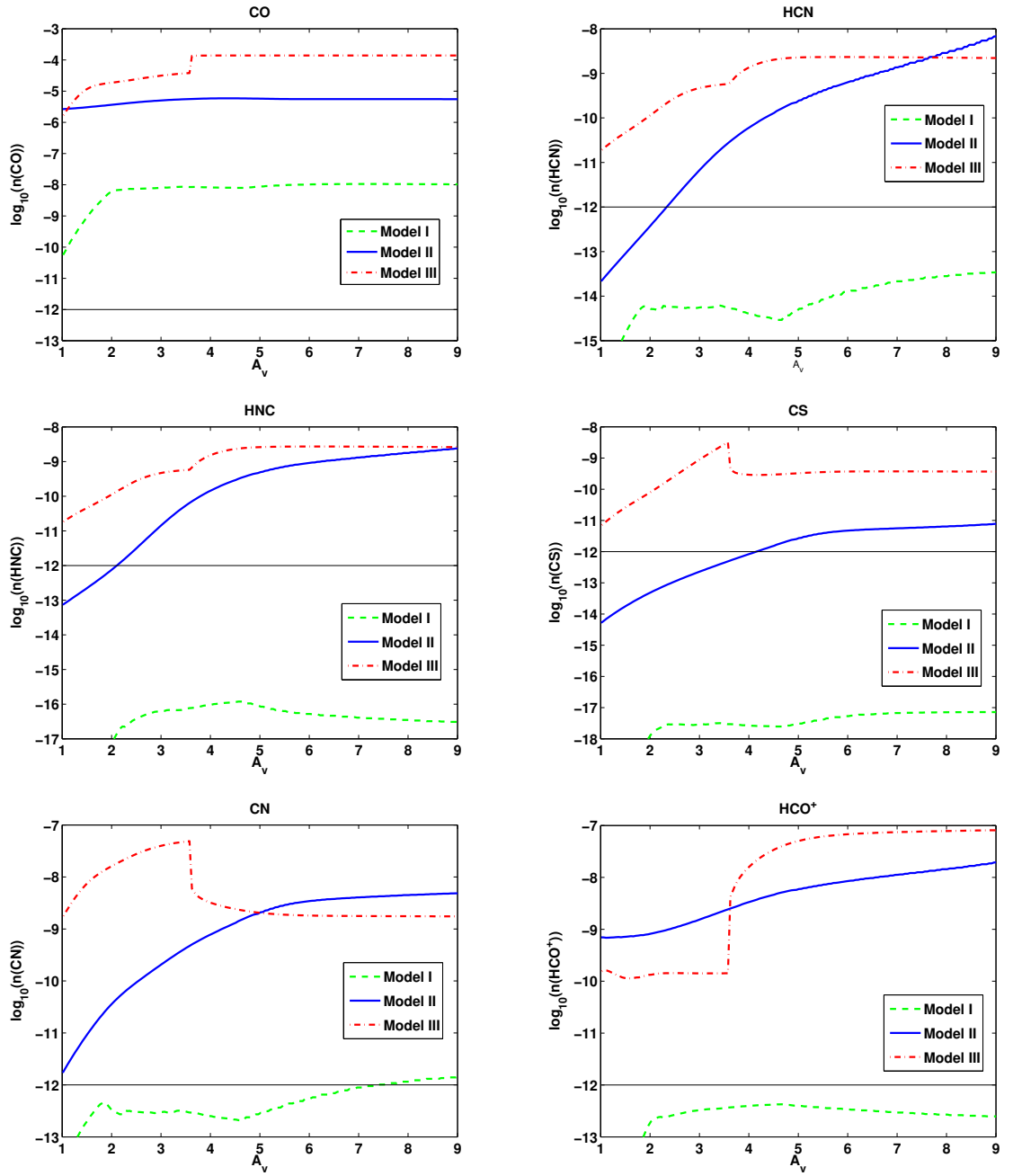
Figure 7.12: Variation of fractional abundances of different molecular species with depth, A_v for high-redshift models (Table 7.1). The solid black line indicates the assumed limit of detectability of 10^{-12}
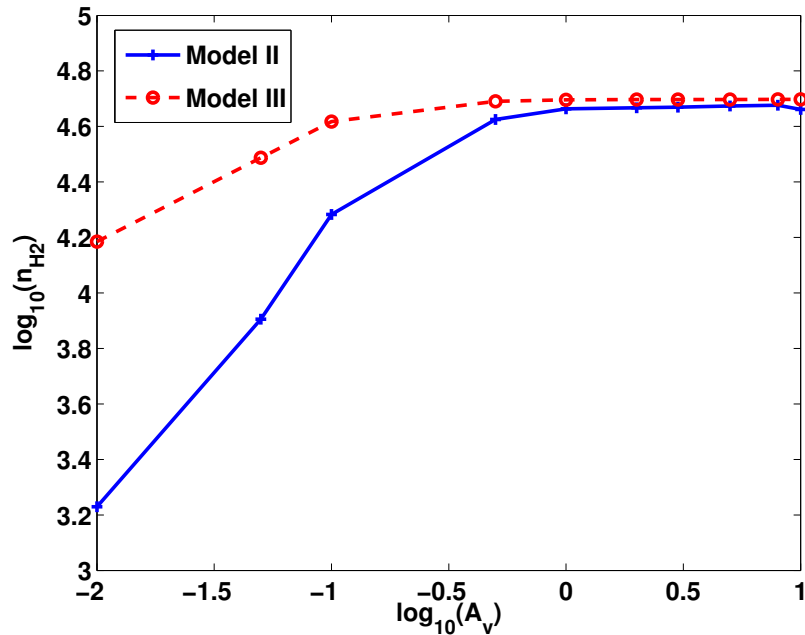
Figure 7.13: The number density of H_2 as a function of A_v in high redshift models II and III.

The trend of HCO$^+$ with A_v provides another possibly interesting diagnostic for different IMFs at high redshift. This molecule is more abundant at low A_v ($A_v \lesssim 3.5$) in the sub-solar metallicity model which is thought to produce an unbiased IMF. However at $A_v \gtrsim 3.5$ it becomes more abundant in the solar metallicity model which is thought to produce a top-heavy IMF. For Model III, there is an obvious change in the chemistry at $A_v \sim 3.5$ and a sharp change in the abundance of all the molecules is seen at this A_v. It is well known that the attenuation of the FUV flux with distance in a photon-dominated region, produces a characteristic depth dependent chemical structure with well-defined chemical zones. At $A_v \sim 3.5$ in this model, we witness the transition from a cloud layer of singly ionized carbon produced by photo-ionization of carbon atoms by the FUV photons, to a layer where most of the atomic carbon becomes locked up in the stable molecule CO due to the inability of the FUV field to penetrate the cloud further. It should be noted that in both of the other high redshift models, which are at sub-solar metallicities, this transition between chemical zones is not seen to occur within the A_v range considered in Figure 7.12.

Although the variation of molecular fractional abundances with A_v demonstrates some interesting differences between the various IMF models, in reality these trends may be hard to observe.

Most observations of extragalactic sources lead to measurements of the total column density of different molecules integrated over the depth of the cloud. Therefore, the observed column density of molecules such as HCO^+ for example in two extragalactic sources with different IMFs may actually be very similar and therefore not a good diagnostic for the form of the IMF.

7.7 Conclusions

If top-heavy IMFs arise from the suppression of low-mass star formation then the galactic physical conditions that inhibit star formation may be crudely defined. Physical conditions in which low-mass star formation is permitted are here assumed to give rise to unbiased IMFs. Since the physical conditions determine the chemistry, potential molecular diagnostics of various types of IMF can be deduced. This study of low-mass star formation in extragalactic environments leads to the following specific conclusions:

- Increasing the density results in the cooling time becoming longer than the free-fall time, so that cores tend to heat up and star formation is inhibited. Assuming that the microscopic properties of dust are similar in extragalactic environments to that in our own galaxy, it is found that the formation of molecular ices is likely to occur at all densities between 100 cm^{-3} and 10^6 cm^{-3}. The ambipolar diffusion timescale is comparable to the free-fall time except at very low densities where it is much longer, suggesting that low mass star-formation is allowed in magnetically sub-critical clouds with densities above 10^3 cm^{-3}.

- Low metallicity systems are characterised by long cooling times compared to the free-fall timescale. Collapsing cores tend to heat up thus inhibiting star formation and collapse. These physical conditions may therefore be suitable for the production of a top-heavy IMF. Due to the low dust grain number density, the desorption time is much shorter than the freeze-out time in low metallicity systems and there is less ice formation than in the Milky Way.

- High cosmic ray ionisation rates and high FUV radiation field strengths are associated with the presence of massive stars. Such systems show rapid cooling times compared to their free-fall timescales and star formation is unimpeded by thermal pressure. The propensity for ice formation is reduced in systems with cosmic ray ionisation rates that are much larger than those in the Milky Way. Freeze-out occurs over long timescales and if any ice was formed, it would evaporate quickly; molecular coolants would be returned to the ISM fur-

ther increasing the star formation efficiency. The freeze-out and desorption timescales are comparable for systems at almost all FUV radiation field strengths so that icy mantles are able to form except at very high values of χ. The ambipolar diffusion timescale is very long for high values of the cosmic ray ionisation rate and radiation field strength. This implies that star-formation may not be viable in clouds that are magnetically sub-critical under these conditions.

- High redshift systems are characterised by high cosmic ray fluxes and FUV radiation field strengths and can be considered to exist at a range of metallicities. All such systems will show enhanced low-mass star formation with the propensity for star formation increasing with the metallicity of the galaxy provided thermal pressure dominates the magnetic pressure. This is certainly shown to be the case in active high redshift galaxies at sub-solar metallicities. However, in active galaxies at solar metallicities, the magnetic field can impede the formation of low-mass stars resulting in a high-mass biased stellar IMF.

While this study is relatively crude in nature, it is instructive in terms of making some predictions about essentially unobservable low-mass star formation in extragalactic environments that are different from our own Galaxy. The kinds of systems in which star formation is likely to be enhanced or inhibited have been defined by considering changes in various timescales relevant for star formation. It has been found, among other things, that low-mass star formation is likely to be encouraged in host galaxies of massive stars and AGN and inhibited in low metallicity systems with low cosmic ray fluxes and FUV radiation field strengths. This study finds some evidence for a top-heavy stellar IMF at high redshifts but only if galaxies at high redshift are considered to be at near solar metallicities.

The sensitivity of the ^{12}CO rotational spectrum to changes in gas number density, metallicity, and cosmic ray and far-UV fluxes are presented and used as a basis for predicting the relative velocity-integrated antenna temperature of the CO rotational spectrum in three models of high redshift active galaxies. While active galaxies with near-solar metallicity (and top-heavy IMFs) produce higher antenna temperatures than those with sub-solar metallicity (and unbiased IMFs) the actual rotational distribution is fairly similar. In sub-solar metallicity counterparts of Milky Way type galaxies, the high-J to peak CO line ratio approaches unity. These physical conditions are thought to produce top-heavy IMFs. However, sub-solar metallicity active galaxies at high redshift also have high-J to peak CO line ratios that approach unity and these physical conditions are thought to produce unbiased IMFs. Solar metallicity active galaxies at high redshift have high-

J to peak CO ratios that drop well below unity and these conditions may produce top-heavy IMFs. The form of the CO SED therefore clearly depends strongly on the metallicity of the galaxy and provided it is known whether the galaxy is active or quiescent, the form of the IMF that may be produced under such physical conditions, can be crudely inferred. High order CO transitions are also found to provide a good diagnostic for high far-UV intensity and low metallicity counterparts of Milky Way type systems both of which show some evidence for producing high-mass biased stellar IMFs.

It is shown that the theoretical predictions for the ^{12}CO rotational spectrum can be matched to observed line ratios of different kinds of extragalactic sources both nearby and in the distant Universe. Potentially exciting new evidence is presented for the Cloverleaf QSO at z$\sim$ 2.5 having the physical conditions necessary for producing a top-heavy IMF. This is consistent with the work of Davé (2008); Wilkins *et al.* (2008) and van Dokkum (2008) who require a top-heavy IMF at $z > 1$ and very recent observations also suggest that the Cloverleaf QSO does indeed have a top-heavy IMF (Bradford *et al.* 2009) - a result that will undoubtedly be further tested with future projects such as ALMA.

Molecular tracers of dense gas are predicted to differ markedly between galaxies with top-heavy and unbiased IMFs. In particular, CO and CS differ significantly over the A_v range 1 to 9 visual magnitudes with these molecules acting as linear tracers of the metallicity. As solar metallicity active galaxies at high redshift are thought to have physical conditions necessary for a top-heavy IMF, detection of elevated levels of CO and CS in high-redshift active galaxies may signal that such physical conditions exist in these sources. HCN, HNC and CN differ between solar and sub-solar metallicity active galaxies at high redshift for small visual extinctions but at large depths, these molecules are found to be independent of the IMF shape. Finally, HCO$^+$ is more abundant in active galaxies with unbiased IMFs at low A_v but, at high A_v, the abundance of this molecule is greater in active galaxies with top-heavy IMFs. Unless the A_v of the host galaxy can be directly measured, this molecule is probably not a good diagnostic for the shape of the IMF as the integrated HCO$^+$ column density that would arise from the two high-redshift models II and III with different IMFs, would probably be very similar.

It can therefore be seen that chemistry may provide a simple and independent means of determining the approximate nature of the IMF of a high redshift galaxy.

SUMMARY AND FUTURE WORK

In this thesis I have explored the properties of distant galaxies in our Universe, in particular their colours, redshifts, morphologies and star formation processes within them. Much of the work carried out has been in the context of current and future astronomical surveys whether they be wide-field imaging surveys from the ground or space that aim to understand the mysterious properties of dark energy or deep spectroscopic surveys that will fathom the processes of galaxy formation and evolution or radio and sub-mm surveys that will allow us to better understand star formation.

8.1 Photometric Redshifts

The first part of the thesis (Chapters 2 to 4) is concerned with photometric redshift estimation techniques. A comparison of different photometric redshift methods on a sample of Luminous Red Galaxies has shown that there still exist many differences between the methods that need to be well understood. While training set methods perform well in regimes where a complete and representative training set is available, template-based codes overtake them when this is no longer the case. If photometric redshift estimates are to be rendered reliable in the future, a more thorough comparison of codes needs to be undertaken and I am currently participating in such a comparison through the Photometric Redshift Accuracy Testing Program (PHAT). The field is also slowly moving towards the development of more *hybrid* template and training methods for photometric redshift estimation but much work still remains to be done in this area. In particular some of the issues that need to be addressed include modifying training set methods such as artificial neural networks to output the full probability distribution associated with each photo-z estimate as well as devising better error diagnostics for photometric redshift estimates.

Recent applications of photometric redshift methods to cosmological studies has illustrated that the most relevant question is not "What is the best photo-z one can estimate?" but rather "Is the photo-z accuracy sufficient to achieve the desired science goal?". In the case of future surveys such as the Dark Energy Survey and Euclid for which I have undertaken preliminary design studies in this thesis, the goal is the calibration of the dark energy equation of state parameter, w at the percent level using various cosmological probes such as galaxy clustering, weak gravitational lensing, galaxy cluster counts and Type 1a supernovae. For these purposes, the machine-learning algorithm, ANNz used in most of this thesis has been shown to perform with reasonable success. Using this neural network method and combining data from the near infra-red Vista Hemisphere Survey to the optical data from the Dark Energy Survey allows for an improvement in the photometric redshift scatter of ∼30% in the redshift range $1 < z < 2$. I have introduced a method for removing catastrophic outliers by *clipping* photo-z catalogues according to their photometric errors. Clipping the catalogue as opposed to using the entire sample has allowed for an improvement of ∼15-20% in the fractional error on the galaxy power spectrum computed using the DES+VHS dataset out to a redshift of 2. I have shown that in the absence of large spectroscopic surveys, the DES+VHS datasets, when combined, will therefore prove extremely effective in constraining dark energy through large-scale structure signals in the galaxy power spectrum.

I have also shown in Chapter 4 that the choice of filters can be crucial to the photo-z accuracy and there is a trade-off between depth in each filter and the colour information gained by having a larger number of filters. A deep optical ground-based survey like LSST has been shown to provide the ideal complement to a space-based near infra-red survey such as Euclid in terms of photometric redshift performance although a survey like DES would also suffice. For shallower ground-based optical surveys such as PS1, considerable exposure in the space-based near infra-red filters will be required to match the required photometric redshift precision. Both the DES+VHS and Euclid design studies have focussed on photometric redshift estimation for field galaxies but new approaches for estimating the photometric redshifts of clusters of galaxies as well as hosts of Type 1a supernovae will also need to be tested for future cosmological surveys such as these.

Much of the focus of the first part of this thesis has also been on the availability of spectroscopic training sets for future surveys. I have shown that if an incomplete training set is used to determine photometric redshifts for a testing set that has not been cut to match the training set, the resulting uncertainties in the photometric redshift bias could lead to errors in w of the order of 10 percent for a DES+VHS type survey. For a Euclid type survey, of the order of 10^5 spectroscopic redshifts will be required for calibration of the photometric redshift estimate. The crucial role that

current data sets play in calibrating future surveys is clearly demonstrated.

8.2 Machine Learning Approaches to Morphological Classification

Another example of an application where current data sets prove invaluable for future surveys is in the morphological classification of astronomical objects. In Chapter 5, almost 1 million astronomical objects in the Sloan Digital Sky Survey are classified using an artificial neural network. These objects have already been visually classified by over 100,000 users as part of the Galaxy Zoo project. This vast sample of visually classified objects provides an invaluable training set for machine-learning codes and I have shown that by training on ∼10% of this sample, an artificial neural network is able to reproduce the classifications for the remaining objects into three classes - ellipticals, spirals and stars - to an accuracy of better than 90%. Furthermore, if the parameters used as inputs to the neural network are chosen to be distance independant e.g colours rather than magnitudes and ratios of radii rather than the absolute radius, the neural network output is not affected by using a training set that is incomplete in magnitude. While this study has shown that the Galaxy Zoo dataset provides a promising training set for automated morphological classification in future surveys, more work remains to be done. For example, other sources of incompleteness also need to be investigated. In particular, it would be interesting to investigate the success of the neural network in identifying blue ellipticals and red spirals as well as other unusual objects when such objects are likely to only sparsely populate the training sets. Moving to high-redshift sources means one also has to deal with seeing limited samples of galaxies and machine-learning codes need to be adapted for such purposes (Huertas-Company *et al.* 2008).

Finally, in this work only parameters derived from astronomical images have been used for morphological classification. Much of the work in this thesis has demonstrated the considerable wealth of information contained in astronomical spectra as compared to images. A logical progression of this work would therefore be to apply machine-learning algorithms to galaxy spectra for the purposes of morphological classification and to determine what combination of images and spectra allows for the most accurate classifications of astronomical objects.

8.3 Massive Red Galaxies and the Stellar Mass Function

In Chapters 6 and 7, I move from statistical studies of distant galaxy populations, to studying the astrophysical processes within them. I start by looking at the evolution of a sample of luminous

red galaxies from the 2dF and SDSS LRG and QSO survey. This sample of LRGs occupies a very unique position within current massive galaxy samples. Firstly, the galaxies occupy a very large volume. I study 8625 LRGs over a survey area of 186 deg^2 in the redshift range $0.4 \leq z < 0.8$. This massive volume makes it unlikely that any of the properties inferred from this sample are affected by large-scale structure and cosmic variance. Secondly, all galaxies in the sample have secure spectroscopic redshifts. Finally, a sizeable subset of the LRGs also have near infra-red photometry available from the UKIDSS Large Area Survey making it possible to estimate stellar masses for these objects. I consider the evolution of the luminosity function and stellar mass function of these objects over this redshift range and find not only that these galaxies show very little evidence for recent star formation, but also that galaxies with stellar masses of greater than $3 \times 10^{11} M_\odot$ were already well assembled at redshifts of 0.8. This observational result presents a significant challenge for current models of galaxy formation which predict that galaxies that reside in the most massive halos are built up through successive mergers of smaller objects until the present day.

In Chapter 6, I also show how colour selected samples of galaxies such as the LRGs which also have non-negligible photometric errors may be contaminated by other sources. This contamination presents a significant problem for some luminosity function estimators such as the STY estimator which can be biased as a result of the photometric errors. In the future, I propose to develop a more robust maximum likelihood estimator for luminosity function estimates of such samples. This will be done by using Monte Carlo techniques to study the selection function of LRGs with non-negligible photometric errors as already discussed in Chapter 6. Finally, in Chapter 2 I have presented the MegaZLRG DR6 photo-z catalogue of LRGs constructed using the 2SLAQ galaxies as a training set. In the future, I hope to use this larger catalogue of 1.5M LRGs to estimate the LRG luminosity and mass functions after deconvolving the photo-z errors according to the method of Sheth (2007). The photo-z errors for this sample have already been well quantified in Chapter 2 of this thesis.

The final part of Chapter 6 studies the evolution of the LRG mass function. Estimates of the stellar mass-to-light ratio and therefore the mass function are shown to be sensitive to the choice of the stellar initial mass function the form of which still remains highly debated, particularly in high redshift systems. In Chapter 7, I present an alternative way of deriving the approximate shape of the stellar IMF by considering the balance of timescales associated with low-mass star forma-tion in different extragalactic environments. These timescales are calculated from the outputs of a radiative transfer model for photon-dominated regions within galaxies. I find that while low metal-

licity systems with normal levels of cosmic ray and FUV flux show evidence for low-mass star formation being impeded by thermal pressure resulting in a top-heavy IMF, the same metallicity active galaxies such as those likely to be found at high redshifts, will probably have an unbiased IMF. In fact active galaxies at nearly solar metallicities show the necessary physical conditions required to halt low-mass star formation through magnetic pressure resulting in a top-heavy IMF. However, these physical conditions may not be sufficient for such an IMF to be present. The last part of Chapter 7 explores trends in molecular emission resulting from these different IMFs. I find that while active galaxies at sub-solar metallicities have high-J to peak CO line ratios of close to unity, the same galaxies at solar metallicities have much lower high-J to peak CO line ratios. The solar metallicity active galaxies also show evidence for elevated levels of the molecules CO and CS. Detections of these molecules in anomalously large quantities in high redshift active galaxies may therefore signal the presence of a top-heavy IMF.

In Chapter 7 I have shown that PDR models can be successfully applied to galaxies in the distant Universe and provide a plethora of information about the astrochemistry of such systems. In the future, I hope to apply these models to massive galaxies such as those studied in Chapters 2 and 6. As already pointed out in this thesis, the formation of such galaxies presents a major conundrum for current theories of galaxy formation. Depending on whether these galaxies were assembled through dry or wet mergers, we would expect them to have very different astrochemical signatures. I propose to use the PDR model used in Chapter 7 to predict the chemical signatures associated with both intense bursts of star formation arising from gas rich mergers as well as those associated with gas poor mergers. By matching these theoretical predictions to observations, we can hope to understand the formation and assembly of the most massive galaxies in our Universe.

We are now entering a new age of astronomical surveys. The plethora of astronomical data that will overwhelm us in coming years covering the entire range of the electromagnetic spectrum and pushing the boundaries of our observable Universe, will need to be fully exploited if we are to make new strides in the fields of observational cosmology and galaxy evolution. In this thesis I have presented some ideas for studying distant galaxies in our Universe using future astronomical surveys. These studies have ranged from photometric redshift estimation and dark energy constraints using optical and near infra-red wide field imaging surveys to studying star formation processes in galaxies using radio and sub-mm surveys. In this chapter, I have concluded this thesis by also presenting some ideas for future work that can be undertaken and results that will be interesting to follow-up in coming years in order that the full potential of future astronomical surveys

can be extracted.

Bibliography

Aarseth, S. J., 2003, *Gravitational N-Body Simulations*

Abazajian et al., 2009, *ApJS*, **182**, 543

Abdalla, F. B., Amara, A., Capak, P., Cypriano, E. S., Lahav, O. & Rhodes, J., 2008*a*, *MNRAS*, **387**, 969

Abdalla, F. B., Banerji, M., Lahav, O. & Rashkov, V., 2008*b*, *ArXiv e-prints*

Abel, T., Bryan, G. L. & Norman, M. L., 2002, *Science*, **295**, 93

Allen, C. W., 1976, *Astrophysical Quantities*

Alongi, M., Bertelli, G., Bressan, A., Chiosi, C., Fagotto, F., Greggio, L. & Nasi, E., 1993, *A&AS*, **97**, 851

Amara, A. & Réfrégier, A., 2007, *MNRAS*, **381**, 1018

Annis, J., Bridle, S., Castander, F. J., Evrard, A. E., Fosalba, P., Frieman, J. A., Gaztanaga, E., Jain, B., Kravtsov, A. V., Lahav, O., Lin, H., Mohr, J., Stebbins, A., Walker, T. P., Wechsler, R. H., Weinberg, D. H. & Weller, J., 2005, *ArXiv Astrophysics e-prints*

Arnaboldi et al., 2007, *The Messenger*, **127**, 28

Assef, R. J., Kochanek, C. S., Brodwin, M., Brown, M. J. I., Caldwell, N., Cool, R. J., Eisenhardt, P., Eisenstein, D., Gonzalez, A. H., Jannuzi, B. T., Jones, C., McKenzie, E., Murray, S. S. & Stern, D., 2008, *ApJ*, **676**, 286

Athreya, R. M., Kapahi, V. K., McCarthy, P. J. & van Breugel, W., 1998, *A&A*, **329**, 809

Bacon, D. J., Refregier, A. R. & Ellis, R. S., 2000, *MNRAS*, **318**, 625

Bailer-Jones, C. A. L., Irwin, M. & von Hippel, T., 1998, *MNRAS*, **298**, 361

Baldry, I. K. & Glazebrook, K., 2003, *ApJ*, **593**, 258

Baldry, I. K., Glazebrook, K., Brinkmann, J., Ivezić, Ž., Lupton, R. H., Nichol, R. C. & Szalay, A. S., 2004, *ApJ*, **600**, 681

Ball, N. M., Loveday, J., Fukugita, M., Nakamura, O., Okamura, S., Brinkmann, J. & Brunner, R. J., 2004, *MNRAS*, **348**, 1038

Banerji, M., Abdalla, F. B., Lahav, O. & Lin, H., 2008, *MNRAS*, **386**, 1219

Banerji, M., Viti, S. & Williams, D. A., 2009*a*, *ApJ*, **703**, 2249

Banerji, M., Viti, S., Williams, D. A. & Rawlings, J. M. C., 2009*b*, *ApJ*, **692**, 283

Barvainis, R., Maloney, P., Antonucci, R. & Alloin, D., 1997, **484**, 695

Bassett, B. A., Nichol, B. & Eisenstein, D. J., 2005, *Astronomy and Geophysics*, **46**, 26

Bate, M. R., Bonnell, I. A. & Bromm, V., 2003, *MNRAS*, **339**, 577

Baugh, C. M., Lacey, C. G., Frenk, C. S., Granato, G. L., Silva, L., Bressan, A., Benson, A. J. & Cole, S., 2005, *MNRAS*, **356**, 1191

Baum, W. A., 1962, in G. C. McVittie (ed.), *Problems of Extra-Galactic Research*, volume 15 of *IAU Symposium*, pp. 390–+

Bayet, E., Gerin, M., Phillips, T. G. & Contursi, A., 2004, **427**, 45

Bayet, E., Gerin, M., Phillips, T. G. & Contursi, A., 2006, **460**, 467

Bayet, E., Lintott, C., Viti, S., Martín-Pintado, J., Martín, S., Williams, D. A. & Rawlings, J. M. C., 2008*a*, *ApJL*, **685**, L35

Bayet, E., Viti, S., Williams, D. A. & Rawlings, J. M. C., 2008*b*, *ApJ*, **676**, 978

Bayet, E., Viti, S., Williams, D. A., Rawlings, J. M. C. & Bell, T., 2009, **696**, 1466

Beck, R., Fletcher, A., Shukurov, A., Snodin, A., Sokoloff, D. D., Ehle, M., Moss, D. & Shoutenkov, V., 2005, *A&A*, **444**, 739

Bell, E. F., Wolf, C., Meisenheimer, K., Rix, H.-W., Borch, A., Dye, S., Kleinheinrich, M., Wisotzki, L. & McIntosh, D. H., 2004, *ApJ*, **608**, 752

Bell, T. A., Roueff, E., Viti, S. & Williams, D. A., 2006, *MNRAS*, **371**, 1865

Bell, T. A., Viti, S. & Williams, D. A., 2007, *MNRAS*, **378**, 983

Benítez, N., 2000, *ApJ*, **536**, 571

Bennett, C. L., Halpern, M., Hinshaw, G., Jarosik, N., Kogut, A., Limon, M., Meyer, S. S., Page, L., Spergel, D. N., Tucker, G. S., Wollack, E., Wright, E. L., Barnes, C., Greason, M. R., Hill, R. S., Komatsu, E., Nolta, M. R., Odegard, N., Peiris, H. V., Verde, L. & Weiland, J. L., 2003, *ApJS*, **148**, 1

Bernardi, M., Sheth, R. K., Nichol, R. C., Schneider, D. P. & Brinkmann, J., 2005, *AJ*, **129**, 61

Bernstein, G. M. & Jarvis, M., 2002, *AJ*, **123**, 583

Bertoldi, F., Cox, P., Neri, R., Carilli, C. L., Walter, F., Omont, A., Beelen, A., Henkel, C., Fan, X., Strauss, M. A. & Menten, K. M., 2003, *A&A*, **409**, L47

Bishop, C. M., 1995, *Neural Networks for Pattern Recognition (New York: Oxford Univ. Press)*

Blake, C. & Bridle, S., 2005, *MNRAS*, **363**, 1329

Blake, C., Collister, A., Bridle, S. & Lahav, O., 2007, *MNRAS*, **374**, 1527

Blake, C., Collister, A. & Lahav, O., 2008, *MNRAS*, **385**, 1257

Blake, C. & Glazebrook, K., 2003, *ApJ*, **594**, 665

Blake et al., 2006, *MNRAS*, **365**, 255

Blanton, M. R. & Roweis, S., 2007, *AJ*, **133**, 734

Bolzonella, M., Miralles, J. M. & Pelló, R., 2000, *A&A*, **363**, 476

Borch, A., Meisenheimer, K., Bell, E. F., Rix, H.-W., Wolf, C., Dye, S., Kleinheinrich, M., Kovacs, Z. & Wisotzki, L., 2006, *A&A*, **453**, 869

Bourke, T. L., Myers, P. C., Robinson, G. & Hyland, A. R., 2001, *ApJ*, **554**, 916

Bower, R. G., Benson, A. J., Malbon, R., Helly, J. C., Frenk, C. S., Baugh, C. M., Cole, S. & Lacey, C. G., 2006, *MNRAS*, **370**, 645

Bower, R. G., Lucey, J. R. & Ellis, R. S., 1992, *MNRAS*, **254**, 601

Bradford, C. M., Aguirre, J. E., Aikin, R., Bock, J. J., Earle, L., Glenn, J., Inami, H., Maloney, P. R., Matsuhara, H., Naylor, B. J., Nguyen, H. T. & Zmuidzinas, J., 2009, *ArXiv e-prints*

Bradford, C. M., Nikola, T., Stacey, G. J., Bolatto, A. D., Jackson, J. M., Savage, M. L., Davidson, J. A. & Higdon, S. J., 2003, *ApJ*, **586**, 891

Brammer, G. B., van Dokkum, P. G. & Coppi, P., 2008, *ApJ*, **686**, 1503

Bressan, A., Fagotto, F., Bertelli, G. & Chiosi, C., 1993, *A&AS*, **100**, 647

Bromm, V., Coppi, P. S. & Larson, R. B., 1999, *ApJL*, **527**, L5

Bruzual, A. G., 2007, in A. Vazdekis & R. F. Peletier (eds.), *IAU Symposium*, volume 241 of *IAU Symposium*, pp. 125–132

Bruzual, A. G. & Charlot, S., 1993, *ApJ*, **405**, 538

Bruzual, G. & Charlot, S., 2003, *MNRAS*, **344**, 1000

Budavári et. al, 1999, in R. Weymann, L. Storrie-Lombardi, M. Sawicki & R. Brunner (eds.), *Photometric Redshifts and the Detection of High Redshift Galaxies*, volume 191 of *Astronomical Society of the Pacific Conference Series*, pp. 19–+

Cabré, A. & Gaztañaga, E., 2009, *MNRAS*, **393**, 1183

Calder, L. & Lahav, O., 2008, *Astronomy and Geophysics*, **49**(1), 010000

Calzetti, D., 1997, *AJ*, **113**, 162

Calzetti, D., Kinney, A. L. & Storchi-Bergmann, T., 1994, *ApJ*, **429**, 582

Calzetti et al., 2000, *ApJ*, **533**, 682

Cannon, R., Drinkwater, M., Edge, A., Eisenstein, D., Nichol, R., Outram, P., Pimbblet, K., de Propris, R., Roseboom, I., Wake, D., Allen, P., Bland-Hawthorn, J., Bridges, T., Carson, D., Chiu, K., Colless, M., Couch, W., Croom, S., Driver, S., Fine, S., Hewett, P., Loveday, J., Ross, N., Sadler, E. M., Shanks, T., Sharp, R., Smith, J. A., Stoughton, C., Weilbacher, P., Brunner, R. J., Meiksin, A. & Schneider, D. P., 2006, *MNRAS*, **372**, 425

Capak et al., 2004, *AJ*, **127**, 180

Cappellari, M., Bacon, R., Bureau, M., Damen, M. C., Davies, R. L., de Zeeuw, P. T., Emsellem, E., Falcón-Barroso, J., Krajnović, D., Kuntschner, H., McDermid, R. M., Peletier, R. F., Sarzi, M., van den Bosch, R. C. E. & van de Ven, G., 2006, *MNRAS*, **366**, 1126

Carilli, C. L., Walter, F., Wang, R., Wootten, A., Menten, K., Bertoldi, F., Schinnerer, E., Cox, P., Beelen, A. & Omont, A., 2008, *ApSS*, **313**, 307

Carliles, S., Budavári, T., Heinis, S., Priebe, C. & Szalay, A., 2008, in R. W. Argyle, P. S. Bunclark & J. R. Lewis (eds.), *Astronomical Data Analysis Software and Systems XVII*, volume 394 of *Astronomical Society of the Pacific Conference Series*, pp. 521–+

Carroll, S. M., Press, W. H. & Turner, E. L., 1992, *ArA&A*, **30**, 499

Chabrier, G., 2003, *PASP*, **115**, 763

Charbonnel, C., Meynet, G., Maeder, A. & Schaerer, D., 1996, *A&AS*, **115**, 339

Chary, R.-R., Stern, D. & Eisenhardt, P., 2005, *ApJL*, **635**, L5

Cimatti, A., Daddi, E. & Renzini, A., 2006, *A&A*, **453**, L29

Cole, S., Percival, W. J., Peacock, J. A., Norberg, P., Baugh, C. M., Frenk, C. S., Baldry, I., Bland-Hawthorn, J., Bridges, T., Cannon, R., Colless, M., Collins, C., Couch, W., Cross, N. J. G., Dalton, G., Eke, V. R., De Propris, R., Driver, S. P., Efstathiou, G., Ellis, R. S., Glazebrook, K., Jackson, C., Jenkins, A., Lahav, O., Lewis, I., Lumsden, S., Maddox, S., Madgwick, D., Peterson, B. A., Sutherland, W. & Taylor, K., 2005, *MNRAS*, **362**, 505

Coleman, G. D., Wu, C. C. & Weedman, D. W., 1980, *ApJS*, **43**, 393

Collister, A., Lahav, O., Blake, C., Cannon, R., Croom, S., Drinkwater, M., Edge, A., Eisenstein, D., Loveday, J., Nichol, R., Pimbblet, K., de Propris, R., Roseboom, I., Ross, N., Schneider, D. P., Shanks, T. & Wake, D., 2007, *MNRAS*, **375**, 68

Collister, A. A. & Lahav, O., 2004, *PASP*, **116**, 345

Connolly, A. J., Szalay, A. S. & Brunner, R. J., 1998, *ApJL*, **499**, L125+

Connolly et al., 1995, *AJ*, **110**, 2655

Conselice, C. J., Bundy, K., Trujillo, I., Coil, A., Eisenhardt, P., Ellis, R. S., Georgakakis, A., Huang, J., Lotz, J., Nandra, K., Newman, J., Papovich, C., Weiner, B. & Willmer, C., 2007, *MNRAS*, **381**, 962

Cool, R. J., Eisenstein, D. J., Fan, X., Fukugita, M., Jiang, L., Maraston, C., Meiksin, A., Schneider, D. P. & Wake, D. A., 2008, *ApJ*, **682**, 919

Cowie, L. L., Barger, A. J., Hu, E. M., Capak, P. & Songaila, A., 2004, *AJ*, **127**, 3137

Croton, D. J., Springel, V., White, S. D. M., De Lucia, G., Frenk, C. S., Gao, L., Jenkins, A., Kauffmann, G., Navarro, J. F. & Yoshida, N., 2006, *MNRAS*, **365**, 11

Crutcher, R. M., 1999, *ApJ*, **520**, 706

Crutcher, R. M., Troland, T. H. & Kazes, I., 1987, *A&A*, **181**, 119

Daddi, E., Dannerbauer, H., Krips, M., Walter, F., Dickinson, M., Elbaz, D. & Morrison, G. E., 2009, *ArXiv e-prints*

Dame, T. M., Hartmann, D. & Thaddeus, P., 2001, **547**, 792

Darg, D. W., Kaviraj, S., Lintott, C. J., Schawinski, K., Sarzi, M., Bamford, S., Silk, J., Proctor, R., Andreescu, D., Murray, P., Nichol, R. C., Raddick, M. J., Slosar, A., Szalay, A. S., Thomas, D. & Vandenberg, J., 2009, *ArXiv e-prints*

Davé, R., 2008, *MNRAS*, **385**, 147

Davis et al., 2003, in P. Guhathakurta (ed.), *Discoveries and Research Prospects from 6- to 10-Meter-Class Telescopes II. Edited by Guhathakurta, Puragra. Proceedings of the SPIE, Volume 4834, pp. 161-172 (2003).*, volume 4834 of *Presented at the Society of Photo-Optical Instrumentation Engineers (SPIE) Conference*, pp. 161–172

de Jong, T., Boland, W. & Dalgarno, A., 1980, *A&A*, **91**, 68

De Lucia, G., Springel, V., White, S. D. M., Croton, D. & Kauffmann, G., 2006, *MNRAS*, **366**, 499

Dekel, A., Birnboim, Y., Engel, G., Freundlich, J., Goerdt, T., Mumcuoglu, M., Neistein, E., Pichon, C., Teyssier, R. & Zinger, E., 2009, *Nature*, **457**, 451

Dicke, R. H., Peebles, P. J. E., Roll, P. G. & Wilkinson, D. T., 1965, *ApJ*, **142**, 414

Draine, B. T., 1978, *ApJS*, **36**, 595

Dressler, A., 1980, *ApJ*, **236**, 351

Dunkley, J., Komatsu, E., Nolta, M. R., Spergel, D. N., Larson, D., Hinshaw, G., Page, L., Bennett, C. L., Gold, B., Jarosik, N., Weiland, J. L., Halpern, M., Hill, R. S., Kogut, A., Limon, M., Meyer, S. S., Tucker, G. S., Wollack, E. & Wright, E. L., 2009, *ApJS*, **180**, 306

Dyson, J. E. & Williams, D. A., 1997, *The physics of the interstellar medium* (The physics of the interstellar medium. Edition: 2nd ed. Publisher: Bristol: Institute of Physics Publishing, 1997. Edited by J. E. Dyson and D. A. Williams. Series: The graduate series in astronomy. ISBN: 0750303069)

Efstathiou, G., Sutherland, W. J. & Maddox, S. J., 1990, *Nature*, **348**, 705

Eisenstein, D. J., Annis, J., Gunn, J. E., Szalay, A. S., Connolly, A. J., Nichol, R. C., Bahcall, N. A., Bernardi, M., Burles, S., Castander, F. J., Fukugita, M., Hogg, D. W., Ivezić, Ž., Knapp, G. R., Lupton, R. H., Narayanan, V., Postman, M., Reichart, D. E., Richmond, M., Schneider, D. P., Schlegel, D. J., Strauss, M. A., SubbaRao, M., Tucker, D. L., Vanden Berk, D., Vogeley, M. S., Weinberg, D. H. & Yanny, B., 2001, *AJ*, **122**, 2267

Eisenstein, D. J. & Hu, W., 1998, *ApJ*, **496**, 605

Eisenstein et al., 2005, *ApJ*, **633**, 560

Elmegreen, B. G., 2000, *ApJ*, **530**, 277

Elmegreen, B. G., 2008, *ArXiv e-prints*

Faber, S. M., Willmer, C. N. A., Wolf, C., Koo, D. C., Weiner, B. J., Newman, J. A., Im, M., Coil, A. L., Conroy, C., Cooper, M. C., Davis, M., Finkbeiner, D. P., Gerke, B. F., Gebhardt, K., Groth, E. J., Guhathakurta, P., Harker, J., Kaiser, N., Kassin, S., Kleinheinrich, M., Konidaris, N. P., Kron, R. G., Lin, L., Luppino, G., Madgwick, D. S., Meisenheimer, K., Noeske, K. G., Phillips, A. C., Sarajedini, V. L., Schiavon, R. P., Simard, L., Szalay, A. S., Vogt, N. P. & Yan, R., 2007, *ApJ*, **665**, 265

Feldman, H. A., Kaiser, N. & Peacock, J. A., 1994, *ApJ*, **426**, 23

Feldmann, R., Carollo, C. M., Porciani, C., Lilly, S. J., Capak, P., Taniguchi, Y., Le Fèvre, O., Renzini, A., Scoville, N., Ajiki, M., Aussel, H., Contini, T., McCracken, H., Mobasher, B., Murayama, T., Sanders, D., Sasaki, S., Scarlata, C., Scodeggio, M., Shioya, Y., Silverman, J., Takahashi, M., Thompson, D. & Zamorani, G., 2006, *MNRAS*, **372**, 565

Ferreras, I., Lisker, T., Carollo, C. M., Lilly, S. J. & Mobasher, B., 2005, *ApJ*, **635**, 243

Ferreras, I., Lisker, T., Pasquali, A. & Kaviraj, S., 2009*a*, *MNRAS*, **395**, 554

Ferreras, I., Lisker, T., Pasquali, A., Khochfar, S. & Kaviraj, S., 2009*b*, *MNRAS*, **396**, 1573

Ferreras, I., Saha, P. & Burles, S., 2008, *MNRAS*, **383**, 857

Fioc, M. & Rocca-Volmerange, B., 1997, *A&A*, **326**, 950

Firth, A. E., Lahav, O. & Somerville, R. S., 2003, *MNRAS*, **339**, 1195

Fitzpatrick, E. L., 1986, *AJ*, **92**, 1068

Flower, D. R. & Launay, J. M., 1985, *MNRAS*, **214**, 271

Folkes, S. R., Lahav, O. & Maddox, S. J., 1996, *MNRAS*, **283**, 651

Fontana, A., Salimbeni, S., Grazian, A., Giallongo, E., Pentericci, L., Nonino, M., Fontanot, F., Menci, N., Monaco, P., Cristiani, S., Vanzella, E., de Santis, C. & Gallozzi, S., 2006, *A&A*, **459**, 745

Franx, M. & Illingworth, G., 1990, *ApJL*, **359**, L41

Fried, J. W., von Kuhlmann, B., Meisenheimer, K., Rix, H.-W., Wolf, C., Hippelein, H. H., Kümmel, M., Phleps, S., Röser, H. J., Thierring, I. & Maier, C., 2001, *A&A*, **367**, 788

Fukugita, M., Nakamura, O., Okamura, S., Yasuda, N., Barentine, J. C., Brinkmann, J., Gunn, J. E., Harvanek, M., Ichikawa, T., Lupton, R. H., Schneider, D. P., Strauss, M. A. & York, D. G., 2007, *AJ*, **134**, 579

Gallazzi, A., Charlot, S., Brinchmann, J. & White, S. D. M., 2006, *MNRAS*, **370**, 1106

Gao, Y. & Solomon, P. M., 2004, *ApJS*, **152**, 63

García-Burillo, S., Graciá-Carpio, J., Guélin, M., Neri, R., Cox, P., Planesas, P., Solomon, P. M., Tacconi, L. J. & Vanden Bout, P. A., 2006, *ApJL*, **645**, L17

Girardi, L., Bertelli, G., Bressan, A., Chiosi, C., Groenewegen, M. A. T., Marigo, P., Salasnich, B. & Weiss, A., 2002, *A&A*, **391**, 195

Girardi, L., Bressan, A., Chiosi, C., Bertelli, G. & Nasi, E., 1996, *A&AS*, **117**, 113

Glazebrook, K., Abraham, R. G., McCarthy, P. J., Savaglio, S., Chen, H.-W., Crampton, D., Murowinski, R., Jørgensen, I., Roth, K., Hook, I., Marzke, R. O. & Carlberg, R. G., 2004, *Nature*, **430**, 181

Granato, G. L., De Zotti, G., Silva, L., Bressan, A. & Danese, L., 2004, *ApJ*, **600**, 580

Green, S. & Chapman, S., 1978, *ApJS*, **37**, 169

Green, S. & Thaddeus, P., 1976, *ApJ*, **205**, 766

Güsten, R., Philipp, S. D., Weiß, A. & Klein, B., 2006, **454**, L115

Güsten, R., Serabyn, E., Kasemann, C., Schinckel, A., Schneider, G., Schulz, A. & Young, K., 1993, *ApJ*, **402**, 537

Guth, A. H., 1981, **23**, 347

Guth, A. H. & Tye, S.-H. H., 1980, *Physical Review Letters*, **44**, 963

Harrison, A., Henkel, C. & Russell, A., 1999, *MNRAS*, **303**, 157

Hartquist, T. W., Doyle, H. T. & Dalgarno, A., 1978, *A&A*, **68**, 65

Hartquist, T. W. & Williams, D. A., 1989, *MNRAS*, **241**, 417

Hewett, P. C., Warren, S. J., Leggett, S. K. & Hodgkin, S. T., 2006, *MNRAS*, **367**, 454

Hoekstra, H., Mellier, Y., van Waerbeke, L., Semboloni, E., Fu, L., Hudson, M. J., Parker, L. C., Tereno, I. & Benabed, K., 2006, *ApJ*, **647**, 116

Hopkins, A. M. & Beacom, J. F., 2006, *ApJ*, **651**, 142

Hubble, E. & Humason, M. L., 1931, *ApJ*, **74**, 43

Hubble, E. P., 1925, *The Observatory*, **48**, 139

Hubble, E. P., 1926, *ApJ*, **64**, 321

Huertas-Company, M., Rouan, D., Tasca, L., Soucail, G. & Le Fèvre, O., 2008, *A&A*, **478**, 971

Ilbert, O., Arnouts, S., McCracken, H. J., Bolzonella, M., Bertin, E., Le Fèvre, O., Mellier, Y., Zamorani, G., Pellò, R., Iovino, A., Tresse, L., Le Brun, V., Bottini, D., Garilli, B., Maccagni, D., Picat, J. P., Scaramella, R., Scodeggio, M., Vettolani, G., Zanichelli, A., Adami, C., Bardelli,

S., Cappi, A., Charlot, S., Ciliegi, P., Contini, T., Cucciati, O., Foucaud, S., Franzetti, P., Gavignaud, I., Guzzo, L., Marano, B., Marinoni, C., Mazure, A., Meneux, B., Merighi, R., Paltani, S., Pollo, A., Pozzetti, L., Radovich, M., Zucca, E., Bondi, M., Bongiorno, A., Busarello, G., de La Torre, S., Gregorini, L., Lamareille, F., Mathez, G., Merluzzi, P., Ripepi, V., Rizzo, D. & Vergani, D., 2006, *A&A*, **457**, 841

Ivezic, Z., Tyson, J. A., Allsman, R., Andrew, J., Angel, R. & for the LSST Collaboration, 2008, *ArXiv e-prints*

Kennicutt, Jr., R. C., 1983, *ApJ*, **272**, 54

Khochfar, S. & Burkert, A., 2005, *MNRAS*, **359**, 1379

Khochfar, S. & Silk, J., 2006, *MNRAS*, **370**, 902

Kim, K.-T., Kronberg, P. P., Dewdney, P. E. & Landecker, T. L., 1990, *ApJ*, **355**, 29

Kinney et al., 1996, *ApJ*, **467**, 38

Knudsen, K. K., Nerié, R., Kneib, J.-P. & van der Werf, P. P., 2009, **496**, 45

Kodama, T. & Arimoto, N., 1997, *A&A*, **320**, 41

Koo, D. C., 1999, in R. Weymann, L. Storrie-Lombardi, M. Sawicki & R. Brunner (eds.), *Photometric Redshifts and the Detection of High Redshift Galaxies*, volume 191 of *Astronomical Society of the Pacific Conference Series*, pp. 3–+

Kotulla, R., Fritze, U., Weilbacher, P. & Anders, P., 2009, *MNRAS*, **396**, 462

Kroupa, P., Tout, C. A. & Gilmore, G., 1993, *MNRAS*, **262**, 545

Kurtz, M. J., Geller, M. J., Fabricant, D. G., Wyatt, W. F. & Dell'Antonio, I. P., 2007, *AJ*, **134**, 1360

Lahav, O., Abdalla, F. B. & Banerji, M., 2009, *Chapter 13: Photometric Redshift Estimation Methods, Bayesian Methods in Cosmology (CUP)*

Lahav, O., Naim, A., Buta, R. J., Corwin, H. G., de Vaucouleurs, G., Dressler, A., Huchra, J. P., van den Bergh, S., Raychaudhury, S., Sodre, Jr., L. & Storrie-Lombardi, M. C., 1995, *Science*, **267**, 859

Lahav, O., Naim, A., Sodré, Jr., L. & Storrie-Lombardi, M. C., 1996, *MNRAS*, **283**, 207

Land, K., Slosar, A., Lintott, C., Andreescu, D., Bamford, S., Murray, P., Nichol, R., Raddick, M. J., Schawinski, K., Szalay, A., Thomas, D. & Vandenberg, J., 2008, *MNRAS*, **388**, 1686

Larson, R. B., 1975, *MNRAS*, **173**, 671

Le Fèvre et al., 2004, *A&A*, **428**, 1043

Le Fèvre et al., 2005, *A&A*, **439**, 845

Le Teuff, Y. H., Millar, T. J. & Markwick, A. J., 2000, *A&AS*, **146**, 157

Leitherer, C., Schaerer, D., Goldader, J. D., Delgado, R. M. G., Robert, C., Kune, D. F., de Mello, D. F., Devost, D. & Heckman, T. M., 1999, *ApJS*, **123**, 3

Lejeune, T., Cuisinier, F. & Buser, R., 1997, *A&AS*, **125**, 229

Lejeune, T., Cuisinier, F. & Buser, R., 1998, *A&AS*, **130**, 65

Lilly, S. J., Le Fevre, O., Hammer, F. & Crampton, D., 1996, *ApJL*, **460**, L1+

Lima, M., Cunha, C. E., Oyaizu, H., Frieman, J., Lin, H. & Sheldon, E. S., 2008, *MNRAS*, **390**, 118

Lin, H., Cunha, C., Lima, M., Oyaizu, H., Frieman, J., Collister, A., Lahav, O. & Dark Energy Survey, 2004*a*, in *Bulletin of the American Astronomical Society*, volume 36 of *Bulletin of the American Astronomical Society*, pp. 1462–+

Lin, H., Yee, H. K. C., Carlberg, R. G., Morris, S. L., Sawicki, M., Patton, D. R., Wirth, G. & Shepherd, C. W., 1999, *ApJ*, **518**, 533

Lin, L., Koo, D. C., Willmer, C. N. A., Patton, D. R., Conselice, C. J., Yan, R., Coil, A. L., Cooper, M. C., Davis, M., Faber, S. M., Gerke, B. F., Guhathakurta, P. & Newman, J. A., 2004*b*, *ApJL*, **617**, L9

Lintott, C. J., Schawinski, K., Slosar, A., Land, K., Bamford, S., Thomas, D., Raddick, M. J., Nichol, R. C., Szalay, A., Andreescu, D., Murray, P. & Vandenberg, J., 2008, *MNRAS*, **389**, 1179

Lutz, D., Sturm, E., Tacconi, L. J., Valiante, E., Schweitzer, M., Netzer, H., Maiolino, R., Andreani, P., Shemmer, O. & Veilleux, S., 2007, *ApJL*, **661**, L25

Ma, Z., Hu, W. & Huterer, D., 2006, *ApJ*, **636**, 21

Mac Low, M.-M. & Klessen, R. S., 2004, *Reviews of Modern Physics*, **76**, 125

Madau, P., 1995, *ApJ*, **441**, 18

Madau, P., Ferguson, H. C., Dickinson, M. E., Giavalisco, M., Steidel, C. C. & Fruchter, A., 1996, *MNRAS*, **283**, 1388

Maraston, C., 1998, *MNRAS*, **300**, 872

Maraston, C., 2005, *MNRAS*, **362**, 799

Maraston, C., Strömbäck, G., Thomas, D., Wake, D. A. & Nichol, R. C., 2009, *MNRAS*, **394**, L107

Mauersberger, R., Henkel, C., Wielebinski, R., Wiklind, T. & Reuter, H.-P., 1996, *A&A*, **305**, 421

McKee, C. F. & Ostriker, E. C., 2007, *ArA&A*, **45**, 565

Meijerink, R., Spaans, M. & Israel, F. P., 2006, *ApJL*, **650**, L103

Mestel, L., 1999, *Stellar magnetism*

Mignoli, M., Cimatti, A., Zamorani, G., Pozzetti, L., Daddi, E., Renzini, A., Broadhurst, T., Cristiani, S., D'Odorico, S., Fontana, A., Giallongo, E., Gilmozzi, R., Menci, N. & Saracco, P., 2005, *A&A*, **437**, 883

Mouschovias, T. C., 1976, *ApJ*, **207**, 141

Mouschovias, T. C., 1979, *ApJ*, **228**, 475

Mouschovias, T. C. & Ciolek, G. E., 1999, in C. J. Lada & N. D. Kylafis (eds.), *NATO ASIC Proc. 540: The Origin of Stars and Planetary Systems*, pp. 305–+

Mouschovias, T. C. & Spitzer, Jr., L., 1976, *ApJ*, **210**, 326

Naim, A., Lahav, O., Sodre, Jr., L. & Storrie-Lombardi, M. C., 1995, *MNRAS*, **275**, 567

Nesvadba, N. P. H., Neri, R., De Breuck, C., Lehnert, M. D., Downes, D., Walter, F., Omont, A., Boulanger, F. & Seymour, N., 2009, *Monthly Notices of the Royal Astronomical Society*, L208+

Newman, J. A., 2008, *ApJ*, **684**, 88

Ohishi, M. & Kaifu, N., 1998, in *Chemistry and Physics of Molecules and Grains in Space. Faraday Discussions No. 109*, pp. 205–+

Ostriker, J. P. & Steinhardt, P. J., 1995, *Nature*, **377**, 600

Oyaizu, H., Cunha, C., Lima, M., Lin, H. & Frieman, J., 2006, in *American Astronomical Society Meeting Abstracts*, volume 208 of *American Astronomical Society Meeting Abstracts*, pp. 60.03—+

Oyaizu, H., Lima, M., Cunha, C. E., Lin, H. & Frieman, J., 2008*a*, *ApJ*, **689**, 709

Oyaizu, H., Lima, M., Cunha, C. E., Lin, H., Frieman, J. & Sheldon, E. S., 2008*b*, *ApJ*, **674**, 768

Padmanabhan, N., Budavári, T., Schlegel, D. J., Bridges, T., Brinkmann, J., Cannon, R., Connolly, A. J., Croom, S. M., Csabai, I., Drinkwater, M., Eisenstein, D. J., Hewett, P. C., Loveday, J., Nichol, R. C., Pimbblet, K. A., De Propris, R., Schneider, D. P., Scranton, R., Seljak, U., Shanks, T., Szapudi, I., Szalay, A. S. & Wake, D., 2005, *MNRAS*, **359**, 237

Penzias, A. A. & Wilson, R. W., 1965, *ApJ*, **142**, 419

Percival, W. J., Nichol, R. C., Eisenstein, D. J., Frieman, J. A., Fukugita, M., Loveday, J., Pope, A. C., Schneider, D. P., Szalay, A. S., Tegmark, M., Vogeley, M. S., Weinberg, D. H., Zehavi, I., Bahcall, N. A., Brinkmann, J., Connolly, A. J. & Meiksin, A., 2007, *ApJ*, **657**, 645

Perlmutter, S., Aldering, G., Goldhaber, G., Knop, R. A., Nugent, P., Castro, P. G., Deustua, S., Fabbro, S., Goobar, A., Groom, D. E., Hook, I. M., Kim, A. G., Kim, M. Y., Lee, J. C., Nunes, N. J., Pain, R., Pennypacker, C. R., Quimby, R., Lidman, C., Ellis, R. S., Irwin, M., McMahon, R. G., Ruiz-Lapuente, P., Walton, N., Schaefer, B., Boyle, B. J., Filippenko, A. V., Matheson, T., Fruchter, A. S., Panagia, N., Newberg, H. J. M., Couch, W. J. & The Supernova Cosmology Project, 1999, *ApJ*, **517**, 565

Poggianti, B. M., Bressan, A. & Franceschini, A., 2001, *ApJ*, **550**, 195

Poli et al., 2003, *ApJL*, **593**, L1

Pozzetti et al., 2009, *ArXiv e-prints*

Prevot, M. L., Lequeux, J., Prevot, L., Maurice, E. & Rocca-Volmerange, B., 1984, *A&A*, **132**, 389

Price, D. J. & Bate, M. R., 2007, *MNRAS*, **377**, 77

Prugniel, P. & Soubiran, C., 2001, *A&A*, **369**, 1048

Rawlings, J. M. C., Hartquist, T. W., Menten, K. M. & Williams, D. A., 1992, *MNRAS*, **255**, 471

Redman, M. P., Rawlings, J. M. C., Nutter, D. J., Ward-Thompson, D. & Williams, D. A., 2002, *MNRAS*, **337**, L17

Riess et al., 1998, *AJ*, **116**, 1009

Ripley, B. D., 1981, *Spatial statistics*

Ripley, B. D., 1988, *Statistical inference for spatial processes*

Roberts, J. F., Rawlings, J. M. C., Viti, S. & Williams, D. A., 2007, *MNRAS*, **382**, 733

Röllig, M., Abel, N. P., Bell, T., Bensch, F., Black, J., Ferland, G. J., Jonkheid, B., Kamp, I., Kaufman, M. J., Le Bourlot, J., Le Petit, F., Meijerink, R., Morata, O., Ossenkopf, V., Roueff, E., Shaw, G., Spaans, M., Sternberg, A., Stutzki, J., Thi, W.-F., van Dishoeck, E. F., van Hoof, P. A. M., Viti, S. & Wolfire, M. G., 2007, *A&A*, **467**, 187

Roseboom et al., 2006, *MNRAS*, **373**, 349

Rowan-Robinson, M., 2003, *MNRAS*, **345**, 819

Ruffle, D. P., Hartquist, T. W., Caselli, P. & Williams, D. A., 1999, *MNRAS*, **306**, 691

Sakamoto, S., 1999, **523**, 701

Salpeter, E. E., 1955, *ApJ*, **121**, 161

Sandage, A., Tammann, G. A. & Yahil, A., 1979, *ApJ*, **232**, 352

Scarlata, C., Carollo, C. M., Lilly, S. J., Feldmann, R., Kampczyk, P., Renzini, A., Cimatti, A., Halliday, C., Daddi, E., Sargent, M. T., Koekemoer, A., Scoville, N., Kneib, J.-P., Leauthaud, A., Massey, R., Rhodes, J., Tasca, L., Capak, P., McCracken, H. J., Mobasher, B., Taniguchi, Y., Thompson, D., Ajiki, M., Aussel, H., Murayama, T., Sanders, D. B., Sasaki, S., Shioya, Y. & Takahashi, M., 2007, *ApJS*, **172**, 494

Schaller, G., Schaerer, D., Meynet, G. & Maeder, A., 1992, *A&AS*, **96**, 269

Schawinski, K., Lintott, C., Thomas, D., Sarzi, M., Andreescu, D., Bamford, S. P., Kaviraj, S., Khochfar, S., Land, K., Murray, P., Nichol, R. C., Raddick, M. J., Slosar, A., Szalay, A., Vandenberg, J. & Yi, S. K., 2009, *MNRAS*, **396**, 818

Schawinski, K., Thomas, D., Sarzi, M., Maraston, C., Kaviraj, S., Joo, S.-J., Yi, S. K. & Silk, J., 2007, *MNRAS*, **382**, 1415

Schlegel, D. J., Finkbeiner, D. P. & Davis, M., 1998, *ApJ*, **500**, 525

Schmidt, B. P., Suntzeff, N. B., Phillips, M. M., Schommer, R. A., Clocchiatti, A., Kirshner, R. P., Garnavich, P., Challis, P., Leibundgut, B., Spyromilio, J., Riess, A. G., Filippenko, A. V., Hamuy, M., Smith, R. C., Hogan, C., Stubbs, C., Diercks, A., Reiss, D., Gilliland, R., Tonry, J., Maza, J., Dressler, A., Walsh, J. & Ciardullo, R., 1998, *ApJ*, **507**, 46

Seaton, M. J., 1979, *MNRAS*, **187**, 73P

Seljak, U. & Zaldarriaga, M., 1996, *ApJ*, **469**, 437

Semboloni, E., Mellier, Y., van Waerbeke, L., Hoekstra, H., Tereno, I., Benabed, K., Gwyn, S. D. J., Fu, L., Hudson, M. J., Maoli, R. & Parker, L. C., 2006, *A&A*, **452**, 51

Seo, H.-J. & Eisenstein, D. J., 2003, *ApJ*, **598**, 720

Sheth, R. K., 2007, *MNRAS*, 402

Shimasaku, K., Fukugita, M., Doi, M., Hamabe, M., Ichikawa, T., Okamura, S., Sekiguchi, M., Yasuda, N., Brinkmann, J., Csabai, I., Ichikawa, S.-I., Ivezić, Z., Kunszt, P. Z., Schneider, D. P., Szokoly, G. P., Watanabe, M. & York, D. G., 2001, *AJ*, **122**, 1238

Silva, L., De Zotti, G., Granato, G. L., Maiolino, R. & Danese, L., 2005, *MNRAS*, **357**, 1295

Somerville, R. S., 1997, *Semi-Analytic Modeling of Galaxy Formation*, Ph.D. thesis, AA(UNIVERSITY OF CALIFORNIA, SANTA CRUZ)

Springel, V., White, S. D. M., Jenkins, A., Frenk, C. S., Yoshida, N., Gao, L., Navarro, J., Thacker, R., Croton, D., Helly, J., Peacock, J. A., Cole, S., Thomas, P., Couchman, H., Evrard, A., Colberg, J. & Pearce, F., 2005, *Nature*, **435**, 629

Stabenau, H. F., Connolly, A. & Jain, B., 2008, *MNRAS*, **387**, 1215

Stanford, S. A., Dickinson, M., Postman, M., Ferguson, H. C., Lucas, R. A., Conselice, C. J., Budavári, T. & Somerville, R., 2004, *AJ*, **127**, 131

Steidel, C. C., Adelberger, K. L., Giavalisco, M., Dickinson, M. & Pettini, M., 1999, *ApJ*, **519**, 1

Storrie-Lombardi, M. C., Lahav, O., Sodre, Jr., L. & Storrie-Lombardi, L. J., 1992, *MNRAS*, **259**, 8P

Strateva et al., 2001, *AJ*, **122**, 1861

Strong, A. W. & Mattox, J. R., 1996, **308**, L21

Suchkov, A., Allen, R. J. & Heckman, T. M., 1993, *ApJ*, **413**, 542

The Dark Energy Survey Collaboration, 2005, *ArXiv Astrophysics e-prints*

Tinsley, B. M., 1972*a*, *A&A*, **20**, 383

Tinsley, B. M., 1972*b*, *ApJ*, **178**, 319

Toomre, A. & Toomre, J., 1972, *ApJ*, **178**, 623

Vader, J. P., Vigroux, L., Lachieze-Rey, M. & Souviron, J., 1988, *A&A*, **203**, 217

van Dokkum, P. G., 2008, *ApJ*, **674**, 29

Van Waerbeke, L., Mellier, Y., Erben, T., Cuillandre, J. C., Bernardeau, F., Maoli, R., Bertin, E., Mc Cracken, H. J., Le Fèvre, O., Fort, B., Dantel-Fort, M., Jain, B. & Schneider, P., 2000, *A&A*, **358**, 30

von Hippel, T., Storrie-Lombardi, L. J., Storrie-Lombardi, M. C. & Irwin, M. J., 1994, *MNRAS*, **269**, 97

Wadadekar, Y., 2005, *PASP*, **117**, 79

Wagg, J., Wilner, D. J., Neri, R., Downes, D. & Wiklind, T., 2005, *ApJL*, **634**, L13

Wake, D. A., Nichol, R. C., Eisenstein, D. J., Loveday, J., Edge, A. C., Cannon, R., Smail, I., Schneider, D. P., Scranton, R., Carson, D., Ross, N. P., Brunner, R. J., Colless, M., Couch, W. J., Croom, S. M., Driver, S. P., da Ângela, J., Jester, S., de Propris, R., Drinkwater, M. J., Bland-Hawthorn, J., Pimbblet, K. A., Roseboom, I. G., Shanks, T., Sharp, R. G. & Brinkmann, J., 2006, *MNRAS*, **372**, 537

Way, M. J., Foster, L. V., Gazis, P. R. & Srivastava, A. N., 2009, *ArXiv e-prints*

Weymann, R. J., Storrie-Lombardi, L. J., Sawicki, M. & Brunner, R., 1999, *PASP*, **111**, 1188

White, S. D. M., Navarro, J. F., Evrard, A. E. & Frenk, C. S., 1993, *Nature*, **366**, 429

White, S. D. M. & Rees, M. J., 1978, *MNRAS*, **183**, 341

Wilkins, S. M., Hopkins, A. M., Trentham, N. & Tojeiro, R., 2008, *ArXiv e-prints*

Williams, D. A., 1998, in *Chemistry and Physics of Molecules and Grains in Space. Faraday Discussions No. 109*, pp. 1–13

Willmer et al., 2006, *ApJ*, **647**, 853

Wirth et al., 2004, *AJ*, **127**, 3121

Wittman, D. M., Tyson, J. A., Kirkman, D., Dell'Antonio, I. & Bernstein, G., 2000, *Nature*, **405**, 143

Wolf, C., Meisenheimer, K., Rix, H.-W., Borch, A., Dye, S. & Kleinheinrich, M., 2003, *A&A*, **401**, 73

Wray, J. J. & Gunn, J. E., 2008, *ApJ*, **678**, 144

Yamauchi, C., Ichikawa, S.-i., Doi, M., Yasuda, N., Yagi, M., Fukugita, M., Okamura, S., Nakamura, O., Sekiguchi, M. & Goto, T., 2005, *AJ*, **130**, 1545

Zucca, E., Pozzetti, L. & Zamorani, G., 1994, *MNRAS*, **269**, 953

Zwicky, F., 1933, *Helvetica Physica Acta*, **6**, 110